UNIVERSITÉ DU
LUXEMBOURG

PhD-FSTM-2022-147
The Faculty of Science, Technology and Medicine

DISSERTATION

Defence held on 13/10/2022 in Belvaux

to obtain the degree of

DOCTEUR DE L'UNIVERSITÉ DU LUXEMBOURG

EN CHIMIE

by

Enzo MORETTO

Born on 21 November 1993 in Thionville, (France)

Toward regio-selectively modified dendritic silica filler for tire tread rubber reinforcement

How silica particles silanization and morphology affect mechanical properties in tire tread rubber

Dissertation defence committee

Dr Maël GUENNOU, Chairman
Assitant Professor, Université du Luxembourg

Dr Laurent VONNA, External member
Maitre de Conférence à l'Université de Haute-Alsace (UHA)

Dr Benoît DUEZ, External member
Chief Engineer Analytical Science Luxembourg at The Goodyear Company

Dr Damien LENOBLE, Supervisor
Director Material Research and Technology department (MRT) at LIST

Dr Jean-Sébastien THOMANN, Member
Group Leader of the Powder and Colloid Engineering group (PaCE) at LIST

Abstract

Tires are essential to our societies as transportation of people and goods are keys to our economies and social interactions. They need to provide satisfying performances in terms of safety, service life and fuel consumption simultaneously. The famous “magic triangle of tire tread” is constituted of the three main parameters that define a tire tread performance level: wet traction, abrasion resistance and rolling resistance. To overcome the boundaries of this triangle requires constant research and engineering work, as these properties work against one another. For instance, lowering the rolling resistance allows to reduce fuel consumption, but also reduces wet grip performances and therefore compromises safety.

The introduction of silica fillers in combination with silane coupling agents is the major innovation that helped to mitigate this issue. It provides better wet traction as well as rolling resistance compared to regular carbon black compounds. The drawback of silica is its tendency to form aggregates in rubber via its polar hydrophilic groups: silanols. They prevent silica particles from interacting with non-polar hydrophobic polymers commonly used in tires. The effectiveness of a reinforcing filler arises from its ability to create a percolating network and to interact with the polymer chains of the matrix. Therefore, silanes are essential to silica for rubber reinforcement. They chemically react with both the silica particles and the polymer chains and grant silica a great dispersibility by converting polar silanols to non-polar organic moieties. They also enable silica particles to become crosslink points in the rubber composites through the reaction of the silane with the polymer chains. Currently, state of the art silane-silica filler systems consist in 10-50 nm silica particles. Upon mixing in rubber matrix, they form a fractal percolating network. The silane carries a sulfide moiety that allow the silica-rubber crosslinking reaction. The limitation of such system resides in two aspects. First, the use of a single silane providing simultaneously coupling and dispersion of the filler prevents to optimize both of these parameters. Secondly, the constitutive aggregates of the percolating network may be subjected to dislocation under stress. This causes unnecessary energy dissipation and irreversible weakening of the material over time. Addressing these two problematics is of great interest for the improvement of tire rubber performances.

For this reason, the present doctoral thesis aims to study and understand the influence of silica surface modification and morphology over mechanical properties of a tire tread rubber compound and more specifically its wet grip, abrasion and rolling resistance indicator. Firstly, we investigated the activation potential of two strong bases, namely sodium hydride and DBU, on silica surface reactivity toward silanization. Then, we studied the effect of coupling and dispersion role dissociation as well as silane length on rubber mechanical properties by synthesizing new dual-silane pre-treated silica fillers. Finally, we present the synthesis of a unique regio-selectively modified dendritic silica and studied the

behavior of the subsequent composite materials by assessing the effect of particle porosity and chemical modification.

Our findings show that the dissociation of coupling and dispersive silane greatly impact rubber properties. The combination of short mercapto and alkylsilane has proven to improve wet grip of composite with a stable rolling resistance indicator. On the other side, the use of longer alkylsilane completely changed the polymer-filler dynamic and resulted in phase segregation around fillers and poor reinforcement. Finally, the spatial segregation of coupling and dispersive function with the newly synthesized regio-selective modified dendritic silica particles induced remarkable changes in the reinforcing behavior. When compared to equivalent non-porous and non-modified silica particle, the permeation of polymer chains in the porous structure and their crosslinking with the coupling silane enable reinforcement while near-perfect dispersion is ensured by the dispersive silane on the outer surface. Unfortunately, this reduces the filler-filler interaction and consequently limit the reinforcement of the rubber. The introduction of a small amount of the fractal filler allowed to fill the gaps between the bigger porous particles. It proved to drastically improved the inter-particles interactions, and thus the reinforcement and dynamic properties of the material beyond previous levels. This work puts light on the potential of porous silica and dual-fillers systems as potent filler for tire tread rubber.

The outcomes of this doctoral thesis participate to better understand the impact of chemical and morphological modifications of silica filler surface, and how it can serve the improvement of the filler technology for the tire industry. It develops the use of porous silica particles as potent fillers for tire tread rubber and brings new insights on reinforcement mechanisms as well as new possibilities in filler architecture and chemistry.

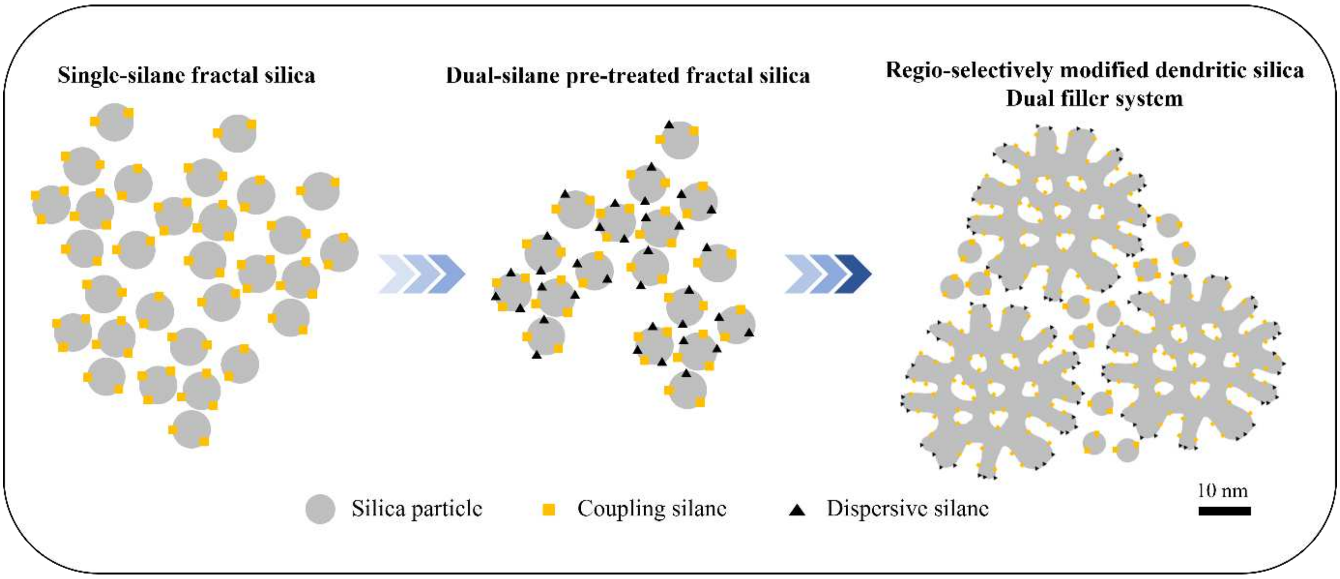

Acknowledgements

This doctoral thesis has been conducted within the Powder and Colloidal Engineering (**PaCE**) research teams, at the Material Research and Technology (**MRT**) department of the Luxembourg Institute of Science and Technology (**LIST**). The supervisor of this doctoral thesis is Dr. Damien LENOBLE. The co-supervisor of this doctoral thesis is Dr. Jean-Sébastien THOMANN.

I would like to thank the Fond National de la Recherche Luxembourg (**FNR**) for the fundings that enabled me to pursue my research.

I would like to offer my special thanks to the Goodyear company for this rich and challenging research opportunity. More particularly, the advice and experience of Dr. Georges Thielen were greatly valued.

I would like to express my gratitude to Dr. Sivashankar KRISHNAMOORTHY for his diligence and continuous support during my time at LIST.

I wish to acknowledge the help and support of Dr. Emmanuel SCOLAN. If not for him, I would not have had the chance to work at LIST.

To Dr. Vincent BERTHE, I would like to express my gratitude for his help and support in the field of polymers processing.

Big thank you to Régis VAUDEMONT and Benoît MARCOLINI. Their expertise, willingness, and support in the field of thermal and mechanical characterization of composite have been essential during these four years.

To the team members of the PaCE group, Dr. David DUDAY, Dr. Didier ARL, Dr. Apostolos KARANASTASIS, I would like to express my gratitude for their help, support, inspiring discussions and critics.

My work at LIST would have been much harder without the daily assistance provided by the MRT Support team, to who I would like to express my gratitude. A special thanks Asmaa EL MOUL and Maud PHILIPPS. Their precious technical expertise, availability and support have been essential to this work.

The assistance and expertise provided by the MRT Advanced Characterization Platform was essential for the success of this work. I would like to thank Patrick GRYSAN, Dr. Nathalie VALLE, Jérôme BOUR, Dr. Gilles FRACHE, Jean-Luc BIAGI, Esther LENTZEN, Brahime EL ADIB and Dr. Adrian-Marie PHILIPPE for their help and support.

A special thanks to all my co-authors: Dr. João Paulo Cosas FERNANDES, Dr. Carlos Eloy FEDERICO, Dr. Mariapaola STAROPOLI, Dr. Jean-Nicolas AUDINOT, Charlotte STOFFELS, Dr. Vincent ROGE, Dr. Reiner DIEDEN and Dr. Chuanyu YAN. Thanks to their expert advice and knowledges, we produced together excellent research outcomes. I am glad to have had the opportunity to collaborate with you. It shows that research cannot be carried alone, and the best results come from teamwork and exchange.

To all my office mates, colleagues but first and foremost friends: Dr. Lauriane CHUZEVILLE, Dr. Tairan DA CUNHA, Dr. Vincent ROGE, Dr. Adrian-Marie PHILIPPE, Nicolas BELLOMO, Charlotte STOFFELS, Nassim CHEKIREB, Dana EL ASSAD, Ahilan MANISEKARAN and Joffrey DIDIERJEAN. I am glad to have met you. For work and for non-work activities, your presence and words made these four years in Belval some of the best so far. I wish you all great success and happiness!

To Dr. Benoît DUEZ and Pascal STEINER, from the Goodyear company, I would like to express my thanks. Their scientific and industrial expertise helped me greatly for my research.

Special thanks to my CET members, Dr. Benoît DUEZ, Dr. Damien LENOBLE, Dr. Jean-Sébastien THOMANN and Pr. Giusy SCALIA. Their guidance and support during my doctoral studies help me to steer in the right direction.

To my PhD thesis director, Dr. Damien LENOBLE, I would like to express my gratitude. His precious advice, support and guidance were essential to the success of this PhD. Thank you, Damien.

I am especially grateful to my PhD thesis supervisor and PaCE group leader, Dr. Jean-Sébastien THOMANN. During these four years of doctoral studies, his support, advice, knowledges, patience, and daily availability have been essential to the success of this research project. Thank you for all the discussions we had and all the good moments. I am proud to have been your student. I wish you all the best for your up-coming projects.

To my parents and my sister, thank you for your long-lasting support. I also here now thanks to all the things you offered me in life.

Finally, Cécile, you have alongside me every day since the beginning of this adventure. Thank you for your relentless support and kind presence. I cannot wait for our up-coming projects!

General Introduction

The organization of our societies and health of our economy heavily rely on road transportation to ship goods and transport passengers. Today more than even before, the decreasing fossil fuel reserves capacity and the already existing severe consequences of our fast-changing climate call for a drastic shift in the way we consume energy. Even with a hypothetical mass electrification of transportation, fuel efficiency remains critical for transportation. Being the only parts of vehicle in contact with the road, tires have an important role to play in fuel efficiency. Low rolling resistance tire are not new, but ever increasing regulatory and consumer pressure push the tire manufacturers to improve their rolling resistance performances, without compromising the safety and durability of their products. The tire technology has been rich in innovations and technologies development. Originally, primitive tires were made from leather and tightly fitted on bicycle wheel rims. The first practical pneumatic rubber tire was made in 1888 by John Boyd Dunlop. Pneumatic tire development also brought improvement to the vulcanization process that had been discovered by Charles Goodyear in 1839. Initially made from natural rubber, shortage in natural latex production helped the invention and production of synthetic rubber by Bayer in 1920. In 1946 the French company Michelin developed the radial tire construction, bringing better handling and lowering fuel consumption.

Modern tires are still made of natural rubber and/or synthetic rubber, while colossal advances have been made on the production of the building materials and the tuning of their properties. Built around its supporting structure - the carcass, a tire consists of an assembly of various rubber pieces, each with different composition in rubber, fillers, and additives. These parts can be reinforced with fabric, may it be natural (cotton) or synthetic (nylon, polyester, polyaramid), and steel cords, especially for truck tires. The part in contact with the rim is called the bead and is usually a coil of steel wire encapsulated in rubber. Finally, the tread is the part in contact with the road. Due to the different solicitation a tire must face, may it be physical or chemical, additives allow it to withstand oxidation from ozone and dioxygen, wear, low and/or high temperature, acceleration, and break. Tire performances were pushed due to increasing requirement level in safety, road performance and cost.

This PhD thesis focuses on the silica filler technology, its silanization and the impact it has on the filler and rubber dynamic, and ultimately the composite materials properties. Silica has been used for tire from the 1940s in combination with carbon black, but the introduction silanes coupling agents really unlocked the potential of silica fillers. They quickly brought drastic improvement in road grip and rolling resistance, as silanes really improved this system by hydrophobizing the mineral filler surface. It ensured good dispersion in the organic polymer matrix, as well as enabling the covalent coupling of silica rubber, hence the name "coupling agents".

The reinforcing effect of fillers originates from their capacity to affect the polymer chains dynamic in the composite material. The interaction of fillers with their neighbors, as well as with the rubber chains are the underlying phenomenon responsible for the viscoelastic performances of a rubber composites. As silanes directly affect the interfacial properties of silica fillers, the study and understanding of silica silanization and its consequences on viscoelastic properties is key to tire tread rubber reinforcement. Finally, the morphology of the silica filler is a determining factor that dictates the dynamic of the filler network under stress in the composite. Silica is versatile material which can be synthesized in many ways. The sol-gel synthesis of mesoporous silica particles is especially interesting as it yields high surface area fillers of various size and geometry. Because the silica fillers network of rubber composite is such an important factor for the viscoelastic properties and the reinforcement of the material, mesoporous silica particles have an unexplored potential for research as well as for industrial applications.

Aim of the thesis

The purpose of the investigations presented in this doctoral thesis is to explore new methods of reinforcement and improvement of the viscoelastic properties of silica-filled tire tread composites, as well as understanding the reinforcing effect of chemically modified porous silica fillers. Bringing new knowledge in the field of filled tire rubber will help the development of new processes and technology to face the current technological challenges but could also benefit to other area in which the understanding of fillers chemistry and reinforcement dynamic is relevant. We studied the potential of porous silica fillers for tire rubber reinforcement, for which surprisingly few research works could be found despite the extensive interest and literature about mesoporous silica particles for all sorts of domain in material science.

Structure of the thesis

The first chapter establishes the state of the art in the field of silica filled rubber and sol-gel synthesis of porous silica particles and silanization. The background of the tire technology, the physical formalism and theory of viscoelastic properties, as well as the background in filler science and silica synthesis are presented.

The results of the research work are presented in Chapters 2 to 4, which consists in three different peer-reviewed articles published or submitted in scientific journals. Chapter 2 deals with the enhancement of silica filler reactivity with original basic catalysts for silanization. Chapter 3 discusses the impact of the separation of the silane’s coupling and dispersive functions on silica filler. The effect of silane combinations over the interfacial properties of the fillers was studied and the subsequent filler-rubber interactions and composite mechanical properties assessed. Chapter 4 presents the synthesis of a new silica filler architecture consisting of regio-selectively modified dendritic porous particles, its full characterization, and the implication of such a filler over the dynamic mechanical properties and reinforcement of a tire tread rubber composite.

This PhD thesis has been conducted at the Luxembourg Institute of Science and Technology (LIST) within the framework of the TireMat project, a partnership with The Goodyear Company.

Table of Contents

Literature review

1 Tire technology

1.1 Tire composition and structure

Many vehicles use tires, from planes, cars, trucks, buses, motorbikes, bicycles, construction work vehicles and specialized vehicles. Not one tire can fit all these usage conditions, hence the diversity of tire construction and composition. This chapter aims to give an overview of what a tire is made of and how it is build, focusing on pneumatic tires for trucks and cars.

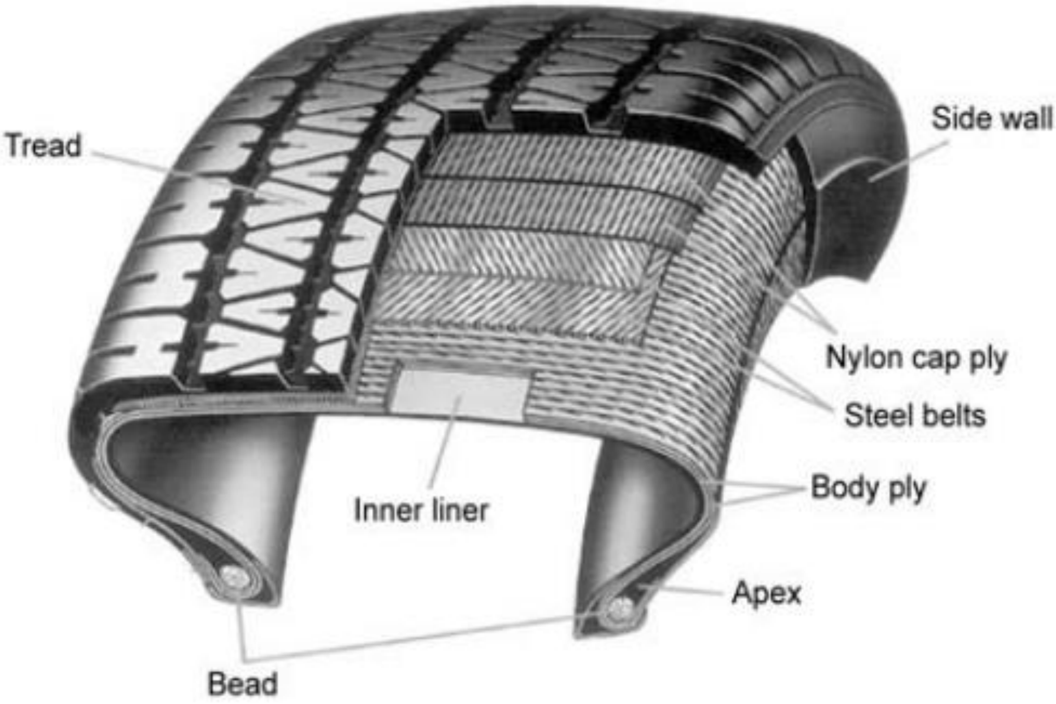

Figure 1. Cross-view schematic of a radial tire[1].

A pneumatic tire consists of a body providing containment for the compressed air and choc absorption, and a tread which is the part in contact with the road, providing traction. A cross-view schematic of a tire in **Figure 1** shows the different constituent elements of a pneumatic tire. This representation shows well the complexity of such object. A tire is an assembly a many different parts made from steel cords, textile fabrics embedded in rubber compounds, and held together by the crosslinking of the latter under high heat and pressure during the vulcanization process. The composition of two different kinds of tires is presented in **Figure 2** below.

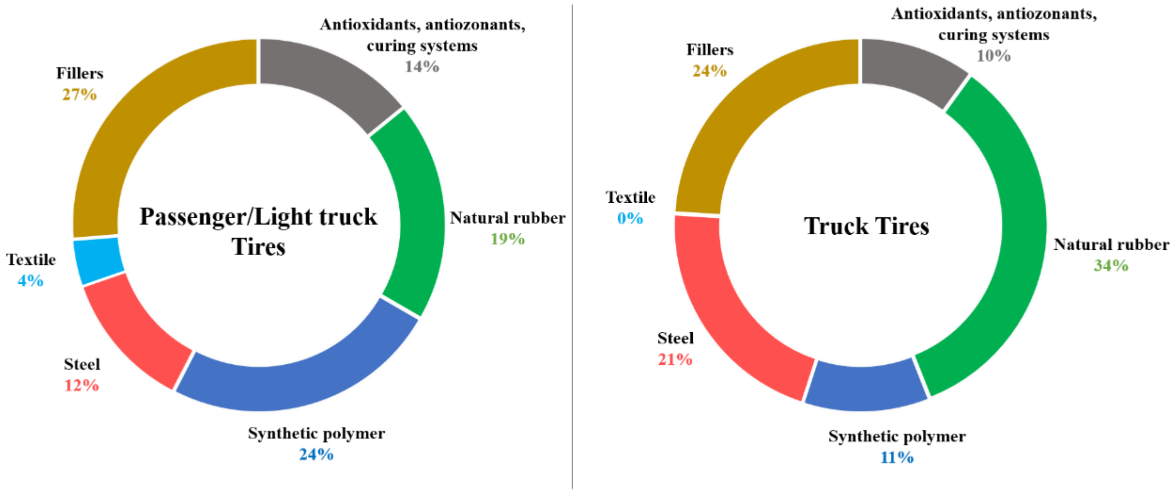

Figure 2. General composition of passenger and truck tires (Reproduction from U.S. Tire Manufacturers Association).

Because trucks carry heavier loads, their tires require stronger materials, like steel instead of synthetic textile fabrics, and more natural rubber, as this polymer provides stronger and more durable compounds than synthetic alternatives. Within a tire, each part is meant to respond to a different solicitation and specific materials are used to provide adequate responses. The inner liner is the layer making the tire air-tight and is in contact with the compressed air. For this reason, it must be more resistant to oxidation and is usually made of halobutyle rubber, a halogenated polymer, which is especially resistant to oxygen and show efficient sealing properties. The apex, where the bead sits, is the part in contact with the rim of the wheel. It is designed to withstand high loads and temperatures. The body ply, steel belts and nylon cap ply are rubber-coated fabric playing a structural and reinforcing role. The cohesion of the rubber with the reinforcing fabric is essential for safety and performance. The side walls are the lateral outer-part of the tire. They protect the inner elements from mechanical tear and wear, as well oxidation from ozone or UV light. Finally, the tire tread, which is the only part of a tire in contact with the road, has a critical role in the tire behavior and performances. The shape and density of the tread pattern are important parameters that enables to design the tire to face different temperature and weather conditions. Equally, the composition of rubber constitutive of the tread will allow for a wide range of properties. A tire tread should be able to evacuate accumulated static charges, provide good road traction for cornering and breaking in any condition, resist to wear for high durability, and have a low rolling resistance to reduce fuel expenditure. These last three characteristics especially are what shapes the so-called “magic triangle” in the rubber industry.

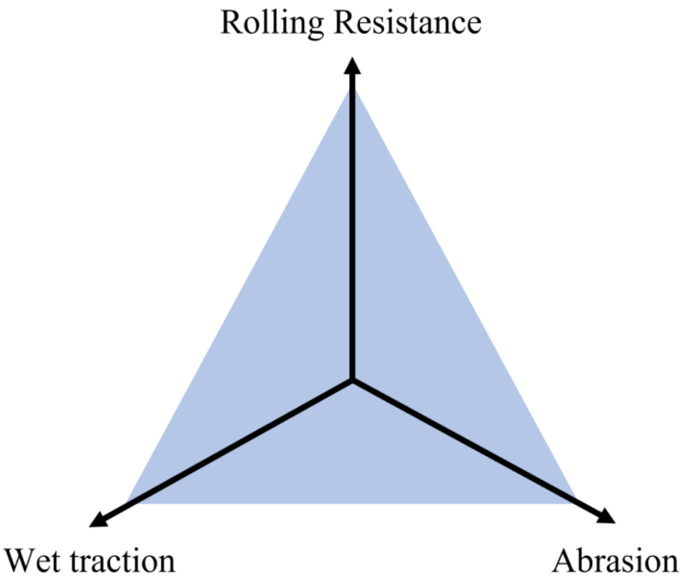

Figure 3. Tire "magic triangle" schematic.

This triangle represents the three major properties of a tire tread and their contradictory mutual relationship. Improving one property will reduce performances in the other two, the wet traction-rolling resistance antagonism being the most predominant one. This triangle illustrates the major challenge in the improvement of tire tread performances. Different research lines have explored solutions like new resins, [2] polymers,[3] innovative fillers systems,[4] the use of grounded tire rubber (GTR),[5] to solve this challenging task. Especially, the introduction of silica particles along carbon black as a reinforcing filler enabled such improvement in several instances, as silica-filled rubbers demonstrated better rolling resistance, similar or higher wet traction and un-changed abrasion resistance. Indeed, the intrinsic properties of silica and the vast potential for modification, may they be chemical or morphologic, make it a major focus in the tire industry and a vast research area with many opportunities for promising advances.

1.2 Rubbers – Chemical and physical properties

Elastomers, meaning elastic-polymer, also denominated rubbers after vulcanization, provide damping and strength to the tire via their viscoelastic properties. The word rubber is now commonly used to designated synthetic polymers and other materials that have properties similar to natural rubber. Historically only natural rubber (NR), consisting mainly in the cis-1,4-polyisoprene isomer (over 99%), was obtained from the latex tree *Hevea brasiliensis* and used for the first tire at the beginning of the industry. The isomer trans-1,4-polyisoprene has different properties and is produced by other tree species like *Palaquium gutta* and *Manilkara bidentata*. Natural rubber is still widely used today, mainly for truck tires. But other polymers, synthetic ones, have been used pushed by the supply difficulties of natural rubber and along with the development of petrochemistry, enabling the production of specific polymers for specialized applications. In **Figure 4** are displayed some of the chemical structures of the main polymers used in a tire.

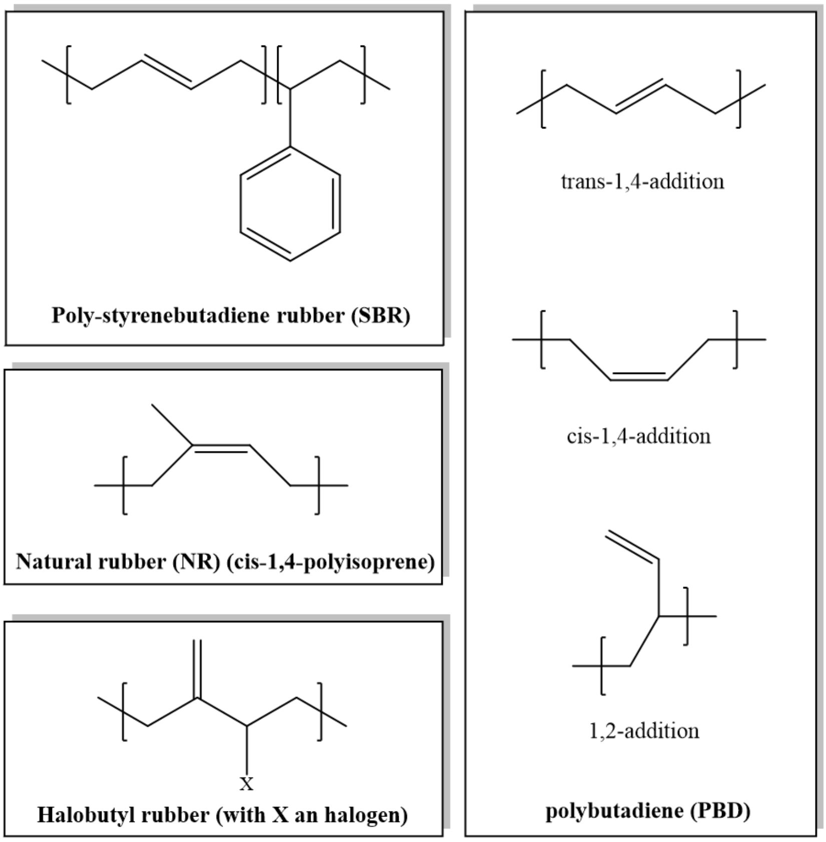

Figure 4. Structures of common polymers used in tires.

Cis- polymers are especially interesting for tire application because of their elastic properties. Indeed, cis-double bonds in polymers allow for less linear chains and therefore lower crystallinity. Consequently, the amorphous part in these polymers is higher, which benefits to the elastic properties needed for tires. From a chemical perspective, the presence of carbon-carbon double bonds is essential for the vulcanization process. It consists of the crosslinking of polymer chains via the reaction of C=C bonds and elemental sulphur. Vulcanization is the chemical reaction that gives the rubber its visco-elastic properties by creating a 3D-crosslinked network of polymer chains. The fundamentals of this reaction are developed and presented in the following sub-chapter.

1.2.1 Vulcanization of rubbers

The term “vulcanization” designated the chemical reaction using sulfur that allows the crosslinking, or covalent bonding, of polymer chains. This creates intermolecular bonds between polymer chains that are then dependent from one another.

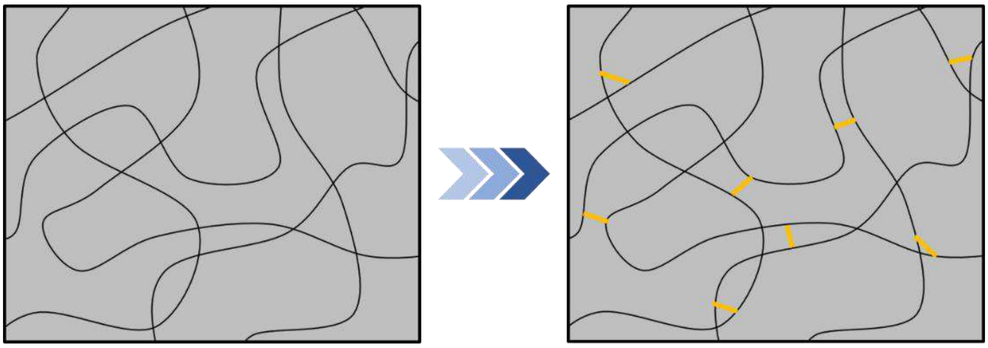

Figure 5. Schematic of sulphur vulcanization of an unsaturated rubber

This reaction is carried at high heat and under pressure. The vulcanization of rubber drastically improves their mechanical properties in terms of strength, elasticity, toughness, and also chemical resistance. It was quickly realized that the use of sulfur alone was not enough, even though crosslinked compounds were clearly over-performing uncured rubbers. It was discovered that the use of various amines worked similarly as aniline [6] as accelerators for vulcanization. There is now a wide variety of accelerators. Some of them are used together and yields significantly better curing.[7] Zinc oxide is also a mandatory chemical as it is considered the best activator for sulfur vulcanization.[8]

Compound	Abbr.	Structure
Benzothiazoles		
2-Mercaptobenzothiazoles	MBT	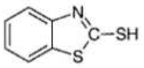
2,2'-Dithiobenzothiazole	MBTS	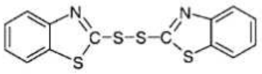
Benzothiazolesulfenamides		
N-Cyclohexylbenzothiazole-2-sulfenamide	CBS	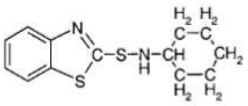
N-tert-butylbenzothiazole-2-sulfenamide	TBBS	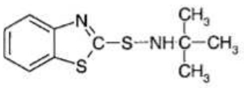
Thiurams		
Tetramethylthiuram disulfide	TMTD	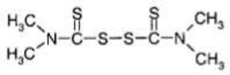
Dithiocarbamates		
Zinc dimethyldithiocarbamate	ZDMC	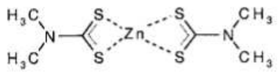

Figure 6. Common accelerators used for sulfur vulcanization.[9]

The mechanism for the chemical reaction of sulfur crosslinking is complex and still the subject of interrogations. It is suggested that it is a mix of radical and ionic mechanism. The figure below presents one possible mechanism for ionic accelerated sulfur crosslinking reaction of an unsaturated polymer.

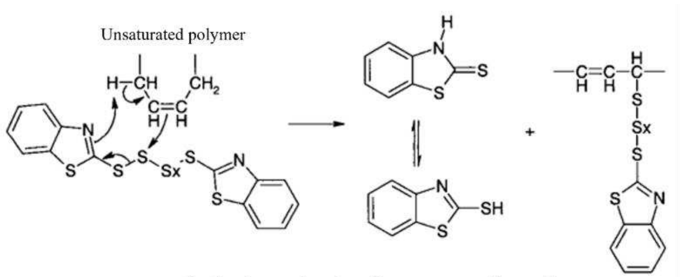

1 - Ionic mechanism for precursor formation

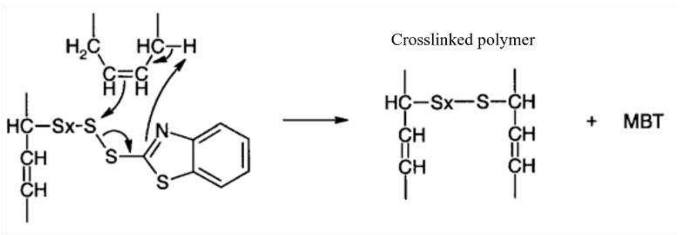

2 - Ionic mechanism for crosslink formation

Figure 7. Possible mechanism for a ionic crosslinking reaction.[9,10]

The increasing amount of crosslink points leads to the stiffening of the material. The vulcanization process of a rubber compound can be followed by measuring its rheological properties during the cure, using a heated moving dye rheometer. Heat and mechanical deformation are applied to the compound, and the torque response is recorded. A typical curing curve is shown in **Figure 8** below.

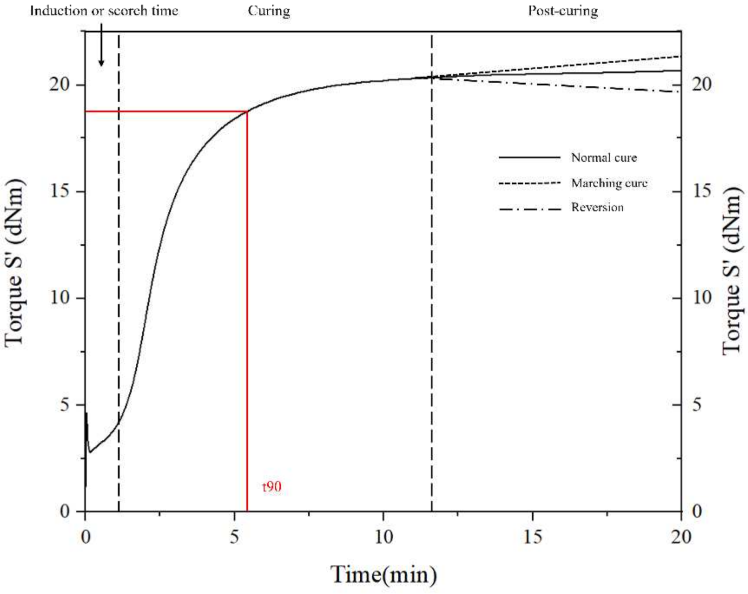

Figure 8. Torque response during vulcanization of a rubber compound.

The vulcanization temperature can vary from 90 to 170°C depending on the size of the tire. During the first seconds, the rubber softens due to the heat, before the vulcanization takes over. This delay is usually called “scorch time”. It is a critical parameter as it defines the time window during which the shaping of the rubber is still possible before its irreversible stiffening with the progressing cure. Then, the torque response of the compound increases with the amount of crosslink generated. The time at which 90% of the maximum torque is reached is called t90 and is usually used as an indicator of the reaction speed. Finally, the vulcanization reaches a plateau. In optimal condition, no reversion nor marching curve is observed. Mastering the cure behavior of a rubber compound is essential to ensure the right final properties as well as to optimize the process. For a whole tire, not all parts have the same thickness nor cure behavior, and thus the reaction may last shorter or longer. The challenge resides in obtaining a homogenous vulcanization across the tire, yielding the targeted properties. Upon vulcanization, the rubber compound gains its viscoelastic properties. This is a major change in the mechanical properties. The sub-chapter 1.2.3 presents the basis of rubber viscoelastic properties and implications on tire tread properties.

1.2.2 Thermal behavior of polymer and rubbers

Polymers see their mechanical properties vary with changing temperature. They can behave as solids, soften, and even melt. The temperature of the material directly affects the mobility of its constitutive macromolecules. At low temperature, the molecular mobility is low, and the material behaves as a glassy solid. The chains mobility increases with temperature, and the polymer softens and can even melt at sufficiently high temperature. Most polymers present a glass transition temperature T_g at which the material transitions from a glassy solid to a soft rubbery solid. The glass transition happens in a range of temperature rather than an exact one. Polymers also present a melting temperature T_m at which it becomes a viscous liquid. The state of the polymer has direct consequences on its mechanical properties, has seen in **Figure 9** below.

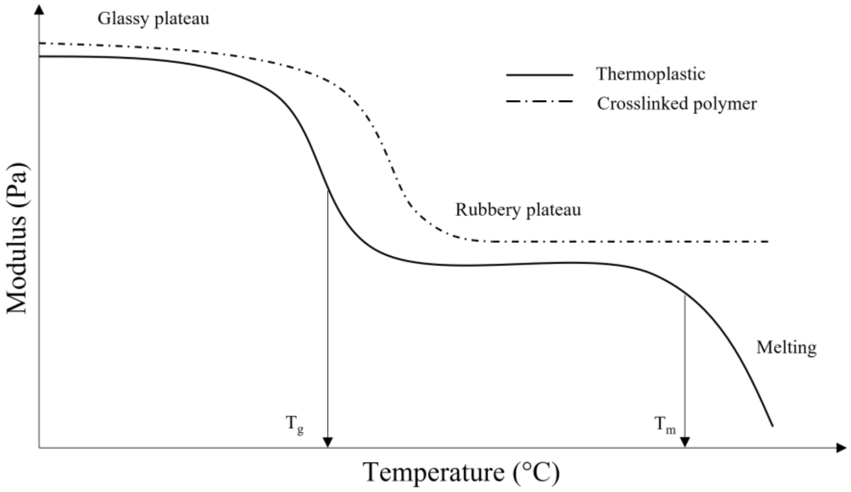

Figure 9. Evolution of polymer module with temperature.

Though their mobility is affected by the temperature, macromolecules interact physically with each other depending on their chemical structure. Consequently, the glass transition temperature and the height of the glassy and rubbery plateau are a consequence of the nature of the polymer. For example, the T_g of polyethylene sits around -100°C whereas the one of polystyrene is around 90°C. This is because unlike polyethylene, polystyrene chains are held together via Pi-stacking of their styrene ring, limiting the chain mobility, and increasing the energy required to allow the motion of the polymer chains. It has to be noted that T_g is also affected by the molecular weight of the chains. Longer chain will have lower mobility than smaller ones. The crystallinity of a polymer also plays an important role. The higher the crystallin volume fraction, the higher the modulus. Finally, the notable difference between thermoplastic or un-cured polymer, and crosslinked polymers, is the absence of melting. The degree of crosslinking of a polymer increases the modulus of its rubbery plateau, and crosslinking in general prevents the inter-connected polymer chains from a too high mobility, synonym of melting. Upon increasing temperature, a crosslinked polymer will degrade and burn rather than melting.

Understanding the thermal behavior of rubbers is of major importance as it enables to design the material for specific temperature range and properties. Indeed, the glass transition defines the temperature at which the material starts to change from a solid-like behavior to a rubbery one. For application such as winter tires, the choice of lower T_g rubber is necessary to ensure that the tire will remain soft and rubbery in colder climate.

1.2.3 Viscoelastic properties of rubbers

Viscoelasticity is the property of a material to present simultaneously elastic and viscous behavior when subjected to a deformation or a stress. A hypothetical purely elastic material will deform under an applied stress and return back to its initial state when the stress is released. On the other hand, a viscous material deformation is permanent and is characterized by the dispersion of energy involved in this deformation. A viscoelastic material combines these two behaviors. Under stress, it will deform and then come back at its initial state, but energy losses will be observed in the process.

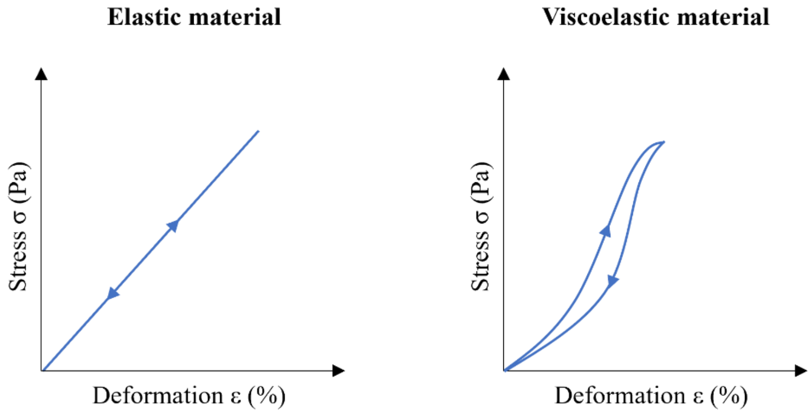

Figure 10. Representation of elastic and viscoelastic behavior.

For the viscoelastic material, the area in between the two curves represents the dissipated energy as heat during the deformation. This is also called a hysteresis loop. The simplest model allowing to represent both elastic and viscous properties of a material is the standard linear solid (SLS) model or Zener model. It consists in a combination of ideal springs and dampers, in series and parallel, that model these two ideal behaviors.

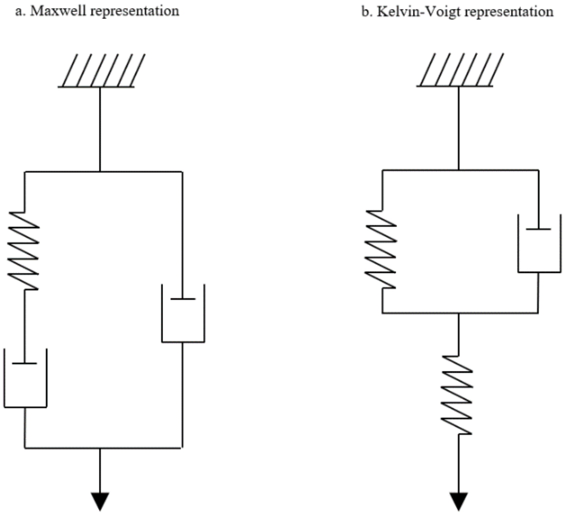

Figure 11. Zener or SLS model - Maxwell (a) and Kelvin Voigt (b) representations.

Upon stress, an ideal spring will deform instantaneously but the damper will slow its motion and dissipate energy. The combination of spring and damper also allow to model the unloading of the material: the spring pulls back to come back at its initial state and the damper dissipate energy again.

This model is a good representation to understand viscoelastic behavior but is too simple to predict complex real materials behaviors.

In real materials, elastic properties arise from the stretching of bonds and viscous properties from the motion and diffusion of molecules. In un-cured elastomers and thermoplastics, intermolecular bonds like Pi-stacking of aromatic rings in polystyrene or hydrogen bonding in polyamides, macromolecules entanglements [11] and crystalline domain of semi-crystallin polymers contribute to give to these material some elastic behavior under stress. But these do not prevent the irreversible motion of polymer chains sliding and reorganizing, called “creep”, responsible for irreversible plastic deformation and energy dissipation. The reticulation of polymers, and the vulcanization of rubber specifically, by generating covalent bonds between polymer chains, limits creeping to chain segment in between crosslink points and gives the material its viscoelastic properties. The back-stress generated by the deformation of the structure and the covalent bonds generate the spring-like force responsible for return of the material to its initial state.

Overall, rubber mechanical properties are dictated by the motion of its polymer chains. They are affected by temperature as well as intra and intermolecular interactions at play in the material. The purpose of the addition of fillers in polymers is precisely to change the dynamic of the polymer chain under stress to change their behavior and bring better properties. The next chapter presents and describes in detail the materials used as fillers for rubber, their physical and chemical properties as well as their impact on the properties of rubbers.

2 Fillers and composites materials

The term filler designated a solid charge that is not soluble but dispersible in a main material. Fillers are used in many products, like paints, concrete, asphalt, paper and polymeric materials like adhesive, coatings, resins, plastics, and rubbers. Ideally, a filler must have a low price to reduce the cost of the overall material. But fillers are mainly used to modify the properties of the matrix they are mixed it. They can affect heat resistance, fire resistance, adhesion properties, oxidation and UV resistance, chemical resistance, color, transparency, dielectric properties, or mechanical properties. Fillers can be mineral particles, like clays, talc, or silica, or fibers, like glass or carbon fibers. Recently, organic bio-sourced fillers, like cellulose fibers and nanocrystals, or lignin particles, are receiving more and more interest in the research and in the industry, as the need to find renewable sources of materials is more and more present.

In this chapter we will present the current state of the art in the field of fillers for tire tread rubber. Then we will go into more details on the physical and mechanical effect of fillers on the polymer chains dynamic and how fillers change the properties of the rubber material and improve their mechanical performances.

2.1 Fillers for tire rubber

The fillers applied to the rubber for tire technology are diverse in nature as well as in shape. The main fillers that have been the subject either of research and/or industrial application are carbon black, sepiolite clay, cellulose fibers and nanocrystals, and lignin nanoparticles. The specific case of silica is developed in a specific chapter.

2.1.1 Carbon black

Carbon black is the most commonly used filler for reinforcing tire rubber. Introduced in 1904 as a replacement for high zinc oxide loadings in rubber blends, it led to the improvement of the wear resistance of the new compounds.[12] Nevertheless, zinc oxide is still used at small amount for the vulcanization of rubber. Today, carbon black is still widely used in tires, despite the share of silica growing due to the better rolling resistance and wet grip properties it brings to the material.

Carbon black is the product resulting from the incomplete pyrolysis of fossil hydrocarbons[13,14] or biomass[15,16] in dedicated furnaces. This material consists in aggregates made of colloidal spheres. These spheres result from the folding and stacking of graphitic units. The source of the raw material for the carbon black production as well as the production process conditions allow for a large variety of filler in term of particle size, surface area and chemistry.[13] **Figure 12** below presents a schematic of carbon black structure.

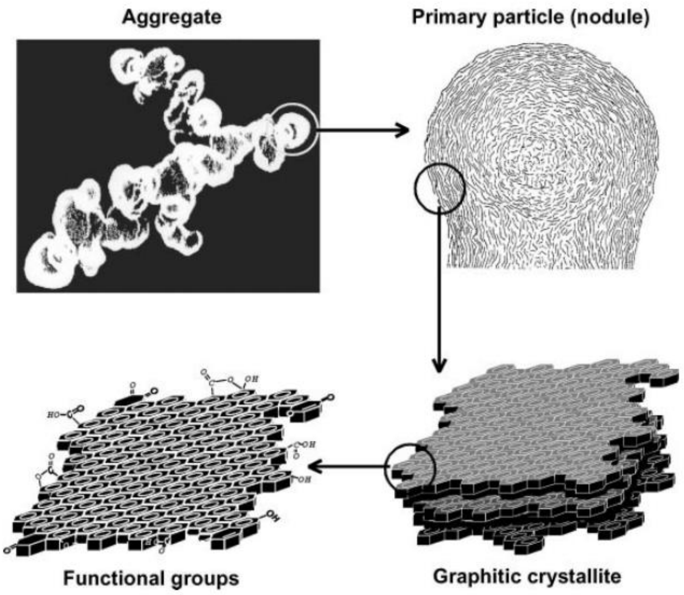

Figure 12. Carbon black structure.[14]

Carbon black by itself is better for rubber reinforcement than silica without silane coupling agents, because of its surface chemistry that naturally enables good dispersion and interaction with the polymer. Indeed, carbon black surface displays very few polar groups, and the aromatic cycles and non-polar hydrocarbons chains that constitute its structure positively interact with the non-polar rubber chains of synthetic or natural rubbers. Another important benefit of carbon black is its capability to convey electrostatic charges.[17,18] This property is crucial to discharge the static charges accumulating in the tire material as it rolls over the road surface.

2.1.2 Sepiolite clay

Sepiolite is a naturally occurring clay, primarily constituted of magnesium and silicon oxide. It comes in various mineral forms and compositions depending on the deposit. The basic structural unit is a TOT sandwich of silicate SiO^- tetrahedral sheets T with octahedral coordinated cation O in between (usually magnesium).

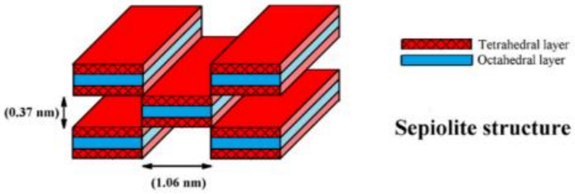

Figure 13. Sepiolite structure.[19]

But unlike other clays that present a 2D-lamellar structure, sepiolite is a phyllosilicate, meaning that the lamellar structure is elongated in one direction, giving sepiolite a needle-like structure.[20] The primary units are long crystal-like fibers of less than 100 nm in thickness.[21,22]

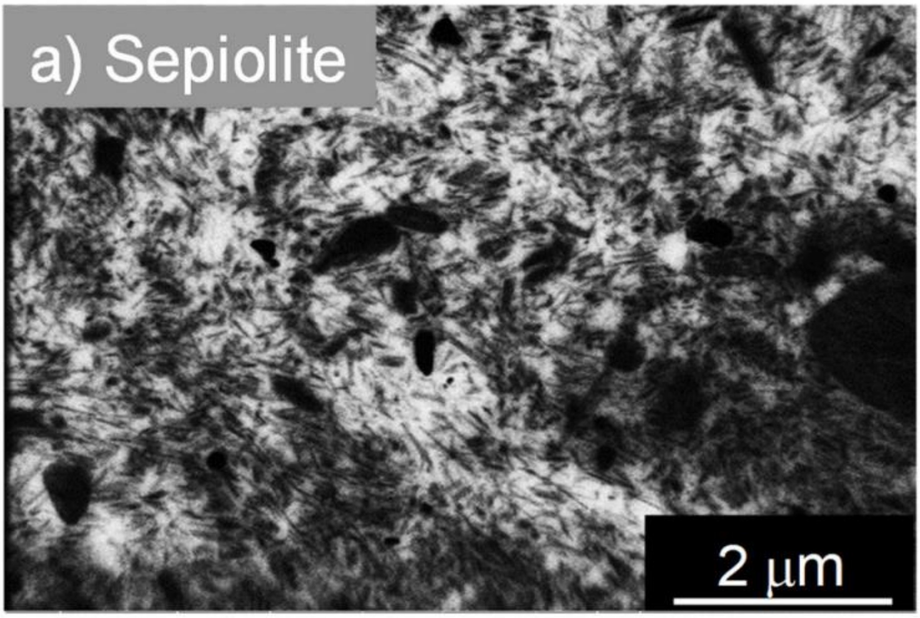

Figure 14. STEM image of sepiolite-SBR rubber composite.[23]

Naturally, these needles are bundled together in thick strands, and the use of quaternary ammonium salts allows to obtain readily dispersible filler.[24] In acidic water, the Mg^{2+} ion can be transferred into solution, transforming the corresponding silicate anions SiO^- into silanols Si-OH, necessary to silanization of sepiolite.[25] Like silica, bare sepiolite is not dispersible in a rubber matrix.[26] Sepiolite has been studied and implemented as a filler for thermoplastics[27,28] and rubber[23,29-31] reinforcement in several research works. The use of sepiolite has shown some improvement in the reinforcement and hysteresis reduction of tire rubber composite.[32]

In the second-author collaborative work entitled "*Hybrid Silica-Based Fillers in Nanocomposites: Influence of Isotropic/Isotropic and Isotropic/Anisotropic Fillers on Mechanical Properties of Styrene-Butadiene (SBR)-Based Rubber",* presented in the appendices, we have implemented the use of nano-sepiolite in SBR rubber compounds in the presence of a precipitated silica filler. We could show with imaging and dynamic mechanical properties measurement that the effect of the anisotropic sepiolite depends on the silica loading. The constrain of high silica loading forces the sepiolite rods to align, giving higher stiffness than sepiolite on its own. This result is key in understanding the important role of filler-filler interactions in composites and especially in hybrid systems.

2.1.3 Cellulose

Cellulose is natural polymer produced by living organisms like plants, fungi, or bacteria, as a structural component. It presents itself as a semi-crystallin fibers, whose aspect ratio and crystallin composition depend on the source.

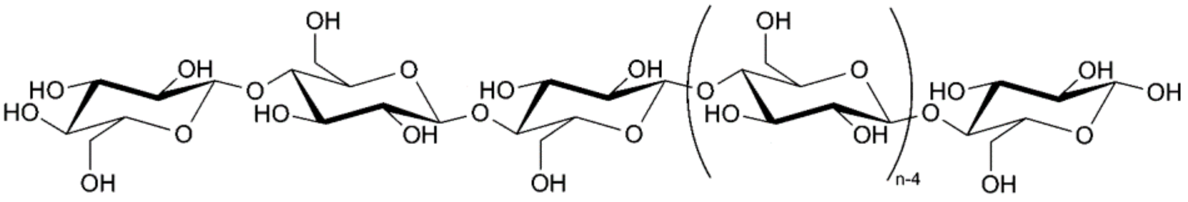

Figure 15. Chemical structure of cellulose.

For composite material reinforcement, cellulose is not used as such but is processed into cellulose nano-crystals.[33,34] These crystals are obtain by the hydrolysis of the amorphous fraction of cellulose by alkaline hydrolysis. They present several interesting properties. Their high strength, abrasion resistance, low density, the presence of reactive sites (mostly alcohols), coupled with a wide availability, a low cost and renewability make cellulose crystals a promising material for rubber reinforcement.[35-37]

Like silica, cellulose requires chemical surface modification to turn the alcohols into moieties beneficial either coupling or dispersion of the filler in a rubber matrix.[38-41] In combination with silica, cellulose crystals have shown to yield promising reinforcement properties to SBR and NR rubber composite.[42,43] The presence of cellulose also presented a plasticizer behavior, allowing to reduce mixing energy during tire production.[44] Because cellulose faces the same challenge of surface modification and compatibility with the rubber matrix, both cellulose and silica can benefits from the advances made in each field.

2.1.4 Lignin

In the late 2010's and since then, lignin is the other bio-polymer that has attracted a lot of interest in various research field, and especially in the nanomaterial and filler area. Like cellulose, it is a structural molecule produce by plants. Therefore, it is widely available at a low cost. Lignin designates a wide variety of polymers that are mainly constituted of phenolic units,[45] as seen in **Figure 16**.

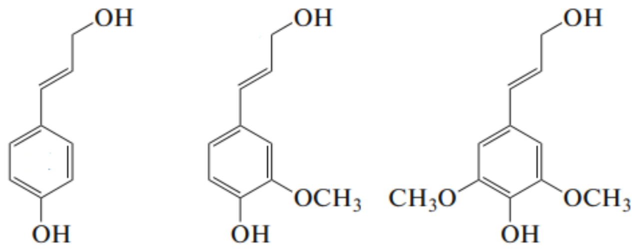

Figure 16. Constitutive phenolic units of lignin.[45]

The structure, composition and subsequent properties of lignin depend on the source and production process. Kraft Lignin is obtained by delignification of wood pulp during alkaline hydrolysis, followed by an acid precipitation.[46,47] This kind of lignin is well known for the formation of lignin particles and is especially interesting for the production of fillers.[48-50] Raw lignin has proven to be an interesting filler to increase the UV or oxidation resistance of rubber [51,52], to modified the aggregation behavior of SBR rubber.[53] So far, tire rubber reinforcement by lignin nanoparticles see only undirect application[54,55]. As the production of lignin nanoparticles is the subject of extensive research and development, one can expect to see significant progress made in the field of lignin-rubber nanocomposites research in the coming years.

2.2 Effect of fillers on the polymer chain dynamic and mechanical properties of rubber

The mechanical behavior of a polymer at the macro-scale is a consequence of the chain's mobility at the molecular scale. This mobility is affected by temperature, as seen previously, but also by the interactions between the macromolecules, like entanglements, hydrogen bonding or crosslinks covalent bonds. The presence of filler in a polymer adds new possible interactions, namely filler-filler and filler rubber interactions. These greatly contribute to affect the polymer chain dynamic and rubber properties.

2.2.1 Effect of the dispersion state on filler and rubber interactions

The dispersion state of the filler particle in the matrix is an important factor as it determines the surface area of particle in contact with rubber, as well as the amount of fillers interacting with their neighbors. The **Figure 17** below represents different possible aggregation states of a filler.

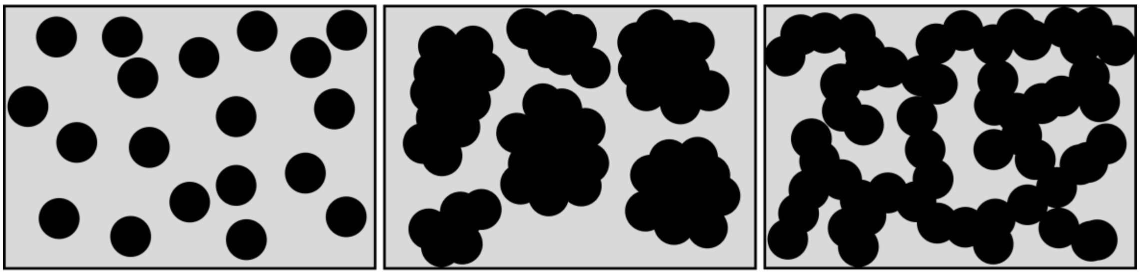

Highly dispersible

Highly aggregated

Percolating network

Figure 17. Schematic representation of different aggregation states of a filler in a matrix.

If the dispersibility of the filler is high, the filler-filler interaction is minimized, and the filler-rubber interaction is maximized. In the case of a filler susceptible to aggregation, the filler-filler interaction is maximized but the filler-rubber is minimized. When a percolating network of filler is formed, filler-filler and filler-rubber interactions are high. Additionally, the cavities formed by the filler network allows to trap rubber. The percolation state is reached when the particles form a network, capable of transmitting the deformation and stress of mechanical deformations.

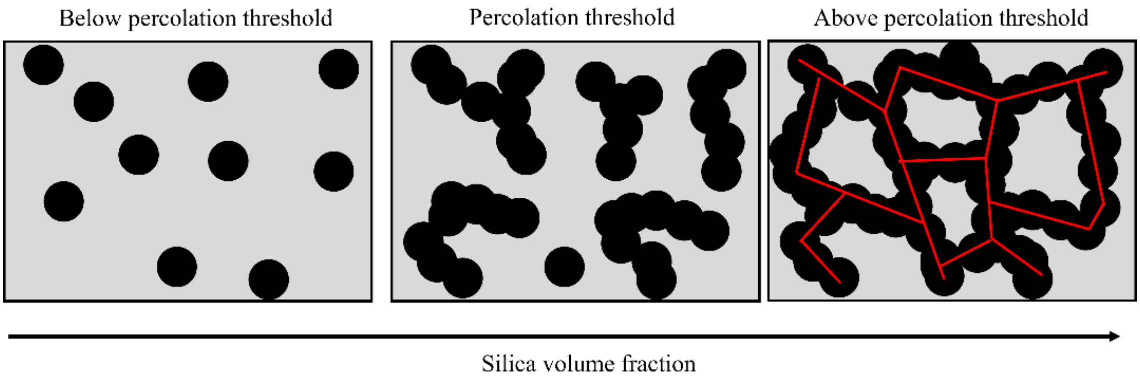

Below percolation threshold

Percolation threshold

Above percolation threshold

Silica volume fraction

Filler-filler interaction brings high reinforcement to the rubber composite thanks to the high contact forces involved, but the trade-off lies into the potential fragility of the filler structure under deformation, leading to reversible or permanent damages depending on the amplitude of the strain. This aspect is developed into more details with the Payne effect later in the manuscript.

2.2.2 Filler-rubber and crosslink interaction

In tire rubber, the covalent filler-rubber interaction is obtained with the use of coupling agents, namely silanes. This allows for more cohesion between fillers and polymer chains, especially at high strain. In the case of silica, it has been demonstrated that up to some extent, the surface modification of filler to increase rubber-filler interaction leads to the decrease of the filler-filler interaction and of the elastic modulus.[56] Indeed, covering particles with a coupling agent prevents the silica particles to interact with their neighbors due to the lack of silanol and hydrogen bonding.

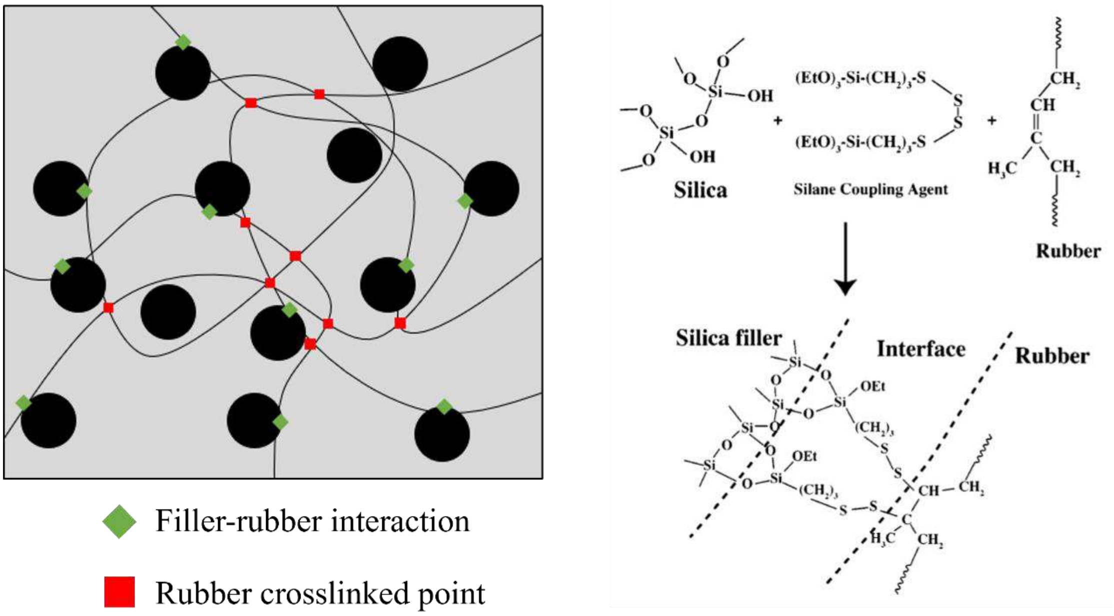

Figure 18. Schematic representation of rubber crosslinks and filler-rubber covalent bonds (left) and chemical structure of filler-rubber bond with a silane coupling agent.[57]

Rubber-filler crosslinks reduce the chain mobility. As a reaction to deformation, the limited motion of the rubber chain give rise to a back stress that pulls back in the material. This is what characterizes the elastic behavior of rubber, seen earlier in **Viscoelastic properties of rubbers.**

2.2.3 Effect of rubber and filler interactions on the elastic modulus

The addition of filler affects the polymer chains mobility and greatly increases its modulus. The modulus gain has two contributions. The first is strain-dependent and is based on the filler-filler interactions. This is called the Payne effect and is observed at small deformation (strain<10%).[58] The underlying phenomenon is the partial and reversible dislocation of the filler aggregates. The second contribution is strain-independent and results from the combination of the filler-rubber interaction, the hydrodynamic effect of the filler and the crosslinked network of the polymer.[59-61] The schematic evolution of the elastic modulus of a filled rubber versus strain, and the contribution of each interaction are depicted in **Figure 19** below.

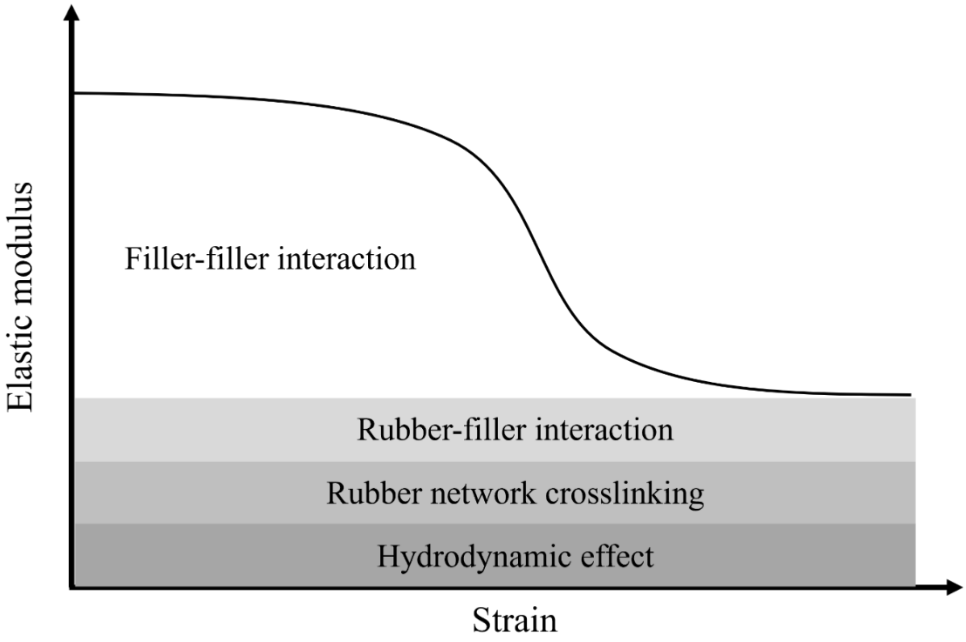

Figure 19. Representation of the different component of the elastic modulus and their evolution with strain.[61,62]

The assessment of the dynamic viscoelastic properties of rubber and the understanding of the underlying phenomenon at play are described by dynamics moduli. This formalism allows to account for the elastic and viscous contribution of the material via the storage and loss moduli respectively. This is presented in the following sub-chapter.

2.3 Dynamic modulus and viscoelastic properties of rubber composites

Viscoelasticity of rubbers is studied using Dynamic Mechanical Analysis (DMA). The material is subjected to an oscillatory deformation (the strain) and the resulting stress response is measured. The deformation can be lateral (shear) or uniaxial (traction).

The sinusoidal strain input written as:

$$\varepsilon = \varepsilon_0 \sin\,(t\omega)$$

And the stress response as:

$$\sigma = \sigma_0 \sin(t\omega + \delta)$$

ε_0 is the strain amplitude (-).

σ_0 is the stress amplitude (MPa).

ω is the frequency of the strain oscillation (s^{-1}) and t is time (s).

δ is the phase lag between the stress and the strain.

For a hypothetical purely elastic material, there is no phase lag, so δ=0. For a hypothetical purely viscous material, $\delta = \frac{\pi}{2}$. For a real viscoelastic material, the phase angle δ is comprised between 0 and $\frac{\pi}{2}$. Complex moduli are noted G^* for the shear deformation and E^* for the traction deformation.

$$E^* = \frac{\sigma_0}{\varepsilon_0} e^{i\delta} = E' + iE''$$

$$G^* = \frac{\sigma_0}{\varepsilon_0} e^{i\delta} = G' + iG''$$

Where $E' = \frac{\sigma_0}{\varepsilon_0} cos\delta$ and $E'' = \frac{\sigma_0}{\varepsilon_0} sin\delta$

$G' = \frac{\sigma_0}{\varepsilon_0} cos\delta$ and $G'' = \frac{\sigma_0}{\varepsilon_0} sin\delta$

With E' (or G') is the storage modulus and represents the elastic component of the complex module.

E'' (or G'') is the loss modulus and represents the viscous component of the complex module.

As a consequence, $\tan \delta = \frac{E''}{E'}$ and $tan\ \delta = \frac{G''}{G'}$.

The ratio of the loss modulus by the storage modulus is called **tan (δ)** and is a key physical quantity for the characterization of the viscoelastic properties and performances of rubber composites. It quantifies the damping capability of a material, meaning its capacity to dissipate energy as heat. DMA is a useful tool that allows to measure the extent of the Payne effect in a filled rubber composite, as well as tan (δ), giving access to the damping performances for each frequency domain corresponding to a real-life mechanical solicitation of a tire. These two aspects are presented below.

2.3.1 Origin and implication of Payne effect

The Payne effect is the decrease of the elastic modulus resulting from the decrease of the filler-filler interaction with increasing strain. At small deformation (<10%), the filler aggregates withstand partial and reversible dislocation, hence the reduction of their interaction and the elastic modulus decrease. This is represented below in **Figure 20**.

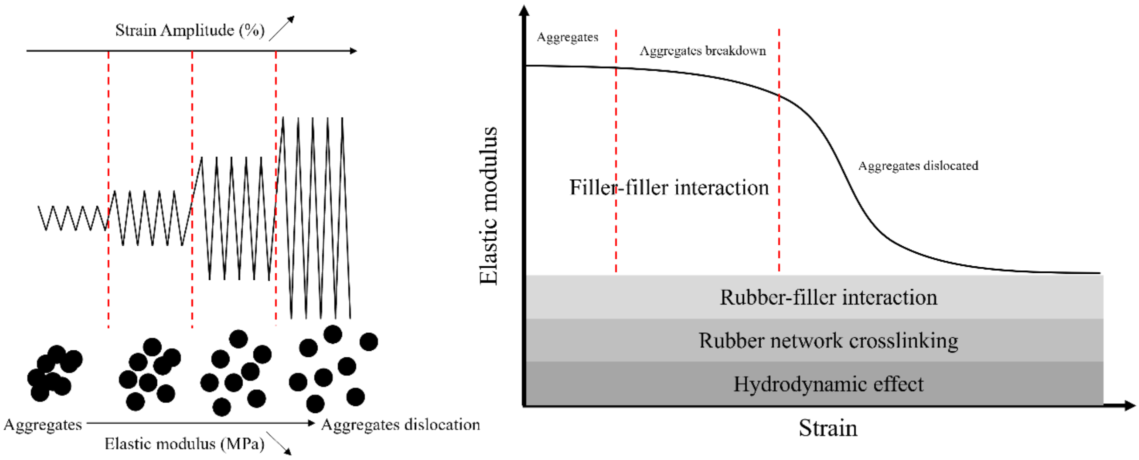

Figure 20. Illustration of the Payne effect and the decrease of elastic modulus.

The Payne effect can be measured by subjecting a rubber sample to an oscillatory strain at a constant frequency and measuring the stress response. The strain amplitude is increased step by step and the decrease in stress is recorded. The Payne effect is estimated with difference in elastic modulus $\Delta E' = E_0' - E_\infty'$. It has been shown that the silanization of silica filler in tire rubber greatly impact the Payne effect.[56] The use of covering agent shows a smaller decrease in Payne effect than the use of coupling agent, as the latter covalently bond the silica with the rubber, drastically diminishing the filler-filler interaction. The measurement of the Payne effect for tire rubber composites is essential in order to understand the behavior of the material with changing deformation.[63,64] In the **Figure 21** below, the effect of silica loading on the filler-filler interaction is illustrated, and its impact the increase of the shear elastic modulus and the Payne effect.[65]

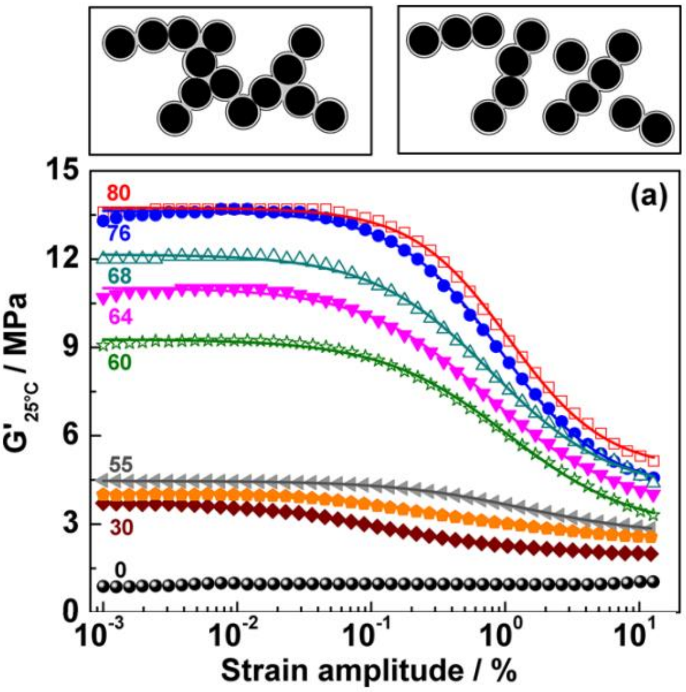

Figure 21. Effect of silica filler loading on elastic modulus and Payne effect in SBR composite.[65]

The increasing silica loading involves a denser filler network. The formation of a percolating filler network happens between 55 and 60 phr of silica in the rubber. It is characterized by the sharp increase of G' modulus and ΔG' increase.

The Payne effect resulting from interaction of fillers is contributing to the energy dissipation in a tire rubber compound. Though it could be seen as a negative phenomenon, it is actually needed as some energy dissipation is necessary for the performances of a tire tread, more precisely breaking and traction performances. This aspect is developed in the following sub-chapter **2.3.2. Time-temperature equivalence and dynamic mechanical analysis.**

The high-strain counterpart of the Payne effect is the Mullins effect.[66] It consists in the irreversible decrease of the elastic modulus originating from the permanent dislocations and damages dealt to the matrix and the filler network after a deformation of the material beyond the prior maximum deformation.

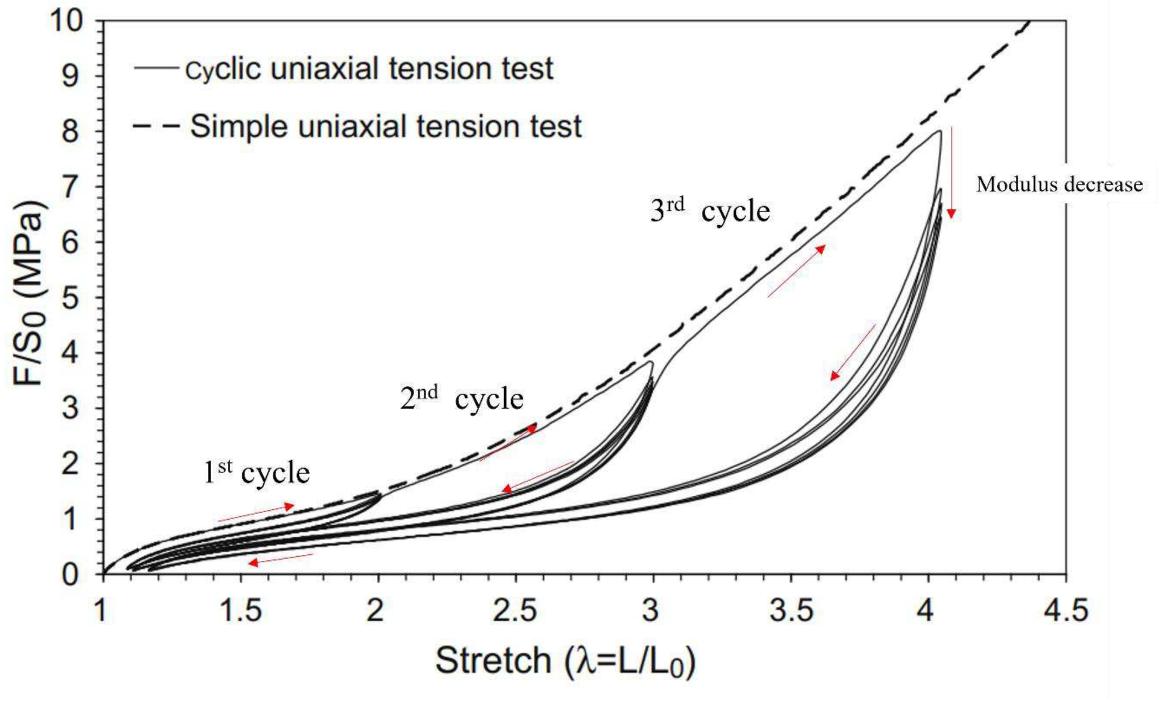

Figure 22. Illustration of the Mullins effect for a uniaxial tension test.[67]

In **Figure 22** above, we can see that at each set of cyclic tensile test, the maximum modulus decreases. This is especially clear in the third set of cycles. At each new cycle at higher deformation, the modulus increases due to the yet un-solicitated filler-filler and filler-rubber structure. Upon relaxation, the damages caused by this new deformation cannot be recovered, hence the decrease in modulus. The Mullins effect leads to an unavoidable and irreversible softening of the rubber material. It is the high-strain trade-off brought by the reinforcing effect of the filler-filler network interactions at lower strain.

2.3.2 Time-temperature equivalence and dynamic mechanical analysis

As a tire rolls on the road surface, it is submitted to a whole spectrum of mechanical solicitations, characterized by their deformation amplitude and frequency range at which they are happening. Typically, the deformation of the rubber over the small defects of the road leads to fast, small-scale deformation of the material, between 10^4 and 10^7 Hz. Alternatively, the rotation of the tire and its cyclic deflection at the contact point with the road corresponds to a larger deformation at frequencies of 10 to 100 Hz.[68,69]

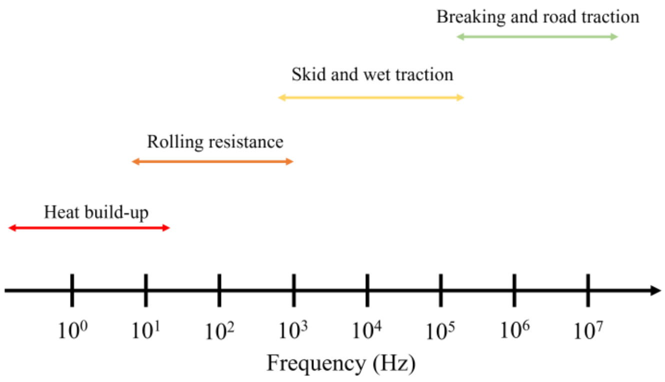

Figure 23. Frequency ranges of typical solicitation of a tire.[68,69]

In a laboratory, high frequency solicitation above 100 Hz cannot be reproduced with the existing measuring devices to characterize the viscoelastic behavior of the rubber material. To overcome this, the Williams-Landel-Ferry (or WLF) empirical law, published in 1955, allows to establish a **time-temperature** equivalence or superposition principle to the mechanical solicitation frequency ranges of a viscoelastic material.[70] This model is relevant up temperatures of T_g+100°C. The WLF equation has the following expression:

$$\log(a_T) = \frac{-C_1(T - T_r)}{C_2(T - T_r)}$$

Where a_T is the shift factor

T is the temperature (°C)

T_r is the chosen reference temperature (°C)

C_1 and C_2 are empirical constants, adjusted to fit the shift factor a_T

The purpose of this time-temperature equivalence is to build a master curve of the evolution of the modulus with regard to the solicitation frequency. In practice, the modulus of a rubber sample is measured for a given frequency range from ω_1 to ω_2 at different constant temperatures. The shift factor a_T is calculated for each temperature and the master curve is constructed by shifting each isothermal modulus curve accordingly.[20] This is illustrated in **Figure 24** below.

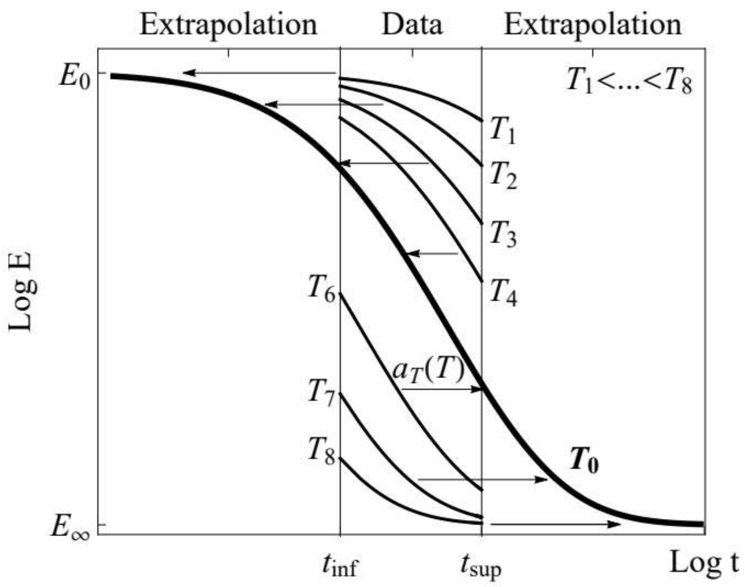

Figure 24. Modulus master curve construction from the extrapolation of isotherms.[71]

The conceptual implication of the time-temperature equivalence principle for viscoelastic material is that the mechanical solicitation frequency can be associated to a given temperature. According to the WLF equation, temperature and frequencies are inversely related. This is illustrated below.

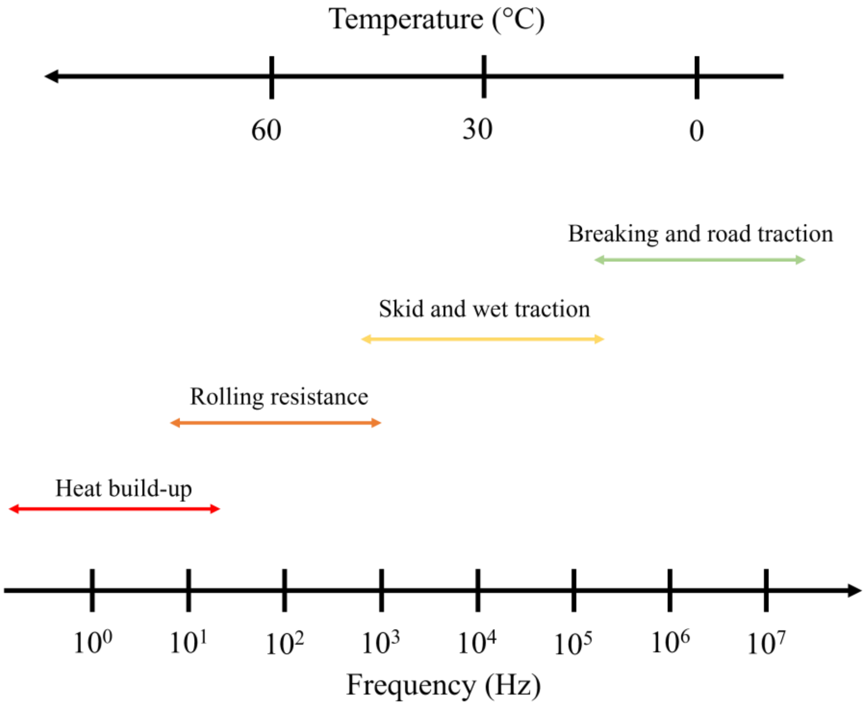

Figure 25. Equivalent temperature ranges for mechanical solicitations.

In practice, the investigation of the viscoelastic properties of a rubber material can be done by measuring the moduli of a rubber sample at a constant frequency of 1 to 10 Hz with a temperature sweep from -100°C to 80°C. The rubber sample is submitted to an oscillatory mechanical deformation at a constant frequency, in a chamber that enables a precise control of the temperature. The storage and loss moduli as well as tan(δ) are recorded and plotted versus temperature. For typical tire tread rubber compounds, it is commonly established that tan(δ) at 0°C corresponds to the energy dissipation of a road traction solicitation, and tan(δ) at 60°C to the energy dissipation of the rolling resistance of the material. These two indicators that are tan(δ) at 0°C and tan(δ) at 60°C are especially important when it comes to assessing the performances of a tire tread rubber compound viscoelastic properties.

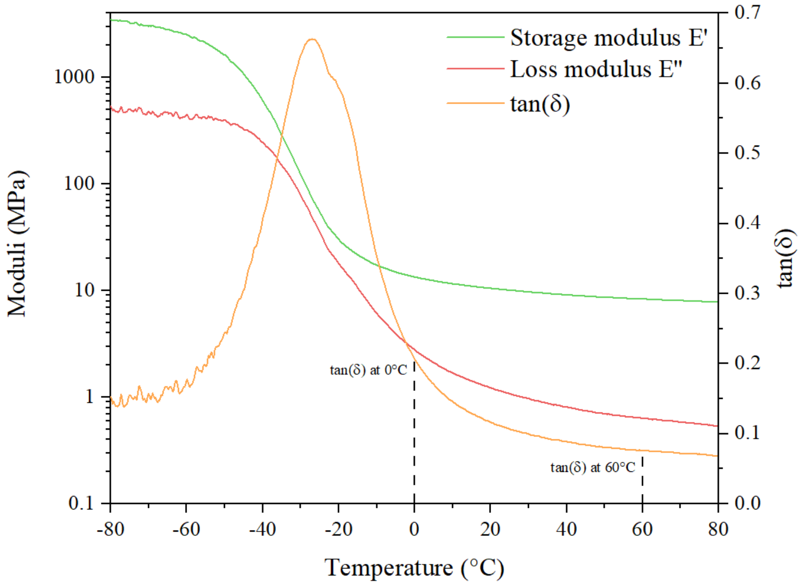

Figure 26. Typical temperature-sweep of tire tread rubber compound in DMA at 1 Hz.

The damping factor tan(δ) is an essential indicator to understand the behavior of a tire and how the measured mechanical properties on lab-scale samples relate to a real-life object. While driving a vehicle, the action of breaking to reduce speed, or turning in a corner, requires energy dissipation. Because the tire tread is the only part of the car in contact with the road, it is the vector of this energy dissipation. Therefore, tires must be capable of dissipating energy efficiently in the adequate range of frequency (traction, wet skid and breaking) to maximize performances and safety, while dissipating the minimum amount of energy in frequency domains corresponding to rolling resistance, where it results in no additional performances and more fuel expenditure.

For these reasons, the evolution of tan(δ) is a key element to investigate the effect of fillers surface modification and understand the consequences on their interaction with the rubber matrix and the final performances of the rubber composites.

3 Silica

Silica is the common name of the natural form of silicon dioxide SiO_2. It is composed of tetrahedral [SiO_4] covalently bonded units. It can be amorphous or crystallin and is a very common mineral in earth crust in its free form (quartz, diatomaceous earth, and chalcedony). Silica is involved in a biogeochemical cycle in which diatoms, a group of microalgae, transform silicic acid dissolved in water into solid silica shells. This process is responsible for the existence of "diatom earth", a silica-rich sediment composed of dead diatoms silica shells.

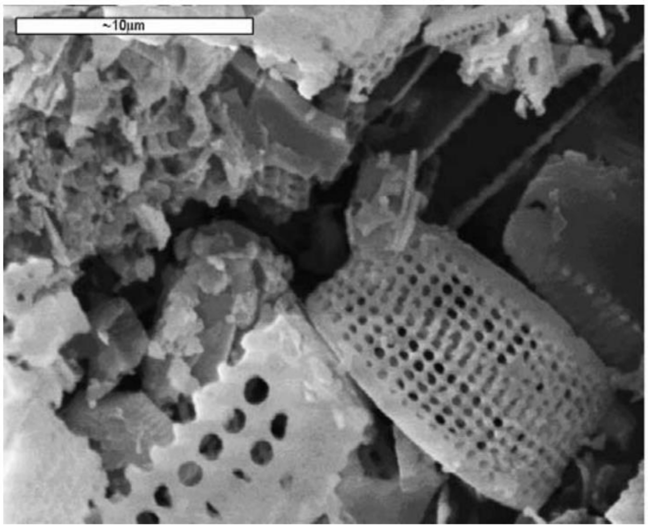

Figure 27. Diatomaceous earth under scanning electron microscope.[72]

Yearly, diatoms are responsible of the generation of 20-50% of earth dioxygen and the intake of about 6.7 billion of tons of silica.[73] Silica is a hard material, hence suited for polymer and rubber reinforcement. Its surface chemistry makes it polar and hydrophilic, which can be problematic for its blending in non-polar hydrophobic polymers. However, the presence of hydroxyls groups on its surface enables the chemical modification to change and tune silica surface properties. In the following sub-chapters, crystallin silica is not discussed as it has no direct relevance in the topic of silica-rubber composites. When the word "silica" is used, it is implied that it means "amorphous silica".

3.1 Silica as a reinforcing filler

Silica as a filler is used in many different fields of applications: food additive and processing agent, cosmetics, cement and concrete, rubber filler for soles or tire, to name few of them. Required properties differ from one application to another and so silica is produced at industrial scales in three main forms: pyrogenic, fumed, and precipitated silica. The production processes directly impact the characteristics and properties of the material. The case of Stöber silica and sol-gel process for silica production is developed further in the manuscript in a dedicated chapter.

3.1.1 Fumed silica

It can be mistaken with the purer pyrogenic silica, as both fabrication processes involve high temperature. Fumed silica is a by-product of the silicon industry, during the process of quartz reduction to produce silicon metal. Silica vapors condense into silica spheres of about 50 to 200 nm and are collected.

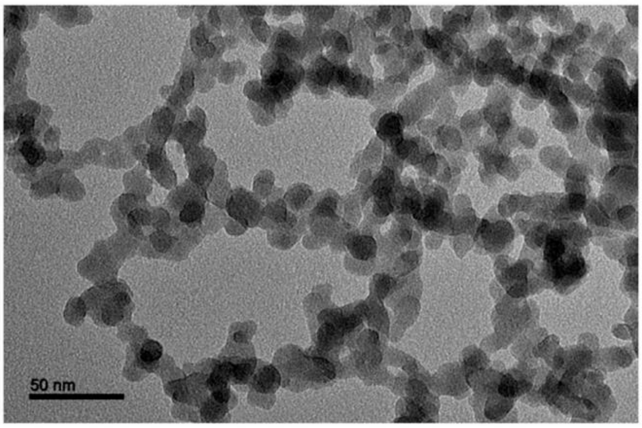

Figure 28. Fumed silica under transmission electron microscope.[74]

Due to the high temperatures involved, the amount of surface hydroxyl groups is low, and this kind of silica is sometimes referred as “hydrophobic silica”. Its main application is in concrete as a heat resistance additive.

3.1.2 Pyrogenic silica

It is produced in gas phase by reacting tetra chlorosilane with air and hydrogen gas. A homogenous gas mixture is burned in a combustion chamber at high temperature. Hydrochloric acid is a by-product of this reaction. This process enables the production of high purity silica. The process parameters, especially the time spent by the particles in the flame, enable to have some control over the size of the particles, their specific surface area and amount of hydroxyl groups on the surface.

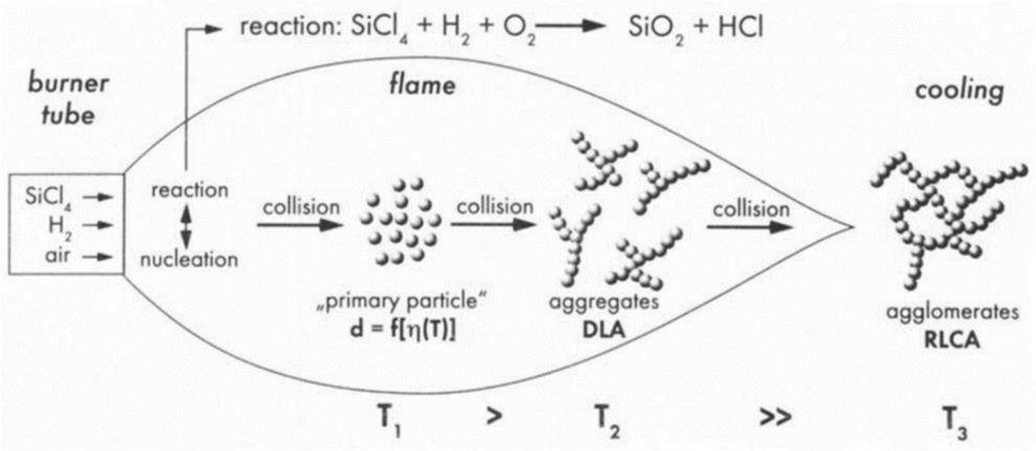

Figure 29. Schematic representation of pyrogenic silica production process.

Like fumed silica, the amount of hydroxyl groups at the surface of the particle tends to be on the lower end because of high temperatures. Pyrogenic silica has a low apparent density (0.16 to 0.19 g.cm$^{-3)}$ and high specific surface area due to the aggregated microstructures resulting from the process of fabrication. It is especially used as a thickening agent and as a filler for polymers.

3.1.3 Precipitated silica

Prepared in liquid phase, precipitated silica is the resulting product of the precipitation of an alkaline silicate solution with sulfuric acid under stirring. Silica particles are filtered and rinsed. During this process, the temperature, the pH, the rate of reagents addition, stirring speed can be adjusted to reach desired silica characteristics.

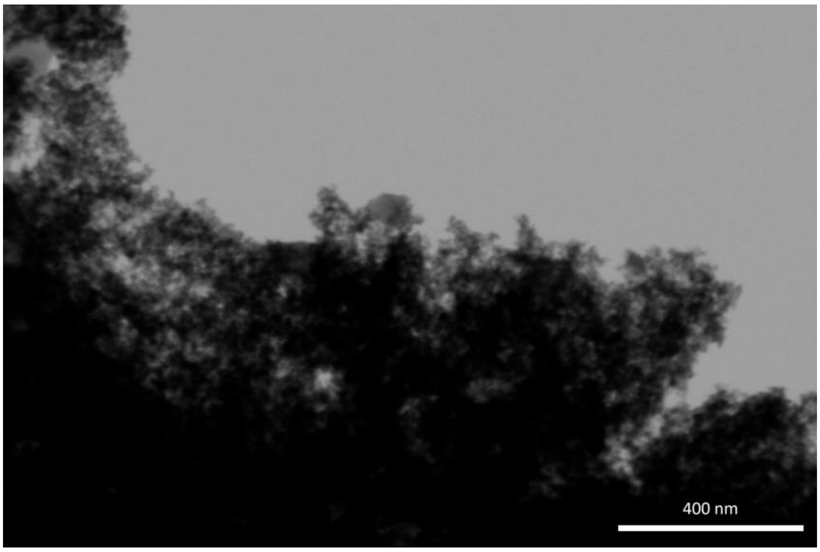

Figure 30. Precipitated silica under scanning transmission electron microscope (STEM).

Precipitated silica range between 5 to 100 nm primary particles size with aggregates up to hundreds of micrometers, and a density of about 1.9 to 2.1 g.cm^{-3}. Unlike the fumed or pyrogenic silica, precipitated silica displays much higher surface hydroxyl groups density.

We have seen how silica can be produced industrially and it affects the morphology, size, and properties of silica particles. The next part develops into more details about silica surface chemistry and properties.

3.2 Silica surface chemistry

Similarly to alcohols where the hydroxyl groups are carried by a carbon atom, hydroxyl groups present at the surface of silica are named "silanols" and are carried by a silicon atom. The silanol density is a direct consequence of the synthesis process of the silica. Indeed, silanol can react through a condensation reaction, forming a siloxane bond Si-O-Si and generating water.

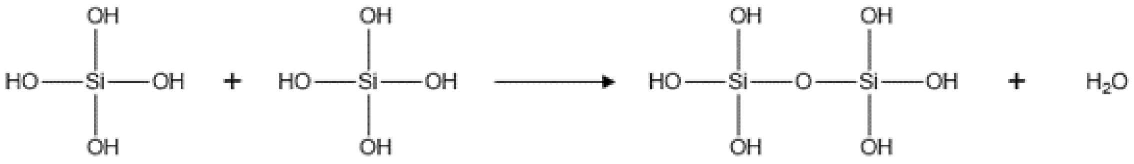

Figure 31. Silanol condensation scheme.

High temperature increases the rate of reaction, also called dehydroxylation. Subsequently, high-temperature production processes tend to yield silica with lower silanols density. Surface properties of silica result from the presence of silanols and their density. They make silica surface polar, susceptible to acido-basic reaction. Silanols are also susceptible to hydrogen bonding and because of this, moisture is almost systematically present on silica surface. Silanols can also react in condensation reactions or nucleophilic substitutions. The hydrophilic character of silica is dependent on its silanol density, and silica with very low surface silanols are considered hydrophobic, like fumed or pyrogenic silica.

Silanols exists in a variety of conformations that deeply impact their properties. Different types have been identified : vicinal or hydrogen bonded, isolated and geminal silanols.[75] Another denomination used for silanols is "Q groups", especially used in silicon Nuclear Magnetic Resonance spectroscopy (NMR). The letters M, D, T, and Q mean that the silicon atom is bonded respectively to one, two, three or four oxygen atoms. The following number designates how many of those oxygen atoms are bonded themselves to another silicon atom. This is illustrated below.

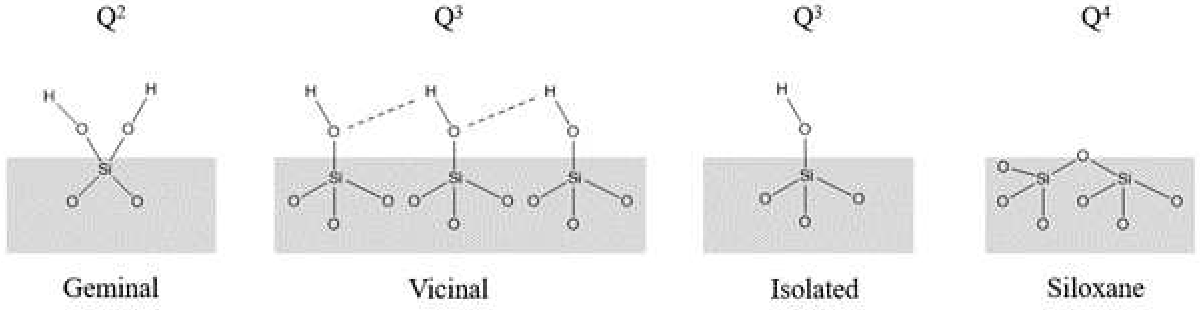

Figure 32. Different silanols conformation on silica surface.

Conformation and physical environment affect the silanols chemical properties. It has been shown that geminal silanols are more reactive, and that not all silanols behave identically with respect to dehydroxylation of silica.[75] For instance, when silica is heated, dehydroxylation happens in a large range of temperature, starting at about 100-120°C up to 1000°C for complete condensation of all silanols.[76] Hydrogen bonded silanols and spatially closed silanols are more likely to react with their neighbors than isolated silanols in a condensation reaction. The characterization of silanol density is usually done by thermogravimetric analysis (TGA) by measuring the weight loss resulting from dehydroxylation, ^{29}Si solid state NMR[76,77] by measuring the amount of Q3 groups, or by infra-red spectroscopy[78,79].

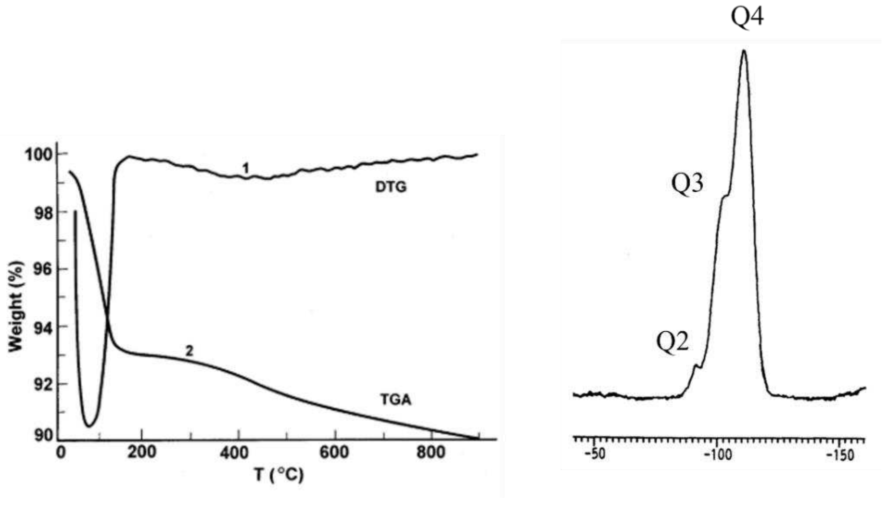

Figure 33. TGA-DTG (left)[75] and ^{29}Si solid state NMR spectrum (right)[80] of silica.

The use of multiple technics allows to balance their respective drawbacks. Thermogravimetric analysis is convenient and fast, but upon heating, the dehydroxylation of different silanols as well as moisture removal can overlap, and it is difficult to impossible to differentiate properly different phenomenon. Silicon solid state NMR allows for a precise measurement of the amount of each kind of silicon atom, but it requires very long acquisition time and high resolution due to the relaxation delay of ^{29}Si and its low natural abundancy.

The characterization of silica is essential when it comes to silica chemistry and modification. It allows to know the starting material and to be able to follow and assess silica surface modification.

The collaborative works "*Revealing the dehydration/deuteration processes at the liquid-solid interface by nuclear magnetic resonance spectroscopy*" and *"Semiquantitative Solid-State NMR Study of the Adsorption of Soybean Oils on Silica and Its Significance for Rubber Processing"*, presented in the appendices, aim to tackle this problematic. The synthesis of a ^{29}Si-enriched precipitated silica material allowed to build and experiment a new solid-state cross proton-silicon NMR polarization technique. It proved to be effective at studying and better understanding the surface silanols and adsorbed water on silica particles surface. The results obtained from this solid-state proton-silicon cross polarization experiment were used for the development of a more convenient liquid state NMR technique. That technique can be applied to hydroxyls containing solids as an alternative to the common TGA methodology.

3.3 Silica surface modification with silanes

The modification of silica surface can be done with many different processes and chemicals depending on the targeted results. In the field of silica filler modification for rubber reinforcement, silanes are the main molecules. According to the IUPAC nomenclature, silane are molecules composed of silicon and hydrogen, similarly to alkanes that are composed of carbon and hydrogen. In the field of the tire industry and silica chemistry, the word silane is used to refer to organosilanes and more generally to the most commonly used alkoxysilanes. Some usual silanes are presented in **Figure 34.**

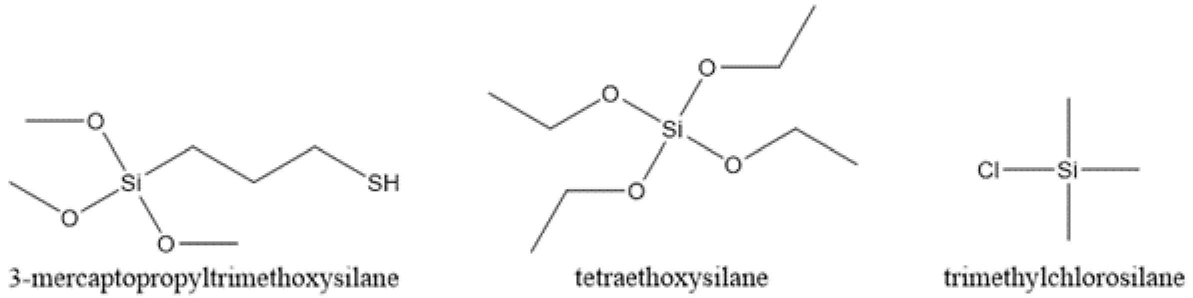

Figure 34. Example of usual organosilanes.

The general structure of organosilanes is $SiX_nR_{(4-n)}$ where X is usually an alkoxy group ($-OCH_3$ or $-OC_2H_5$) or a chlorine atom, and R an organic radical. The X group can be easily hydrolyzed to form a silanol Si-OH meant to further react by condensation with silica or another hydrolyzed silane to form silane oligomers or polymers. The use of alkoxysilanes is preferred to chlorosilanes whenever possible, as they release alcohol instead of harmful hydrochloric acid gas.

The modification of silica fillers for tire rubber can be done in two different ways. The first one, typical of the industrial production of tire compound, consists in adding the liquid silane to the rubbery polymer blend altogether with the fillers and other additives in a mixing chamber.[81,82] The most commonly used silanes in the tire rubber industry are TESPT and TESPD. The chemical structure of bis-triethoxysilylpropyltetrasulfide, or TESPT, is shown in **Figure 35** below.

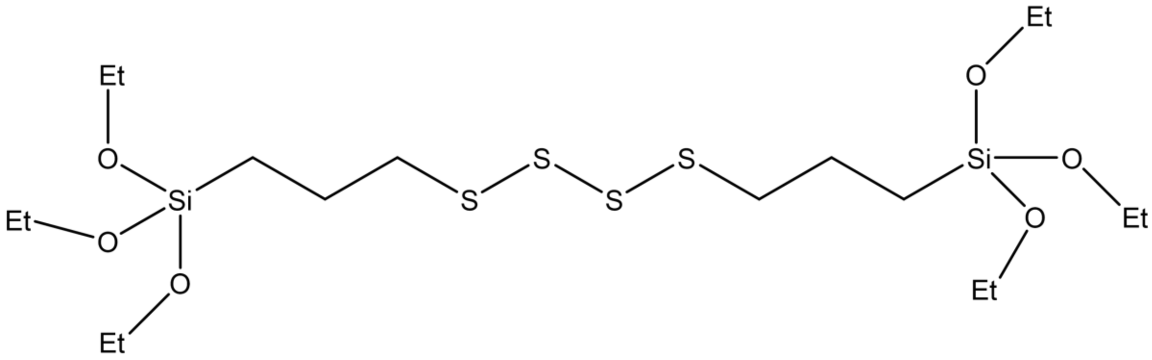

Figure 35. Chemical structure of bis-triethoxysilylpropyltetrasulfide (TESPT).

The usefulness of this molecule resides in its ability to react both with silica, via the hydrolysis of its ethoxy groups, and with rubber unsaturated carbon-carbon bonds via the opening of the tetra sulfide bridge[57]. Silanization occurs in the soft polymer blend at temperatures of about 140-150°C, originating from the mixing action at high energy. The second method is the pre-treatment of the silica with the silane in solution, before mixing the filler into the rubber. Silanization of silica can be carried in water, or in organic solvent. Aqueous silanization is preferred because it is safer and does not require potentially harmful and eco-toxic solvents, but the range of useful silane is limited to the water-soluble ones. Silane hydrolysis and condensation can be catalyzed either in acid or basic condition. This doctoral thesis only uses and investigates silica silanization in liquid solution.

3.3.1 Alkoxysilane hydrolysis and condensation reactions

The mechanism of hydrolysis in both acid and basic conditions is represented below in **Figure 36** and **Figure 37**.

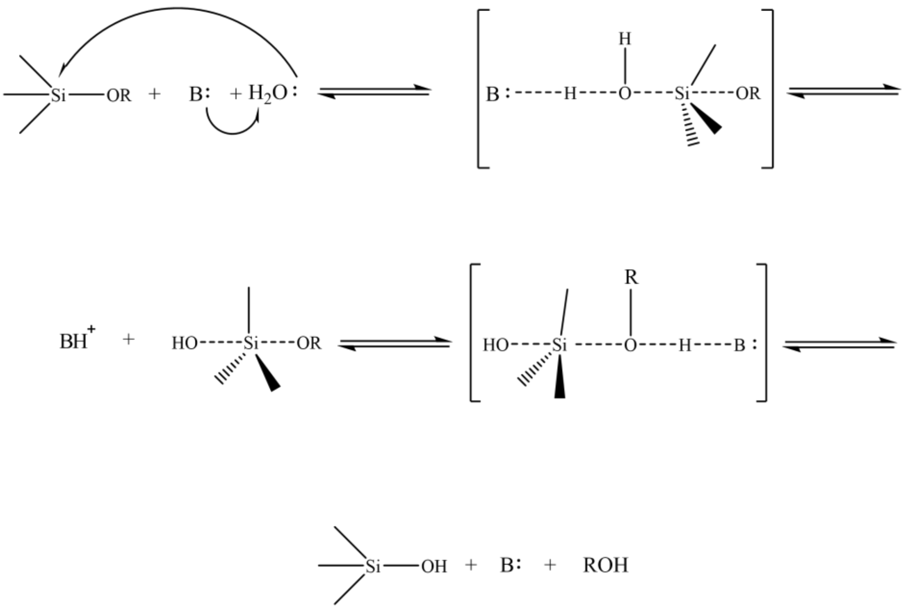

Figure 36. Base catalysis of alkoxysilane hydrolysis.[83-85]

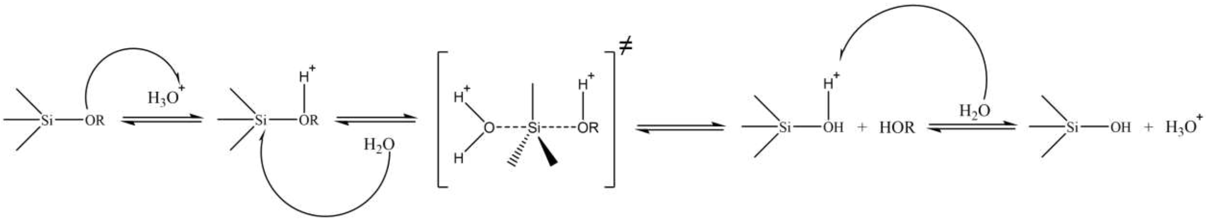

Figure 37. Acid catalysis of alkoxysilane hydrolysis.[83-85]

The rate of hydrolysis reaction in both basic and acidic conditions has been investigated in several studies for different silanes.[86,87] It has been shown that the rate of hydrolysis is inversely proportional to the size of the alkoxy group.[87] The condensation in both acid and basic conditions are represented in **Figure 38** and **Figure 39** below.

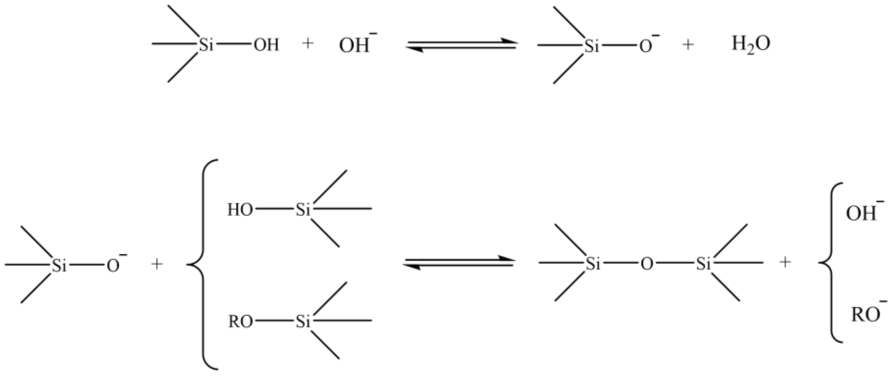

Figure 38. Condensation of alkoxysilane in basic condition.[88]

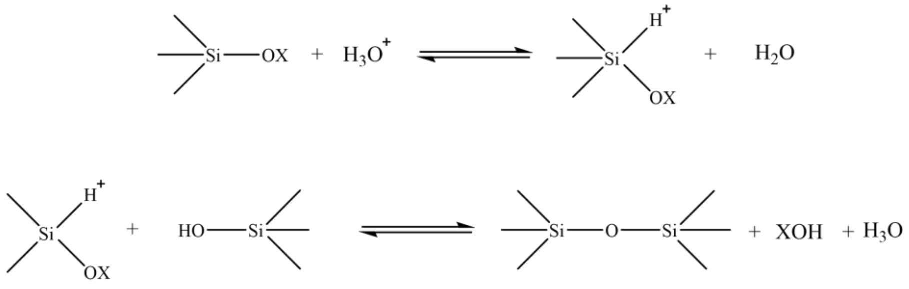

Figure 39. Condensation of alkoxysilane in acidic condition.[88]

The condensation rate and efficiency are affected by the organic groups R carried by the silane. The increase of alkoxy groups size and number, as well as the size of the organic radical R have steric effect at the vicinity of the silanols during the approach of the silane molecule.[89] Also, the electronic structure of the organic radical has an effect on the electron density of the silicon atom and therefore on the reaction rate.[90-92] Additionally, the nature of the organic part may change the solubility of the silane and impact its availability depending on the solvent used. Finally, some silanes carrying polar functions like amines, thiols, acetic acids, or acrylates may interact with the silica surface via these organic groups through hydrogen bonding for example. Moreover, some silanes, especially amino-silanes, that are widely used, are known to increase the condensation rate, as amine can play the role of a base catalyst.[93-95]

In organic solvent, the availability of water for hydrolysis depends on its miscibility with the solvent. In protic solvent like alcohols, water is very miscible and homogeneously dispersed in the liquid. Whereas in toluene, in which the miscibility is almost non-existent, water exist as minuscule suspended droplets. Additionally, in water or water-alcohol solution, the silane is more likely to react with itself and form silane oligomers than in an organic solvent[96,97] where water is mostly available at the surface of silica. For this reason organic solvents are usually preferred, in order to control and focus the silanization on silica particle, to target a monolayer grafting rather than a multilayer one.

It has been shown that silica particles affect hydrolysis and condensation of silanes. Surface silanols have an effect on acidity of the solution, which increases reaction kinetic.[98-100]

3.3.2 Chemical surface modification of silica by silanization

The reaction of organosilanes with the silica surface follow the hydrolysis-condensation scheme described earlier. Upon hydrolysis, the silane can bond with the silica surface via hydrogen bonding before withstanding the condensation and covalently bond with the particle surface. Alkoxysilanes give off their equivalent alcohol when reacting. **Figure 40** below represents schematically the grafting reaction of mono and trialkoxysilanes with a silica surface.

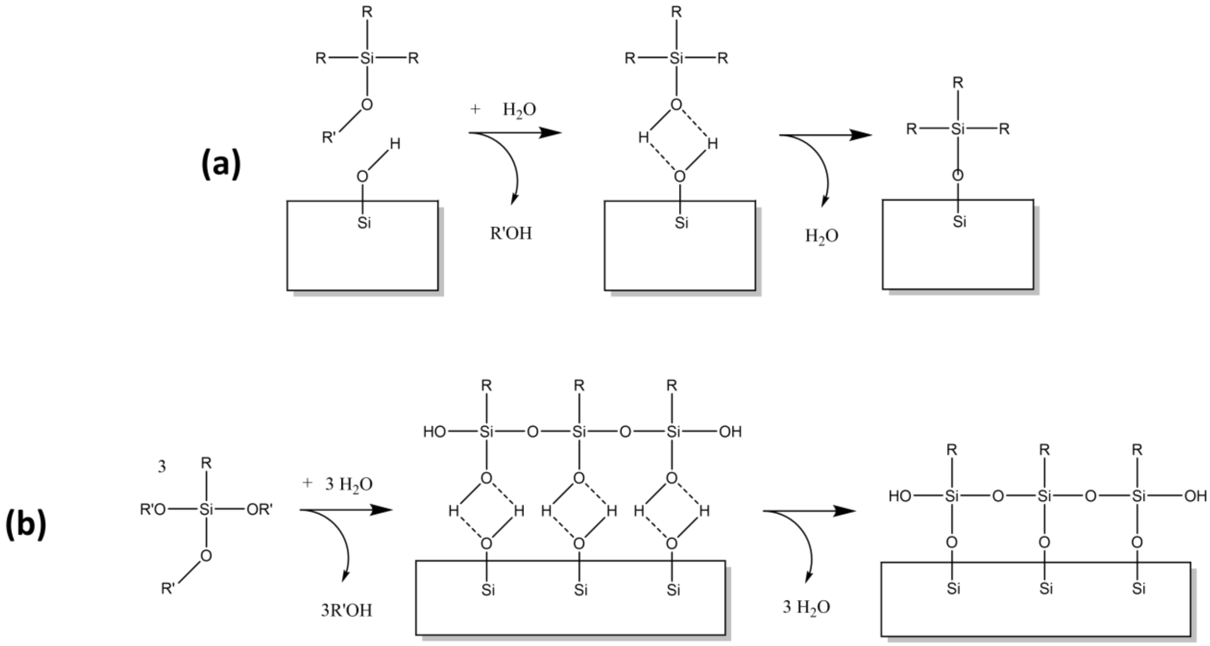

Figure 40. Grafting of silane on silica surface of a monoalkoxysilane (a) and trialkoxysilane (b).[79,90,101]

This representation is idealized and used for illustration purpose. A real situation is expected to be more complex, especially for multifunctional silanes. After hydrolysis, they can poly-condensate onto themselves and form silane oligomers, susceptible to further reaction with silica surface afterward. The schematic representation in **Figure 41** below illustrates this.

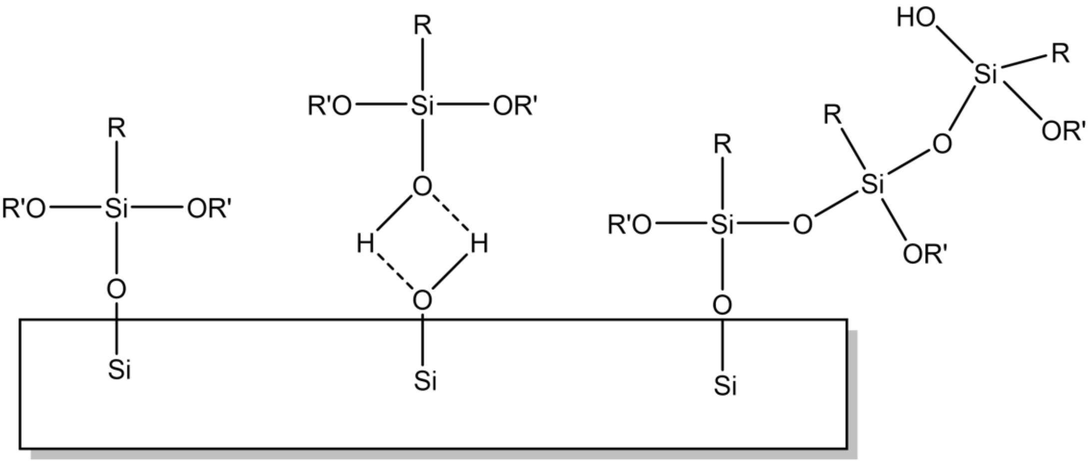

Figure 41. Possible silane-silica interaction.

The nature of the solvent is an important parameter to achieve a specific grafting morphology.[102] The use of dry organic solvent will favor a linear surface grafting in the form of a monolayer. It will restrain the possibility of hydrolysis and condensation at the silica surface, where water is available[77,103]. On the opposite, the silanization of silica in water on in water-miscible solvent will allow the hydrolysis and condensation of silane molecules in the bulk of the solvent, away from any silica surface. This gives the opportunity to the silane to form oligomers before reacting with silica.

Depending on the desired goal, the experimental conditions can be chosen to achieve one or the other grafting morphology. Finally, the bonding mode of di- and trialkoxysilane over a silica surface is to be qualified. Indeed, the reaction of all the two or even three alkoxy reactive groups of a silane on silica surface is unlikely due steric effect and spatial distribution of silanols over the surface. The probability of having three silanol at the right distance to each other to enable the trialkoxysilane to react is very low. [89,104-106] This is confirmed by the T_1, T_2 and T_3 groups distribution measured in ^{29}Si NMR on silane grafted silica. T_1 and T_2 groups a predominantly present at low grafting and the amount of T_3 groups increases as grafting density increases. This is represented in **Figure 42** below.

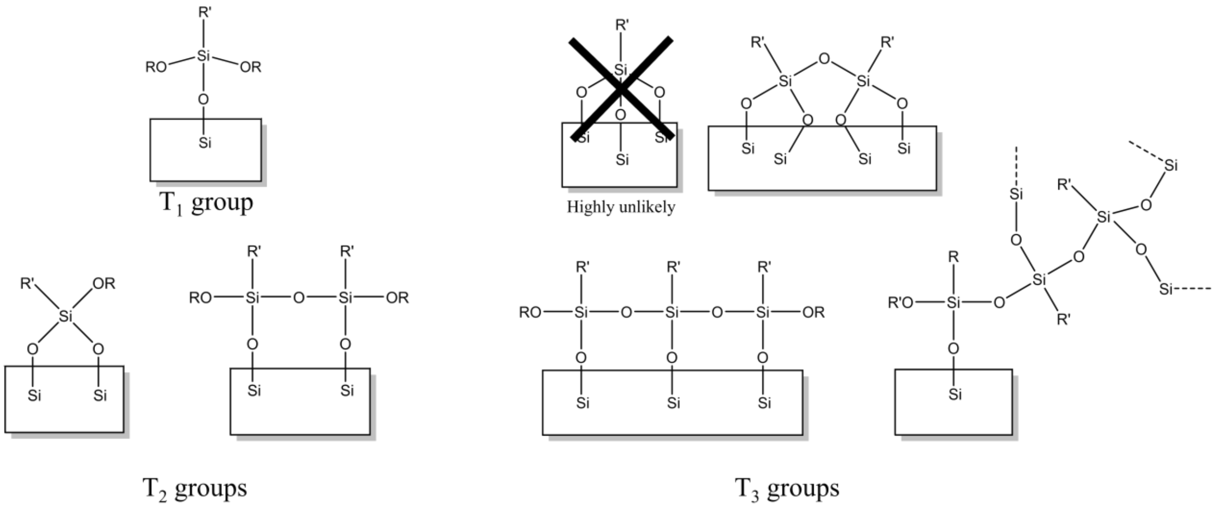

Figure 42. Different surface grafting mode of a trialkoxysilane on a silica surface.

The main consequence of such variety in silane grafting mode is the difficulty to precisely assess the morphology of the grafted layer. A silane monolayer can yield the same loading as multiple patches of grafted silane oligomers over a silica particle. This can be problematic if the quantification of silanization grafting yield is intended. For example, T_3 groups can be a marker for a silane monolayer as well as for silane oligomers. Silica particles surface is irregular, rough and particles always have some size polydispersity. Consequently, the silanization of such surface cannot realistically achieve a perfect monolayer coverage, like it is the case for self-assembled monolayer (SAM) of silane over a quartz surface.[107,108] These considerations are especially important when silanization yield measurement or process optimization are pursued.

Beyond the silica surface chemicals modification, the ability for multifunctional organosilanes to polymerize can be used to synthesize silica particles. This process is called sol-gel and allows to produce amorphous solid (the gel) from a solution (the sol). This is presented and developed in the following sub chapter.

3.4 Sol gel process for silica filler synthesis

A sol-gel process is the production of a solid material, small particles, or a block, via a solution of a monomers that can polymerize. It is generally used for the production of metal oxides such as zinc, titanium, or silicon oxide (silica). Metal-alkoxides are used as monomers and polymerize in a solution, very often in water or water-alcohol. The general scheme of a sol-gel process is presented in **Figure 43** below.

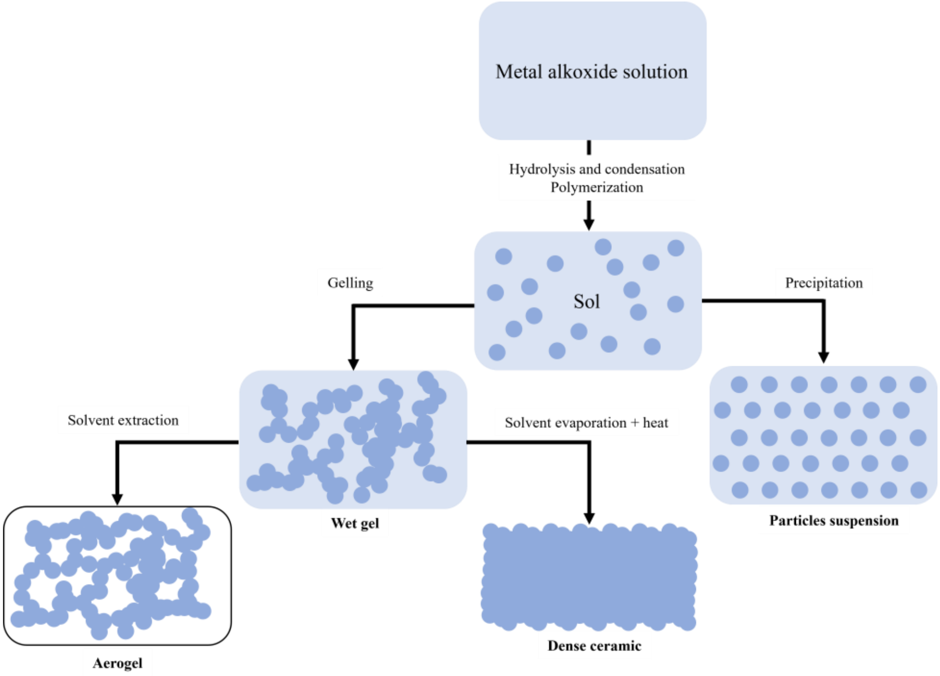

Figure 43. Sol-gel process schematic.

The sol is generated by the metal alkoxides hydrolysis and condensation to form oligomeric seeds that can evolve differently depending on the reaction conditions. The relative rate of hydrolysis and condensation can be adjusted with the concentration of monomers, the temperature, the pH or the nature of the solvent, in order to lead to different outcomes. Aerogels, ceramics, or particles can be obtained from a sol. We will go into further details in the synthesis of silica filler particles using the sol-gel process.

3.4.1 Basic of sol gel synthesis of silica

The first reported synthesis of micrometer silica particles, now known as Stöber particles, was carried in 1968.[109] The reaction consists in the controlled hydrolysis and condensation of tetraethoxysilane, or tetraethyl orthosilicate (TEOS), in ethanol in the presence of water and ammonia. The two latter allow for the basic catalysis of hydrolysis and condensation. Several factors allow the formation of small, monodispersed sized particles instead of the formation of a gel[110]. Indeed, to form particles, one needs to optimize the reaction conditions to favor the nucleation and growth of individual particles[111] and avoid aggregation.

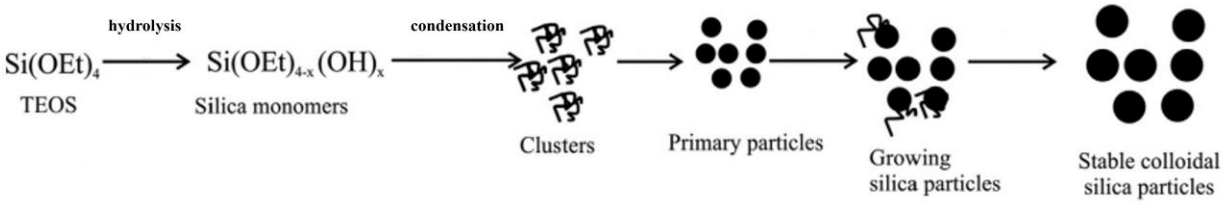

Figure 44. Stöber particles formation.[43]

Carrying the reaction in alcohol allows to control and slow down the hydrolysis reaction, as it favors the esterification of the hydrolyzed TEOS silanols and mitigates the hydrolysis speed[112,113]. The low concentration of TEOS reagent in ethanol favors the nucleation and growth of independent particles. Finally, at basic pH, silica silanols are partially deprotonated, giving particles an overall negative charge. This enables the electrostatic repulsion of the particles in the solution and prevents their aggregation[114]. In an acid solution, the protonated silanols favor hydrogen bonding and aggregation of the particles. It has been shown that the reaction conditions enable to target precise particles size with a monodisperse distribution even at the sub micro-meter scale.[115,116] Stöber silica particles are a very useful material, as a substrate for even more advanced materials, or as a model particles scientific research. Unfortunately, the low yield of the synthesis, due to the low TEOS concentration requirement, prevents it to be filler of choice for the reinforcement of tire rubber.

The sol-gel process is very versatile and opens the possibility to synthesis silica particles a various shapes and sizes, with the potential of chemical modification. The so-called silica mesoporous particles are a vast area of research with plenty of applications. In the following sub-chapter, we will present their synthesis, properties, and application, as well as their potential as rubber tire filler.

3.4.2 Highly-ordered mesoporous silica - Synthesis by soft-templating sol-gel process

Highly ordered mesoporous silicas are a class of particles featuring an ordered porous structure at the meso-scale, i.e. between 2-50 nm of pore size[117]. The discovery of highly ordered mesoporous particles named MCM-41 by scientist at the Mobil Oil company[118] opened the doors for the research in this field. Unlike a classic sol-gel process in which the amorphous silica structure displays a random organization and irregular porosity, the soft-templating process allows to synthesize ordered but still amorphous particles. Ordered mesoporous silicas display unique morphology, featuring various pore sizes (2 to 15 nm), large specific surface area (from 500 to 1000 m²/g) and geometry. The tunability of the particles size and the possibility of chemical modification via different processes have made these particles the topic of extensive research and great interest for many fields of application, like catalysis[119,120], drug delivery, multi-modal imaging and nano-medicine,[121,122] water depollution,[123,124], or column chromatography[125,126].

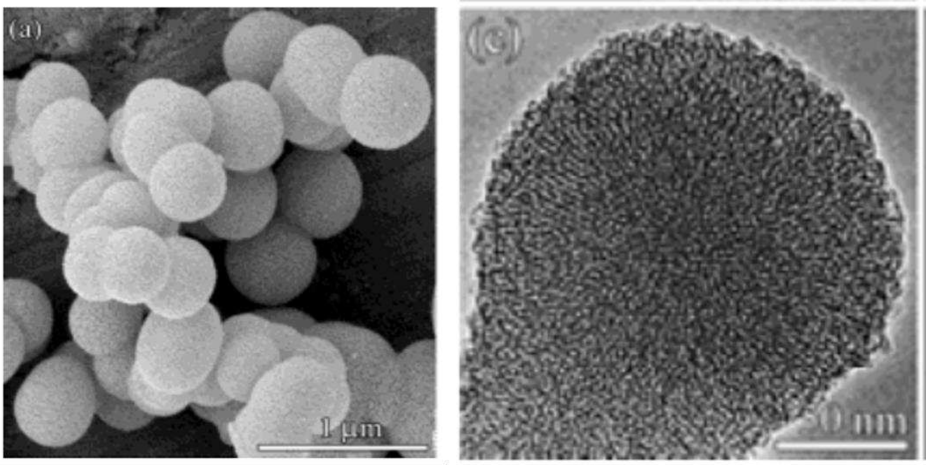

Figure 45. MCM-41 images under electron microscope.[127]

The synthesis of such material is based on the sol-gel reaction of TEOS, coupled with the use of surfactants. This process is called “soft-templating sol-gel process” or “liquid crystal templating” (LCT). A surfactant forms a “liquid crystal” by self-assembling into micelles, and the polymerization of TEOS occurs at the vicinity of the micelles. In the case of MCM-41, the surfactant is CTAB (for cetyltrimethylammonium bromine). Other surfactants can be used, like the non-ionic Pluronic type. These surfactants are polyethylene oxide-polypropylene oxide block copolymers. The variation in the block length, sequence and number allow for a variety of properties. SBA-15 silica particles are obtained from this surfactant system.[128,129]

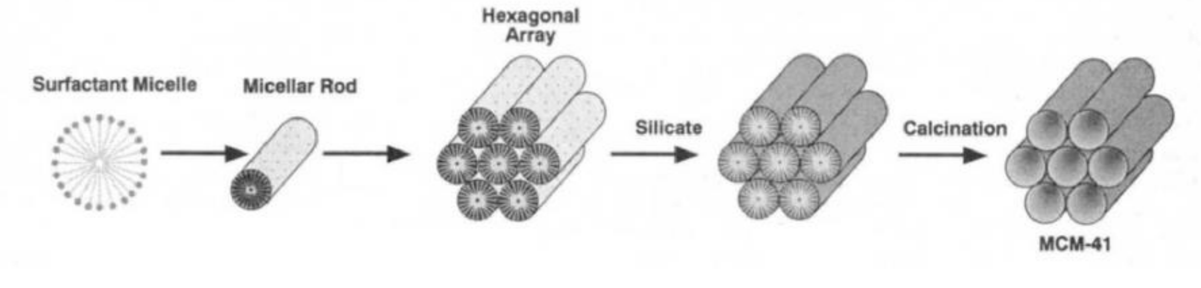

Figure 46. MCM-41 structure formation suggested by Beck et al.[130]

The synthesis of the particles follows the same nucleation-growth pathway as Stöber silica particles described earlier. After the removal of the surfactant, one obtains the silica complementary shape. The versatility of this method resides in many factors. The variety of surfactants and the variety of surfactant’s micellar phases allow for different particles shapes as well as pore size and geometry. The pores size can be tuned by the use of different surfactants or the use of swelling agents.[131]

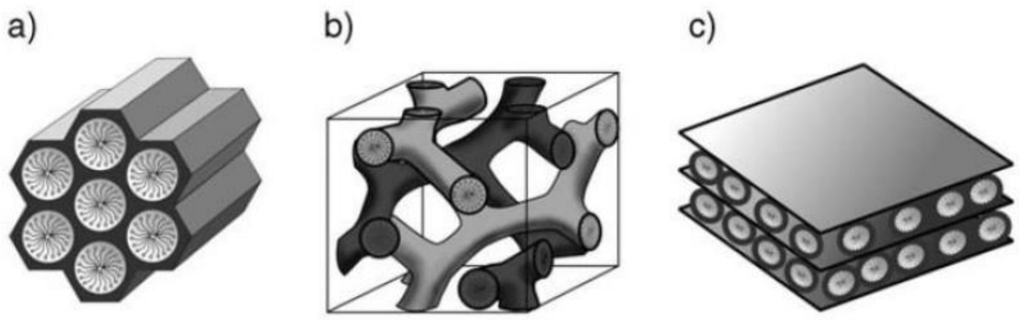

Figure 47. Porous structure of MCM-41 (a), MCM-48(b) and MCM-50 (c).[132]

3.4.3 Interactions between surfactant and porous particles

The cohesion of surfactant micelles with growing metal oxide structure is dictated by the nature of the interactions between these two actors. Surfactants can be cationic, anionic, or non-ionic. The synthesis pH can be acidic or basic, and the solvent and co-solvent also can have an effect. **Figure 48** below illustrates and summarizes these parameters. “**S**” stands for surfactant, “**I**” stands for the inorganic metal oxide framework, “**M**” and “**X**” stands for their respective counter ions. Solvent is not represented except for the triangles. Dashed lines represent the hydrogen bonds. The black spheres and tails represent the surfactant molecules. For example, the synthesis of MCM-41 particles, using a positively charged quaternary ammonium terminated surfactant, under basic pH conditions falls into the “**$S^{+}I^{-}$**“category.

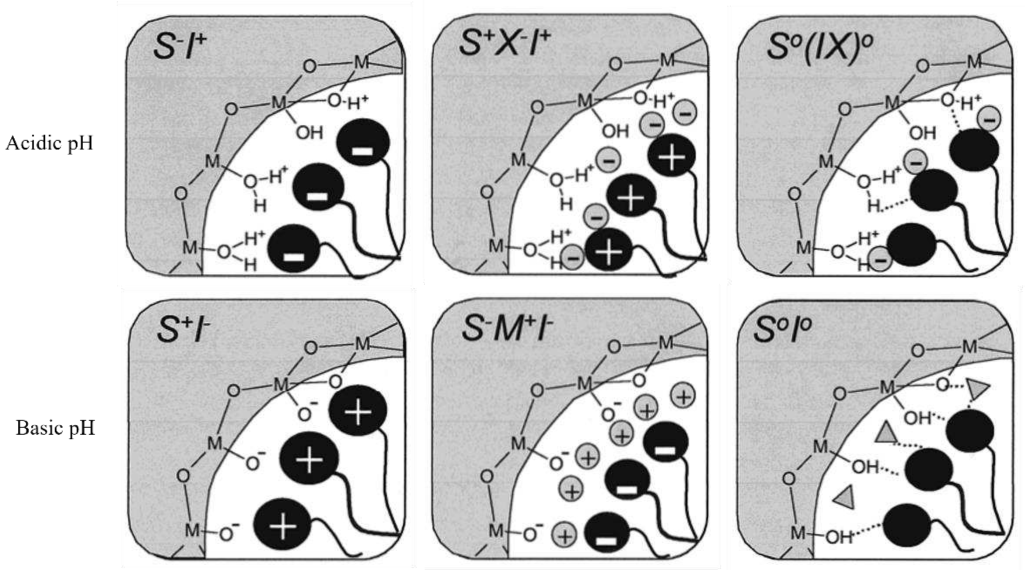

Figure 48. Metal oxide-surfactant interactions.[133]

3.4.4 Influence of pH on silica synthesis

The synthesis of mesoporous silica particles is usually done at slightly basic pH. In this condition, the particles are electrostatically stabilized, and the relative speeds of hydrolysis and condensation allow for particle production. Indeed, for the growth of silica to be possible, both hydrolysis and condensation rates have to be greater than zero, and condensation rate must be greater than hydrolysis. If not, the newly formed silica would be hydrolyzed back to the monomeric form. This is illustrated by the **Figure 49** below.

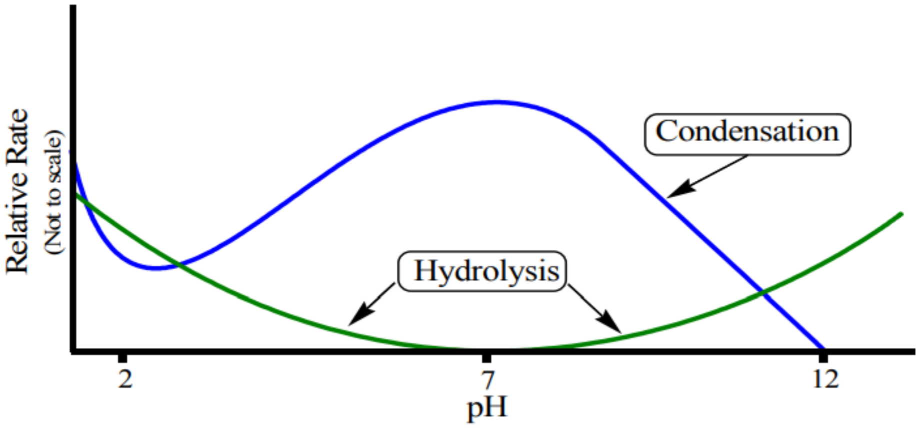

Figure 49. Relative rate of hydrolysis and condensation of TEOS as a function of pH.[84]

From this, we understand that the pH ranges at which silica is possible are pH<1 and 8<pH<11. In both cases silica will grow, but at acidic pH, the particles will aggregate and form micro or macroparticles. This can be overcome by the use different synthesis processes,[134] like the spray-drying of an acidic solution of TEOS. The silica grows in acidic conditions, but the particles size is limited by the droplets size, avoiding over-growth and aggregation. The droplets act as micro-reactor that limit the particles size.

3.4.5 Template extraction

The elimination of the soft template is an important step in the synthesis of mesoporous silica. They are synthesized for their large specific area, so freeing the pores of any material is mandatory. Additionally, the soft template can in some case be detrimental for the final application. For instance, toxic surfactants like CTAB or CTACl are used for the synthesis of MCM-41, which has seen many applications in bio-medicine and drug delivery. Several methods exist for the removal of the soft-template from the porous silica framework.

The calcination at temperatures above 600°C for several hours is straight-forward and yields a material free of any organic matter.[135,136] The limitations are the significant loss of silanols due to dehydroxylation, and the impossibility to perform pyrolysis on organosilanes modified silica which would also suffer from pyrolysis. Also, the dehydroxylation process can lead to the permanent aggregation of the particle via the condensation of the silanols, and lead to the impossibility to redisperse the material.

Extraction of the soft template with a solvent allows to overcome most of the previously mentioned limitations. The synthesized silica material is mixed in a solvent capable of solubilizing the surfactant template.[135,136] Upon heating and mixing, the surfactant migrates into the solvent. Fresh solvent is used several times until the removal of all the template. The addition of an acid, in the case of cationic surfactant like CTAB, allows to increase the efficiency of the extraction with the exchanged proton provided by the acid. The use of specific apparatus, like a Soxhlet montage, eases the template extraction process and saves solvent.

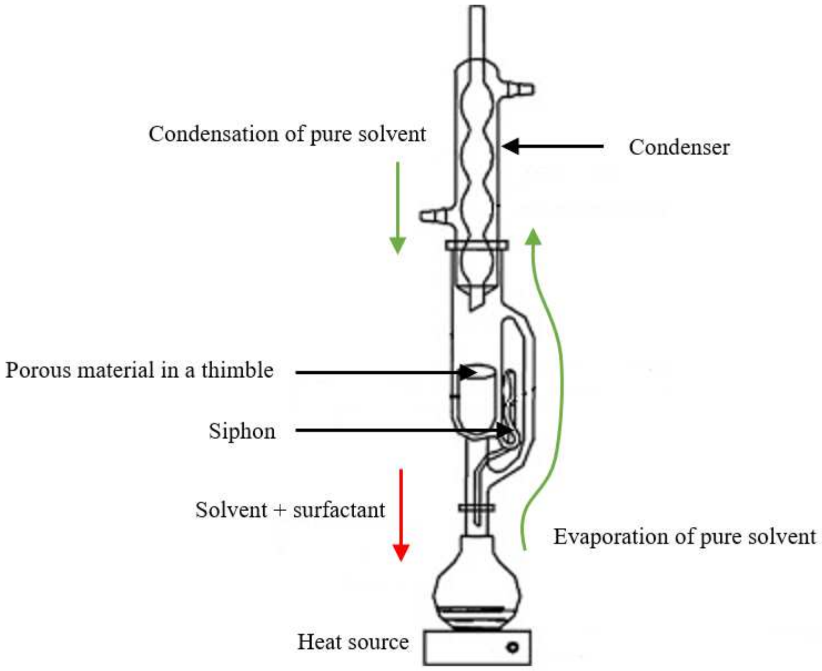

Figure 50. Soxhlet extraction montage.

This montage allows to proceed to multiple extraction cycles with a single volume of solvent. The solvent is evaporated and condensed with a condenser. This pure solvent fills a container in which the material to be extracted is placed, usually in a retaining thimble. The surfactant diffuses from the pores into the pure solvent. Once the solvent level reaches the siphon, the solvent is flushed down, back into the boiling flask. As the solvent is flushed, it carries away the surfactant. The solvent is boiled again to repeat the cycle, but the surfactant remains in the boiling flask and is further concentrated after repeated cycles. This solvent extraction method has the advantage to preserve any surface modification as well as silanols.

Finally, the third method consists in the oxidative digestion of the surfactant.[137] The mesoporous material is mixed in a highly oxidative solution, usually hydrogen peroxide mixed with sulfuric or nitric acid. It has the advantage of preserving the silanols of the silica but is not compatible with silanized materials. Also, this process uses hazardous corrosive chemicals.

4 Functionalization of porous silica particles by silanization

The versatility of soft-templated mesoporous silica resides in the various possibility of chemical surface modification. These can provide the material with additional functionalities and change the properties of the particles. Silanes allow for an extended chemistry with silica as a support. They extend from silanols and their limited chemistry, to any chemical function, allowing to further proceed to many chemical reactions. In the case of silica particles as fillers for tire rubber, the chemical modification is essential to ensure the good dispersion of the silica in the polymer, as well as to promote the chemical reaction between the particles and the polymer chains, in order to crosslink the particles with the matrix. We will present here the different possibility that mesoporous silica offers for chemical modification.

4.1 Post-growth grafting

The functionalization of porous silica particles can be carried after the growth phase. The silanes react with the silanols to covalently bond to the particles. This has been extensively used throughout many studies.[138] The reaction conditions may be changed in order to accommodates certain parameters that depend on the nature of the organosilanes, like its solubility in the solvent or the chemical functions it carries that may be sensitive. The post-growth grafting of silanes can be carried before or after the soft template removal. This allows to target specific regions of the particle for silanization. Modification of the particle before template removal ensures that minimal amount of silane will diffuse into the pores, still filled with surfactant. This way, only the outskirt of the silica particle will carry the new functionalization. If the functionalization is carried after the template removal, the silane will be able to diffuse in the pores and a gradient of functionalization can be observed in the porous structure.

4.2 Co-condensation during particle growth.

Identically to the co-polymerization of synthetic organic polymers, the polymerization of TEOS can be complemented with other organosilanes to included organic functionalities inside the silica particle frame: this method is called co-condensation. This way, the new organic functions can be distributed evenly inside the frame of the particle. It has to be noted that the inclusion of hetero-silanes in ordered mesoporous silica can disturb the organization of the structure[139] or even completely change the morphology of porous particles, from a sphere to a rod shape for example.[140] Indeed, the organosilanes can interfere with the surfactant and the growing particles, disturbing the interaction seen previously in the chapter **Interactions between surfactant and porous particles.**

Finally, post-growth grafting and co-condensation can be combined together, before and/or after the surfactant template removal, to produce complex particle architecture, as shown in the diagram below in **Figure 51**.

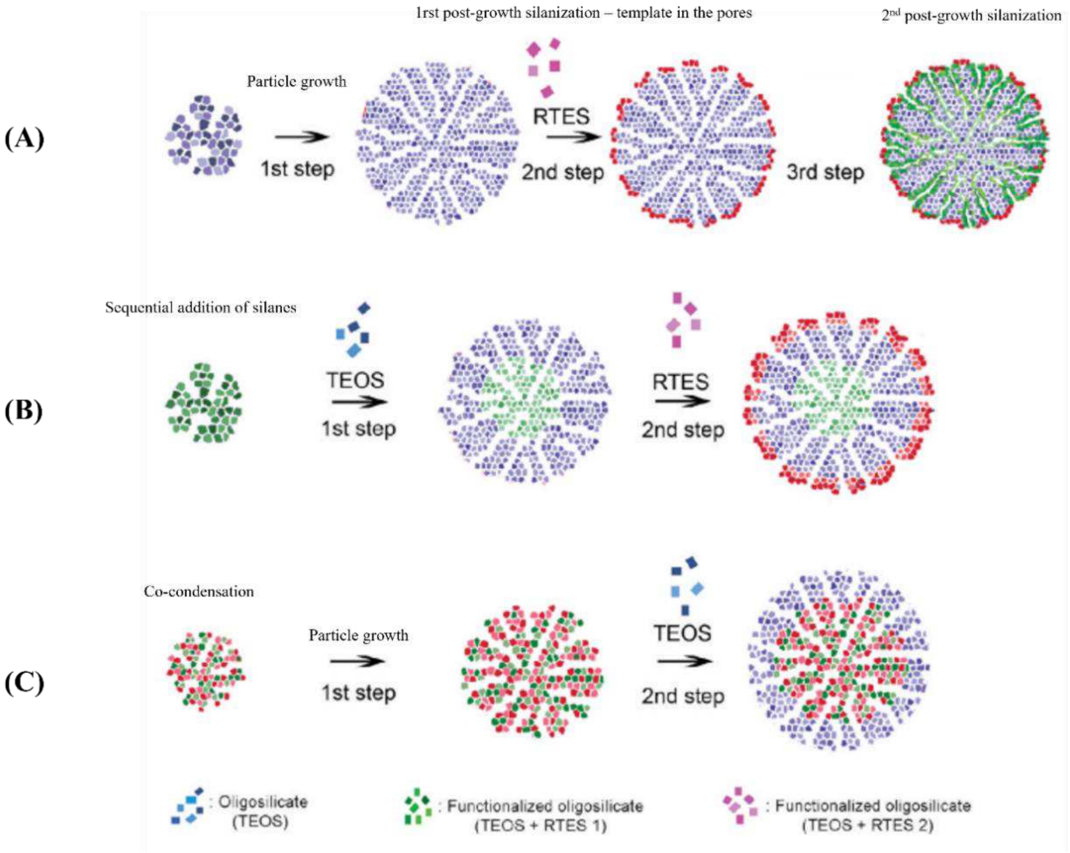

Figure 51. Schematic of different synthetic approaches.[141]

In the case **(A)**, after the growth of the particle with the condensation of TEOS, a first silane is reacted at the surface of the particle and does not diffuse in the pores as the surfactant is still present in the pores. A second silanization allow to cover the pores walls with a second silane after the template removal. In the case **(B)**, the particle is grown in three steps with the sequential addition of three different silanes. In the case **(C)**, the particle is first grown by the co-condensation of two silanes. Then TEOS is added to cover the particle. So far, this kind of complex particle architecture has only been performed on ordered narrow pores systems. Larger pores structures add difficulty for an outer surface functionalization because it is trickier to prevent the silane diffusion inside the porous structure.

In Chapter 3, we investigated the impact of regio-selectively modified dendritic silica on tire rubber properties. We hypothesize that large-pore silica particles are more efficient than ordered narrow at trapping rubber inside their structure. We used the possibilities given by the soft templating sol-gel synthesis to produce a regio-selectively modified dendritic silica with larger pores.

5 Current state of the art, research strategy and relevance of results

5.1 The potential of mesoporous silica as reinforcing fillers

The morphology and surface chemistry of silica filler greatly affect how the filler and the polymer interact within the composite material, and ultimately influence the mechanical properties of this material. These two parameters also have an influence on the capability of the filler to form a reinforcing percolation network.[142] For these reasons, industry and researcher have been focused on developing silica fillers and compatibilizing agents in order to target the specific requirements of tire tread rubber composites. Namely, a low rolling resistance, high wet traction and abrasion resistance.

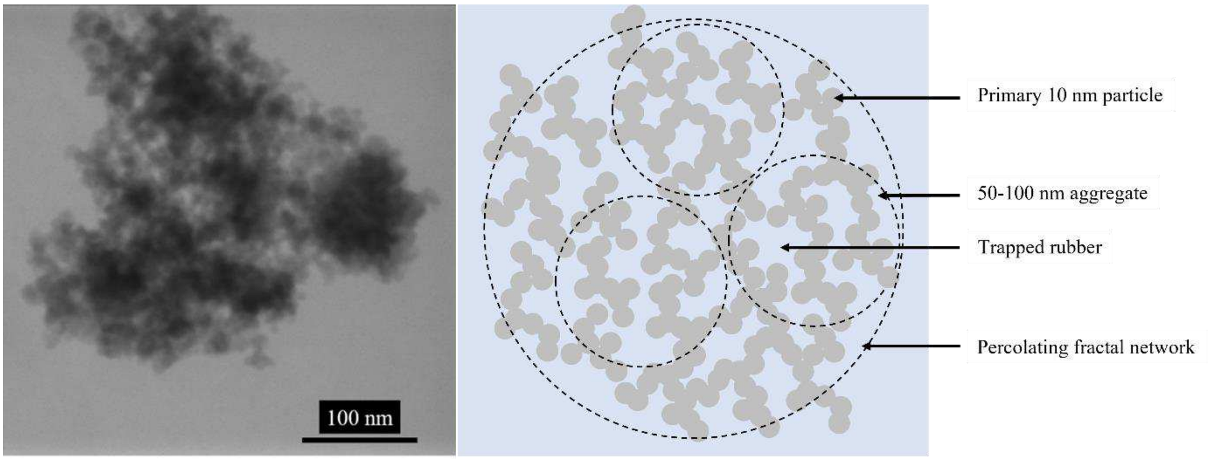

Figure 52. Left – HDS 200MP precipitated fractal silica in STEM microscopy. Right – Schematic representation of a silica filler fractal structure in rubber.

The morphology and surface chemistry of silica filler greatly affect how the filler and the polymer interact within the composite material, and ultimately influence the mechanical properties of this material. These two parameters also have an influence on the capability of the filler to form a reinforcing percolation network.[142] For these reasons, industry and researcher have been focused on developing silica fillers and compatibilizing agents in order to target the specific requirements of tire tread rubber composites. Namely, a low rolling resistance, high wet traction and abrasion resistance.

Current silica fillers used in industrial tire tread rubbers consists of small (about 10 nm) precipitated silica particles, covalently bond into aggregates of about 50-100 nm. These aggregates self-organize when mixed in rubber and form a fractal percolating network. The advantage of this kind of structure is the optimization of the filler surface area exposed to rubber, the filler-filler interaction, as well as rubber interlock inside inter-particles porosity. The silanization of this silica is done in-situ by the addition of TESPT silane during silica and rubber mixing. For this system, two limitations are observed. The first resides in the nature of the filler's reinforcement. Based on a percolating network made of fractal silica aggregates, the dislocation of such network allows for more hysteresis and hinder potential improvement of the rolling resistance.[143] The second limitation reside in the single silane in-situ silanization. Current silanes enable two things: covalent bonding of silica with rubber and better dispersion of silica via its surface hydrophobization. Using only one silane prevents to optimize both components, and therefore prevents the optimization of filler-rubber and filler-filler interaction.

Mesoporous silica particles seem to offer a good base for the development of performant fillers. After the first patent in 1971, and then the synthesis of MCM-41 and SBA-15, [128,130] this material has seen extensive research being conducted in many fields, such as catalysis, drug delivery, medical imagery, water treatment or gas separation, [122,144-147] thank to their high specific surface area. During their synthesis process, one has the opportunity to tune the shape, size, pore size and surface chemistry of the particles. Added to their large specific surface area, this material is a good candidate for reinforcing tire tread rubber composite. Despite these apparent qualities, mesoporous silicas have not seen a widespread application in rubber composite material research field. The few works reporting the use of porous silica used narrow pore particles, [148,149] and did not compare these new particles to state-of-the-art reinforcing silica such as precipitated of fused silica. In addition, the capability of mesoporous silica to form reinforcing percolating network has barely been questioned. The main purpose of this PhD thesis is therefore to explore and bring new insights in the field of silica rubber nanocomposite. Studying and understanding how the specific features of mesoporous silica can affect the filler-polymer interactions, and the subsequent consequences on their reinforcing potential for tire tread rubber compound will bring new elements for the research as well as for potential industrial application.

5.2 Research strategy

Because the silanization of the silica filler is a critical step, our research strategy first focused on developing a better understanding of the silica reactivity toward silanization and its optimization. Indeed, the chemical modification of flat silica substrates with silanes, such as quartz of silicon wafers have been extensively studied. But not all learning can be transferred to silica particles, mostly due to the difference in surface morphology, that affect the possibility to probe the initial state of the substrate, its modification and its characterization after silanization.

Thus, studying and understanding how silanization conditions (moisture content, solvent, influence of the catalyst, …) can be optimized and used to target specific silica surface modification is an important first step. These results are presented in the first chapter of this manuscript entitled “Original Basic Activation for Enhancing Silica Particle Reactivity: Characterization by Liquid Phase Silanization and Silica-Rubber Nanocomposite Properties”. In this work, we studied the possibility to enhance the silica surface reactivity as a mean to better control the deposition of silane on the particle surface.

Building upon this work, we proposed the synthesis and application of dual-silane pre-treated silica for tire tread rubber composite. This is presented in the second chapter “Dual-Silane Pre-modified Silica Nanoparticles: Synthesis and Interplay between Chemical, Mechanical, and Curing Properties of Silica − Rubber Nanocomposites: Application to Tire Tread Compounds”. By separating the reactive and dispersive function, we could study the effect of the respective silane length on the final mechanical properties of the composite and the dispersion of the filler.

Finally, we combined the previously acquired knowledge on silica reactivity and silanization in order to synthesize an innovative regio-selectively modified silica particle. Ideally, a mercapto- moieties are located within the pores, while alkyl chains are grafted on the outer silica surface of the particle. The rationale behind this design is to enable an efficient dispersion of the particles in the elastomeric matrix with the peripheric alkyl chains, while promoting the coupling reaction of silica and the polymer inside the porosity with the mercapto groups. Indeed, the interest created by mesoporous silica as reinforcing filler revolve around its high specific surface area, and the fact that the immobilization of polymer chains changes its dynamic and participates to the reinforcement of composite. So far, most of the studies relating the use of mesoporous silica particles in a polymer or in an elastomer have used narrow pore particles, like MCM-41, with a typical pore diameter of 2 to 3 nm. Also, it has not been confirmed that polymer chains penetrate such narrow pore. The only occurrences of polymer constrained in mesopores have been reported with technic such as supercritical CO2, high pressure, or impregnation of liquid monomer before polymerization. Especially under normal operation condition of rubber compounding, it is unlikely that polymer chains would permeate inside such narrow pores. For this reason, a dendritic morphology was selected. It offers wide open pores, and the synthetic process yields a high yield, which can only be beneficial with a perspective of industrial application. The silanization of such particle is still required in order to ensure its dispersion as well as its chemical coupling with the rubber.

5.3 Results in light of the state of the art

The results obtained along this thesis contribute to the field of nanocomposite and silica reinforced rubbers in different aspects. The study of silica reactivity enhancement developed in the first chapter brings a new insight on silica silanization. Usually, mild organic bases are used to increase the silanization yield. [150-153] The use of strong base such as DBU, or inorganic molecules such as sodium hydride have never been investigated in such context. The silanization of silica in organic solvent with alkylsilane of different length, as well as the in-situ silanization of silica in rubber were used to benchmark the reactivity of the activated silica. NMR and TGA characterization enabled to conclude that DBU is the most effective catalyst for silica pre-treatment in an organic solvent, while sodium hydride yields better nanocomposite mechanical properties. Interestingly, the activation of silica with sodium hydride increases the silanol density of the silica particles. Even though some elements in the literature help to understand the possible on-going reactions, [154,155] it is something that has been studied extensively and would potentially lead to interesting results. Indeed, the silanol density of a silica filler is a critical property for the fabrication of silica reinforced nanocomposites. [61,156] The novel use of DBU and NaH as silica reactivity enhancer proposes another way to control silica silanization as well as the silanol density of particles.

We used this result to synthesize dual-silane pre-treated silica, presented in chapter two. These pretreated fillers are designed as follow: a mercapto and an alkylsilane are grafted on the surface of DB-activated precipitated fractal silica. Different primary chain lengths have been tested in order to study the relative shielding effect of one silane over the other. The silanes have been grafted sequentially, and DBU was used to enhance the reactivity of the silica during the first silanization. These new fillers were used to produce silica nanocomposites, which mechanical properties and filler dispersion were characterized. The results showed that the short-short silane combination gives off the best dynamic mechanical performances with an improved wet grip compared to state-of-the-art precipitated silica filler. Interestingly, the grafting of long alkylsilane (18 carbons) completely disturb the silica-rubber interface, as demonstrated by AFM results. A dispersive layer can be spotted around particles, due to the over-hydrophobization of the silica surface. This prevents the formation of a percolation network, favors the aggregation of the filler, leading to poor reinforcement and poor dynamic mechanical properties, showing the importance of the direct relation between the silica-rubber interface, at the microscopic scale, and the performances of the final material at the macroscopic scale. As it has already been demonstrated, the silica-rubber interface greatly influences the composite properties. [157,158] Based on this, the results of this study bring new elements in the understanding of the role of- silane and silanization on the modification of the silica-rubber nanocomposites properties.

The final chapter of the thesis is dedicated to the study of the potential of mesoporous silica particles as potent fillers for tire tread rubber. Firstly, we present the for the first time, the synthesis of a regio-selectively modified dendritic silica (RMDS) particle, as well as its direct elemental imaging and characterization by HIM-SIMS. Even if similar structures have been synthesized in the past, none were characterized to this extent. Additionally, this work constitutes the first application of large pores silanized silica particles as reinforcing filler for rubber, and especially tire rubber. Other porous silica particles have been used as reinforcing fillers, but only with narrow pores, and a simple silanization. [148,149] For the first time, we discuss in this chapter the percolating capabilities of such spherical porous particle. Through a comparative study, we show that the architecture of this particle does not allow to form a reinforcing network. The addition of small amount of smaller precipitated silica is sufficient to overcome this limitation. The fact that most of the filler consists of mesoporous silica particles is especially important. These particles act as “unbreakable reinforcing aggregates” when submitted to a deformation, unlike the classical precipitated silica, which relies on aggregation for its reinforcing properties. This “unbreakable aggregate” behavior implies a lower Payne effect, while providing simultaneously a higher reinforcement and better dynamic performances. This major result is a breakthrough is the field of rubber nanocomposite by giving the opportunity to control the amount of Payne effect of the system by varying the amount of porous silica. It interrogates the classical mechanism proposed for the mechanical reinforcement, and open the way for another one.

To conclude, this PhD thesis is focused on the study of silica silanization, silica filler architecture, and the study of the relation between the silica-rubber interface and the mechanical performances. The reported work participated to extend the knowledge of silica silanization and its impact on silica-rubber properties. More specifically, the limitation and reinforcing potential of porous silica were studied and confirmed.

6 Bibliography

1. GHOREYSHI, M.H.R. A state of the art review of the finite element modelling of rolling tyres. **2008**.

2. Weng, P.; Tang, Z.; Guo, B. Solving “magic triangle” of tread rubber composites with phosphonium-modified petroleum resin. *Polymer* **2020**, *190*, 122244.

3. Kern, W.; Futamura, S. Effect of tread polymer structure on tyre performance. *Polymer* **1988**, *29*, 1801-1806.

4. Jung, J.; Sodano, H.A. Aramid nanofiber reinforced rubber compounds for the application of tire tread with high abrasion resistance and fuel saving efficiency. *ACS Applied Polymer Materials* **2020**, *2*, 4874-4884.

5. Araujo-Morera, J.; Hernández Santana, M.; Verdejo, R.; López-Manchado, M.A. Giving a Second opportunity to tire waste: An alternative path for the development of sustainable self-healing styrene–butadiene rubber compounds overcoming the magic triangle of tires. *Polymers* **2019**, *11*, 2122.

6. Hofmann, W. *Vulcanization and vulcanizing agents*; Maclaren London: 1967.

7. Krejsa, M.; Koenig, J. A review of sulfur crosslinking fundamentals for accelerated and unaccelerated vulcanization. *Rubber Chem. Technol.* **1993**, *66*, 376-410.

8. Heideman, G.; Datta, R.; Noordermeer, J.W.; Baarle, B.v. Influence of zinc oxide during different stages of sulfur vulcanization. Elucidated by model compound studies. *J. Appl. Polym. Sci.* **2005**, *95*, 1388-1404.

9. Heideman, G.; Datta, R.N.; Noordermeer, J.W.; van Baarle, B. Activators in accelerated sulfur vulcanization. *Rubber Chem. Technol.* **2004**, *77*, 512-541.

10. Coran, A.Y. Vulcanization. In *Science and technology of rubber*; Elsevier: 1994; pp. 339-385.

11. Wool, R.P. Polymer entanglements. *Macromolecules* **1993**, *26*, 1564-1569.

12. Wolff, S. Chemical aspects of rubber reinforcement by fillers. *Rubber Chem. Technol.* **1996**, *69*, 325-346.

13. Studebaker, M.L. The chemistry of carbon black and reinforcement. *Rubber Chem. Technol.* **1957**, *30*, 1400-1483.

14. Wang, M.J.; Gray, C.A.; Reznek, S.A.; Mahmud, K.; Kutsovsky, Y. Carbon black. *Kirk-Othmer Encyclopedia of Chemical Technology* **2000**.

15. Toth, P.; Vikström, T.; Molinder, R.; Wiinikka, H. Structure of carbon black continuously produced from biomass pyrolysis oil. *Green Chemistry* **2018**, *20*, 3981-3992.

16. Lay, M.; Rusli, A.; Abdullah, M.K.; Hamid, Z.A.A.; Shuib, R.K. Converting dead leaf biomass into activated carbon as a potential replacement for carbon black filler in rubber composites. *Composites Part B: Engineering* **2020**, *201*, 108366.

17. Medalia, A.I. Electrical conduction in carbon black composites. *Rubber Chem. Technol.* **1986**, *59*, 432-454.

18. Huang, J.C. Carbon black filled conducting polymers and polymer blends. *Advances in Polymer Technology: Journal of the Polymer Processing Institute* **2002**, *21*, 299-313.

19. Cecilia, J.; Vilarrasa-García, E.; Cavalcante Jr, C.; Azevedo, D.; Franco, F.; Rodríguez-Castellón, E. Evaluation of two fibrous clay minerals (sepiolite and palygorskite) for CO2 Capture. *Journal of environmental chemical engineering* **2018**, *6*, 4573-4587.

20. Ruiz-Hitzky, E.; Aranda, P.; Álvarez, A.; Santarén, J.; Esteban-Cubillo, A. Advanced materials and new applications of sepiolite and palygorskite. In *Developments in Clay Science*; Elsevier: 2011; Volume 3, pp. 393-452.

21. Preisinger, A. Sepiolite and related compounds: its stability and application. *Clays Clay Miner.* **1961**, *10*, 365-371.

22. Suárez, M.; García-Romero, E. Variability of the surface properties of sepiolite. *Applied Clay Science* **2012**, *67*, 72-82.

23. Staropoli, M.; Rogé, V.; Moretto, E.; Didierjean, J.; Michel, M.; Duez, B.; Steiner, P.; Thielen, G.; Lenoble, D.; Thomann, J.-S. Hybrid silica-based fillers in nanocomposites: Influence of isotropic/isotropic and isotropic/anisotropic fillers on mechanical properties of styrene-butadiene (SBR)-based rubber. *Polymers* **2021**, *13*, 2413.

24. Galimberti, M. *Rubber-clay nanocomposites: science, technology, and applications*; John Wiley & Sons: 2011.

25. Valentín, J.L.; López-Manchado, M.; Posadas, P.; Rodríguez, A.; Marcos-Fernández, A.; Ibarra, L. Characterization of the reactivity of a silica derived from acid activation of sepiolite with silane by 29Si and 13C solid-state NMR. *J. Colloid Interface Sci.* **2006**, *298*, 794-804.

26. Hernández, L.G.l.; Ibarra Rueda, L.M.; Antón, C.C. Magnesium silicate filler in rubber tread compounds. *Rubber Chem. Technol.* **1987**, *60*, 606-617.

27. Bernardo, V.; Martín-de León, J.; Laguna-Gutiérrez, E.; Rodríguez-Pérez, M.Á. PMMA-sepiolite nanocomposites as new promising materials for the production of nanocellular polymers. *Eur. Polym. J.* **2017**, *96*, 10-26.

28. Ma, J.; Bilotti, E.; Peijs, T.; Darr, J. Preparation of polypropylene/sepiolite nanocomposites using supercritical CO2 assisted mixing. *Eur. Polym. J.* **2007**, *43*, 4931-4939.

29. Bokobza, L.; Leroy, E.; Lalanne, V. Effect of filling mixtures of sepiolite and a surface modified fumed silica on the mechanical and swelling behavior of a styrene–butadiene rubber. *Eur. Polym. J.* **2009**, *45*, 996-1001.

30. Di Credico, B.; Cobani, E.; Callone, E.; Conzatti, L.; Cristofori, D.; D'Arienzo, M.; Dirè, S.; Giannini, L.; Hanel, T.; Scotti, R. Size-controlled self-assembly of anisotropic sepiolite fibers in rubber nanocomposites. *Applied Clay Science* **2018**, *152*, 51-64.

31. Tagliaro, I.; Cobani, E.; Carignani, E.; Conzatti, L.; D'Arienzo, M.; Giannini, L.; Martini, F.; Nardelli, F.; Scotti, R.; Stagnaro, P. The self-assembly of sepiolite and silica fillers for advanced rubber materials: The role of collaborative filler network. *Applied Clay Science* **2022**, *218*, 106383.

32. Tadiello, L.; Guerra, S.; Giannini, L. Sepiolite-Based Anisotropic Nanoparticles: A New Player in the Rubber Reinforcement Technology for Tire Application. *Applied Sciences* **2022**, *12*, 2714.

33. Favier, V.; Canova, G.; Cavaillé, J.; Chanzy, H.; Dufresne, A.; Gauthier, C. Nanocomposite materials from latex and cellulose whiskers. *Polym. Adv. Technol.* **1995**, *6*, 351-355.

34. Silva, M.; Sanches, A.; Medeiros, E.; Mattoso, L.; McMahan, C.; Malmonge, J. Nanocomposites of natural rubber and polyaniline-modified cellulose nanofibrils. *J. Therm. Anal. Calorim.* **2014**, *117*, 387-392.

35. Siqueira, G.; Bras, J.; Dufresne, A. Cellulose whiskers versus microfibrils: influence of the nature of the nanoparticle and its surface functionalization on the thermal and mechanical properties of nanocomposites. *Biomacromolecules* **2009**, *10*, 425-432.

36. Eichhorn, S.J. Cellulose nanowhiskers: promising materials for advanced applications. *Soft Matter* **2011**, *7*, 303-315.

37. Moon, R.J.; Martini, A.; Nairn, J.; Simonsen, J.; Youngblood, J. Cellulose nanomaterials review: structure, properties and nanocomposites. *Chem. Soc. Rev.* **2011**, *40*, 3941-3994.

38. Eyley, S.; Thielemans, W. Surface modification of cellulose nanocrystals. *Nanoscale* **2014**, *6*, 7764-7779.

39. Masłowski, M.; Miedzianowska, J.; Strzelec, K. Silanized cereal straw as a novel, functional filler of natural rubber biocomposites. *Cellulose* **2019**, *26*, 1025-1040.

40. Miedzianowska, J.; Masłowski, M.; Rybiński, P.; Strzelec, K. Properties of chemically modified (selected silanes) lignocellulosic filler and its application in natural rubber biocomposites. *Materials* **2020**, *13*, 4163.

41. Jo, J.; Kim, H.; Jeong, S.-Y.; Park, C.; Hwang, H.S.; Koo, B. Changes in mechanical properties of polyhydroxyalkanoate with double silanized cellulose nanocrystals using different organosiloxanes. *Nanomaterials* **2021**, *11*, 1542.

42. Ali, S.D.; Imiete, I.E.; Orlandi, M.E.; Castellani, L.; Hanel, T.; Zoia, L. Novel CNC/silica hybrid as potential reinforcing filler for natural rubber compounds. *J. Appl. Polym. Sci.* **2020**, *137*, 48332.

43. Bailey, J.; Mecartney, M. Formation of colloidal silica particles from alkoxides. *Colloids and Surfaces* **1992**, *63*, 151-161.

44. Bhattacharyya, S.K.; Parmar, B.S.; Chakraborty, A.; Dasgupta, S.; Mukhopadhyay, R.; Bandyopadhyay, A. Exploring microcrystalline cellulose (mcc) as a green multifunctional additive (MFA) in a typical solution-grade styrene butadiene rubber (S-SBR)-based tread compound. *Industrial & engineering chemistry research* **2012**, *51*, 10649-10658.

45. Feofilova, E.; Mysyakina, I. Lignin: Chemical structure, biodegradation, and practical application (a review). *Appl. Biochem. Microbiol.* **2016**, *52*, 573-581.

46. Zakzeski, J.; Bruijnincx, P.C.; Jongerius, A.L.; Weckhuysen, B.M. The catalytic valorization of lignin for the production of renewable chemicals. *Chem. Rev.* **2010**, *110*, 3552-3599.

47. Figueiredo, P.; Lintinen, K.; Hirvonen, J.T.; Kostiainen, M.A.; Santos, H.A. Properties and chemical modifications of lignin: Towards lignin-based nanomaterials for biomedical applications. *Prog. Mater Sci.* **2018**, *93*, 233-269.

48. Zhao, W.; Simmons, B.; Singh, S.; Ragauskas, A.; Cheng, G. From lignin association to nano-/micro-particle preparation: extracting higher value of lignin. *Green Chemistry* **2016**, *18*, 5693-5700.

49. Si, M.; Zhang, J.; He, Y.; Yang, Z.; Yan, X.; Liu, M.; Zhuo, S.; Wang, S.; Min, X.; Gao, C. Synchronous and rapid preparation of lignin nanoparticles and carbon quantum dots from natural lignocellulose. *Green Chemistry* **2018**, *20*, 3414-3419.

50. Manisekaran, A.; Grysan, P.; Duez, B.; Schmidt, D.F.; Lenoble, D.; Thomann, J.-S. Solvents drive self-assembly mechanisms and inherent properties of Kraft lignin nanoparticles (< 50 nm). *J. Colloid Interface Sci.* **2022**, *626*, 178-192.

51. Yu, P.; He, H.; Jia, Y.; Tian, S.; Chen, J.; Jia, D.; Luo, Y. A comprehensive study on lignin as a green alternative of silica in natural rubber composites. *Polym. Test.* **2016**, *54*, 176-185.

52. Barana, D.; Ali, S.D.; Salanti, A.; Orlandi, M.; Castellani, L.; Hanel, T.; Zoia, L. Influence of lignin features on thermal stability and mechanical properties of natural rubber compounds. *ACS Sustainable Chemistry & Engineering* **2016**, *4*, 5258-5267.

53. Jiang, C.; He, H.; Yao, X.; Yu, P.; Zhou, L.; Jia, D. The aggregation structure regulation of lignin by chemical modification and its effect on the property of lignin/styrene–butadiene rubber composites. *J. Appl. Polym. Sci.* **2018**, *135*, 45759.

54. Jiang, C.; Bo, J.; Xiao, X.; Zhang, S.; Wang, Z.; Yan, G.; Wu, Y.; Wong, C.; He, H. Converting waste lignin into nano-biochar as a renewable substitute of carbon black for reinforcing styrene-butadiene rubber. *Waste Manage. (Oxford)* **2020**, *102*, 732-742.

55. Parvathy, G.; Sethulekshmi, A.; Jayan, J.S.; Raman, A.; Saritha, A. Lignin based nano-composites: Synthesis and applications. *Process Saf. Environ. Prot.* **2021**, *145*, 395-410.

56. Ramier, J.; Gauthier, C.; Chazeau, L.; Stelandre, L.; Guy, L. Payne effect in silica-filled styrene–butadiene rubber: influence of surface treatment. *J. Polym. Sci., Part B: Polym. Phys.* **2007**, *45*, 286-298.

57. Dohi, H.; Horiuchi, S. Locating a silane coupling agent in silica-filled rubber composites by EFTEM. *Langmuir* **2007**, *23*, 12344-12349.

58. Payne, A.R. The dynamic properties of carbon black-loaded natural rubber vulcanizates. Part I. *J. Appl. Polym. Sci.* **1962**, *6*, 57-63.

59. Donnet, J.-B. Black and white fillers and tire compound. *Rubber Chem. Technol.* **1998**, *71*, 323-341.

60. Wolff, S.; Wang, M.-J. Filler—elastomer interactions. Part IV. The effect of the surface energies of fillers on elastomer reinforcement. *Rubber Chem. Technol.* **1992**, *65*, 329-342.

61. Fröhlich, J.; Niedermeier, W.; Luginsland, H.-D. The effect of filler–filler and filler–elastomer interaction on rubber reinforcement. *Composites Part A: Applied Science and Manufacturing* **2005**, *36*, 449-460.

62. Sarkawi, S.; Dierkes, W.K.; Noordermeer, J.W. Elucidation of filler-to-filler and filler-to-rubber interactions in silica-reinforced natural rubber by TEM Network Visualization. *Eur. Polym. J.* **2014**, *54*, 118-127.

63. Wang, M.-J. The role of filler networking in dynamic properties of filled rubber. *Rubber Chem. Technol.* **1999**, *72*, 430-448.

64. Papon, A.; Montes, H.; Lequeux, F.; Oberdisse, J.; Saalwaechter, K.; Guy, L. Solid particles in an elastomer matrix: impact of colloid dispersion and polymer mobility modification on the mechanical properties. *Soft Matter* **2012**, *8*, 4090-4096.

65. Mujtaba, A.; Keller, M.; Ilisch, S.; Radusch, H.-J.; Thurn-Albrecht, T.; Saalwachter, K.; Beiner, M. Mechanical properties and cross-link density of styrene–butadiene model composites containing fillers with bimodal particle size distribution. *Macromolecules* **2012**, *45*, 6504-6515.

66. Mullins, L. Softening of rubber by deformation. *Rubber Chem. Technol.* **1969**, *42*, 339-362.

67. Diani, J.; Fayolle, B.; Gilormini, P. A review on the Mullins effect. *Eur. Polym. J.* **2009**, *45*, 601-612.

68. Wang, M.-J. Effect of polymer-filler and filler-filler interactions on dynamic properties of filled vulcanizates. *Rubber Chem. Technol.* **1998**, *71*, 520-589.

69. Saito, Y. New polymer development for low rolling resistance tyres. *Kautschuk und Gummi, Kunststoffe* **1986**, *39*, 30-32.

70. Williams, M.L.; Landel, R.F.; Ferry, J.D. The temperature dependence of relaxation mechanisms in amorphous polymers and other glass-forming liquids. *J. Am. Chem. Soc.* **1955**, *77*, 3701-3707.

71. Álvarez-Vázquez, A.; Fernández-Canteli, A.; Castillo Ron, E.; Fernández Fernández, P.; Muñiz-Calvente, M.; Lamela Rey, M.J. A novel approach to describe the time–temperature conversion among relaxation curves of viscoelastic materials. *Materials* **2020**, *13*, 1809.

72. Tsai, W.-T.; Lai, C.-W.; Hsien, K.-J. Characterization and adsorption properties of diatomaceous earth modified by hydrofluoric acid etching. *J. Colloid Interface Sci.* **2006**, *297*, 749-754.

73. Treguer, P.; Nelson, D.M.; Van Bennekom, A.J.; DeMaster, D.J.; Leynaert, A.; Quéguiner, B. The silica balance in the world ocean: a reestimate. *Science* **1995**, *268*, 375-379.

74. Feray, A.; Szely, N.; Guillet, E.; Hullo, M.; Legrand, F.-X.; Brun, E.; Pallardy, M.; Biola-Vidamment, A. How to address the adjuvant effects of nanoparticles on the immune system. *Nanomaterials* **2020**, *10*, 425.

75. Zhuravlev, L. The surface chemistry of amorphous silica. Zhuravlev model. *Colloids Surf. Physicochem. Eng. Aspects* **2000**, *173*, 1-38.

76. Yan, C.; Moretto, E.; Kachouri, O.; Biagi, J.-L.; Thomann, J.-S.; Kayser, F.; Dieden, R. Revealing the dehydration/deuteration processes at the liquid-solid interface by nuclear magnetic resonance spectroscopy. *Colloids Surf. Physicochem. Eng. Aspects* **2022**, *637*, 128260.

77. Sindorf, D.W.; Maciel, G.E. Silicon-29 nuclear magnetic resonance study of hydroxyl sites on dehydrated silica gel surfaces, using silylation as a probe. *The Journal of Physical Chemistry* **1983**, *87*, 5516-5521.

78. Anderson Jr, J.; Wickersheim, K. Near infrared characterization of water and hydroxyl groups on silica surfaces. *Surf. Sci.* **1964**, *2*, 252-260.

79. Azzopardi, M.; Arribart, H. In situ FTIR study of the formation of an organosilane layer at the silica/solution interface. *The Journal of Adhesion* **1994**, *46*, 103-115.

80. Luhmer, M.; d'Espinose, J.; Hommel, H.; Legrand, A. High-resolution 29Si solid-state NMR study of silicon functionality distribution on the surface of silicas. *Magn. Reson. Imaging* **1996**, *14*, 911-913.

81. Baeza, G.P.; Genix, A.-C.; Degrandcourt, C.; Petitjean, L.; Gummel, J.; Couty, M.; Oberdisse, J. Multiscale filler structure in simplified industrial nanocomposite silica/SBR systems studied by SAXS and TEM. *Macromolecules* **2013**, *46*, 317-329.

82. Ramier, J.; Chazeau, L.; Gauthier, C.; Guy, L.; Bouchereau, M.-N. Grafting of silica during the processing of silica-filled SBR: comparison between length and content of the silane. *J. Polym. Sci., Part B: Polym. Phys.* **2006**, *44*, 143-152.

83. Osterholtz, F.; Pohl, E. Kinetics of the hydrolysis and condensation of organofunctional alkoxysilanes: a review. *J. Adhes. Sci. Technol.* **1992**, *6*, 127-149.

84. ALOthman, Z. A review: fundamental aspects of silicate mesoporous materials. *Materials* **2012**, *5*, 2874-2902.

85. Hench, L.L.; West, J.K. The sol-gel process. *Chem. Rev.* **1990**, *90*, 33-72.

86. Jiang, H.; Zheng, Z.; Li, Z.; Wang, X. Effects of temperature and solvent on the hydrolysis of alkoxysilane under alkaline conditions. *Industrial & engineering chemistry research* **2006**, *45*, 8617-8622.

87. Bernards, T.; Van Bommel, M.; Boonstra, A. Hydrolysis-condensation processes of the tetra-alkoxysilanes TPOS, TEOS and TMOS in some alcoholic solvents. *J. Non-Cryst. Solids* **1991**, *134*, 1-13.

88. Brinker, C.J.; Scherer, G.W. *Sol-gel science: the physics and chemistry of sol-gel processing*; Academic press: 2013.

89. Derouet, D.; Forgeard, S.; Brosse, J.C.; Emery, J.; Buzare, J.Y. Application of solid-state NMR (13C and 29Si CP/MAS NMR) spectroscopy to the characterization of alkenyltrialkoxysilane and trialkoxysilyl-terminated polyisoprene grafting onto silica microparticles. *J. Polym. Sci., Part A: Polym. Chem.* **1998**, *36*, 437-453.

90. Tesoro, G.; Wu, Y. Silane coupling agents: the role of the organofunctional group. *J. Adhes. Sci. Technol.* **1991**, *5*, 771-784.

91. Chen, a.K.; Tsuchiya, T.; Mackenzie, J.D. Sol-gel processing of silica: I. The role of the starting compounds. *J. Non-Cryst. Solids* **1986**, *81*, 227-237.

92. Schmidt, H.; Scholze, H.; Kaiser, A. Principles of hydrolysis and condensation reaction of alkoxysilanes. *J. Non-Cryst. Solids* **1984**, *63*, 1-11.

93. Kannan, B.; Higgins, D.A.; Collinson, M.M. Aminoalkoxysilane reactivity in surface amine gradients prepared by controlled-rate infusion. *Langmuir* **2012**, *28*, 16091-16098.

94. Salon, M.-C.B.; Belgacem, M.N. Competition between hydrolysis and condensation reactions of trialkoxysilanes, as a function of the amount of water and the nature of the organic group. *Colloids Surf. Physicochem. Eng. Aspects* **2010**, *366*, 147-154.

95. Manzano, J.S.; Wang, H.; Kobayashi, T.; Naik, P.; Lai, K.C.; Evans, J.W.; Slowing, I.I. Kinetics of the functionalization of mesoporous silica nanoparticles: Implications on surface group distributions, adsorption and catalysis. *Microporous Mesoporous Mater.* **2020**, *305*, 110276.

96. Mark E. McGovern, K.M.R.K., and Michael Thompson. Role of Solvent ont the Silanization of Glass with Octadecyltrichlorosilane. *Langmuir* **1994**, *10*, 3607-3614.

97. Smirnov*, A.V.K.a.S.N. Effect of Water on Silanization of Silica by Trimethoxysilanes. *Langmuir* **2002**, *18*.

98. Daniels, M.W.; Sefcik, J.; Francis, L.F.; McCormick, A.V. Reactions of a trifunctional silane coupling agent in the presence of colloidal silica sols in polar media. *J. Colloid Interface Sci.* **1999**, *219*, 351-356.

99. Rankin, S.E.; Macosko, C.W.; McCormick, A.V. Sol-gel polycondensation kinetic modeling: Methylethoxysilanes. *AICHE J.* **1998**, *44*, 1141-1156.

100. Nishiyama, N.; Horie, K.; Asakura, T. Adsorption behavior of a silane coupling agent onto a colloidal silica surface studied by 29Si NMR spectroscopy. *J. Colloid Interface Sci.* **1989**, *129*, 113-119.

101. Sutra, P.; Fajula, F.; Brunel, D.; Lentz, P.; Daelen, G.; Nagy, J.B. 29Si and 13C MAS-NMR characterization of surface modification of micelle-templated silicas during the grafting of organic moieties and end-capping. *Colloids Surf. Physicochem. Eng. Aspects* **1999**, *158*, 21-27.

102. Behringer, K.D.; Blümel, J. Reactions of ethoxysilanes with Silica: A solid-state NMR Study. *J. Liq. Chromatogr. Rel. Technol.* **1996**, *19*, 2753-2765.

103. Philipse, A.; Vrij, A. Preparation and properties of nonaqueous model dispersions of chemically modified, charged silica spheres. *J. Colloid Interface Sci.* **1989**, *128*, 121-136.

104. Lee, L.-H. Wettability and conformation of reactive polysiloxanes. *J. Colloid Interface Sci.* **1968**, *27*, 751-760.

105. Lochmuller, C.; Colborn, A.; Hunnicutt, M.; Harris, J. Organization and distribution of molecules chemically bound to silica. *Anal. Chem.* **1983**, *55*, 1344-1348.

106. Lochmuller, C.; Colborn, A.; Hunnicutt, M.; Harris, J. Bound pyrene excimer photophysics and the organization and distribution of reaction sites on silica. *J. Am. Chem. Soc.* **1984**, *106*, 4077-4082.

107. Fang, J.; Knobler, C.M. Control of density in self-assembled organosilane monolayers by Langmuir-Blodgett deposition. *The Journal of Physical Chemistry* **1995**, *99*, 10425-10429.

108. Fang, J.; Knobler, C.M. Phase-separated two-component self-assembled organosilane monolayers and their use in selective adsorption of a protein. *Langmuir* **1996**, *12*, 1368-1374.

109. Stöber, W.; Fink, A.; Bohn, E. Controlled growth of monodisperse silica spheres in the micron size range. *J. Colloid Interface Sci.* **1968**, *26*, 62-69.

110. Tan, C.; Bowen, B.; Epstein, N. Production of monodisperse colloidal silica spheres: Effect of temperature. *J. Colloid Interface Sci.* **1987**, *118*, 290-293.

111. Han, Y.; Lu, Z.; Teng, Z.; Liang, J.; Guo, Z.; Wang, D.; Han, M.-Y.; Yang, W. Unraveling the growth mechanism of silica particles in the stober method: in situ seeded growth model. *Langmuir* **2017**, *33*, 5879-5890.

112. Malay, O.; Yilgor, I.; Menceloglu, Y.Z. Effects of solvent on TEOS hydrolysis kinetics and silica particle size under basic conditions. *J. Sol-Gel Sci. Technol.* **2013**, *67*, 351-361.

113. Ghimire, P.P.; Jaroniec, M. Renaissance of Stöber method for synthesis of colloidal particles: New developments and opportunities. *J. Colloid Interface Sci.* **2021**, *584*, 838-865.

114. Kobayashi, M.; Juillerat, F.; Galletto, P.; Bowen, P.; Borkovec, M. Aggregation and charging of colloidal silica particles: effect of particle size. *Langmuir* **2005**, *21*, 5761-5769.

115. Kim, J.; Kim, L.; Kim, C. Size control of silica nanoparticles and their surface treatment for fabrication of dental nanocomposites. *Biomacromolecules* **2007**, *8*, 215-222.

116. Bell, N.C.; Minelli, C.; Tompkins, J.; Stevens, M.M.; Shard, A.G. Emerging techniques for submicrometer particle sizing applied to Stober silica. *Langmuir* **2012**, *28*, 10860-10872.

117. Sing, K.S. Reporting physisorption data for gas/solid systems with special reference to the determination of surface area and porosity (Recommendations 1984). *Pure Appl. Chem.* **1985**, *57*, 603-619.

118. Trewyn, B.G.; Slowing, I.I.; Giri, S.; Chen, H.-T.; Lin, V.S.-Y. Synthesis and functionalization of a mesoporous silica nanoparticle based on the sol–gel process and applications in controlled release. *Acc. Chem. Res.* **2007**, *40*, 846-853.

119. Lin, Y.; Li, Z.; Chen, Z.; Ren, J.; Qu, X. Mesoporous silica-encapsulated gold nanoparticles as artificial enzymes for self-activated cascade catalysis. *Biomaterials* **2013**, *34*, 2600-2610.

120. Iwamoto, M.; Tanaka, Y.; Sawamura, N.; Namba, S. Remarkable effect of pore size on the catalytic activity of mesoporous silica for the acetalization of cyclohexanone with methanol. *J. Am. Chem. Soc.* **2003**, *125*, 13032-13033.

121. Perton, F.; Tasso, M.; Medina, G.A.M.; Ménard, M.; Blanco-Andujar, C.; Portiansky, E.; van Raap, M.B.F.; Bégin, D.; Meyer, F.; Begin-Colin, S. Fluorescent and magnetic stellate mesoporous silica for bimodal imaging and magnetic hyperthermia. *Applied Materials Today* **2019**, *16*, 301-314.

122. Perton, F.; Harlepp, S.; Follain, G.; Parkhomenko, K.; Goetz, J.G.; Bégin-Colin, S.; Mertz, D. Wrapped stellate silica nanocomposites as biocompatible luminescent nanoplatforms assessed in vivo. *J. Colloid Interface Sci.* **2019**, *542*, 469-482.

123. Liu, Y.C.; Liu, S.T. A Recyclable Thiol-Functionalized Mesoporous Silica for Detection and Removal of Cu (II) Ions. *J. Chin. Chem. Soc.* **2010**, *57*, 946-949.

124. Tao, J.; Xiong, J.; Jiao, C.; Zhang, D.; Lin, H.; Chen, Y. Hybrid mesoporous silica based on hyperbranch-substrate nanonetwork as highly efficient adsorbent for water treatment. *ACS Sustainable Chemistry & Engineering* **2016**, *4*, 60-68.

125. Dabre, R.; Schwämmle, A.; Lämmerhofer, M.; Lindner, W. Statistical optimization of the silylation reaction of a mercaptosilane with silanol groups on the surface of silica gel. *J. Chromatogr. A* **2009**, *1216*, 3473-3479.

126. Mesa, M.; Sierra, L.; López, B.; Ramirez, A.; Guth, J.-L. Preparation of micron-sized spherical particles of mesoporous silica from a triblock copolymer surfactant, usable as a stationary phase for liquid chromatography. *Solid State Sciences* **2003**, *5*, 1303-1308.

127. Pauwels, B.; Van Tendeloo, G.; Thoelen, C.; Van Rhijn, W.; Jacobs, P.A. Structure determination of spherical MCM-41 particles. *Adv. Mater.* **2001**, *13*, 1317-1320.

128. Zhao, D.; Feng, J.; Huo, Q.; Melosh, N.; Fredrickson, G.H.; Chmelka, B.F.; Stucky, G.D. Triblock copolymer syntheses of mesoporous silica with periodic 50 to 300 angstrom pores. *Science* **1998**, *279*, 548-552.

129. Han, Y.; Ying, J.Y. Generalized fluorocarbon-surfactant-mediated synthesis of nanoparticles with various mesoporous structures. *Angew. Chem.* **2005**, *117*, 292-296.

130. Beck, J.S.; Vartuli, J.C.; Roth, W.J.; Leonowicz, M.E.; Kresge, C.; Schmitt, K.; Chu, C.; Olson, D.H.; Sheppard, E.; McCullen, S. A new family of mesoporous molecular sieves prepared with liquid crystal templates. *J. Am. Chem. Soc.* **1992**, *114*, 10834-10843.

131. Fan, J.; Yu, C.; Lei, J.; Zhang, Q.; Li, T.; Tu, B.; Zhou, W.; Zhao, D. Low-temperature strategy to synthesize highly ordered mesoporous silicas with very large pores. *J. Am. Chem. Soc.* **2005**, *127*, 10794-10795.

132. Hoffmann, F.; Cornelius, M.; Morell, J.; Fröba, M. Silica-based mesoporous organic–inorganic hybrid materials. *Angew. Chem. Int. Ed.* **2006**, *45*, 3216-3251.

133. Soler-Illia, G.J.d.A.; Sanchez, C.; Lebeau, B.; Patarin, J. Chemical strategies to design textured materials: from microporous and mesoporous oxides to nanonetworks and hierarchical structures. *Chem. Rev.* **2002**, *102*, 4093-4138.

134. Brinker, C.J.; Lu, Y.; Sellinger, A.; Fan, H. Evaporation-induced self-assembly: nanostructures made easy. *Adv. Mater.* **1999**, *11*, 579-585.

135. Marcilla, A.; Beltran, M.; Gómez-Siurana, A.; Martinez, I.; Berenguer, D. Template removal in MCM-41 type materials by solvent extraction: Influence of the treatment on the textural properties of the material and the effect on its behaviour as catalyst for reducing tobacco smoking toxicity. *Chem. Eng. Res. Des.* **2011**, *89*, 2330-2343.

136. Hitz, S.; Prins, R. Influence of template extraction on structure, activity, and stability of MCM-41 catalysts. *J. Catal.* **1997**, *168*, 194-206.

137. Tian, B.; Liu, X.; Yu, C.; Gao, F.; Luo, Q.; Xie, S.; Tu, B.; Zhao, D. Microwave assisted template removal of siliceous porous materials. *Chem. Commun.* **2002**, 1186-1187.

138. Kobler, J.; Möller, K.; Bein, T. Colloidal suspensions of functionalized mesoporous silica nanoparticles. *Acs Nano* **2008**, *2*, 791-799.

139. Liang, R.; Fang, X.; Qiu, B.; Zou, H. One-step synthesis of golf ball-like thiol-functionalized silica particles. *Soft Matter* **2020**, *16*, 9113-9120.

140. Möller, K.; Kobler, J.; Bein, T. Colloidal suspensions of mercapto-functionalized nanosized mesoporous silica. *J. Mater. Chem.* **2007**, *17*, 624-631.

141. Cauda, V.; Schlossbauer, A.; Kecht, J.; Zürner, A.; Bein, T. Multiple core− shell functionalized colloidal mesoporous silica nanoparticles. *J. Am. Chem. Soc.* **2009**, *131*, 11361-11370.

142. Zhao, D.; Ge, S.; Senses, E.; Akcora, P.; Jestin, J.; Kumar, S.K. Role of filler shape and connectivity on the viscoelastic behavior in polymer nanocomposites. Macromolecules 2015, 48, 5433-5438.

143. Yang, R.; Song, Y.; Zheng, Q. Payne effect of silica-filled styrene-butadiene rubber. Polymer 2017, 116, 304-313.

144. Luo, Y.; Lin, J. Synthesis and characterization of Co (II) salen functionalized MCM-41-type hybrid mesoporous silicas and their applications in catalysis for styrene oxidation with H2O2. Microporous Mesoporous Mater. 2005, 86, 23-30.

145. Palanikumar, L.; Choi, E.S.; Cheon, J.Y.; Joo, S.H.; Ryu, J.H. Noncovalent polymer-gatekeeper in mesoporous silica nanoparticles as a targeted drug delivery platform. Adv. Funct. Mater. 2015, 25, 957-965.

146. Lin, L.C.; Thirumavalavan, M.; Lee, J.F. Facile Synthesis of Thiol-functionalized Mesoporous Silica – Their Role for Heavy Metal Removal Efficiency. CLEAN–Soil, Air, Water 2015, 43, 775-785.

147. Ghalei, B.; Pournaghshband Isfahani, A.; Sadeghi, M.; Vakili, E.; Jalili, A. Polyurethane-mesoporous silica gas separation membranes. Polym. Adv. Technol. 2018, 29, 874-883.

148. Nuntang, S.; Poompradub, S.; Butnark, S.; Yokoi, T.; Tatsumi, T.; Ngamcharussrivichai, C. Novel mesoporous composites based on natural rubber and hexagonal mesoporous silica: synthesis and characterization. Mater. Chem. Phys. 2014, 143, 1199-1208.

149. Perez, L.D.; Lopez, B.L. Thermal characterization of SBR/NBR blends reinforced with a mesoporous silica. J. Appl. Polym. Sci. 2012, 125, E327-E333.

150. Hayichelaeh, C.; Reuvekamp, L.; Dierkes, W.; Blume, A.; Noordermeer, J.; Sahakaro, K. Enhancing the silanization reaction of the silica-silane system by different amines in model and practical silica-filled natural rubber compounds. Polymers 2018, 10, 584.

151. Xu, D.; Sun, L.; Li, H.; Zhang, L.; Guo, G.; Zhao, X.; Gui, L. Hydrolysis and silanization of the hydrosilicon surface of freshly prepared porous silicon by an amine catalytic reaction. New J. Chem. 2003, 27, 300–306.

152. White, L.; Tripp, C. Reaction of (3-aminopropyl) dimethylethoxysilane with amine catalysts on silica surfaces. J. Colloid Interface Sci. 2000, 232, 400–407.

153. Kaas, R.; Kardos, J. The interaction of alkoxy silane coupling agents with silica surfaces. Polym. Eng. Sci. 1971, 11, 11–18.

154. Greenberg, S. The depolymerization of silica in sodium hydroxide solutions. J. Phys. Chem. 1957, 61, 960–965.

155. Pawlenko, S. Organosilicon Chemistry; De Gruyter Inc.: Berlin, Germany; Boston, MA, USA, 1986.

156. Arrighi, V.; McEwen, I.; Qian, H.; Prieto, M.S. The glass transition and interfacial layer in styrene-butadiene rubber containing silica nanofiller. Polymer 2003, 44, 6259–6266.

157. Park, S.-J.; Cho, K.-S. Filler−elastomer interactions: influence of silane coupling agent on crosslink density and thermal stability of silica/rubber composites. J. Colloid Interface Sci. 2003, 267 (1), 86−91.

158. Tadiello, L.; D'Arienzo, M.; Di Credico, B.; Hanel, T.; Matejka, L.; Mauri, M.; Morazzoni, F.; Simonutti, R.; Spirkova, M.; Scotti, R. The filler-rubber interface in styrene butadiene nanocomposites with anisotropic silica particles: Morphology and dynamic properties. Soft Matter 2015, 11, 4022–4033.

Chapter 1 - Original Basic Activation for Enhancing Silica Particle Reactivity: Characterization by Liquid Phase Silanization and Silica-Rubber Nanocomposite Properties

The first chapter, *"Original Basic Activation for Enhancing Silica Particle Reactivity: Characterization by Liquid Phase Silanization and Silica-Rubber Nanocomposite Properties"* investigates the possibility and consequences of the enhancement of the silica particles reactivity toward silanization for tire tread rubber, using two original bases: sodium hydride and DBU.

The silanization of silica as a filler for tire rubber is essential for its good dispersion and interaction with the rubber matrix. It can be achieved by two different processes: by pre-treatment in a chemical reactor, or in-situ during the mixing of silica filler with the rubber during the tire production process. In both cases, a catalyst in needed to push the reaction. When the silane is mixed in-situ, the amine diphenyl-guanidine (DPG), traditionally used as vulcanization accelerant in tire rubber blends set alkaline conditions that are favorable for the silanization.

In the case of silica pre-treatment in a chemical reactor, the conditions allow a more controlled silanization and target mono-layer silane coverage over silica particles. To do so, one needs to favor the silica-silane reaction at the silica surface and prevent the silane oligomerization in the solution. For the latter, silanization is carried in a dry organic solvent, to reduce the odds of silanes reacting with miscible water in solution. To maximize the silica-silane reaction at the particle surface, we pre-loaded the silica particle with the base catalyst to enhance silica reactivity toward the silane. Therefore, in this paper we investigated the impact of original base catalyst, DBU and NaH on the silanization of silica, and compared their effect to in-situ silanization.

After base pre-loading for silica reactivity enhancement, the silanization of the particles by different silanes was carried in dry toluene. The assessment of the impact of the base over silica reactivity was done by using molecular characterization measurement, TGA and ^{1}H and ^{29}Si NMR, as well by measuring the composite mechanical properties.

We concluded that DBU is the most efficient base for silica particle pre-treatment and allow for superior grafting yield and particle coverage than other bases, whereas sodium hydride is more suited for in-situ silanization of the filler, yielding better mechanical properties.

polymers

MDPI

Article

Original Basic Activation for Enhancing Silica Particle Reactivity: Characterization by Liquid Phase Silanization and Silica-Rubber Nanocomposite Properties

Enzo Moretto [1], Chuanyu Yan [1], Reiner Dieden [1], Pascal Steiner [2], Benoît Duez [2], Damien Lenoble [1] and Jean-Sébastien Thomann [1,*]

[1] MRT Department, Luxembourg Institute of Science and Technology, 41 Rue du Brill, L-4422 Belvaux, Luxembourg; enzo.moretto@list.lu (E.M.); chuanyu.yan@list.lu (C.Y.); reiner.dieden@list.lu (R.D.); damien.lenoble@list.lu (D.L.)

[2] Goodyear S.A, Avenue Gordon Smith, L-7750 Colmar-Berg, Luxembourg; pascal_steiner@goodyear.com (P.S.); benoit_duez@goodyear.com (B.D.)

* Correspondence: jean-sebastien.thomann@list.lu

Citation: Moretto, E.; Yan, C.; Dieden, R.; Steiner, P.; Duez, B.; Lenoble, D.; Thomann, J.-S. Original Basic Activation for Enhancing Silica Particle Reactivity: Characterization by Liquid Phase Silanization and Silica-Rubber Nanocomposite Properties. *Polymers* **2022**, *14*, 1676. https://doi.org/10.3390/polym14091676

Academic Editor: Zhenyu Li

Received: 21 March 2022
Accepted: 18 April 2022
Published: 20 April 2022

Abstract: Silica fillers are used in various nanocomposites in combination with silanes as a reinforcing filler. In tire technology, silica is generally functionalized before (pre-treated) or during mixing (in-situ silanization or post-treated). In both cases, a soft base catalyst (e.g., triethylamine or diphenyl guanidine, DPG) is typically used to accelerate and increase the yield of the silane/silica coupling reaction. In this study, we investigated how pre-treatments of silica particles with either strong amine or hydride bases impact the silanization of silica prior to or during SBR mixing for silica-rubber nanocomposite fabrication. Our findings are supported by molecular characterization (solid state ^{29}Si NMR, ^{1}H NMR and TGA), and scanning electron microscopy. In addition, the impact of these silica pre-treatments on a nanocomposite's mechanical properties was evaluated using dynamic mechanical analysis (DMA).

Keywords: silica; silica reactivity; silanization; organic-inorganic hybrids; silica-rubber composite

1. Introduction

Silane-modified silica particles are used in many different fields and applications, such as column chromatography [1], nanomedicine [2], concrete mix [3] or silica filler materials in tires [4]. The need for silanization is driven either by compatibilizing the filler with the matrix or by modifying the surface of the particles to create additional properties [5,6]. Silanization can be carried out in the gas, liquid or even solid phases when silica is mixed with the matrix at a high enough temperature. Chlorosilanes are widely used, but when mild reactivity, safer handling, and storage are required, alkoxysilanes like ethoxy or methoxysilane are preferred [7,8]. Silanization in liquid media is often carried out in aqueous or alcohol/water-based solutions or in an organic solvent [9–11], provided that the silane is soluble. Silanes are usually reacted via a hydrolysis-condensation reaction, and catalyzed either in acidic or basic conditions, hence the central role of water in the process. In dry organic solvent, chlorosilane does not react with hydroxyls unless water is present [10]. Alkoxysilane may react via the nucleophilic displacement of the alkoxy group, thereby generating alcohol [11], but the role of a catalyst appears essential, whether it is water or organic bases like amines. In the tire industry, the silanization of silica is usually catalyzed by mild amines, such as triethylamine or di-phenylguanidine and other works have investigated the impact of various amines on this process [12–15]. Increasing the silica reactivity is of interest for higher silane grafting efficiency. We hypothesize that the use of stronger bases could increase the amount and reactivity of silanol groups, and therefore silica. In this work, we investigated the impact of sodium hydride (NaH) and

1,5-diazabicyclo [5.4.0] undec-5-ene (DBU) as base catalysts to enhance silica reactivity. To our knowledge, these two base chemicals, and especially metal hydrides, have never before been used for silica reactivity enhancement. The impact of NaH and DBU on the morphology and surface of silica particles was examined with scanning electron microscope images and ^{29}Si NMR. Then, to evaluate the effects of the bases on silica reactivity, we first used silica silanization as a simplified quantitative model. Silane grafting was quantified by ^{1}H-NMR and TGA. Base catalyst-loaded silicas were then incorporated into rubber nanocomposites to create a more complex model to account for the effect of the catalysts. The effect of silica reactivity enhancement was evaluated via the mechanical properties of the materials obtained, using dynamic mechanical analysis (DMA).

2. Materials and Methods

Precipitated silica (10 nm primary particle size, 200 m^2/g), 1,5-diazabicyclo [5.4.0] undec-5-ene (DBU), triethylamine (TEA), sodium hydride (NaH), tetrahydrofuran (THF), toluene, cesium fluoride, deuterated water (D_2O), deuterated hydrochloric acid 35 wt. % (DCl), deuterated chloroform ($CDCl_3$), and octamethylcyclotetrasiloxane (OMCTS) were purchased from Merck (Darmstadt, Germany). Hexyltrimethoxysilane (C6), dodecyltrimethoxysilane (C12), and octadecyltrimethoxysilane (C18) were purchased from Gelest (Morrisville, PA, USA).

For the fabrication of a silica-rubber composite, pre-made base-loaded silica, polystyrene-butadiene (SBR) and polybutadiene rubber (BR), treated distillate aromatic extracted (TDAE) lubricating oil, zinc oxide, stearic acid, N-(1,3-dimethylbutyl)-N′-phenyl-p-phenylenediamine (6-PPD), sulfur, 2-mercaptobenzothaizole (MBT), di-phenylguanidine (DPG), and N-cyclohexyl-2-benzothiazolesulfenamide (CBS) were used.

2.1. Silica Pre-Loading of the Base Catalyst

Two organic bases were selected, 1,5-diazabicyclo [5.4.0] undec-5-ene (DBU) and triethylamine (TEA), as well as the inorganic base sodium hydride (NaH) base, to catalyze the silanization reaction of silica particles. We followed a silica pre-loading method, in which the particles were first blended with an organic base in a solvent, prior to the actual silanization.

1 g of silica particles was suspended in 100 mL of THF and was stirred vigorously at room temperature. Then, 6 mmol of DBU, NaH or TEA were added, and the mixture was further stirred for 15 min. In the specific case of sodium hydride being used, gas bubbles were observed when silica and NaH were mixed together. The suspension was then dried under reduced pressure to remove all solvent. The pre-loaded base silica particles were stored under argon in a sealed container.

2.2. Silica Silanization

For the silanization reaction, 1 g of silica particles in a 250 mL round-bottom flask was mixed with 100 mL of toluene. The mix was brought to reflux and 0.78 mmol of either C6, C12 or C18 silane was added. The reaction was carried out at reflux temperature for 24 h under vigorous stirring. Then, the silanized silica was separated by centrifugation at $10{,}000\times g$ for 3 min, the liquid was poured away, and fresh toluene was added. The centrifuge tube was shaken vigorously, and this washing cycle is repeated twice. Subsequently, the moist silanized silica particles were dried under reduced pressure and stored in a glass vial under inert argon atmosphere.

2.3. Preparation of ^{1}H NMR Samples

First, simple silane solutions were prepared for the identification of the silane's signals. 0.01 mmol of each silane was solubilized in 1 mL of deuterated chloroform ($CDCl_3$).

To obtain the spectrum of the silane after the reaction with the cesium fluoride/deuterated hydrochloric acid (CsF/DCl) solution, silane was reacted with the CsF/DCl solution. The subsequent solubilized silane residue signal obtained was compared to the internal standard signal by reacting 30 mg of silane with 1 mL of a 310 mg/mL CsF solution in deuterated water (D_2O) and 260 µL of DCl (35 wt. %) in a 2 mL PP tube. The tube was left to react for 24 h at room temperature. Subsequently, 1 mL of 0.01 mmol/mL octamethylcyclotetrasiloxane in deuterated chloroform (OMCTS in $CDCl_3$) solution was added to the tube. The tube was shaken vigorously by hand and left to settle for the two phases to separate. A 600 µL sample of the chloroform phase was poured into a glass NMR tube suitable for ^{1}H NMR analysis.

For silanized-silica grafting quantification, 10 to 20 mg of silanized silica were added into a 2 mL PP-tube. Then, 1 mL of a 310 mg/mL CsF solution in D_2O and 260 µL of DCl were added. The solution was left to react under stirring for 24 h at room temperature. Subsequently, 1 mL of an OMCTS-$CDCl_3$ solution at 0.01 mmol/mL was added, the tube was shaken vigorously and a 600 µL sample of the chloroform phase was poured into a glass tube suitable for ^{1}H-NMR.

2.4. Silica-Rubber Composite Fabrication

All ingredients were mixed using a HAAKE™ PolyLab™ QC ThermoScientific (ThermoScientific, Waltham, MA, USA) internal mixer and a roll mill at each mixing step. Component quantities and mixing steps were summed up in Table 1 below. Quantities are given in phr, a mass unit meaning per hundred rubber. Thus, 80 phr of silica means that for a total of 100 g of rubber, 80 g of silica are used. All green composite materials were cured in a hydraulic press at 170 °C for 10 min. at 150 kPa.

Table 1. Composition and mixing steps for silica-rubber composite fabrication.

	Components	phr	Mixing Conditions
Step 1	Polystyrene-butadiene	80	80 °C for 10′
	Polybutadiene	20	
	TDAE Oil	25	
	Zinc oxide	0.5	
	Stearic acid	3	
	Silica	65	
Step 2	Step 1 compound	-	80 °C for 7′
	Silica	15	
	Silane (TESPD)	8	
	6PPD	2.5	
Step 3	Step 2 compound	-	60 °C for 1′45″
	Zinc oxide	2	
	Sulfur	1.1	
	MBT	0.3	
	DPG	3.2	
	CBS	2.3	

2.5. Characterization

The mass loss of silanized silica powders was recorded on a Mettler Toledo TGA 2 (Mettler-Toledo, Columbus, OH, USA) in an alumina crucible, at a heating rate of 10 °C/min from 25 °C to 1000 °C, with a 20 min stabilization step at 25 °C and under nitrogen atmosphere.

The mechanical properties of the resulting composite materials were tested by dynamic mechanical analysis (DMA) at 1 Hz and 10 Hz, at a free length of 5 mm and a temperature sweep from -80 °C up to 100 °C.

NMR spectroscopy was performed on a Bruker AV III 600HD instrument (Bruker, Billerica, MA, USA) (600 MHz ^{1}H frequency). ^{1}H NMR spectra were recorded using a 5 mm BBO probe with z-gradients at 298 K using a 30° pulse, a sweep width of 40 ppm, and 8 transients (160 k datapoints each) were acquired. The data were processed using Topspin 3.5pl7, which zero filled once and multiplied with an exponential line-broadening function of 0.50 Hz prior to Fourier-transform.

^{29}Si MAS NMR spectra were recorded on the same spectrometer with a 4 mm H/X probe, using direct polarization (HPDEC pulse program) at 303 K and 8 kHz MAS frequency. The ^{29}Si 90° pulse was 2.5 µs, and a decoupling field of 100 kHz was applied during the acquisition of 900 transients (each with 2048 datapoints), separated by a 120 s relaxation delay and a sweep width of 300 ppm centered on −50 ppm.

3. Results and Discussion

3.1. Impact of Basic Activation on Silica Particles

The SEM images (Figure 1) show non-treated silica, DBU, and NaH-loaded silica at two different magnifications. When base-loaded silicas are compared to the untreated silica, the particles look less spherical. We attribute this morphological change to the chemical interaction of the bases with the particles. Additionally, the SEM images of DBU-loaded silica show the presence of residual DBU molecules in the form of a white cloudy halo surrounding the silica; this is typical of organic matter under an electron beam and is not observed when sodium hydride is used.

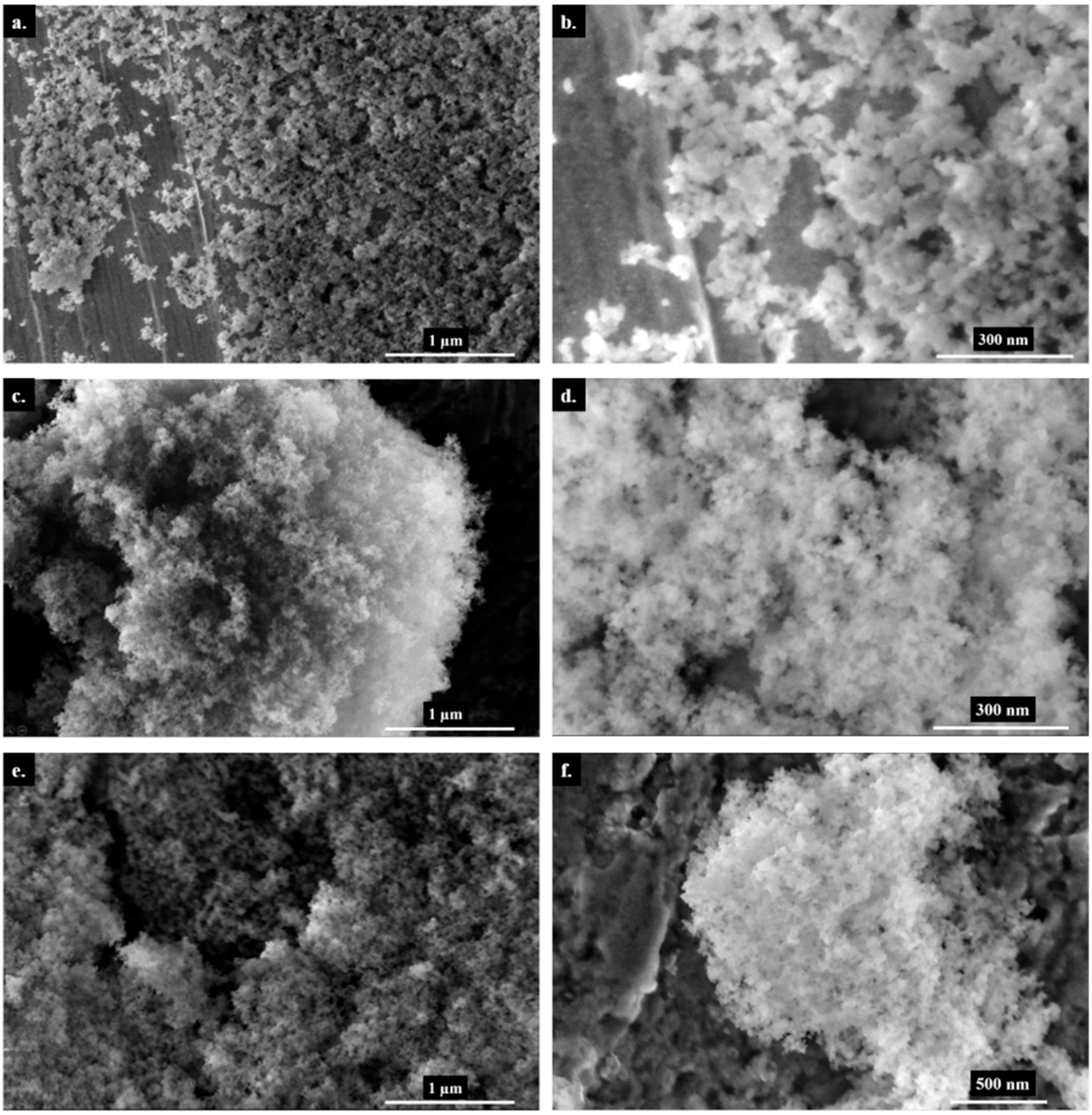

Figure 1. Scanning Electron Microscopy images of silica particles—Non-treated (**a**,**b**), DBU−loaded (**c**,**d**) and NaH−loaded (**e**,**f**).

^{29}Si ssNMR confirms a chemical reaction between silica and sodium hydride NaH. The Q3 signal at −102.5 ppm (see Figure 2) clearly shows an increase in Si-OH content for NaH-loaded silica. However, DBU does not seem to have the same effect on silica. We initially hypothesized that both bases would react with the surface water of the silica and form HO^- hydroxide ions. Indeed, hydroxide solutions are capable of hydrolyzing amorphous silica [16], however, our conditions (stirring at room temperature for 15 min) do not fulfill the thermodynamic requirement for this reaction. Another possible reaction is the acido-basic interaction of DBU or NaH with silica. If the alkaline character of DBU or NaH was responsible for the extra silanol production, the rise of the Q3 signal would be observed in both cases. Despite both bases having a high enough pKa (13.5 for DBU [17,18] and 50 for H_2 [19,20], the conjugated acid of the hydride H^-) that are sufficient to deprotonate Si-OH silanols and form the conjugated base Si-O^-, the increase in the Q3 signal is only observed in the case of NaH. Because of this, the production of silanols is not a result of the alkaline character of sodium hydride, but rather, of its nucleophilicity. On the other hand, DBU is a poor nucleophile since its basic nitrogen atom is obstructed by the structure of the molecule. Therefore, we suggest that a possible explanation for the action of sodium hydride on silica is that the nucleophilic H^- of sodium hydride reacts with the Si-O-Si siloxane bridges of the silica in a nucleophilic attack and generates Si-H and Si-O^-Na^+. Finally, Si-H reacts with HO^- or H_2O to form Si-OH and H_2 [21], which would explain the observed bubbling and the increase of the Q3 signal in the NMR spectra. The expected presence of Na^+ or DBU^+ counter ions at the silica surface would change the particle's cohesion behavior, since less Si-OH are available for hydrogen bonding, thus reinforcing our observations on the morphology change of the silica particles discussed earlier and shown in Figure 1.

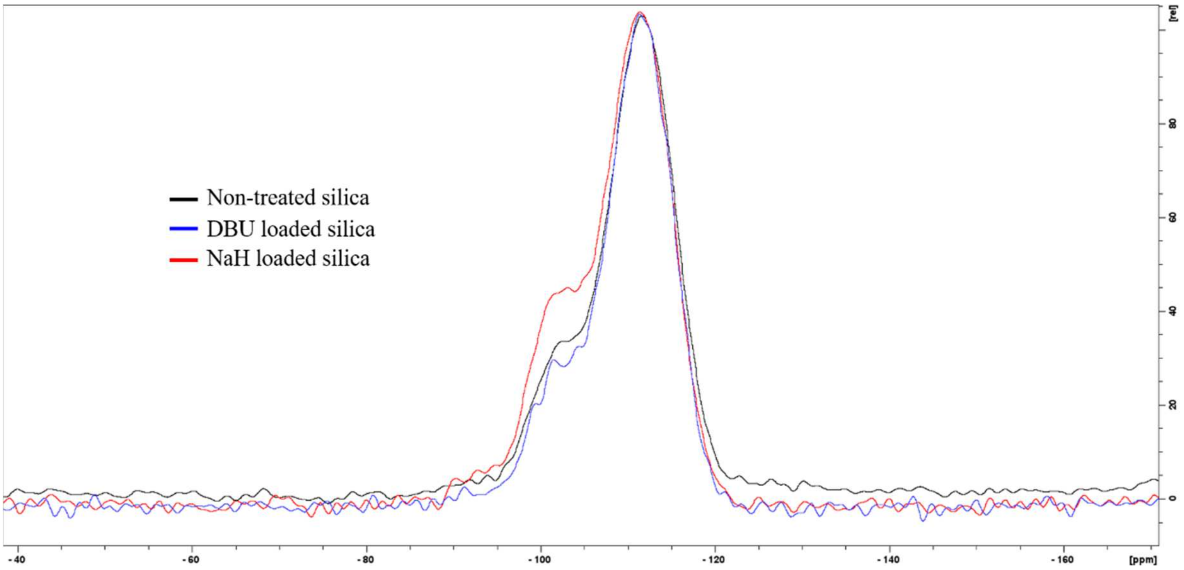

Figure 2. ^{29}Si ssNMR of untreated silica (black), DBU−loaded silica (blue), and NaH−loaded silica (red).

3.2. Silica Reactivity Enhancement Evaluation

We decided to evaluate the effect of bases on silica reactivity using two models. The first one quantifies the yield of a simple silica silanization in a liquid organic solvent. In the second model, we used the base-loaded silica for the fabrication of a silica-rubber composite and measured the mechanical properties of the corresponding materials.

Silanization generally designates the grafting of organosilanes on a substrate to modify its surface properties. The yield of this reaction is directly influenced by the number of reactive sites on silica (i.e., silanols) and their reactivity. Silica particles were reacted with simple alkyltrimethoxysilanes of different lengths in the organic solvent toluene. The main reason for choosing these conditions was to minimize the self-condensation of the silanes that could then react with silica. Indeed, the self-condensation of silanes generates silane oligomers that are still capable of reacting with silica particles. This phenomenon causes the grafting of more silane onto silica, irrespective of the silica reactivity, and artificially boosts the silanization yield. To quantify the silanization yield, we chose two characterization methods, i.e., thermogravimetric analysis (TGA) and ^{1}H NMR.

3.3. Thermogravimetric Analysis

Performing thermogravimetric analysis on silanized silica at sufficiently high enough temperatures allows us to measure the mass loss associated with silane pyrolysis. However, the calculation of the silanization yield is not straightforward, as other phenomena can occur simultaneously during heating, like in our case, the desorption of volatile compounds and dehydroxylation of the silica itself. Although these different events happen at determined temperature ranges, they can overlap, as is well documented with the case of silica dehydroxylation [22]. Dehydroxylation occurs at temperatures ranging from 110 °C to 1000 °C and the amount of water generated depends on the type of silica. To account for the mass loss due to the dehydroxylation of the silica during the silane pyrolysis, we recorded the thermograms of the untreated silicas and subtracted them from those of the silanized silicas. The silane mass-loss is calculated, for all samples, by subtracting the residual mass at 600 °C from that at 400 °C. Grafting yields are then calculated by dividing the mass loss between 400 °C and 600 °C by the molar mass of the organic residual part of the silane molecule. This calculation method was discussed by Kunc et al. [23], and can be considered correct if we hypothesize that all silanized-silica samples undergo the same dehydroxylation under heating. However, as in the case of silanized silica, that this is not the case, there is also an argument against this method, as the silanization reaction consumes hydroxyl groups on the surface of the silica, and therefore lowers the final number of hydroxyl groups to be dehydroxylated. Also, the remaining unreacted alkoxy groups of silanes still present on the final material account for part of the recorded mass loss. This can lead to an over-estimation of the mass loss attributed to the grafted silane. Moreover, this method cannot be used in the case of multiple and different silanes being grafted onto silica particles as all silanes would decompose over the same temperature range, unless an additional characterization method is potentially used in parallel with TGA, such as infra-red or mass spectrometry. TGA thermograms for C18-silanized silica with different base catalysts are shown below in Figure 3.

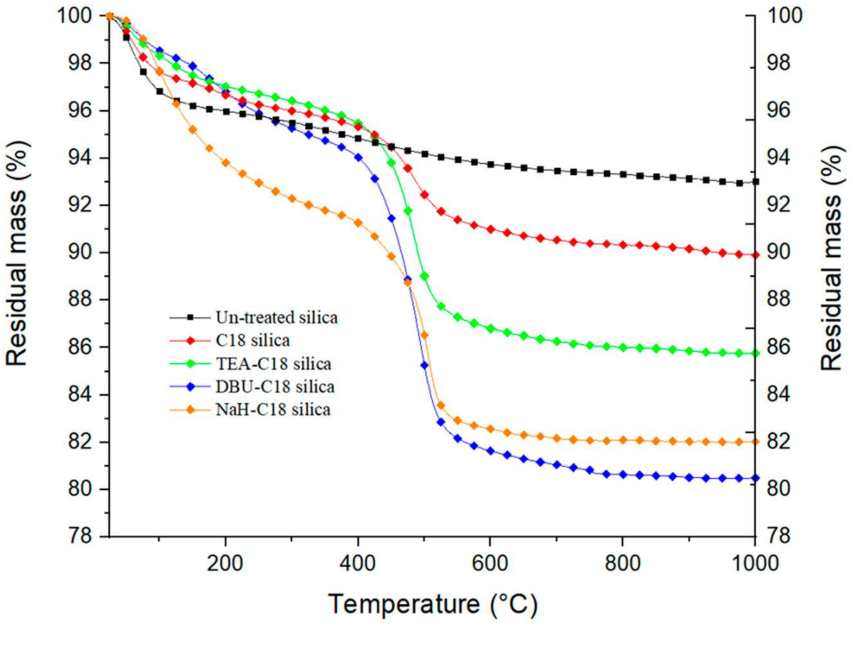

Figure 3. Thermogravimetric curves of untreated and C18−silanized silica.

From the analysis of the thermograms, we observe that the use of a base catalyst considerably increases the amount of grafted silane. The difference between NaH and DBU is less obvious due to the degradation of the remaining storage oil of NaH and DBU residue. Figures S1 and S2 in the Supplementary Information show TGA thermograms for C12 silanized silica activated with NaH and DBU, respectively. Plotting dTGA vs. temperature helps to better differentiate the degradation phenomenon occurring. In the case of NaH (Figure S1), from 25 to about 100 °C, the mass loss is attributed to moisture and the solvent remaining on the silica. The two peaks centered at 300 °C and 400 °C, respectively, are present for both NaH-activated silica and silanized silica. We attribute these two peaks to the remaining silicon oil used for the storage and conservation of NaH. Finally, the peak centered at 500 °C and only present for silanized silica is attributed to the degradation of the grafted silane. For DBU in Figure S2, the same peak from 25 to 100 °C is attributed to moisture and residual solvent. The peak at 150–240 °C is attributed to the remaining DBU molecules. It may be noted that with both bases, the base residue is lower for silanized silica. The counter ions DBU^+ and Na^+ are expected to be released after the SiO^- reaction with the silane. In addition, silanized silica has seen more washing steps, helping to remove oil residues for NaH. Finally, for Figure S2, the major mass loss at 300 °C, only present in the case of silanized silica, is attributed to the degradation of the silane.

3.4. ^1H *Liquid State NMR*

Pure silanes were reacted with the $CsF/D_2O/DCl$ solution for the identification of peaks, as shown in Figure 4. Alkylsilane (C6, C12 and C18) peaks are identified as follows: 0.64 ppm Si-CH_2, 0.88 ppm CH_3, 1.2 to 1.45 ppm aliphatic CH_2, 1.57 ppm residual water, and 3.56 ppm are O-CH_3 groups. Octamethylcyclotetrasiloxane was chosen as the internal standard because of its good solubility in chloroform, and the fact that it gives rise to only one signal (0.09 ppm CH_3 of OMCTS) in a range that does not overlap with the signal from the samples.

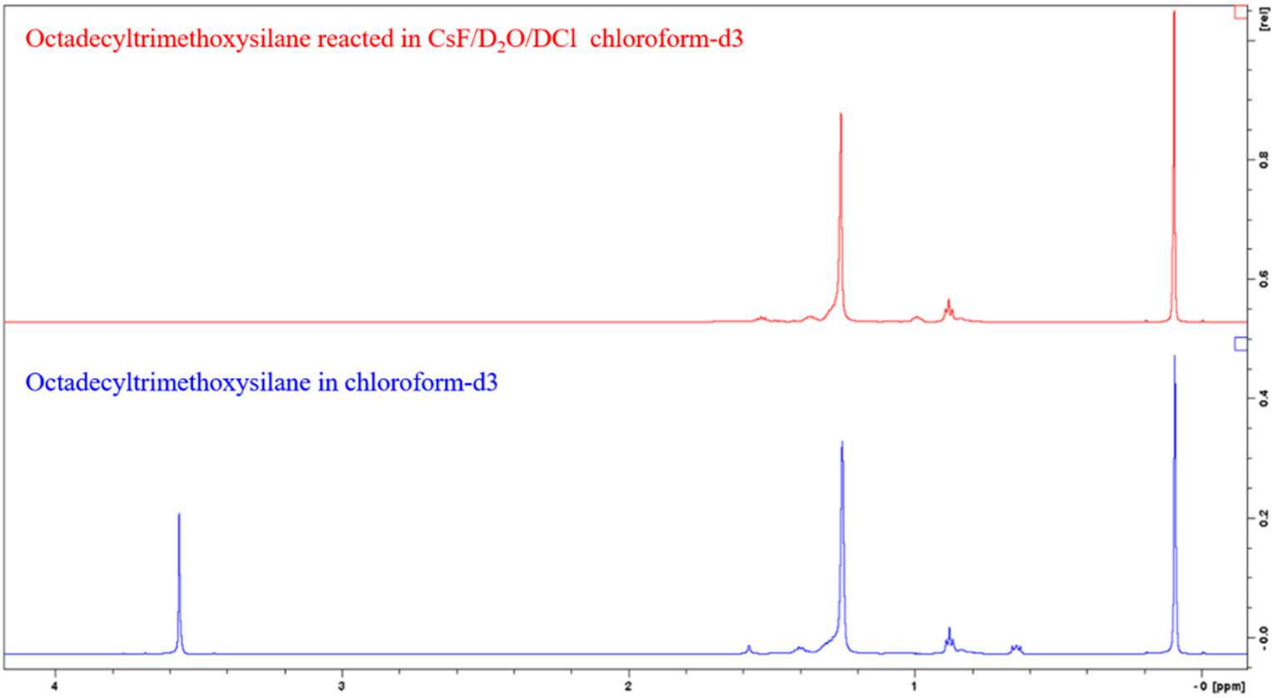

Figure 4. ^1H spectra of C18 silane in chloroform (**bottom**), and reacted in $CsF/D_2O/DCl$ and extracted with chloroform (**top**).

We first observe that the peak at 3.56 ppm disappears after the hydrolysis of the methoxy groups of methoxysilanes, and we do not observe a peak at 3.49 ppm that could be attributed to methanol in solution. We suggest that the methanol remained in the aqueous phase during the extraction with chloroform because of its polarity. The peak at 0.64 ppm is also absent. We could not find an explanation for this, as we do not expect to break a C-C bond in these conditions. Unlike Yang et al. [24], we do not observe any signal being the sign of alcohol in solution that would be the results of the opening of the Si-C bond, and oxidation of the carbon into alcohol. Practically, when pure silanes or silanized silica were reacted with CsF/D_2O/DCl after 24 h, a thin white hydrophobic film appears on the tube walls. For a control sample consisting of unmodified silica mixed with the CsF/D_2O/DCl solution, no such film was not observed. Upon contact with the deuterated chloroform extraction solution, this film solubilizes and is absent from the tube walls. We identify this as a sign of the reaction of the silane with cesium fluoride and hydrochloric acid and their removal from the silica. We also observe that prior to the reaction, modified silica wettability toward the aqueous solution was very poor, as silica floated onto the liquid and did not get wet when vigorously shaking the tube, as is expected from hydrophobized silica. After the 24-h. reaction, silica particles displayed good wettability toward the aqueous solution and sank to the bottom of the tube, consolidating the idea of the silane removal from the silica.

For the integration of the signals, the peak at 0.88 ppm was chosen to quantify the amount of silane in solution. Typical ^{1}H NMR spectra of silanized silica with C6, C12, and C18 are shown in Figure 5. Peaks of interest are integrated, and numerical values are obtained in Equation (1) below.

$$nsilane = \frac{ACH3}{AOMCTS} \times \frac{NOMCTS}{NCH3} \times nOMCTS \tag{1}$$

where

$nsilane$ is the amount of silane in solution (mmol),
ACH_3 is the area of the CH_3 peak at 0.88 ppm,
$AOMCTS$ is the area of the OMCTS peak at 0.09 ppm,
$NOMCTS$ is the number of hydrogen nuclei generating the signal,
NCH_3 is the number of hydrogen nuclei generating the signal,
$nOMCTS$ is the amount of OMCTS internal standard in the $CDCl_3$ solution (mmol).

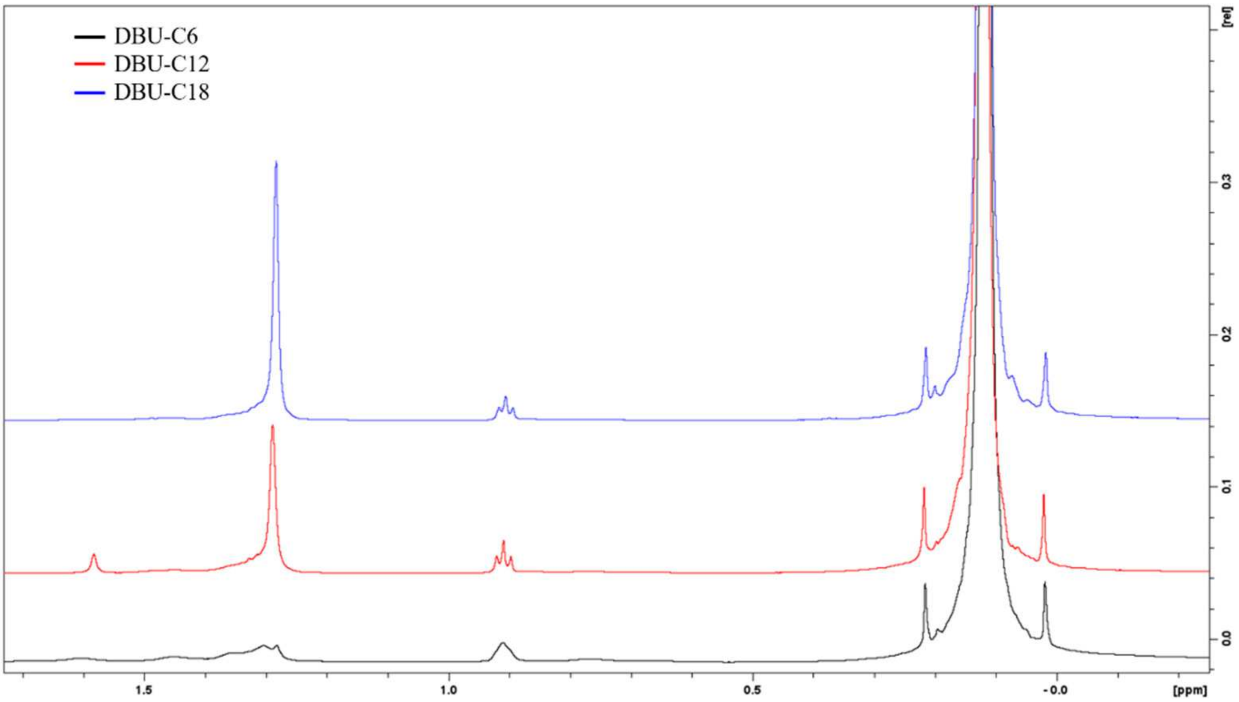

Figure 5. ^{1}H NMR spectra of C6 (**bottom**), C12 (**middle**), and C18 (**top**) silanized silica.

Quantitative results from TGA and ^{1}H NMR are displayed in Table 2 and Figure 6. It must be noted that TGA values are always higher than the corresponding ^{1}H NMR values. The reasons cited earlier, i.e., residual base catalyst, water from silica dehydroxylation, and unreacted alkoxy groups may account for a fraction of the measured weight loss but do not actually represent silane grafting. As for the silane length, the longer it is, the lower the grafting yield. This trend is to be expected due to the bulkiness of the long silane, which reduces the reaction kinetic via steric hindrance.

Table 2. Silica silanization grafting yield calculated from TGA and ^{1}H NMR (in mmol/g).

	C6	C12	C18	TEA-C6	TEA-C12	TEA-C18	DBU-C6	DBU-C12	DBU-C18	NaH-C6	NaH-C12	NaH-C18
TGA	0.418	0.165	0.128	0.383	0.381	0.3	0.582	0.508	0.447	0.271	0.314	0.301
^{1}H NMR	0.274	0.176	0.186	0.185	0.198	0.173	0.299	0.289	0.206	0.188	0.149	0.165

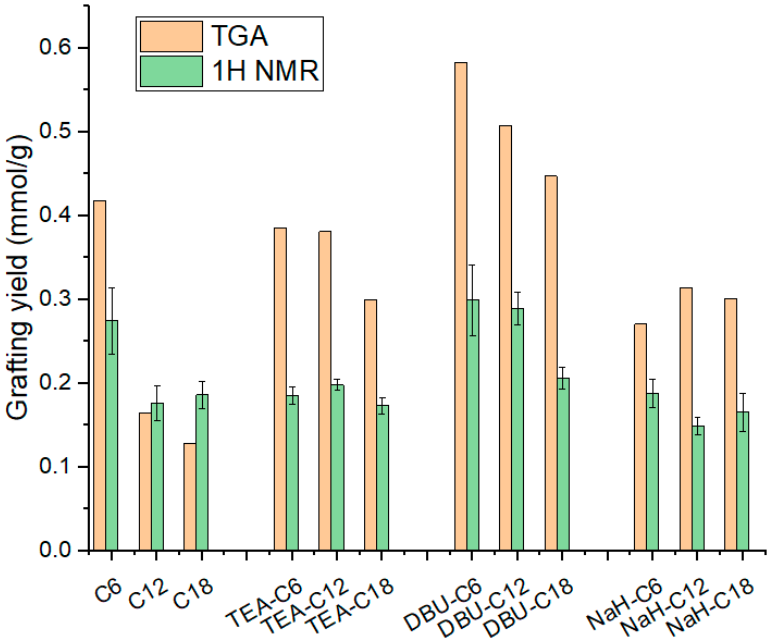

Figure 6. Silica silanization grafting yield from TGA and ^{1}H NMR.

Through the quantification of silanization on base-loaded silica we already have elements to comment on the respective effect of DBU and NaH. DBU maximizes grafting, followed by NaH, and finally TEA, as follows: no base < TEA < NaH < DBU.

3.5. Evaluation of Silica Reactivity Enhancement in Rubber-Silica Composites

The effect of base-loading for the in-situ silanization of silica was measured using dynamic mechanical analysis to test the nanocomposite's mechanical properties, which reflect the way filler particles interact with the matrix. Indeed, the motion of polymer chains increases as the temperature increases. The glass transition temperature T_g, defined in DMA by the position of the tan(δ) peak, is the temperature range where the polymer transitions from a glassy to visco-elastic state. The more polymer chains participating in the transition, the higher the T_g peak. It has been demonstrated that a strong polymer-filler interaction can prevent a fraction of the chains from moving [25,26], thus lowering the T_g peak in DMA. In silica-filled rubber composites, filler-polymer interactions originate from rubber trapped between filler aggregates and rubber bonded to silica via the interaction of the silane with the fillers and the polymer, which increases the storage modulus of the composite [26–29].

Of the three samples tested, NaH-loaded silica demonstrated the highest conservation and loss module, followed by the untreated silica, and finally DBU-loaded silica. When looking at tan(δ), the base-loading of silica clearly affects the visco-elastic behavior of the composite material. In our case, the base activation of silica increases the filler-polymer interactions, as T$_g$ peaks in Figure 7 are lower for DBU and even lower for NaH-loaded silica. Interestingly, DBU is better for silane grafting in the liquid phase, but NaH provides better reinforcement properties to the composite. One hypothesis is that the DBU$^+$ counter ion, because of its size, has more shielding power in a polymer blend than Na$^+$ and thus prevents, to some extent, the reaction of silanes with the surface of silica in rubber. In a liquid phase silanization, in which the molecular mobility is much greater, this effect may be minimized. Another hypothesis is that it is easy for NaH-loaded silica, thanks to its extra silanols, to generate aggregates trapping the rubber matrix, thus resulting in this additional stiffening effect.

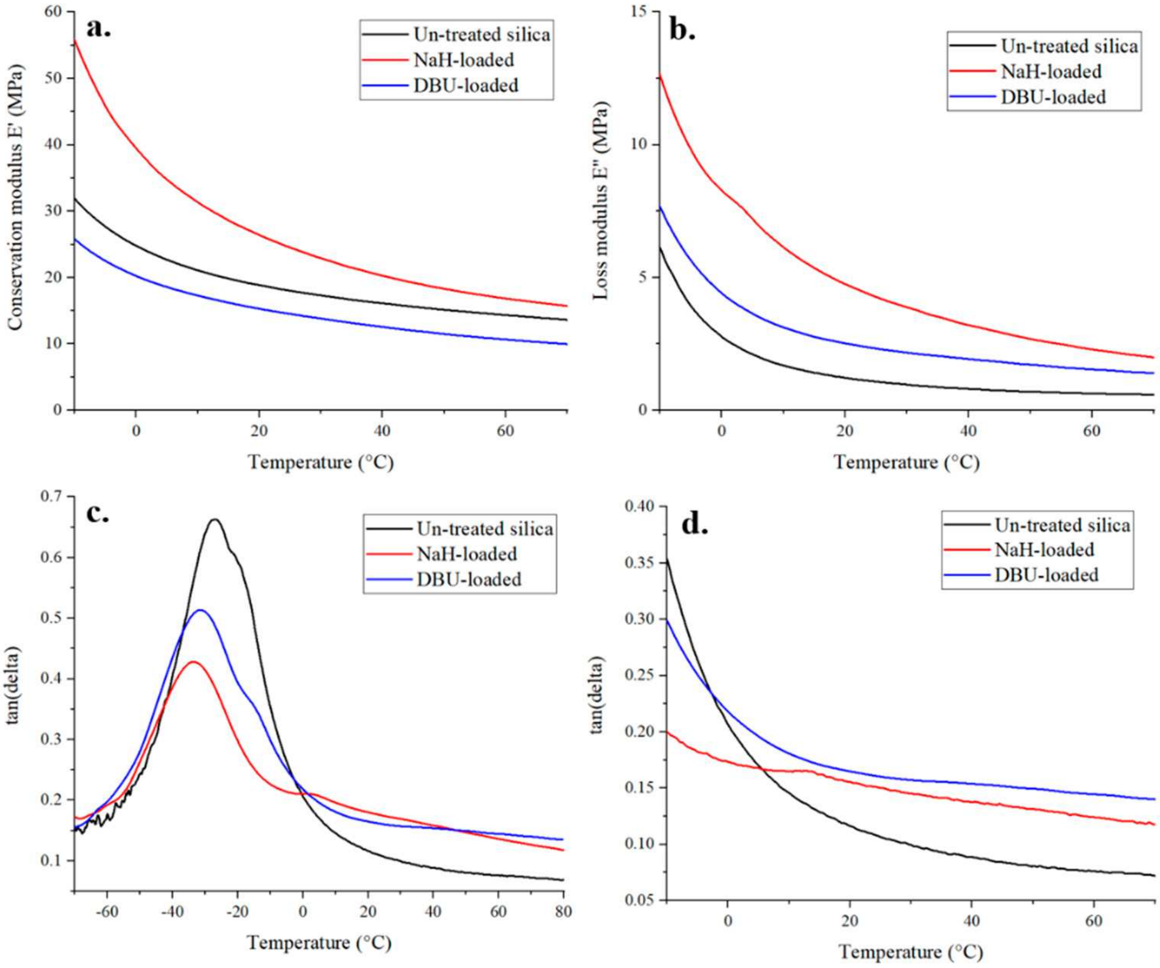

Figure 7. DMA curves of base−loaded silica−rubber composites—E′ (**a**), E” (**b**) and tan(δ) (**c**,**d**).

4. Conclusions

The present study investigated the effect of two unusual base catalysts, DBU and NaH, for silica silanization in the liquid phase, as well as in situ during the curing of SBR-silica nanocomposite. DBU demonstrates a higher grafting yield than NaH and TEA, and the size of silane influences the amount grafted onto the silica particles. This was confirmed by the ^{1}H-NMR and TGA silanization yield quantification, despite the discrepancy still present between the two techniques. Base-loaded silica were included in the fabrication of nanocomposites, and their subsequent mechanical properties were measured by DMA to study the impact of base loading. Contrary to the trend observed in liquid phase silanization, NaH-loaded silica yielded better reinforcing properties than DBU. We hypothesize that the DBU counter ion can shield silane from silica in the polymer melt, and that extra silanols from NaH-loaded silica can generate more silica aggregates in the composite and trap more rubber, bringing a higher degree of reinforcement to the composite.

Supplementary Materials: The following supporting information can be downloaded at: https://www.mdpi.com/article/10.3390/polym14091676/s1, Figure S1: Thermograms of NaH activated and C12 silanized silica, Figure S2: Thermograms of DBU activated and C12 silanized silica, Figure S3: Photograph of the white residual film after the reaction of C12 silane with the CsF/DCl/D_2O solution.

Author Contributions: Conceptualization, E.M., C.Y. and J.-S.T.; methodology, E.M., C.Y., R.D., P.S. and J.-S.T.; validation, B.D., D.L. and J.-S.T.; formal analysis, E.M., C.Y., R.D. and J.-S.T.; investigation, E.M., C.Y. and R.D.; resources, B.D., D.L. and J.-S.T.; writing—original draft preparation, E.M.; writing—review and editing, E.M., C.Y., R.D., P.S., B.D., D.L. and J.-S.T.; supervision, B.D., D.L. and J.-S.T.; project administration, D.L. and J.-S.T.; funding acquisition, B.D. and D.L. All authors have read and agreed to the published version of the manuscript.

Funding: Supported by the Luxembourg National Research Fund (FNR) through the IPBG16/11514551/TireMat-Tech project.

Institutional Review Board Statement: Not applicable.

Informed Consent Statement: Not applicable.

Data Availability Statement: Data is contained within the article or Supplementary Materials.

Acknowledgments: The authors would like to thank Goodyear S.A. for permission to publish the paper. In addition, the authors thank Régis Vaudemont, Benoit Marcolini, and Vincent Berthe for their support on mechanical characterization. Finally, we would like to thank Lindsay Auguin for her expertise on language and sentence revision, which helped a lot in improving the manuscript.

Conflicts of Interest: The authors declare no conflict of interest.

References

1. Forzano, A.V.; Cain, C.N.; Rutan, S.C.; Collinson, M.M. In situ silanization for continuous stationary phase gradients on particle packed LC columns. *Anal. Methods* **2019**, *11*, 3648–3656. [CrossRef]
2. Perton, F.; Tasso, M.; Medina, G.A.M.; Ménard, M.; Blanco-Andujar, C.; Portiansky, E.; van Raap, M.B.F.; Bégin, D.; Meyer, F.; Begin-Colin, S. Fluorescent and magnetic stellate mesoporous silica for bimodal imaging and magnetic hyperthermia. *Appl. Mater. Today* **2019**, *16*, 301–314. [CrossRef]
3. Gao, J.; Geng, Y.; Li, S.; Chen, X.; Shi, D.; Zhou, P.; Zhou, Z.; Wu, Z. Effect of silane emulsion on waterproofing and Anti-icing performance of foamed concrete. *Constr. Build. Mater.* **2021**, *301*, 124082. [CrossRef]
4. Lee, S.Y.; Kim, J.S.; Lim, S.H.; Jang, S.H.; Kim, D.H.; Park, N.-H.; Jung, J.W.; Choi, J. The investigation of the silica-reinforced rubber polymers with the methoxy type silane coupling agents. *Polymers* **2020**, *12*, 3058. [CrossRef] [PubMed]
5. Goerl, U.; Hunsche, A.; Mueller, A.; Koban, H. Investigations into the silica/silane reaction system. *Rubber Chem. Technol.* **1997**, *70*, 608–623. [CrossRef]
6. Fukuda, T.; Fujii, S.; Nakamura, Y.; Sasaki, M. Mechanical properties of silica particle-filled styrene-butadiene rubber composites containing polysulfide-type silane coupling agents: Influence of loading method of silane. *J. Appl. Polym. Sci.* **2013**, *130*, 322–329. [CrossRef]
7. Castellano, M.; Conzatti, L.; Turturro, A.; Costa, G.; Busca, G. Influence of the silane modifiers on the surface thermodynamic characteristics and dispersion of the silica into elastomer compounds. *J. Phys. Chem. B* **2007**, *111*, 4495–4502. [CrossRef]
8. Hui, R.; Yixin, Q.; Suhe, Z. Reinforcement of styrene-butadiene rubber with silica modified by silane coupling agents: Experimental and theoretical chemistry study. *Chin. J. Chem. Eng.* **2006**, *14*, 93–98.
9. Wang, M.; He, D.; Xie, H.; Fu, L.; Yu, Y.; Zhang, Q. Characterization of bis-[triethoxysilylpropyl] tetrasulfide layers on aluminum based on water-based silanization solution. *Thin Solid Films* **2012**, *520*, 5610–5615. [CrossRef]
10. McGovern, M.E.; Kallury, K.M.R.; Michael, T. Role of Solvent ont the Silanization of Glass with Octadecyltrichlorosilane. *Langmuir* **1994**, *10*, 3607–3614. [CrossRef]
11. Kallury, K.M.; Macdonald, P.M.; Thompson, M. Effect of surface water and base catalysis on the silanization of silica by (aminopropyl) alkoxysilanes studied by X-ray photoelectron spectroscopy and 13C cross-polarization/magic angle spinning nuclear magnetic resonance. *Langmuir* **1994**, *10*, 492–499. [CrossRef]
12. Hayichelaeh, C.; Reuvekamp, L.; Dierkes, W.; Blume, A.; Noordermeer, J.; Sahakaro, K. Enhancing the silanization reaction of the silica-silane system by different amines in model and practical silica-filled natural rubber compounds. *Polymers* **2018**, *10*, 584. [CrossRef] [PubMed]

13. Xu, D.; Sun, L.; Li, H.; Zhang, L.; Guo, G.; Zhao, X.; Gui, L. Hydrolysis and silanization of the hydrosilicon surface of freshly prepared porous silicon by an amine catalytic reaction. *New J. Chem.* **2003**, *27*, 300–306. [CrossRef]
14. White, L.; Tripp, C. Reaction of (3-aminopropyl) dimethylethoxysilane with amine catalysts on silica surfaces. *J. Colloid Interface Sci.* **2000**, *232*, 400–407. [CrossRef]
15. Kaas, R.; Kardos, J. The interaction of alkoxy silane coupling agents with silica surfaces. *Polym. Eng. Sci.* **1971**, *11*, 11–18. [CrossRef]
16. Greenberg, S. The depolymerization of silica in sodium hydroxide solutions. *J. Phys. Chem.* **1957**, *61*, 960–965. [CrossRef]
17. Kaupmees, K.; Trummal, A.; Leito, I. Basicities of strong bases in water: A computational study. *Croat. Chem. Acta* **2014**, *87*, 385–395. [CrossRef]
18. Kütt, A.; Selberg, S.; Kaljurand, I.; Tshepelevitsh, S.; Heering, A.; Darnell, A.; Kaupmees, K.; Piirsalu, M.; Leito, I. pKa values in organic chemistry–Making maximum use of the available data. *Tetrahedron Lett.* **2018**, *59*, 3738–3748. [CrossRef]
19. Morris, R.H. Brønsted–Lowry acid strength of metal hydride and dihydrogen complexes. *Chem. Rev.* **2016**, *116*, 8588–8654. [CrossRef]
20. Ortuño, M.A.; Lledós, A. How acid can become a dihydrogen complex in water? A DFT study. *J. Organomet. Chem.* **2021**, *949*, 121957. [CrossRef]
21. Pawlenko, S. *Organosilicon Chemistry*; De Gruyter Inc.: Berlin, Germany; Boston, MA, USA, 1986.
22. Zhuravlev, L. The surface chemistry of amorphous silica. Zhuravlev model. *Colloids Surf. Physicochem. Eng. Asp.* **2000**, *173*, 1–38. [CrossRef]
23. Kunc, F.; Balhara, V.; Sun, Y.; Daroszewska, M.; Jakubek, Z.J.; Hill, M.; Brinkmann, A.; Johnston, L.J. Quantification of surface functional groups on silica nanoparticles: Comparison of thermogravimetric analysis and quantitative NMR. *Analyst* **2019**, *144*, 5589–5599. [CrossRef] [PubMed]
24. Yang, A.; Li, T. Oxidative Cleavage of Carbon−Silicon Bond as a New Method to Characterize Bonded Stationary Phases on Silica Gel. *Anal. Chem.* **1998**, *70*, 2827–2830. [CrossRef]
25. Berriot, J.; Montes, H.; Lequeux, F.; Long, D.; Sotta, P. Evidence for the shift of the glass transition near the particles in silica-filled elastomers. *Macromolecules* **2002**, *35*, 9756–9762. [CrossRef]
26. Kapgate, B.P.; Das, C.; Basu, D.; Das, A.; Heinrich, G. Rubber composites based on silane-treated stöber silica and nitrile rubber: Interaction of treated silica with rubber matrix. *J. Elastomers Plast.* **2015**, *47*, 248–261. [CrossRef]
27. Yasin, K.A.; Ansarifar, A.; Hameed, S.; Wang, L. A new method for crosslinking and reinforcing acrylonitrile–butadiene rubber using a silanized silica nanofiller. *Polym. Adv. Technol.* **2011**, *22*, 215–224. [CrossRef]
28. Fröhlich, J.; Niedermeier, W.; Luginsland, H.-D. The effect of filler–filler and filler–elastomer interaction on rubber reinforcement. *Compos. Part A Appl. Sci. Manuf.* **2005**, *36*, 449–460. [CrossRef]
29. Arrighi, V.; McEwen, I.; Qian, H.; Prieto, M.S. The glass transition and interfacial layer in styrene-butadiene rubber containing silica nanofiller. *Polymer* **2003**, *44*, 6259–6266. [CrossRef]

Original basic activation for enhancing silica particles reactivity: characterization by liquid phase silanization and silica-rubber nanocomposite properties

Enzo Moretto[1], Chuanyu Yan[1], Reiner Dieden[1], Pascal Steiner[2], Benoît Duez[2], Damien Lenoble[1], Jean-Sébastien Thomann[1, *]

[1] MRT Department, Luxembourg Institute of Science and Technology, 41 Rue du Brill, Belvaux, L-4422 Luxembourg, Luxembourg; enzo.moretto@list.lu (E.M.), chuanyu.yan@list.lu (C.Y.), reiner.dieden@list.lu (R.D.), damien.lenoble@list.lu (D.L.)
[2] Goodyear S.A, Avenue Gordon Smith, Colmar-Berg, L-7750 Luxembourg, Luxembourg; benoit_duez@goodyear.com (B.D.); pascal_steiner@goodyear.com (P.S.)
* Correspondence: jean-sebastien.thomann@list.lu (J.-S.T.)

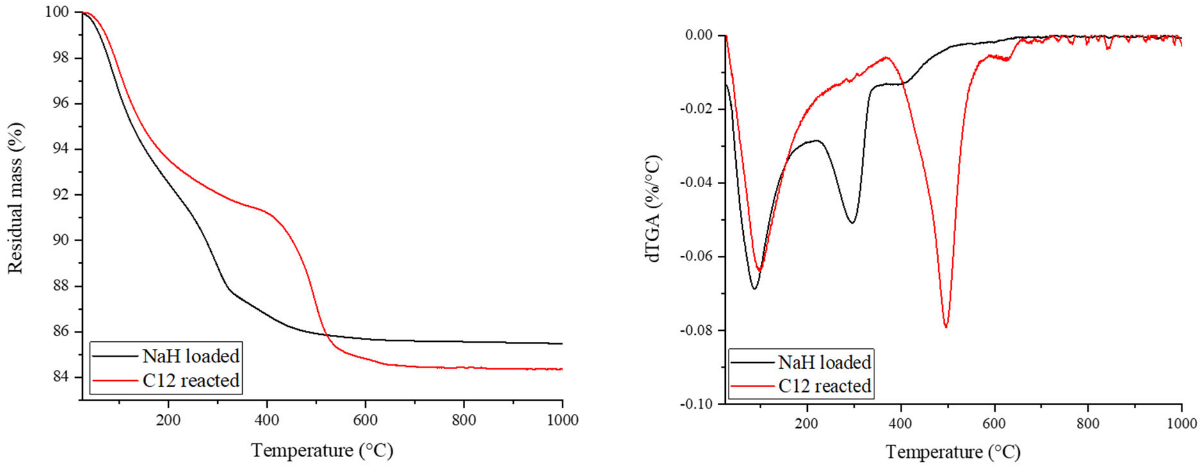

Figure S1 – Thermogram (left) and dTGA (right) curves of NaH activated silica (black) and NaH-C12 reacted silica (red)

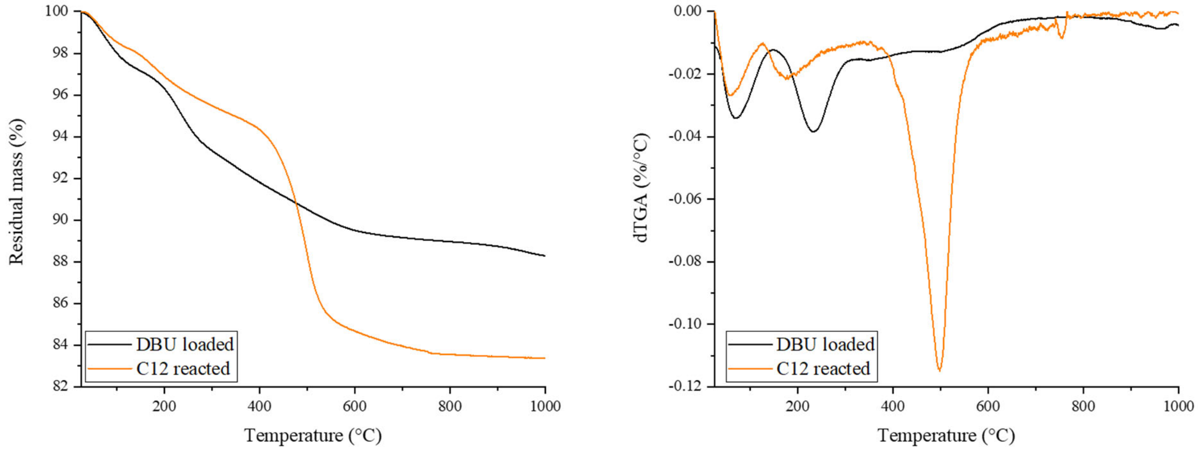

Figure S2 – Thermogram (left) and dTGA (right) curves of DBU-activated silica (black) and DBU-C12 reacted silica (orange)

Figure S3 – Photograph of the white residual film after reaction of C12 silane with $CsF/DCl/D_2O$ solution

Chapter 2 - Dual-Silane Pre-modified Silica Nanoparticles: Synthesis and Interplay between Chemical, Mechanical, and Curing Properties of Silica−Rubber Nanocomposites: Application to Tire Tread Compounds

The second chapter, *“Dual-Silane Pre-modified Silica Nanoparticles: Synthesis and Interplay between Chemical, Mechanical, and Curing Properties of Silica−Rubber Nanocomposites: Application to Tire Tread Compounds”* studies the possibility of the synthesis of a pre-treated silica filler with two different organosilanes grafted on the surface, and the effect of silane size over the composite micro and macro properties of the composite material.

The current tire technology uses a single silane system, usually TESPT, that enables to covalently link silica and rubber and hydrophobize the filler for better dispersion. In this work, both roles where investigated – dispersion and coupling – by separating them on the silica surface.

Dual-silane pre-modified silica particles were synthesized via a two-step sequential silanization on silica in an organic solvent. For the coupling function, a mercaptosilane is grafted first, then, for the dispersion of the silica, an alkylsilane is grafted afterward. The length of each silane was varied in various combination to investigate their effect over mechanical properties and the steric effect of the alkylsilane over the reactivity of the mercaptosilane with regard to the rubber vulcanization reaction.

The impact of the different fillers on the composite material was characterized by DMA to assess the viscoelastic properties of the material and its wet grip and rolling resistance performances. Atomic Force Microscopy (AFM) allowed to assess the silica dispersion and interfacial properties into the rubber matrix.

It was shown that the surface silane modification greatly impacts how the filler interacts with the surrounding polymer matrix and subsequently the wet traction and rolling resistance properties of the compound. Indeed, the use of grafting of long alkylsilane in combination with short mercaptosilane prevents the fillers to properly interact together. Therefore, a clear decrease in reinforcement wet traction is observed due to the lack of energy dissipation though filler-filler interaction. On the other end, short mercapto and alkyl combination show the best performances and a better wet grip indicator than the reference compound, while keeping a lower resistance. This silane combination therefore increases filler-filler interaction and energy dissipation in the range of interest without increasing unnecessary energy dissipation via rolling resistance. This work adds knowledge on the interaction at play between filler and polymer and how it can be used to improve the properties of a tire tread compound.

ACS OMEGA

http://pubs.acs.org/journal/acsodf

Article

Dual-Silane Premodified Silica Nanoparticles—Synthesis and Interplay between Chemical, Mechanical, and Curing Properties of Silica–Rubber Nanocomposites: Application to Tire Tread Compounds

Enzo Moretto, João P. C. Fernandes, Mariapaola Staropoli, Vincent Rogé, Pascal Steiner, Benoît Duez, Damien Lenoble, and Jean-Sébastien Thomann*

Cite This: *ACS Omega* 2022, 7, 17692−17702

Read Online

ABSTRACT: In silica−rubber based nanocomposites, a single organo-silicon is often used to compatibilize and covalently link silica to rubber. In this work, we have investigated the impact, at micro- and macroscales, of the decoupling of the hydrophobization and the coupling activity of silane by pretreating silica with two different silane chemistries. The first one, a mercaptosilane, is the coupling agent that promotes a covalent link between silica and rubber during the sulfur-mediated vulcanization reaction. The second one, an alkylsilane, aims to improve the silica dispersion. For both kind of silanes, we have varied the chain length and studied at macroscale the dynamic mechanical properties through the key indicators that are E'' as loss modulus, E' as storage modulus, and their respective ratio tan δ. The shorter silanes combination yielded an improvement in terms of wet grip indicators with tan δ at 0 °C increasing from 0.205 to 0.237 while maintaining rolling resistance indicators at the same level. We have evaluated the impact of the silane chemistry onto the cross-linking reactivity within the fabricated rubber-based nanocomposites by using moving-dye rheometer measurements (MDR). By purposely using atomic force microscopy (AFM), we have studied the silica dispersion in the matrix and the rubber/silica interface and provided the rationale explanation of the mechanical properties observed at the macroscale. AFM observation pointed out the existence of a soft interface around silica fillers when long alkylsilanes were used. We infer that this interface impacts the polymer−filler dynamic and subsequently affects the mechanical properties of the composite material.

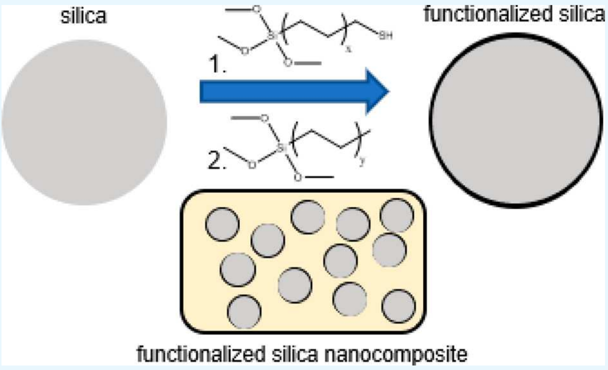

INTRODUCTION

Historically, tire rubber compounds were reinforced using carbon black. The good interaction between this filler and the usual polymers matrices implies very good performances as well as an easy mixing of the filler with the polymer blend. Later, silica was introduced as a potent filler, but due to its hydrophilic nature, new strategies had to be found to compatibilize the particles with the matrix to reach desirable performances. Organosilanes have been the first choice as they allow covalent bonding of silica with the polymer and hydrophobize the surface of the particles, inducing a much better dispersion and reinforcement of structure. Since then, researchers have been working on these two filler properties and investigating various strategies to improve performances, using new materials and processes. The *in situ* growth of silica particles has proven to be an efficient way to achieve a very high dispersion of such particles into the matrix.[1,2] Other works investigated the use of nonsilane coupling agents.[3,4] Beyond silica and carbon black, innovative alternative fillers such as silicon particle and graphene oxide are developed.[5] With the growing need to find sustainable filler materials, research in the fillers domain becomes driven by the challenging task to make new fillers cope with previous technology performance levels.[6] The filler morphology is another important research topic, and extensive work is being conducted on the use of anisotropic fillers[7−10] based on silica, clay, or cellulose nanocrystals. Other strategies, not focusing on the filler itself, work around the opportunity to valorize waste as a usable resource for the tire industry.[11] Tire-tread compounds face a challenge in which wet-grip performances need to be sustained, while improving rolling resistance in

Received: February 1, 2022
Accepted: April 26, 2022
Published: May 18, 2022

https://doi.org/10.1021/acsomega.2c00665
ACS Omega 2022, 7, 17692−17702

order to comply with new environmental regulations and original equipment manufacturers requirements.[12] The introduction of silica as a filler opened the door of progress for wet traction while decreasing significantly rolling resistance, even it was mainly the use of silanes that really enabled it.[13] By creating an interface between the silica particles and the polymer matrix, silanes modify interactions and forces transmission during the mechanical solicitation of the material. Usually, silanes are added into the rubber blend during the mixing of the polymer, silica, and other ingredients. It allows for a simple and effective way to incorporate them. Another strategy is the pretreatment of the silica particles before their addition. This method enables a better control of the silanization and finer tuning of the final material properties, as well as helping to avoid alcohol production in the blend when silanes react. This method of processing rubber is safer and simplified. The idea of multiple silanes on silica to bring out new properties is not recent,[14] and has been already been proven to be an efficient way to solve the aggregation issue in bitumen filled silica.[15] But according the best of our knowledge, dual-silane silica has not been applied to tire tread rubber. Our work on presilanized silica stands within this context. Silanes are used with silica not only as binding agent with the rubber matrix, but also as antiflocculent ingredients which increase the silica dispersibility in the polymer.[16] Indeed, silica is a mineral hydrophilic filler and tends to aggregate through hydrogen bonding when mixed with polymers. Silane molecules, when reacting with hydroxyl groups on the silica surface, turn the silica hydrophilic surface into a hydrophobic one, hence increasing compatibility with the rubber matrix.[17,18] Bis-triethoxysilylpropyltetrasulfide (TESPT) for example is a widely used silane, as it plays the role of coupling agent between silica and rubber through its tetra sulfide bond and participates in the hydrophobization of the filler.[19,20] Another aspect of the silanization of silica particles is that it affects the vulcanization behavior of a rubber compound and more specifically the cross-link density and the scorch time.[18,21−23] The concept of scorch time is essential when it comes to rubber compounding as it describes the time window during which the green compound is still shapeable before becoming irreversibly rubbery. The introduction of silanes in the system changes the cure dynamic by affecting the molecular mobility within the matrix. It also affects the cross-link density, as mercaptosilanes can react with the polymer chains and bridge them with silica particles or other polymer chains. Many studies worked out the impact of silanes on rubber compounds, especially the effect of silanes on rubber cross-linking and silica dispersion.[24,25] Usually, only one silane is used in the compound, or different silanes are compared one-to-one in order to understand the impact of their structures on the system.[18,26,27] In this work, we investigate the idea of a dual-silane presilanized silica, where two different silanes are grafted onto silica particles. For this matter, we used a method that we call "base catalyst pre-loading", to achieve high silica coverage of silane without creating multiple layers on particles. As silanes promote the silica binding to the polymeric matrix as well as the dispersion of particles into the polymer,[24,25] we want to tailor silica surfaces with two different silanes populations. A first silane plays the role of coupling agent by chemically bridging silica and rubber. The second acts as a hydrophobicity enhancer for the silica particles and mitigates the coupling reaction of silica with rubber. Indeed, severe silica aggregation can occur with silanes bridging themselves when polymerizing together due to their chemical structure and reactivity. For this matter, we study here how the respective molecular size of the two silanes affects each other. By combining alkylsilanes with mercaptosilanes, we investigate the possibility of mitigating the coupling silane reactivity by means of steric hindrance to open new and original chemical routes aiming at improving the cure behavior and the mechanical properties of the rubber-based nanocomposite.

■ EXPERIMENTAL SECTION

For this study, high dispersibility silica (HDS) was used. This silica is obtained industrially by a wet precipitation process which results in 10 nm primary particles size with a specific surface area of 200 m^2/g (see Figures S1 and S2 in Supporting Information). An infrared spectrum of this silica is provided in Figure S3. 3-Mercaptopropyltrimethoxysilane (MPTS), 11-mercaptoundecyltrimethoxysilane (MUTS), hexyltrimethoxysilane (C6), dodecyltrimethoxysilane (C12), and octadecyltrimethoxysilane (C18) were supplied by Gelest. Synthesis grade toluene, THF, and 1,5-diazabicyclo [5.4.0] undec-5-ene (DBU) were supplied by Sigma-Aldrich. The chemical structures of silanes and DBU are shown in Figure 1.

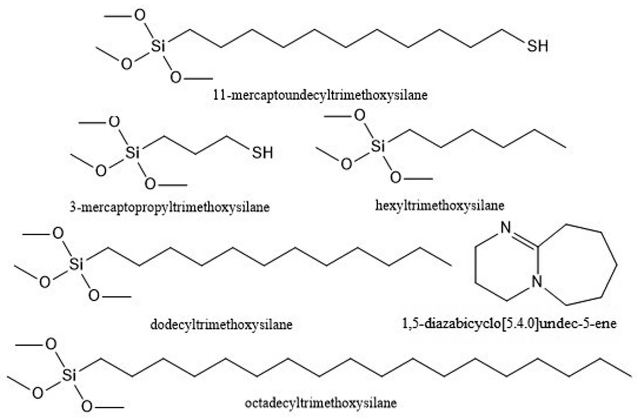

Figure 1. Chemical structures of silanes and base catalyst.

Dual-Silane Premodified Silica Synthesis. A typical presilanization is performed in three steps. First the base catalyst is preloaded as follows: 30 g of HDS silica are suspended in 500 mL of a solution of 0.34 g/L of DBU in THF under stirring at room temperature for 10 min. The silica is then separated by centrifugation and dried under reduced pressure at room temperature. In the second step, 30 g of DBU-treated silica are suspended in 167 mL of toluene. The suspension is heated up to 110 °C and 0.023 mol of MPTS or MUTS are added. The reaction is carried at 110 °C under stirring for 24 h. Then silica is separated and rinsed with fresh toluene and centrifugation. The silica washing operation is repeated three times to ensure that no unreacted silane is left on the silica. In the third step, 30 g of the previously modified silica are suspended in 167 mL of toluene. The suspension is heated up to 110 °C and 0.023 mol of the desired alkylsilane are added. The reaction is carried at 110 °C under stirring for 24 h. Then silica is separated by centrifugation and cleaned with fresh toluene. This operation is also repeated three times to ensure that no unreacted silane is left on the silica. Finally, the dual-silane premodified silica particles are dried under

Table 1. - Silanes/Compounds Correspondence Table

compounds names	silane 1	silane 2
reference HDS silica	N/A	N/A
C3SH+C6	3-mercaptopropyltrimethoxysilane	hexyltrimethoxysilane
C3SH+C12	3-mercaptopropyltrimethoxysilane	dodecyltrimethoxysilane
C3SH+C18	3-mercaptopropyltrimethoxysilane	octadecyltrimethoxysilane
C11SH+C6	11-mercaptoundecyltrimethoxysilane	hexyltrimethoxysilane

vacuum at room temperature and stored in a glass container for later use.

Silica Mixing in Rubber Matrix. Polystyrene-butadiene (SBR, solution SBR, 21% styrene, 50% vinyl) polybutadiene rubber (BR, neodymium catalyzed polybutadiene), treated distillate aromatic extracted (TDAE) lubricating oil, zinc oxide, stearic acid, *N*-(1,3-dimethylbutyl)-*N*′-phenyl-*p*-phenylenediamine (6-PPD), sulfur, 2-mercaptobenzothaizole (MBT), diphenylguanidine (DPG), and *N*-cyclohexyl-2-benzothiazolesulfenamide (CBS) have been used. At each mixing step ingredients have been mixed using a HAAKE PolyLab QC ThermoScientific internal mixer, and then the compound was further mixed in a roll-mill. Component quantities and mixing steps have been summed up in the Table 2. All green composite materials have been cured in a hydraulic press at 170 °C for 10 min under a pressure of 150 kPa or in a moving-dye rheometer (MDR) measuring device for the curing behavior measurements. Table 1 below shows the correspondence between compounds names and silanes grafted onto silica.

Table 2. Composition and Mixing Steps of Compounds

components	phr	mixing conditions
	Step 1	
polystyrene-butadiene	80	80 °C for 10 min
polybutadiene	20	
TDAE oil	25	
zinc oxide	0.5	
stearic acid	3	
dual-silane silica	65	
	Step 2	
Step 1 compound		80 °C for 7 min
dual-silane silica	15	
6PPD	2.5	
	Step 3	
Step 2 compound		60 °C for 1 min 45 sec
zinc oxide	2	
sulfur	1.1	
MBT	0.3	
DPG	3.2	
CBS	2.3	

Characterization. Dual-silane premodified silica fillers have been characterized by thermogravimetric analysis (TGA) and solid state nuclear magnetic resonance of silicon 29 (^{29}Si ssNMR). Silane loading was quantified by TGA as followed: 10 to 20 mg of silica powder was placed in an alumina crucible and heated from 25 to 1000 °C at 10 °C/min. An empty alumina crucible is also placed in the furnace for reference. Solid-state $^{\mathrm{Si}}$ MAS (Magic Angle Spinning) NMR spectra were acquired on a Bruker Avance 400 MHz spectrometer (9.4 T wide bore magnet) equipped with a 4 mm BL4 X/Y/H probe. Magic angle spinning was performed at 6.5 kHz using ceramic zirconia rotors of 4 mm in diameter. The signal of talc was used to calibrate the silicon chemical shift scale (−98 ppm). Acquisition parameters used were the following: a spectral width of 300 ppm, a 90° pulse length of 4.5 μs, an acquisition time of 15 ms, a recycle delay time of 60 s, and about 3000 accumulations (48 h). High power proton dipolar decoupling during the acquisition time was set to 70 kHz. Solid-state ^{29}Si MAS (magic angle spinning) NMR spectra were also acquired on an Agilent VNMRS DirectDrive 400 MHz spectrometer (9.4 T wide bore magnet) equipped with a T3HX 3.2 mm probe. Magic angle spinning was performed at 6.5 kHz using ceramic zirconia rotors of 3.2 mm in diameter, the signal of talc was used to calibrate the silicon chemical shift scale (−98 ppm). Acquisition parameters used were the following: a spectral width of 300 ppm, a 90° pulse length of 5 μs, an acquisition time of 15 ms, a recycle delay time of 60 s, and about 4400 accumulations (72 h). High power proton dipolar decoupling during the acquisition time was set to 70 kHz. Mechanical properties of the resulting composite materials have been tested by dynamic mechanical analysis (DMA) at 1 and 10 Hz, a free length of 5 mm and a temperature sweep from −80 °C up to 100 °C. The curing behavior of the green compounds was evaluated by MDR with a MDR 2000 rheometer from Alpha Technologies, at a frequency of 1.667 Hz, a strain of 0.5 degree, at a temperature of 160 °C during 60 min. Sample dimensions are 43 mm in diameter and 2 mm thickness. Atomic force microscopy images of cryo-ultramicrotomed surfaces of the samples were acquired using the AM-FM mode of the MFP-3D Infinity AFM instrument (Asylum Research). All measurements were made under ambient conditions, and a standard cantilever holder for operation in air was used. Images of 10 × 10 μm^2, 5 × 5 μm^2, and 2 × 2 μm^2 areas were taken with a resolution of 256 × 256 pixels at a scan rate of 1 Hz. Cantilevers' spring constants used in this study were about 30 N/m (AC160TS-R3 model from Olympus). The first and second resonant frequencies for AC160TS-R3 cantilevers were about 300 kHz and 1.6 MHz, respectively. To ensure repulsive intermittent contact mode, the amplitude set point was adjusted so that the phase is well fixed below 90°. This allows for the acquisition of complementary stiffness contrast images simultaneously with topography.

RESULTS AND DISCUSSION

Synthesis of the Dual-Silane Silica Particles and Their Characterization. The main objective of the synthesis method is to increase the yield of silane grafting on silica particles without falling into a multilayer regime. Consequently, experimental conditions focused on promoting a silica−silane surface reaction and preventing the oligomerization of silane in the solvent. First, silica particles are loaded with the base catalyst DBU to increase reactivity on the surface. DBU has a strong pK_a (∼13.5 in water[28,29]). Thus, DBU may lead to substantially deprotonate hydroxyl groups of the silica surface due to the pK_a difference. If so, the silica surface should be more prone to react with silanes. The presence of an amine catalyst also improves the grafting yield and the stability of the silane−silica bond.[30] Second, the reaction is carried in toluene, as it solubilizes silanes and has relatively a high boiling point compared to another hydrocarbon solvent. Also, toluene is a good middle ground when it comes to the formation of hydrophobic monolayer on silica, as it naturally solubilizes enough water in order to induce silanol formation from alkoxysilane, without promoting polymerization of the alkoxysilane by solubilizing too much water.[31]

We can observe a significant difference of the residual mass below 130 °C when considering the thermograms of Figure 3. In the case of the HDS silica, the mass loss is attributed to the desorption of water from the silica surface. In the case of modified silica, we attribute the mass loss to the loss of the remaining alkoxy groups originating from the grafted silanes. This difference originates from the fact that HDS silica is a precipitated silica, hence featured by the absence of alkoxy groups, contrary to our modified silica for which we used methoxysilanes. Also, the initially adsorbed water on the unmodified silica is lost through the silanization and drying steps being performed to obtain dual silane modified silica. Surface hydroxyls groups Si−OH have a key role, and it has been documented[32] that silica reactivity toward alkoxysilanes is enabled by the presence of silanols at the surface. Silica's silanols undergo a condensation reaction with silane's silanols, form a Si−O−Si bond, and covalently bond the silane to the silica. Prior to the condensation step, silanes must be hydrolyzed from the alkoxy form to silanols Si−OH. Since the HDS silica is produced via a wet precipitation process, silanols groups Si−OH feature the surface of such particles. An infrared spectrum of the HDS silica used in this study is shown in Figure S3 of the Supporting Information and further highlights the presence of Si−OH. The physical interaction between silanes and silica is also an important parameter, especially through hydrogen bonding of silanes onto silica. The capability of thiols to form hydrogen bonds has been questioned for a long time with few studies to shed light on this phenomenon. This is of major consideration especially in biology as sulfur and thiols are important constituents of many molecules. Some recent experimental and computational works have brought more understanding on the topic.[33,34] According to the best of our knowledge, the interaction of a thiol−silane with silica through hydrogen bonding has not been reported and studied, unlike the very well-known interaction of amine−silane with silica.[35] Due to the lower electronegativity difference of the sulfur−hydrogen bond (Δ ∼ 0.38) compared to the nitrogen−hydrogen bond (Δ ∼ 0.84) or oxygen−hydrogen bond (Δ ∼ 1.24), the strength of the hydrogen bond involving thiol is expected to be weak. In the case of back-bonding of the silane to the silica via hydrogen bonding, we could expect to have residual silane weakly bonded to the silica remaining after the reaction. Another critical aspect is the potential interaction between DBU and the mercaptosilane during silanization, and the possibility to deprotonate the terminal thiol of this silane. It has been reported that the pK_a of DBU is about 13.5,[28,29] and the pK_a of an aliphatic thiol is around 11.[36] For the pK_a of silanols, various values have been reported ranging from 5 to 9.5.[37] The difficulty of determining the pK_a of silanols comes from the variety of spatial conformation of silanols, such as geminal, vicinal, and isolated or H-bonded silanols. All these parameters impact the acidity of the silanols. We can affirm that DBU will first deprotonate the most acidic silanols, then the less acidic ones, and finally eventually the thiol group of the silane. This is the reason why we did not mix as such DBU and the silane in the silanization media. We preferred an approach in which we deprotonated the silica's silanols by premixing DBU and silica in a first step, then silanization is carried out as described in the Experimental Section. To assess the amount of silane grafted onto silica, the mass loss associated with the silane pyrolysis is recorded via TGA. The mass loss is calculated by subtracting the residual mass loss value at 600 °C from the value at 125 °C to isolate the silane contribution to the total mass loss of the sample. This method of calculation is inspired from the work of Kunc et al.[38] TGA thermograms in Figure 2 and values in Table 3 show the difference between no catalysis and DBU preloading on silica. For the system without any base catalyst preloading, all silanes yield about 3.5 to 4% of mass-loss, whereas DBU preloaded silica displays a much higher grafting yield of respectively 6.95%, 10.85%, and 13.89% for C6, C12, and C18. The use of DBU clearly yields a higher silane loading on silica. The silane loading for dual-silane pretreated silica has also been characterized by thermogravimetric analysis (Figure 3) and 29Si ssNMR (Figure 5).

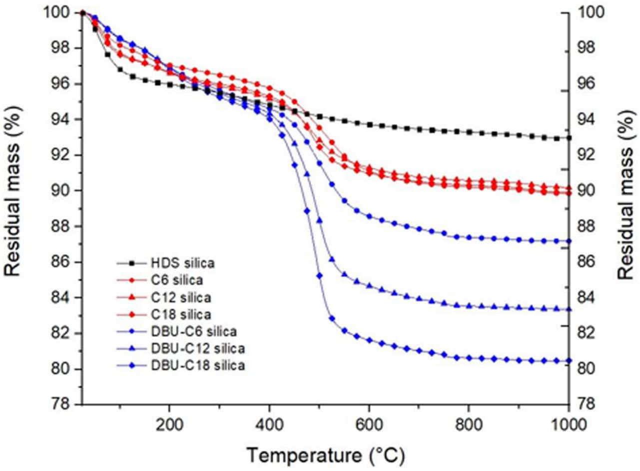

Figure 2. TGA curves of silanized silica (C6, C12, and C18), with and without DBU preloading.

Table 3. TGA Values for Modified Silica with and without DBU Preloading

sample name	residual mass at 125 °C (%)	residual mass at 600 °C (%)	mass loss (%)
HDS silica	96.44	93.74	2.7
C6 silica	97.88	91.13	4.05
C12 silica	97.43	91.31	3.42
C18 silica	97.37	91	3.67
DBU-C6 silica	98.23	88.58	6.95
DBU-C12 silica	98.22	84.67	10.85
DBU-C18 silica	98.22	81.63	13.89

Scheme in Figure 4 illustrate the two-step process of dual-silane pretreated silica silanization. From the mass loss values in Table 4 we observe that most of silane is grafted during the first step. When accounting for the mass of mercaptosilane

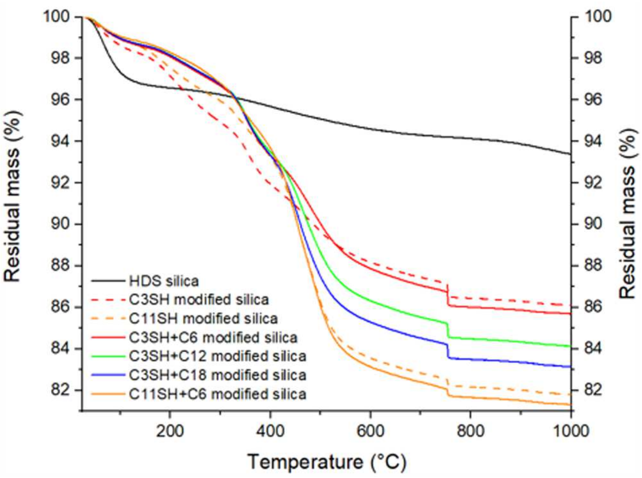

Figure 3. TGA curves for dual-silane premodified silica.

Table 4. TGA Mass Loss Values for Dual Silane Modified Silica

sample name	residual mass at 125 °C (%)	residual mass at 600 °C (%)	mass loss (%)
HDS silica	96.9	94.6	2.3
C3SH modified silica	97.7	87.6	10.1
C3SH+C6 modified silica	98.2	87.4	10.8
C3SH+C12 modified silica	98.3	85.9	12.4
C3SH+C18 modified silica	98.3	84.9	13.4
C11SH modified silica	98.2	83.1	15.1
C11SH+C6 modified silica	98.4	82.7	15.7

grafted on silica during the first step (10.1% mass loss), alkylsilane grafted in the second step accounts for respectively 0.7%, 2.3%, and 3.3% of the total mass loss for C3SH+C6, C3SH+C12, and C3SH+C18, respectively, which corresponds to 6.9%, 22.7%, and 32.7% of the mercaptosilane mass. Similarly, C11SH is added in the first step (15.1% of total mass) and the addition of C6 accounts for 0.6% of total mass loss and 4% of silane mass loss, which is consistent. This result comes from the fact that the mercaptosilane is added first and covers most of the surface. Alkylsilanes act as a cap and fill the remaining empty gaps of the silica surface.

Figure 5 displays the results of ^{29}Si ssNMR. The peak at 0 ppm corresponds to the internal standard TMS (3-(trimethylsilyl)-1-propanesulfonic acid sodium salt). Signals at −90, −100, and −110 ppm correspond to Q2, Q3, and Q4 groups. Q2 and Q3 being respectively geminal and single silanol and Q4 being the Si−O−Si bond forming the bulk of the silica. Signals at about −50, −60, and −70 ppm, respectively, correspond to T1, T2, and T3 groups. T groups are formed by the reaction of the -trimethoxysilanes on the silica surface or with another silane. This signal confirms the presence of silanes on the silica particles. It has been shown that trifunctional silanes do not react on silica surface with their three reactive groups, but with a maximum of two of them, for spatial reasons. It leads to the formation of mostly T1 and T2 groups. However, the formation of T3 groups is not impossible, and happens when silanes react together, away from the surface.[39] We suggest that the higher content of T3 groups versus T1 and T2 results from the two-step silanization. The second silane can react with unreacted methoxy or silanol groups of first silane to yield T3 groups. The clear decrease in the Q3 peak intensity is also an evidence of the silanization reaction consuming surface hydroxyl groups. Based on the internal standard quantity and the deconvolution method, we can estimate the amount of grafted silane onto the silica. Those results are summed up in Table 5. We note a difference between samples with C3SH and the one with C11SH. With a shorter mercaptosilane as the first silane, the final silane loading is very similar. When the longer C11SH silane is used first, the final silane loading is lower. This likely comes from the higher steric hindrance displayed by the longer silane when reacting in first with the silica surface.

Dynamical Mechanical Properties. Tire tread performances, namely grip and rolling resistance, can be estimated at the material stage by testing dynamic mechanical properties of the cured rubber composite. The measurement of loss tangent tan δ on a range of temperature allows characterization of the behavior of the material.

$$\tan \delta = \frac{E''}{E'} \tag{1}$$

As the ratio of the loss modulus (E'') and storage modulus (E') in eq 1, the tan δ describes the capability of the material to dissipate energy in the form of heat through vibrational dampening. The time−temperature superposition principle allows for temperature ranges to be transposed to frequency

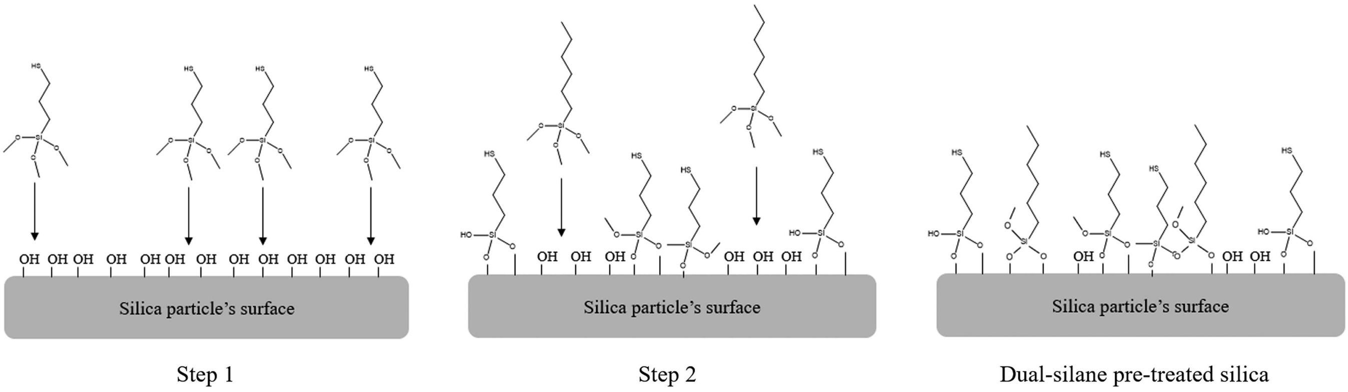

Figure 4. Scheme of dual-silane pretreated silica silanization process.

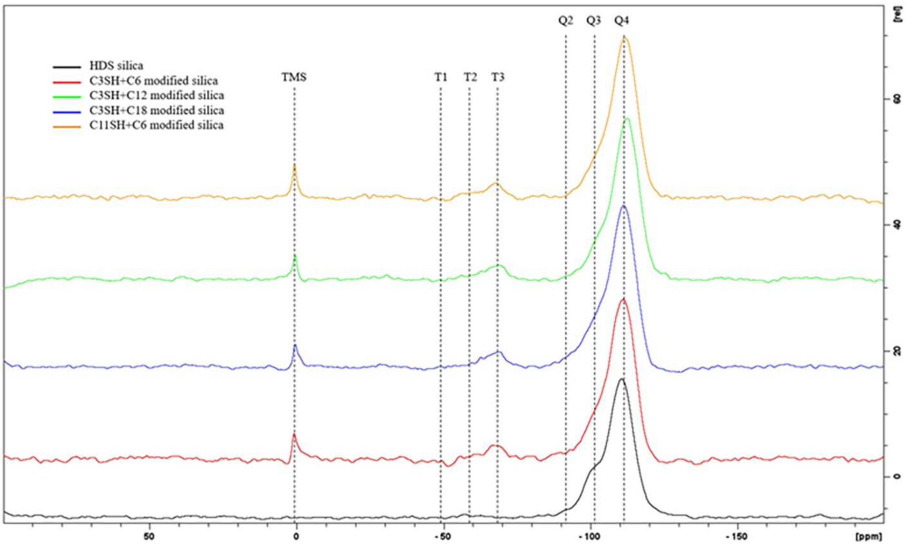

Figure 5. 29Si ss NMR spectra of control and dual-silane premodified silica.

Table 5. Silane Grafting Values Based on Deconvolution of 29Si ssNMR Spectra

	HDS control	C3SH +C6	C3SH +C12	C3SH +C18	C11SH +C6
T1 (mmol)		0.00	0.00	0.00	0.00
T2 (mmol)		0.02	0.27	0.54	0.06
T3 (mmol)		0.73	0.76	0.68	0.38
total (mmol)		0.75	1.03	1.22	0.45
silane loading (mmol/g of silica)		2.48	3.32	4.05	1.49

ranges.[40] Certain mechanical frequency ranges can be associated with mechanical solicitation of the tire tread. Therefore, tan δ at 0 °C is a good indicator for grip performances and tan δ at 60 °C a good indicator for the rolling resistance of a tire. Good grip properties are equivalent to high tan δ at 0 °C and good rolling resistance properties are equivalent to low tan δ at 60 °C.[41,42] Ideally, one wants to maximize tan δ at 0 °C and minimize tan δ at 60 °C. The storage modulus E' and tan δ of the different composite materials are represented in Figure 6, and numerical values are gathered in Table S1 of Supporting Information.

The control sample is a standard compound optimized for an 80 phr silica load and in situ silanization. Compounds with dual-silane premodified silica do not exhibit the same behavior as the control compound. Storage modulus E' and tan δ decrease faster in dual-silane pretreated silica than in the

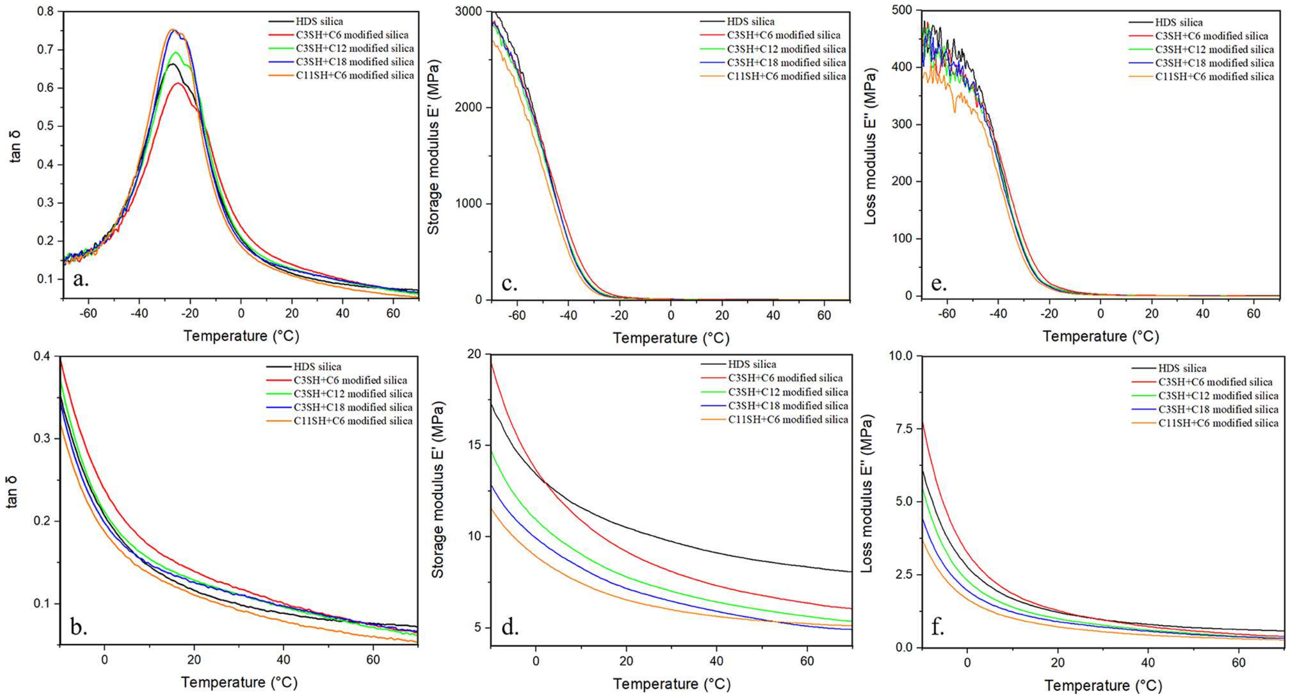

Figure 6. Tan (δ) (a,b), storage modulus E' (c,d), and loss modulus E'' (e,f) vs temperature, for various dual-silane modified silica rubber composites.

https://doi.org/10.1021/acsomega.2c00665
ACS Omega 2022, 7, 17692−17702

control, allowing altogether for relatively higher tan δ at low temperature and low tan δ at high temperature. Samples C3SH+C6 and C3SH+C12 show improved performances for both indicators. The other two samples having slightly lower tan δ at 60 °C than the control, C11SH+C6 having a much lower tan δ than any sample. Increasing silane chain length clearly causes a decrease in storage modulus and tan δ at low temperature. The part of the curves in the −40 to −10 °C range is representative of the phase transition that the material withstands with temperature changes. Usually attributed to the glass transition temperature in polymers and rubbers, it can also display the effect of fillers.[43] Indeed, filler particles change the polymer chain dynamic when incorporated in polymers.[27] In our case, two overlapping peaks can be observed for all samples. The peak further on the right shifts depending on the sample. This shifting trend follows the decrease in storage modulus for all samples. It can be attributed to the increasing content of polymer chains for which the dynamic is modified by the dual-silanization. The increase of the alkyl chain length, both for the mercaptosilane and the alkylsilane, seems to lead to a decrease of the fraction of immobilized rubber. The composite sample using C3SH+C6 modified silica shows one dominant peak at lower temperature corresponding to the T_g, and a second weaker relaxation process, occurring at higher temperature, probably correlated to rubber immobilized by the fillers. In view of the better dispersibility of the modified silica, the immobilization may be due to covalent linking with the SH, polymer absorbed to unshielded silica surface or perhaps to rubber which got occluded inside smaller aggregates. These two peaks seem to be separated in temperature indicating two distinct thermal transitions. The increase of the alkyl chain length for C3SH+C12 modified silica leads to an increase of the intensity of both peaks as well as to an enhanced peak-overlap of the two transitions. This may be explained by an increased amount of polymer chains involved in the relaxation processes and therefore a lower constraint exerted by the fillers on the polymer dynamics. Samples C3SH+C18 modified silica and C11SH+C6 modified silica, characterized by the longest alkyl portion in the silica-rubber coupling, exhibit very similar curves. In both cases, a sharp peak in the glass transition region is reported. In addition, an overlap of the two peaks is observed, suggesting that the dynamics of the polymer at the rubber−filler interphase and in proximity of the glass transition are very similar. Curing the green rubber compounds under a moving dye rheometer showed that the vulcanization behavior of dual-silane pretreated silica composites is completely different from that of the reference sample. These results can be seen in Figure 8.

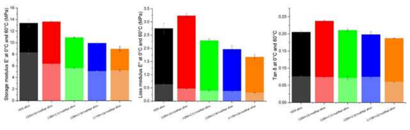

Figure 7. Tan δ and storage and loss modulus at 0 °C (dark colors) and at 60 °C (light colors).

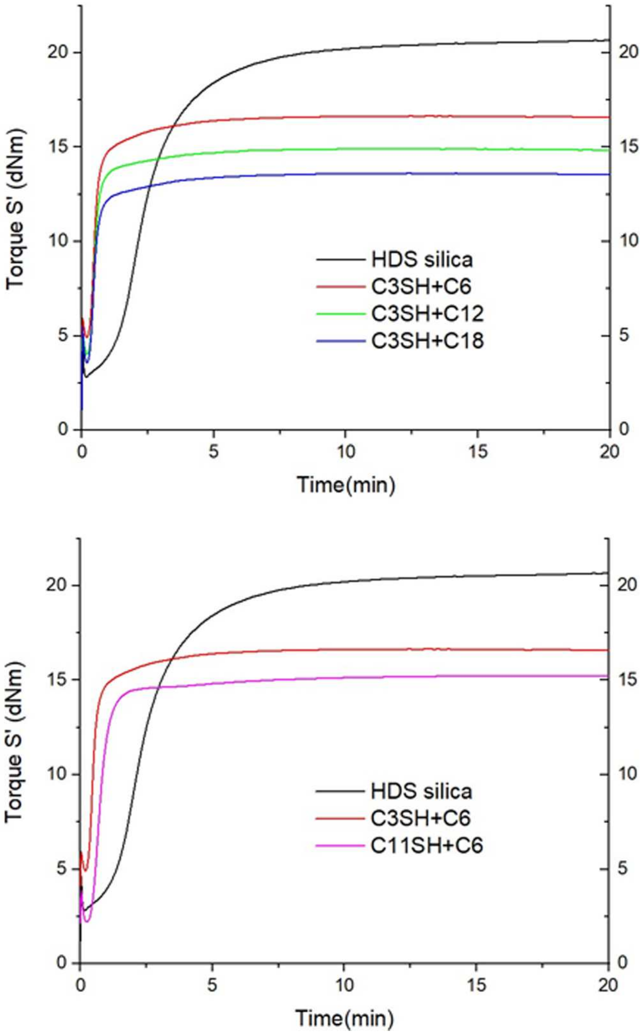

Figure 8. Cure behavior of green composites material measured by MDR.

Vulcanization conditions are optimized for the reference compound and have been chosen to be the same for all compounds. For dual-silane pretreated silica, vulcanization conditions are not optimal, as the scorch times are shorter, and the cure faster. No reversion is seen in any composition. The final torques are lower for all samples, suggesting that the vulcanization process may be affected, and the final cross-link density of the rubbers is lower. We suggest that the silica pretreatment and the alkylsilanes may affect the final cross-link density, leading to a lower final torque. The effect is clear for the variation in alkylsilane, where the longer is the silane, the lower is the final torque. For the longer C18 silane, the effect may be so important that it shields completely the mercaptosilane, explaining the very low storage modulus and final torque. As for the mercaptosilane variation, the initial torque difference prior to the curing of the composite is conserved and can be seen in the final torque attained in the end of the vulcanization. Both mercaptosilanes display a terminal thiol and thus show the same reactivity despite having different chain length. The sample C11SH+C6 display about the same mechanical properties as the sample C3SH+C12, where silanes are of similar length. These observations allow us to suggest that the chain length of any silane is more important than the relative size of the coupling and dispersive silanes. The initial slopes of the curves are characteristic of the cure speed. Compounds with dual-silane pretreated silica display a much faster cure behavior than the control sample. This fast cure behavior is known for premodified silica particles. Indeed, in standard tire rubber compounds, it is also intended that the silane should screen the silica particles from the polar organic

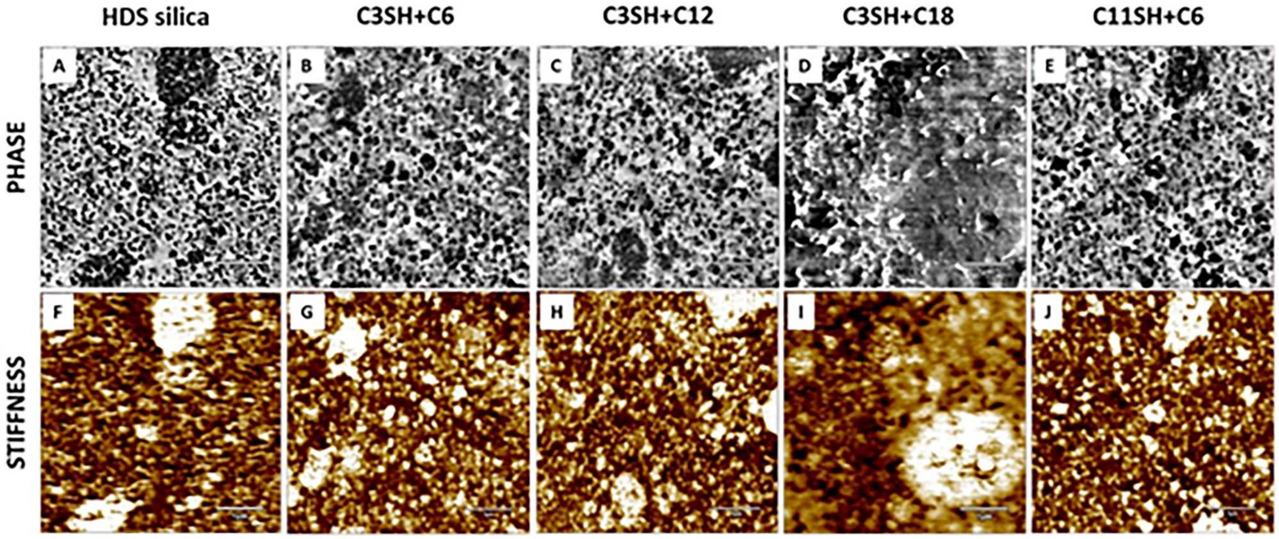

Figure 9. AFM phase and stiffness contrast images in areas of 5 × 5 μm^2 of HDS silica (a,f), C3SH+C6 (b,g), C3SH+C12 (c,h), C3SH+C18 (d,i), and C11SH+C6 (e,j) composite materials.

molecule of curing package, such as diphenyl guanidine, in order to prevent these molecules from being excessively adsorbed on the particles and therefore not available for the vulcanization reaction. In our case because the silica is highly silanized, DPG and other vulcanizing elements are highly available in the rubber matrix and are very likely to be responsible of this fast cure.[16]

AFM images were recorded in order to investigate the effects of the silane couplings on the materials phase and the local stiffness of the composites. This technique has the advantage of displaying a very good contrast and lateral resolution, in addition of providing complementary stiffness information. Figure 8 shows a representative AFM phase and stiffness contrast images in areas of 5 × 5 μm^2 of the different composite materials. In the phase images, silica particles appear as dark round shape features with about 60 nm in diameter, dispersed in the rubber matrix (lighter contrast). The complementary stiffness contrast images taken simultaneously highlight the higher mechanical properties of the particles (light yellow) compared to the softer rubber matrix, confirming the attribution. Agglomerates of particles in the composites are expected, due to the high filler content in the compound, and can be seen in both phase and stiffness images, attaining even several micrometers in length (shown in the Supporting Information). The sample using C3SH+C18 silane chemistry shows large agglomerates and does not feature a similar particle distribution as the others, see Figure 9d,i.

Atomic Force Microscopy. The average distance between particles was measured using images of similar areas in each sample for more reliable results. Focused attention should be given in zones where the presence of agglomerates is less pronounced, but since the distribution in sample C3SH+C18 was very different from the others, no reliable measurements were obtained in smaller areas. Results are shown in Table 6 and Figure 10. No significant interparticle distance difference can be observed between samples, except for C3SH+C18, for which big agglomerates form. The final mechanical properties of the material are defined by complex relations between morphology, particles sizes and distribution, but also vulcanization kinetics and interfacial interactions between components. Therefore, the dispersion of the filler alone, cannot explain the dynamical properties observed, but the higher agglomeration of the particles in sample C3SH+C18 certainly hampers the final mechanical properties of the compound.

Table 6. Average Distance between Particles (nm)

	average distance between particles (nm)		
sample/area	10 × 10 μm^2	5 × 5 μm^2	2 × 2 μm^2
HDS control	60 ± 27	43 ± 24	28 ± 19
C3SH+C6	63 ± 31	49 ± 28	40 ± 26
C3SH+C12	71 ± 38	48 ± 27	35 ± 23
C3SH+C18	204 ± 144	120 ± 86	
C11SH+C6	72 ± 36	46 ± 26	45 ± 31

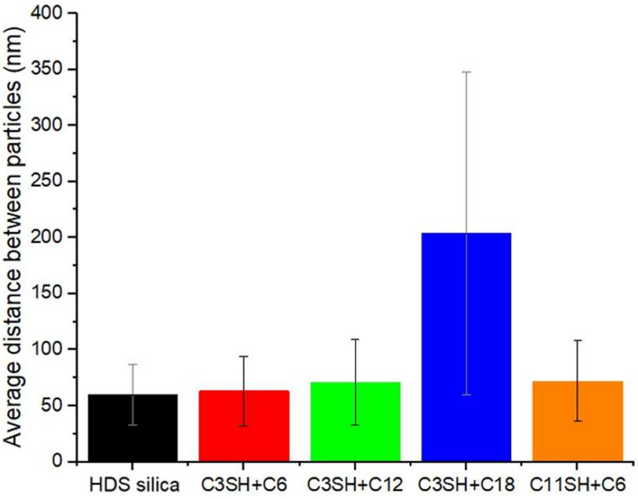

Figure 10. Average distance between particles (based on 10 × 10 μm images).

In a closer look of the rubber−particle interface, we observe for the sample C3SH+C18 a 40 nm thick-layer around some nonaggregated particles, composed most likely of a mix of the silane and processing oil around the fillers. A comparison with the control sample is highlighted in Figure 11 where the control compound does not present such features. An explanation would come from the very long and therefore

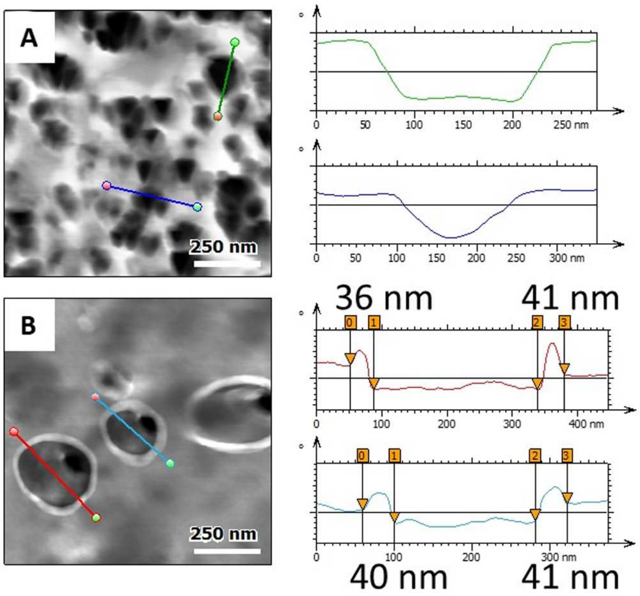

Figure 11. AFM phase images of areas of 1 × 1 μm^2 and sections over silica particles of samples (A) HDS silica and (B) C3SH+C18.

hydrophobic C18 silane, attracting enough oil to change the polymer chains dynamic at the interface between the filler and matrix. This effect was only observed for the longest silane, thus we suggest that the interface of the filler with the matrix can be controlled by the length of the silane and plays a great role in the dispersion of the silica and in the mechanical behavior of the composite.

CONCLUSION

We synthesized dual-silane pretreated silica by preloading a basic catalyst on the particles prior to a two-step silanization. These particles were incorporated in a typical tire tread blend to investigate two major properties of tires: wet grip and rolling resistance. Short coupling silane combined with short dispersive silane demonstrated a very good compromise of properties, with high tan δ at 0 °C and low tan δ at 60 °C. We observed a clear trend in which the longer is the alkylsilane, the lower is the elastic modulus. Also, for long alkylsilane, the final torque measured by MDR is very low, suggesting a low cross-link density. We proposed that alkylsilane shields its mercaptosilane companion, decreasing its reactivity and prohibiting partially the cross-linking reaction to occur, depending on its length. It was confirmed by AFM that particles have a higher affinity to themselves with increasing silane length, thus leading to their aggregation. Even with a long mercaptosilane such as C11SH, the storage modulus and final torque are very low, suggesting that the silane is not reactive enough. The C3SH+C18 sample even displays a different phase around the filler particles, possibly due to oils attracted onto the modified particles resulting from the long silane grafted to them. This new interface is believed to deeply modify the interaction between the filler and the matrix and thus greatly impact the final composite mechanical properties. Overall, dual-silane pretreated silica have a different behavior compared to the control filler: higher tan δ at low temperature and lower tan δ at higher temperature are achieved for the shorter alkylsilane C6 and C12 when paired with C3SH. Pretreatment of the silica before incorporation in rubber allows for more control over silane grafting on the particles, as well as avoiding the production of subsequent alcohols resulting from the silanization during rubber mixing. The use of two silanes shows new behavior of the nanocomposites as well as specific limits: a short silanes combination brings better mechanical properties, namely higher tan δ at 0 °C suggesting better wet grip, but longer alkylsilanes, especially C18, fail to ensure reinforcement and lead to lower performance with regards to tire-tread properties requirements. The longer is the alkyl chain, the more intersilane interactions via weak van der Waals forces are enhanced, creating a packed layer of alkyl chains around the silica particles and resulting in poor interaction with the polymer matrix. Additionally, long alkyl chains diminish the accessibility of thiol grafted onto silica for vulcanization and cross-linking, leading to even less interaction between silica and the matrix and resulting in insufficient reinforcement. As tan δ alone cannot describe the entire behavior of the rubber of a tire, further studies should focus on testing such dual-silane pretreated silicas on a large scale volume to test the subsequent ultimate properties of a real tire.

ASSOCIATED CONTENT

Supporting Information

The Supporting Information is available free of charge at https://pubs.acs.org/doi/10.1021/acsomega.2c00665.

Additional silica SEM images, silica infrared spectrum, DMA data table, and AFM micrograph (PDF)

AUTHOR INFORMATION

Corresponding Author

Jean-Sébastien Thomann − *MRT Department, Luxembourg Institute of Science and Technology, L-4422 Belvaux, Luxembourg;* orcid.org/0000-0003-1381-8349; Email: jean-sebastien.thomann@list.lu

Authors

Enzo Moretto − *MRT Department, Luxembourg Institute of Science and Technology, L-4422 Belvaux, Luxembourg*
João P. C. Fernandes − *MRT Department, Luxembourg Institute of Science and Technology, L-4422 Belvaux, Luxembourg*
Mariapaola Staropoli − *MRT Department, Luxembourg Institute of Science and Technology, L-4422 Belvaux, Luxembourg;* orcid.org/0000-0002-8226-8769
Vincent Rogé − *MRT Department, Luxembourg Institute of Science and Technology, L-4422 Belvaux, Luxembourg*
Pascal Steiner − *Goodyear S.A, L-7750 Colmar-Berg, Luxembourg*
Benoît Duez − *Goodyear S.A, L-7750 Colmar-Berg, Luxembourg*
Damien Lenoble − *MRT Department, Luxembourg Institute of Science and Technology, L-4422 Belvaux, Luxembourg*

Complete contact information is available at: https://pubs.acs.org/10.1021/acsomega.2c00665

Author Contributions

The manuscript was written through contributions of all authors as following: Conceptualization, E.M., B.D., and J.S.T.; methodology, E.M., J.P.C.F., M.S., V.R., P.S., and J.S.T.; validation, B.D., P.S., D.L., and J.S.T.; formal analysis, E.M., J.P.C.F., and J.S.T.; resources, B.D., D.L., and J.S.T.; writing−original draft preparation E.M. and J.P.C.F.; writing−review and editing, E.M., J.P.C.F., M.S., V.R., B.D., D.L., and J.S.T;

supervision, B.D., D.L., and J.S.T.; project administration, D.L. and J.S.T.; funding acquisition, B.D. and D.L.

Funding

The authors would like to thank the National Research Found of Luxembourg (FNR) for their financial support through the IPBG16/11514551/TireMat-Tech project.

Notes

The authors declare no competing financial interest.

■ ACKNOWLEDGMENTS

We thank Régis Vaudémont and Benoît Marcolini for their precious help on thermal characterization on our fillers and composite, Vincent Berthé for advice on composite processing, Reiner Dieden and Chuanyu Yan for their help on NMR data processing.

■ ABBREVIATIONS

MDR moving dye rheometer
TESPT bis-triethoxypropylsilyltetrasulfide
HDS high dispersibility silica
C3SH 3-mercaptopropyltrimethoxysilane
C11SH 11-mercaptoundecyltrimethoysilane
C6 hexyltrimethoxysilane
C12 dodecyltrimethoxysilane
C18 octadecyltrimethoxysilane
THF tetrahydrofuran
DBU 1,5-diazabicyclo[5.4.0]undec-5-ene
SBR styrene−butadiene rubber
BR butadiene rubber
TDAE oil treated distillate aromatic extracted oil
6-PPD *N*-(1,3-dimethylbutyl)-*N*′-phenyl-p-phenylenediamine
MBT 2-mercaptobenzothaizole
DPG diphenylguanidine
CBS *N*-cyclohexyl-2-benzothiazolesulfenamide
TGA thermogravimetric analysis
^{29}Si MAS ssNMR silicon 29 magic angle spinning solid state nuclear magnetic resonance spectrometry
DMA dynamic mechanical analysis
AFM atomic force microscopy
TMS 3-(Trimethylsilyl)-1-propanesulfonic acid sodium salt

■ REFERENCES

(1) Utrera-Barrios, S.; Perera, R.; León, N.; Santana, M. H.; Martínez, N. Reinforcement of natural rubber using a novel combination of conventional and in situ generated fillers. *JCOMC* **2021**, *5*, 100133.

(2) Ohashi, T.; Tohsan, A.; Ikeda, Y. Role of in situ generated s ilica for rubber science and technology. *Polym. Int.* **2017**, *66* (2), 250−259.

(3) Ye, N.; Zheng, J.; Ye, X.; Xue, J.; Han, D.; Xu, H.; Wang, Z.; Zhang, L. Performance enhancement of rubber composites using VOC-Free interfacial silica coupling agent. *Compos. B. Eng.* **2020**, *202*, 108301.

(4) Yuan, J.; Liu, L.; Wang, X.; Xu, L.; Zhang, L. Structure and Performance of Silica-Grafted Epoxidized Solution-Polymerized Styrene−Butadiene Nanocomposites. *Ind. Eng. Chem. Res.* **2022**, *61*, 3031.

(5) Zhang, Z.; Chen, P.; Nie, W.; Xu, Y.; Zhou, Y. Enhanced mechanical, thermal and solvent resistance of silicone rubber reinforced by organosilica nanoparticles modified graphene oxide. *Polymer* **2020**, *203*, 122772.

(6) Hait, S.; De, D.; Ghosh, A. K.; Al Aiti, M.; Ghosh, P.; Chanda, J.; Mukhopadhyay, R.; Dasgupta, S.; Wießner, S.; Heinrich, G.; Das, A. Treasuring waste lignin as superior reinforcing filler in high cis-polybutadiene rubber: A direct comparative study with standard reinforcing silica and carbon black. *J. Clean. Prod.* **2021**, *299*, 126841.

(7) Staropoli, M.; Rogé, V.; Moretto, E.; Didierjean, J.; Michel, M.; Duez, B.; Steiner, P.; Thielen, G.; Lenoble, D.; Thomann, J.-S. Hybrid silica-based fillers in nanocomposites: Influence of isotropic/isotropic and isotropic/anisotropic fillers on mechanical properties of styrene-butadiene (SBR)-based rubber. *Polymers* **2021**, *13* (15), 2413.

(8) Ali, S. D.; Imiete, I. E.; Orlandi, M. E.; Castellani, L.; Hanel, T.; Zoia, L. Novel CNC/silica hybrid as potential reinforcing filler for natural rubber compounds. *J. Appl. Polym. Sci.* **2020**, *137* (5), 48332.

(9) Tadiello, L.; D'Arienzo, M.; Di Credico, B.; Hanel, T.; Matejka, L.; Mauri, M.; Morazzoni, F.; Simonutti, R.; Spirkova, M.; Scotti, R. The filler−rubber interface in styrene butadiene nanocomposites with anisotropic silica particles: morphology and dynamic properties. *Soft Matter* **2015**, *11* (20), 4022−4033.

(10) Scotti, R.; Conzatti, L.; D'Arienzo, M.; Di Credico, B.; Giannini, L.; Hanel, T.; Stagnaro, P.; Susanna, A.; Tadiello, L.; Morazzoni, F. Shape controlled spherical (0D) and rod-like (1D) silica nanoparticles in silica/styrene butadiene rubber nanocomposites: Role of the particle morphology on the filler reinforcing effect. *Polymer* **2014**, *55* (6), 1497−1506.

(11) Araujo-Morera, J.; Hernández Santana, M.; Verdejo, R.; López-Manchado, M. A. Giving a Second opportunity to tire waste: An alternative path for the development of sustainable self-healing styrene−butadiene rubber compounds overcoming the magic triangle of tires. *Polymers* **2019**, *11* (12), 2122.

(12) Hall, D. E.; Moreland, J. C. Fundamentals of rolling resistance. *Rubber Chem. Technol.* **2001**, *74* (3), 525−539.

(13) Wolff, S. Chemical aspects of rubber reinforcement by fillers. *Rubber Chem. Technol.* **1996**, *69* (3), 325−346.

(14) Alauzun, J.; Mehdi, A.; Reyé, C.; Corriu, R. J. Mesoporous materials with an acidic framework and basic pores. A successful cohabitation. *J. Am. Chem. Soc.* **2006**, *128* (27), 8718−8719.

(15) Karnati, S. R.; Oldham, D.; Fini, E. H.; Zhang, L. Application of surface-modified silica nanoparticles with dual silane coupling agents in bitumen for performance enhancement. *Constr. Build. Mater.* **2020**, *244*, 118324.

(16) Brinke, J.W.t.; Debnath, S.C.; Reuvekamp, L.A.E.M.; Noordermeer, J.W.M. Mechanistic aspects of the role of coupling agents in silica−rubber composites. *Compos. Sci. Technol.* **2003**, *63* (8), 1165−1174.

(17) Goerl, U.; Hunsche, A.; Mueller, A.; Koban, H. Investigations into the silica/silane reaction system. *Rubber Chem. Technol.* **1997**, *70* (4), 608−623.

(18) Wang, D.; Chen, S.; Chen, L.; Chen, B.; Ren, F.; Zhu, C.; Feng, J. Investigation and improvement of the scorch behavior of silica-filled solution styrene-butadiene rubber compound. *J. Appl. Polym. Sci.* **2019**, *136* (35), 47918.

(19) Ansarifar, A.; Azhar, A.; Ibrahim, N.; Shiah, S.; Lawton, J. The use of a silanised silica filler to reinforce and crosslink natural rubber. *Int. J. Adhes. Adhes.* **2005**, *25* (1), 77−86.

(20) Hashim, A.; Azahari, B.; Ikeda, Y.; Kohjiya, S. The effect of bis (3-triethoxysilylpropyl) tetrasulfide on silica reinforcement of styrene-butadiene rubber. *Rubber Chem. Technol.* **1998**, *71* (2), 289−299.

(21) Luginsland, H.-D.; Frohlich, J.; Wehmeier, A. Influence of different silanes on the reinforcement of silica-filled rubber compounds. *Rubber Chem. Technol.* **2002**, *75* (4), 563−579.

(22) Park, S.-J.; Cho, K.-S. Filler−elastomer interactions: influence of silane coupling agent on crosslink density and thermal stability of silica/rubber composites. *J. Colloid Interface Sci.* **2003**, *267* (1), 86−91.

(23) Chonkaew, W.; Minghvanish, W.; Kungliean, U.; Rochanawipart, N.; Brostow, W. Vulcanization characteristics and dynamic mechanical behavior of natural rubber reinforced with silane modified silica. *J. Nanosci. Nanotechnol* **2011**, *11* (3), 2018−2024.

(24) REN, H.; QU, Y.; ZHAO, S. Reinforcement of styrene-butadiene rubber with silica modified by silane coupling agents: Experimental and theoretical chemistry study. *Chin. J. Chem. Eng.* **2006**, *14* (1), 93−98.

(25) Castellano, M.; Conzatti, L.; Turturro, A.; Costa, G.; Busca, G. Influence of the silane modifiers on the surface thermodynamic characteristics and dispersion of the silica into elastomer compounds. *J. Phys. Chem. B* **2007**, *111* (17), 4495−4502.

(26) Zheng, J.; Han, D.; Ye, X.; Wu, X.; Wu, Y.; Wang, Y.; Zhang, L. Chemical and physical interaction between silane coupling agent with long arms and silica and its effect on silica/natural rubber composites. *Polymer* **2018**, *135*, 200−210.

(27) Suzuki, N.; Ito, M.; Yatsuyanagi, F. Effects of rubber/filler interactions on deformation behavior of silica filled SBR systems. *Polymer* **2005**, *46* (1), 193−201.

(28) Kütt, A.; Selberg, S.; Kaljurand, I.; Tshepelevitsh, S.; Heering, A.; Darnell, A.; Kaupmees, K.; Piirsalu, M.; Leito, I. pKa values in organic chemistry−Making maximum use of the available data. *Tetrahedron Lett.* **2018**, *59* (42), 3738−3748.

(29) Kaupmees, K.; Trummal, A.; Leito, I. Basicities of strong bases in water: a computational study. *Croat. Chem. Acta* **2014**, *87* (4), 385−395.

(30) Chen, T.; Brauer, G. Solvent effects on bonding organo-silane to silica surfaces. *J. Dent. Res.* **1982**, *61* (12), 1439−1443.

(31) McGovern, M. E.; Kallury, K. M. R.; Thompson, M. Role of Solvent ont the Silanization of Glass with Octadecyltrichlorosilane. *Langmuir* **1994**, *10*, 3607−3614.

(32) Osterholtz, F.; Pohl, E. Kinetics of the hydrolysis and condensation of organofunctional alkoxysilanes: a review. *J. Adhes. Sci. Technol.* **1992**, *6* (1), 127−149.

(33) Lobo, I. A.; Robertson, P. A.; Villani, L.; Wilson, D. J.; Robertson, E. G. Thiols as Hydrogen Bond Acceptors and Donors: Spectroscopy of 2-Phenylethanethiol Complexes. *J. Phys. Chem. A* **2018**, *122* (36), 7171−7180.

(34) Paul, A.; Thomas, R. Evidences for sulfur centered hydrogen bond with sulfur atoms as a donor in aromatic thiols and aliphatic thiols in aqueous solution. *J. Mol. Liq.* **2022**, *348*, 118078.

(35) Chiang, C.-H.; Liu, N.-I.; Koenig, J. L. Magic-angle cross-polarization carbon 13 NMR study of aminosilane coupling agents on silica surfaces. *J. Colloid Interface Sci.* **1982**, *86* (1), 26−34.

(36) Nair, D. P.; Podgorski, M.; Chatani, S.; Gong, T.; Xi, W.; Fenoli, C. R.; Bowman, C. N. The thiol-Michael addition click reaction: a powerful and widely used tool in materials chemistry. *Chem. Mater.* **2014**, *26* (1), 724−744.

(37) Miller, M.; Linton, R.; Maciel, G.; Hawkins, B. Characterization of silanol reactivity and acidity on octadecyl-bonded chromatographic supports by29Si solidstate nuclear magnetic resonance spectroscopy and surface titration. *J. Chromatogr. A* **1985**, *319*, 9−21.

(38) Kunc, F.; Balhara, V.; Sun, Y.; Daroszewska, M.; Jakubek, Z. J.; Hill, M.; Brinkmann, A.; Johnston, L. J. Quantification of surface functional groups on silica nanoparticles: comparison of thermogravimetric analysis and quantitative NMR. *Analyst* **2019**, *144* (18), 5589−5599.

(39) Derouet, D.; Forgeard, S.; Brosse, J. C.; Emery, J.; Buzare, J. Y. Application of solid-state NMR (13C and 29Si CP/MAS NMR) spectroscopy to the characterization of alkenyltrialkoxysilane and trialkoxysilyl-terminated polyisoprene grafting onto silica microparticles. *J. Polym. Sci., Part A: Polym. Chem.* **1998**, *36* (3), 437−453.

(40) Williams, M. L.; Landel, R. F.; Ferry, J. D. The temperature dependence of relaxation mechanisms in amorphous polymers and other glass-forming liquids. *J. Am. Chem. Soc.* **1955**, *77* (14), 3701−3707.

(41) Takino, H.; Nakayama, R.; Yamada, Y.; Kohjiya, S.; Matsuo, T. Viscoelastic properties of elastomers and tire wet skid resistance. *Rubber Chem. Technol.* **1997**, *70* (4), 584−594.

(42) Li, Y.; Han, B.; Wen, S.; Lu, Y.; Yang, H.; Zhang, L.; Liu, L. Effect of the temperature on surface modification of silica and properties of modified silica filled rubber composites. *Compos. - A: Appl. Sci. Manuf.* **2014**, *62*, 52−59.

(43) Berriot, J.; Montes, H.; Lequeux, F.; Long, D.; Sotta, P. Evidence for the shift of the glass transition near the particles in silica-filled elastomers. *Macromolecules* **2002**, *35* (26), 9756−9762.

Dual-silane pre-modified silica nanoparticles – Synthesis and interplay between chemistry, mechanical and curing properties of silica-rubber nanocomposites: Application to tire tread compounds

*Enzo Moretto[1], João P. C. Fernandes[1], Mariapaola Staropoli[1], Vincent Rogé[1], Pascal Steiner[2], Benoît Duez[2], Damien Lenoble[1], Jean-Sébastien Thomann[1]**

[1] Luxembourg Institute of Science and Technology, MRT department; 41 rue du Brill, L-4422 Belvaux, Luxembourg; jean-sebastien.thomann@list.lu

[2] Goodyear S.A, Avenue Gordon Smith, L-7750 Colmar-Berg, Luxembourg; benoit_duez@goodyear.com

Correspondence: jean-sebastien.thomann@list.lu

KEYWORDS: Silica, silane, silanization, filler interphase characterization, nanocomposite, tire tread.

Supporting Information

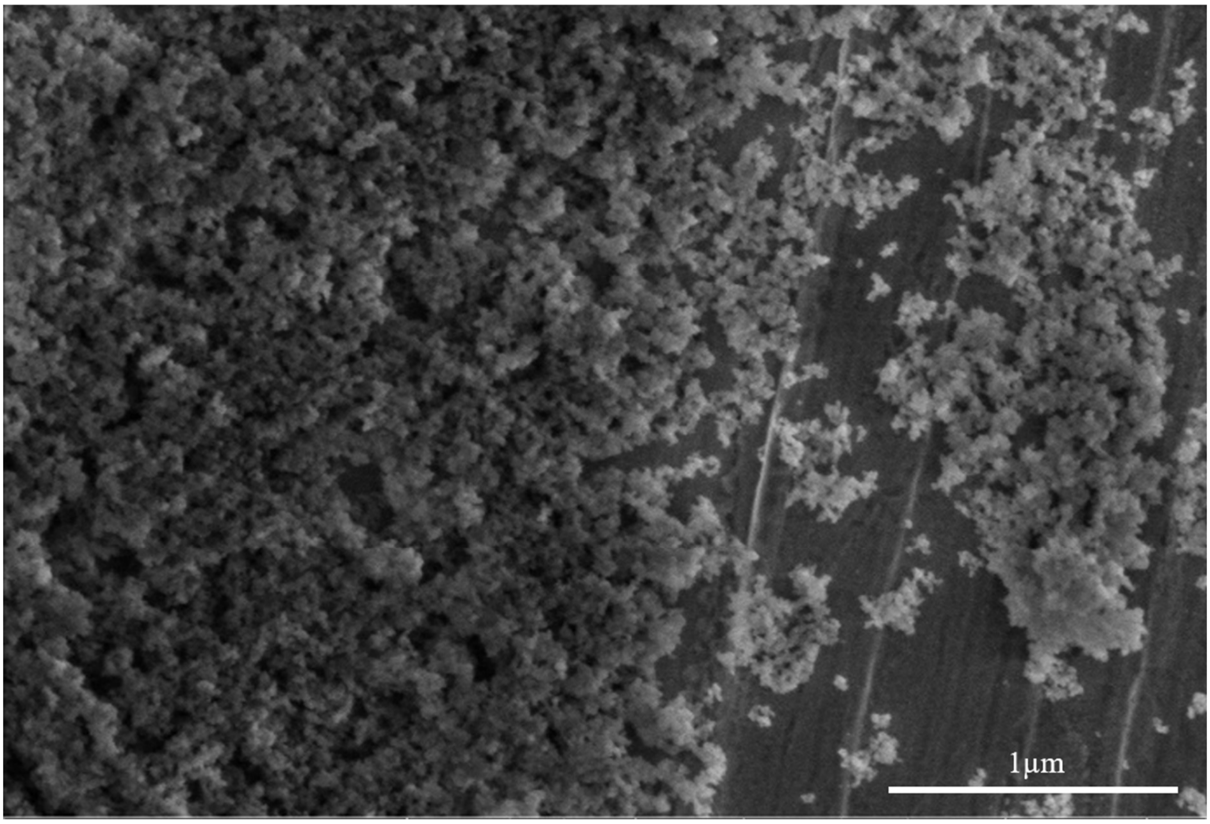

Figure S 1 - HDS precipitated silica under scanning electron microscope

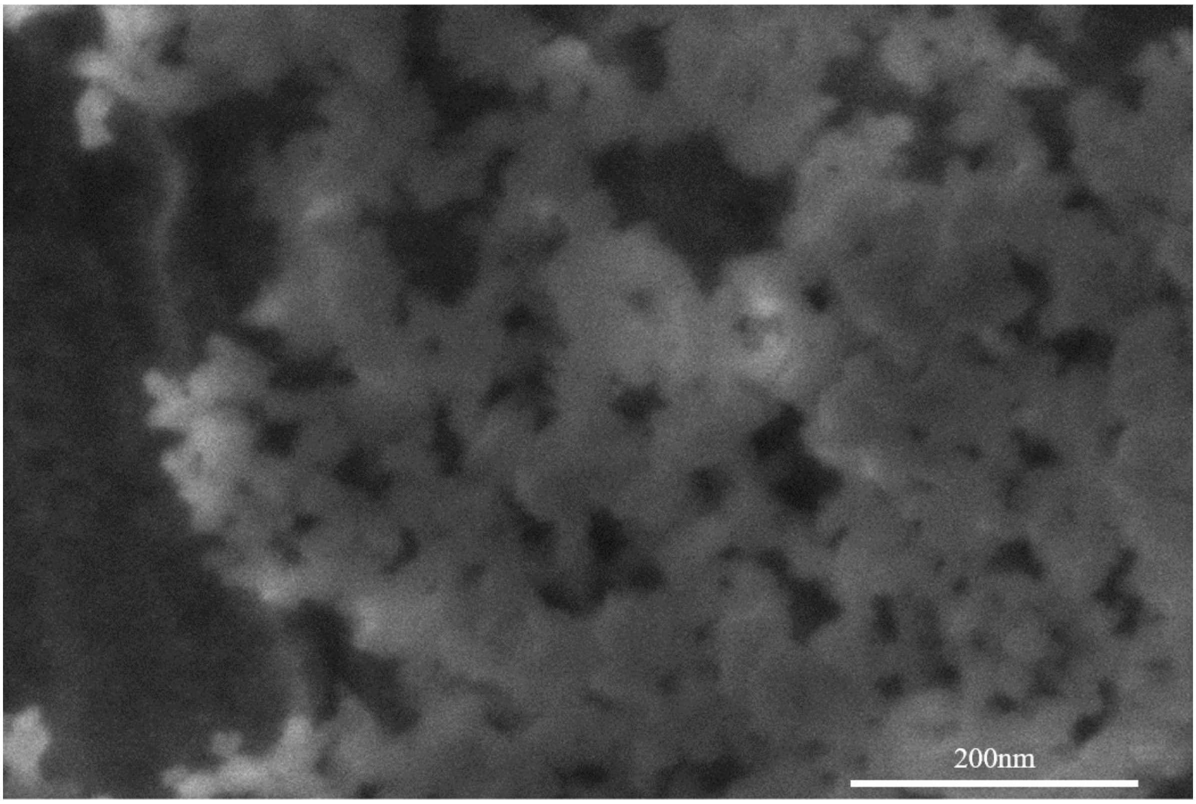

Figure S 2 - HDS precipitated silica under scanning electron microscope

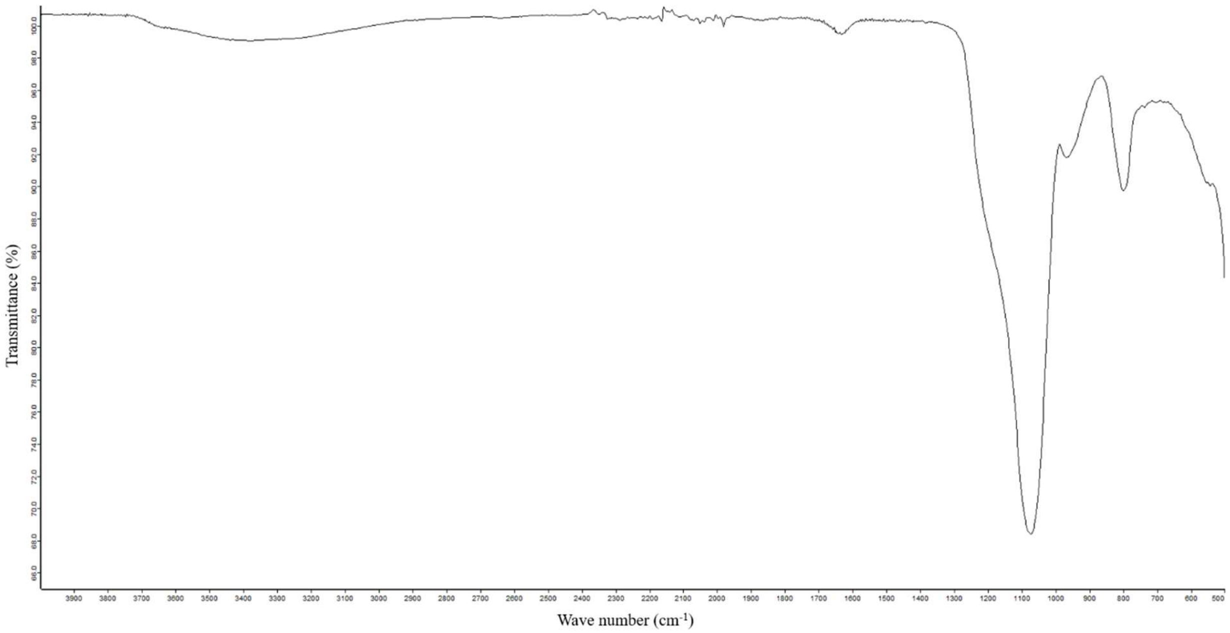

Figure S 3 - ATR infrared spectrum of HDS precipitated silica

Si-OH adsorption band : 3000-3800cm^{-1}

Si-O-Si adsorption band : 470, 800 and 1070cm^{-1}

Table S 1 - Storage modulus E', loss modulus E'' and tan(δ) of dual-silane silica rubber composite

		Storage modulus E'		Loss modulus E''		Tan δ	
		at 0°C (MPa)	at 60°C (MPa)	at 0°C (MPa)	at 60°C (MPa)	at 0°C	at 60°C
HDS control		13.39±0.60	8.35±0.34	2.75±0.19	0.63±0.04	0.205±0.005	0.076±0.002
C3SH	C6	13.63±0.16	6.37±0.12	3.23±0.07	0.47±0.01	0.237±0.002	0.074±0.001
C3SH	C12	10.90±0.075	5.63±0.059	2.29±0.05	0.40±0.03	0.210±0.003	0.070±0.005
C3SH	C18	9.963±0.27	5.10±0.091	1.96±0.13	0.38±0.01	0.198±0.008	0.074±0.002
C11SH	C6	8.933±0.41	5.242±019	1.67±0.08	0.31±0.01	0.187±0.001	0.060±0.003

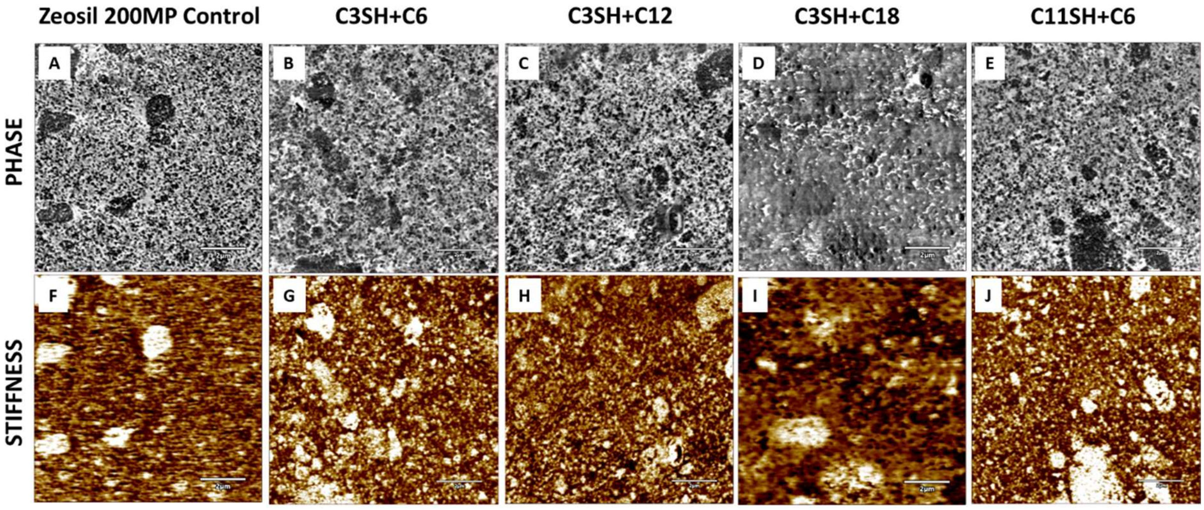

Figure S 4 - AFM phase and stiffness contrast images in areas of 10x10 µm² of the different composite materials.

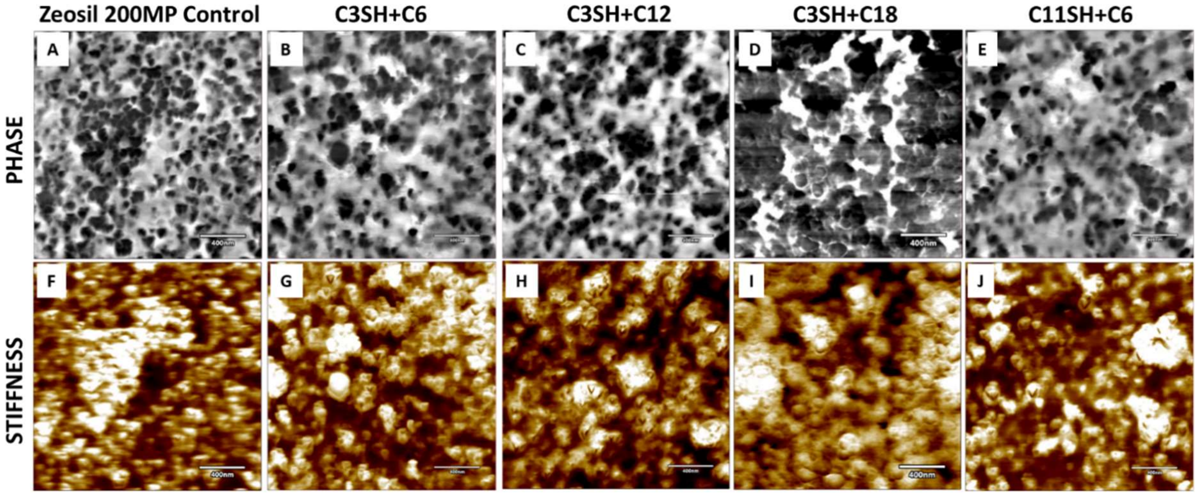

Figure S 5 - AFM phase and stiffness contrast images in areas of 2x2 µm² of the different composite materials

Chapter 3 - Interplay of regio-selectively modified dendritic silica particles with styrene-butadiene rubber: The route towards better tires with lower rolling-resistance and higher grip

The third chapter, *"Interplay of regio-selectively modified dendritic silica particles with styrene-butadiene rubber: The route towards better tires with lower rolling-resistance and higher grip"* discloses the synthesis and full characterization of a porous dendritic silica particle with a regio-selective silanization, as well as the implementation of the new filler in a tire tread compound.

It was shown in the introduction and chapter 2 that the filler-filler interaction and filler-rubber interaction dictate the reinforcement and viscoelastic behavior of a rubber composite. Filler-filler interaction is affected by the filler dispersion and its capability to form a percolating network in order to maximize its effect on rubber. The filler-rubber interaction arises from the chemical nature of the filler surface and how it interacts with the polymer chain. Silane coupling agent are used to covalently bond filler and rubber, and thus increase their mutual interaction.

To get better performances than state-of-the-art tire tread rubber that uses percolating fractal fillers, the key is to change the filler network dynamic under deformation, in order to improve the traction and rolling resistance simultaneously. With that in mind, in chapter 3 is presented the first synthesis of large pores dendritic silica particle with a regio-selective silanization, and the study of the dynamic mechanical properties of the new dual-filler rubber compound formed by this particle and a precipitated fractal silica.

Cutting-edge technique such as TEM-EDS and Helium Ion Microscope coupled with Secondary Ion Mass Spectrometer (HIM-SIMS) enabled to confirm the regio-selective grafting of two different silane over a 110 nm dendritic porous silica particle. RMDS composite showcases unique properties. Indeed, it was demonstrated that this newly synthesized filler, thanks to its morphology and surface functionalization, presents better rolling resistance and fatigue properties than a state-of-the-art industrial tire tread compound. This is due to its ability to resist dislocation during mechanical solicitation, unlike fractal aggregates. Nonetheless, RMDS composite shows insufficient wet grip and reinforcing properties, because of its lack of filler-filler interaction. To remedy that, the addition of a small amount of a smaller, fractal filler proved to be efficient, and the dual-filler system presents the advantages of both fillers without their drawbacks. Beyond the technical advance, this result brings more knowledge in the field of reinforced rubber to better understand the reinforcement mechanism at stake in a composite and how fillers can be tuned to target specific properties.

Chemical Engineering Journal 461 (2023) 141964

Contents lists available at ScienceDirect

Chemical Engineering Journal

journal homepage: www.elsevier.com/locate/cej

Interplay of regio-selectively modified dendritic silica particles with styrene-butadiene rubber: The route towards better tires with lower rolling-resistance and higher grip

Enzo Moretto [a,c], Charlotte Stoffels [a], Carlos Eloy Federico [a], Vincent Rogé [a], Mariapaola Staropoli [a], Iikpoemugh Elo Imiete [a], Jean-Nicolas Audinot [a], Pascal Steiner [b], Benoît Duez [b], Damien Lenoble [a], Jean-Sébastien Thomann [a,*]

[a] *Materials Research and Technology Department, Luxembourg Institute of Science and Technology, 41 Rue du Brill, L-4422 Belvaux, Luxembourg*
[b] *Goodyear S.A, Avenue Gordon Smith, L-7750 Colmar-Berg, Luxembourg*
[c] *Department of Physics and Materials Science, University of Luxembourg, L-4365 Esch-sur-Alzette, Luxembourg*

ARTICLE INFO

Keywords:
Mesoporous silica
Silica-rubber composite
Silanization
Regio-selective silanization
SIMS
Elemental mapping

ABSTRACT

The current study presents for the very first time to our knowledge the synthesis, characterization, and application of regio-selectively modified dendritic silica particles (RMDS) in tire rubber composites. So far, no study has ever reported mesoporous silica bringing greater mechanical properties than small fractal precipitated silica. With mechanical testing (DMA, tensile strength) and advanced imaging (TEM-EDS, HIM-SIMS, micro-CT), it was demonstrated that dendritic particles enable superior mechanical reinforcement of rubber-based nanocomposites without any drawback as usually reported with fractal fillers. On one side, their modified porous surface mimics the porous aggregates formed by classic fillers, enabling the rubber chains to permeate the pores and closely interact with the particles. On the other side, unlike fractal fillers, RMDS consist of single particles instead of aggregates, and therefore do not suffer as much from the Payne effect and irreversible dislocations under mechanical solicitations. Also, the excellent dispersibility of RMDS allows to combine them with small amount of fractal filler. Dual filler composite shows superior mechanical performances versus materials using one filler family, leading to higher reinforcement, better traction and rolling resistance indicators. The use of porous particles as "unbreakable" fillers for rubber with a small amount of fractal silica as additive fillers paves the way for novel reinforcing dual-filler systems to be used in disruptive tires technology.

1. Introduction

For technical applications, polymers are almost always combined with fillers to drastically improve their performances, as neat polymer properties are often unsatisfactory. For the reinforcement of rubber-based tires, silica has been used for decades and since then many advances in this technology have been made. The first and major one has been the use of organosilanes that enable better dispersion and interaction between the mineral polar hydrophilic material silica and the organic hydrophobic polymer matrix. Today, many different strategies aiming at further rubber reinforcement from fillers have been investigated. Original materials like clays [1], or graphene oxide [2] have been the topic of extensive research and brought new functionality to composite materials. Other strategies focus on the filler morphology and its effect on the composite properties are well investigated [1,3,4]. When it comes to the morphology of silica particles, mesoporous structures are a vast area of research. Since the first filed patent [5] in 1971, and the emergence of MCM-41[6] and SBA-15 structures [7], research in this area has flourished in wide variety of applications as scientists have recognized the potential of these structures. Initially seen as potent molecular sieves, their large specific surface area, the variety of structures, size, and synthesis processes opened the way for a wide range of applications. Mesoporous silica has been reported for drug delivery systems [8,9], contrast enhancing agent carriers in medical imagery [10], water depollution [11], gas separation [12], column chromatography [13], or catalysis [14,15]. More specifically for rubber materials, porous systems have been used to enhance silicon thermal and optical properties [16], or as antioxidant release in styrene-butadiene rubber

---

* Corresponding author.
E-mail address: jean-sebastien.thomann@list.lu (J.-S. Thomann).

https://doi.org/10.1016/j.cej.2023.141964
Received 14 October 2022; Received in revised form 11 January 2023; Accepted 14 February 2023

(SBR) composites [17]. For their mechanical reinforcement, the interest in mesoporous silica is driven by the high surface area that leads to strong interactions between fillers and the polymeric matrix. Indeed, the reinforcing effect of fillers relies on its ability to interact with the polymer and to change the chains dynamic. On top of its ability to bond with the matrix, the percolation and the formation of a filler network use to transmit stresses and to trap rubber in between particles. When it comes to percolation, the particle size and shape play a major role. It has been shown that silica forming fractal-shaped aggregates have a lower percolation threshold than spherical colloidal particles [18]. Indeed, fractal-shaped clusters expose a greater surface area and trap more polymer at lower filler loading. The same reasoning applies to mesoporous silica particles because porosity provides a high surface of interaction due to the permeation of the polymer inside it. One limitation of fractal fillers is the irreversible deformation and reorganization caused by the mechanical solicitation of fractal aggregates, leading to energy dispersive phenomenon known as Payne and Mullins effect [19–21]. The hypothetical expected benefit of porous silica particles over fractal fillers can be described as follows. The porous particles are not subjected to irreversible mechanical deformation, unlike small silica particles aggregates of comparable surface, while still endorsing the role of crosslink nodes and reinforcing agents. This may reduce the rolling resistance behavior of such composites, whilst providing properties such as traction to such tire tread materials. So far, most studies have used the ordered, narrow pore size (2–3 nm) MCM-41 mesoporous silica, with or without surface modification, in combination with natural rubber (NR) [22], styrene-butadiene rubber SBR [23], styrene-butadiene and nitrile-butadiene rubber (SBR-NBR) [24], and ethylene-propylene diene monomer rubber (EPDM) rubber [25], and have shown reinforcement. However, there is no clear perspective about the role played either by the porous structure features or by the chemical modification of the silica surface on the composite properties. Indeed, for pores as small as the one of MCM-41 (2–3 nm channel diameter), no study relates that rubber polymer chains of 10 000 g/mol – 100 000 g/mol permeate inside pores under classic rubber dry mixing conditions and generate reinforcement. Studies achieving the polymer confinement inside mesopores used either high pressures [26], super-critical CO_2 as solvent for the monomer [27], low molecular weight resins [28] or modified silica [29,30] that are infiltrated with monomers upon further vulcanization. The use of larger pore sizes and larger structures [31,32] or in combination with silanization of silica foam [33] has proven to be an efficient way to reinforce epoxy resin. Unfortunately, the cluster size is too large for rubber reinforcement. Another critical physical aspect of the polymer reinforcement with silica is the fillers dispersion and their coupling to the matrix. The usual strategy is to graft organosilanes on particles to increase their hydrophobicity and to enable their bonding to the polymer chains. In our previous work [34], the strategy of a silica pre-treated with two different silane for reinforcing rubber was reported. The mercaptosilane was used as the coupling agent, and the alkylsilane was designed to mitigate the mercaptosilane reactivity and to enhance the silica dispersion. In the present work, we achieved a unique regio-selective silanization of dendritic silica particles featured by large pores size. The mercaptosilane is co-condensed in the frame of the silica during the particle growth, and an alkylsilane is grafted on the periphery of particles by preventing it to access inside the pores with the soft template already in place. A few mesoporous silica with selective dual functionalization have been reported [35,36], and all with pore below 10 nm, which are more convenient to control and prevent silane migration inside the pores. The full characterization of the newly synthesized regio-selectively modified dendritic particles (RMDS) and its application to tire rubber compounds are reported here. Furthermore, the regio-selective silanization of the porous particles was confirmed via their direct elemental mapping with the help of a Helium Ion beam Microscope (HIM) coupled with a Secondary Ion Mass Spectroscopy (SIMS). After incorporation into an SBR-BR rubber matrix and the characterization of its mechanical properties, this newly synthesized filler was compared to a fractal commercial filler used in an industrial tire tread compounds provided by Goodyear. RMDS provides reinforcement with better fatigue resistance and rolling resistance of tire tread rubber composites. The permeation of polymer into the mesopores and the absence of particles dislocations (unlike the aggregates of fractal fillers) leads to a low hysteresis and a reduced Payne effect. Only a very low number of cavities are detected by computed micro-tomography after cycling the RMDS compounds with tensile fatigue testing. However, the excellent dispersibility of the filler, its size, and its spherical shape prevent sufficient rubber reinforcement to reach the performance level of HDS 200MP. Thus, adding a small amount of fractal fillers, fills the gaps between RMDS particles and increases the filler-filler interaction. This new dual-filler system leads to significantly improved properties of rubber-based nanocomposites in terms of reinforcement, fatigue resistance, wet traction and rolling resistance indicators.

2. Experimental section

The list of chemicals used in the experimental section and the description of the equipment and measurements methodologies used for the synthesis and characterization of silica particles and silica-rubber composites are available in the **experimental section of the Supporting Information.**

2.1. Synthesis of regio-selectively modified dendritic silica particles

The synthesis of regio-selectively modified dendritic silica particles is derived from the synthesis of stellate mesoporous silica particles previously reported [37]. In an Orb Pilot 50 L reaction vessel, 34.7 g of triethanolamine and 192.0 g of hexadecyltrimethylammonium p-toluene sulfonate are dissolved in 10.0 L of de-ionized water. The solution is heated at 80 °C and mixed for 120 min. Then, 1458.0 g of tetraethoxysilane (TEOS) are added. The reaction starts and is kept at 80 °C under stirring until the end of the process. 15 min after the addition of TEOS, 166.3 g of 3-mercaptopropyltriethoxysilane (MPTES) are added to the reaction vessel. 120 min after the addition of TEOS, 167.3 g of hexyltrimethoxysilane (C6) are added. The reaction is then carried out for another 120 min at 80 °C under stirring. At the end of the reaction, stirring is stopped and the silica particles are let to settle at the bottom of the reaction vessel. The supernatant above the settled silica is removed from the vessel via a pump and 15 L of de-ionized water are added. Silica and water are mixed for 12 h at room temperature, stirring is stopped and the silica particles are let to settle at the bottom of the reaction vessel. Again, the supernatant is removed, and 15 L of ethanol are added. Silica and ethanol are mixed for 12 h. at reflux temperature under stirring. Finally, stirring is stopped and silica particles are let to settle at the bottom of the reaction vessel. The ethanol supernatant is removed. The highly concentrated silica particles in ethanol are then separated by centrifugation (4700 g for 1 h). Regio-selectively functionalized stellate silica is then dried in an oven at 110 °C for 48 h and stored in a sealed container. Additionally, Stöber particles, non-modified stellate mesoporous silica particles and bromine-labelled regio-selectively modified dendritic silica particles have been synthesized. Their respective synthesis protocol is available in **Supporting Information**. Stöber particles consist in spherical and non-porous colloidal silica of a controlled size (here with a diameter of 110 nm). Together with non-modified stellate mesoporous silica, these particles have been used to assess the impact of morphology and silanization onto the rubber composite properties. Bromine-labelled regio-selectively modified dendritic silica particles have been synthesized for imaging purposes.

2.2. Silica-rubber composites fabrication

Silica particles were incorporated in a SBR-BR rubber matrix for the fabrication of silica-rubber composites. The ingredients and recipe for the fabrication of silica-rubber composites can be found in **Table S1 of**

the Supporting Information. The silica composition of the composites is summarized in **Table S2 of the Supporting Information**.

3. Results and discussions

3.1. Synthesis and characterization of regio-selectively modified dendritic silica (RMDS)

The dendritic silica particles were synthesized via a surfactant soft-templating sol–gel method. During such a process, the silica precursor, usually TEOS, polymerizes via hydrolysis-condensation to form the silica particles. The soft template surfactant is forming micelles whose shape and size are dictated by concentration and temperature conditions. The inter-molecular interactions between the surfactant and silica oligomers allow for the silica frame to grow around the surfactant micelle. This phenomenon causes the growth of the dendritic porous silica. Advantage was taken of this process to purposely graft silanes at specific location. First, the mercaptosilane MPTES was co-condensed with TEOS during the growth of the particles. This approach ensures its uniform distribution on the silica frame. At this stage, the pores of particles are still filled with the surfactant. Taking advantage of these circumstances, grafting of the alkylsilane is the next logical step to ensure this silane is mainly connected to the periphery of silica particles. After synthesizing the silica particles, the surfactant is removed to reveal the pores. Fig. 1 below illustrates schematically the synthesis of the regio-selectively modified dendritic silica.

The reaction conditions and the concentration of mercaptosilane were carefully chosen to ensure that the co-condensation of the mercaptosilane did not affect the size nor the structure of particles. Indeed, it has been reported that the use of organosilane may disturb the inter-molecular interactions of surfactant molecules or the silica-micelles interaction. This has been described by Möller et al. for the synthesis of fiber-like mesoporous silica [38]. The step of alkylsilane grafting is carried out as a simple post-growth modification of the particles. The newly synthesized regio-selectively modified dendritic silica particle were fully characterized and results are shown in **Figure S1 of the Supporting Information**.

Transmission Electron Microscope (TEM) images in Fig. S1a. and b. show that the dendritic porous structure is retained despite the introduction of MPTES in the silica matrix. TGA curves display the mass-losses associated with volatiles desorption (below 100 °C), surfactant traces desorption and pyrolysis at 240 °C and silane pyrolysis at around 500 °C-550 °C. It has been reported that alkyl chains are more stable at a higher temperature than mercapto moieties, hence different pyrolysis temperature are observed [38]. TGA data of un-modified stellate silica and mercapto-functionalized (Stellate-SH) are presented in **Figure S2 of the Supporting Information**. The lack of peak at about 130 °C on the dTGA spectrum of silanized silica particles reveals different de-hydroxylation mechanisms when compared to the non-modified mesoporous silica ones. This observation can be explained by the lower amount of silanol left to be de-hydroxylated on modified silica particles after their consumption by silanization. Regio-selectively modified dendritic silica share the same two peaks at respectively 370 °C and 500 °C that are attributed to the pyrolysis of mercapto groups and alkyl chain (propyl and hexyl), respectively. The intensity of the second peak is higher in the case of the regio-selectively silanized silica because of the grafting of hexyltrimethoxysilane, increasing the amount of alkyl chains present within the material. In the case of non-modified stellate silica particles, two peaks can also be observed, even though the first one is centered around a lower temperature than in the case of modified silica. Those two peaks are assigned to the pyrolysis of the residual surfactant. The co-condensation of MPTES in the stellate frame leads to the addition of 3.8 % of mass. The grafting of hexyltrimethoxysilane adds 5.7 % of additional mass. Overall, about 9.5 % of the mass of RMDS particles correspond to the grafted silanes. The sharp drops in mass observed at 750 °C in TGA and dTGA curves of Fig. S1**(c) and S2** result from the gas switch from pure N_2 to N_2/O_2 mixture at 750 °C. It leads to the oxidation of the remaining organic matter. Covalent bonding of silane is confirmed by ^{29}Si solid state NMR in Fig. S1**d.**, with the presence of T groups between −50 ppm and −70 ppm. Nitrogen adsorption porosimetry results are presented in Fig. S1**e. and S1f**. The introduction of mercaptopropyl moieties reduces the pore volume and specific surface area, but not as much as the addition of hexyl chains, which seems to drastically reduce the adsorption of the gas molecules to the mesoporous surface, as proven by the decrease of pore volume from 2.61 cm^{-3}/g to 1.54 cm^{-3}/g. The pore size distribution was calculated from the nitrogen adsorption data using the DFT model [39]**.** It shows wide open pores with a diameter of about 28 nm, close from sizes observed by SEM (see **Figure S12, 19** nm ± 6 nm). XRD characterization of RMDS material was not carried as it does not display an organized "crystalline-like" structure.

3.2. Dendritic silica regio-selective modification characterization

The regio-selective grafting of the mercaptosilane within the silica frame and the alkylsilane on the out-skirt of the particles has been characterized by Scanning Transmission Electron Microscopy coupled to an Energy Dispersive X-rays Spectroscope (STEM-EDS) and Helium Ion Microscope coupled with a Secondary Ion Mass Spectrometer (HIM-SIMS). STEM-EDS micrographs and as well as Scanning Electron Microscopy (SEM) images are shown in Fig. 2**.** Image (b) shows sulphur atoms in green. Compared to the particles structure depicted in (a), it can be confirmed that sulfur is distributed evenly across the silica particles and no segregation can be observed from these images. SEM images (c) et (d) offer another perspective on the silica particle size distribution and porous structure.

To investigate the consequences of the two-steps silanization process of dendritic silica and the spatial distribution of the alkylsilane on the porous silica particles, an alternative regio-selectively modified dendritic silica was synthesized by substituting the hexyltrimethoxysilane by 7-bromoheptyltrimethoxysilane (see synthesis protocol in

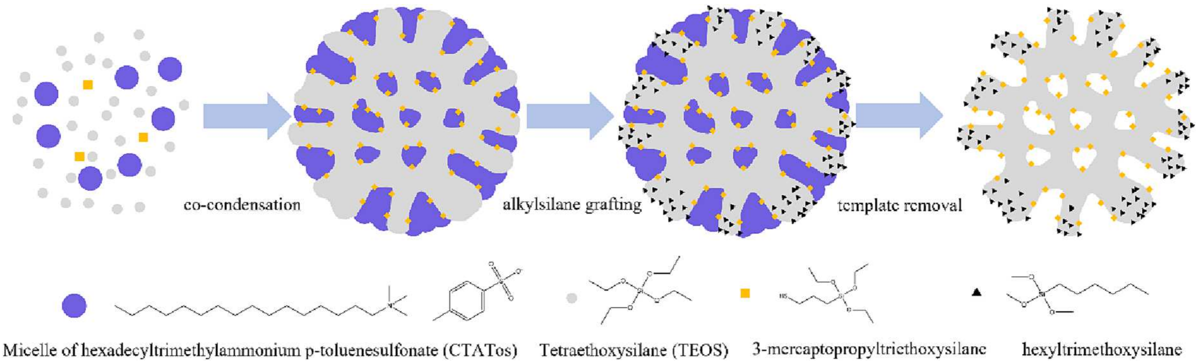

Fig. 1. Schematic view of the regio-selectively modified dendritic silica particles (RMDS).

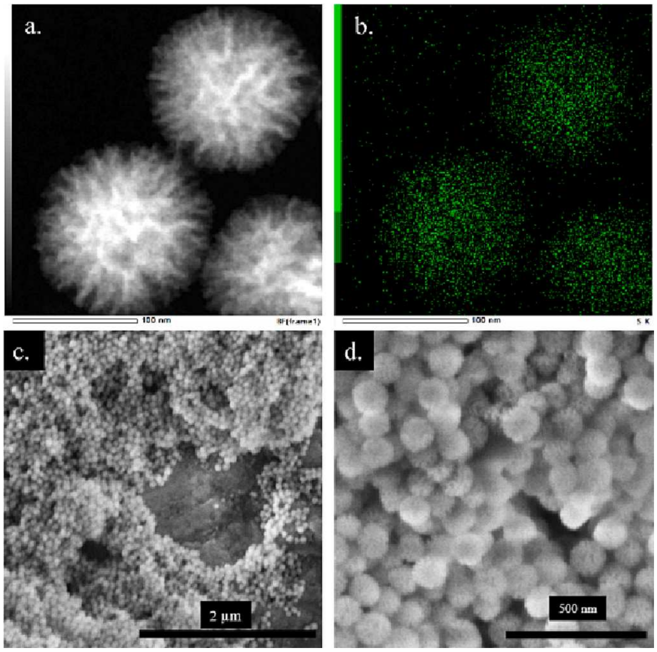

Fig. 2. STEM bright field (BF) images of regio-selectively modified dendritic silica particles (a) and EDS micrographs of sulphur (b), and SEM images (c,d).

Supporting Information). This silane was chosen for its similar size and structure, to mimic as much as possible the original hexyltrimethoxysilane. The bromine atom is used as a labelling agent as carbon alone would not enable to discriminate mercapto- from alkylsilane since both contain carbon atoms.

The distribution of bromine across the silica was mapped by elemental mapping of the particles by nano-Secondary Ion Mass Spectroscopy (SIMS) using a Helium Ion Microscope coupled with a SIMS detector. Fig. 3 display oxygen (^{16}O), carbon (^{12}C–^{12}C), and bromine (^{79}Br) distribution. Larger field of view images are shown in **Figure S3** **of Supporting Information**.

Oxygen mapping allows to clearly distinguish the silica particles. The distribution of carbon across the particles is homogeneous and in agreement with the TEM-EDS images. This is to be expected due to the co-condensation of the mercaptopropyl silane during the particle's growth. Despite the low concentration of bromide per molecule, and by voxel sputtered, the SIMS mapping shows the decrease of bromine density inside particles. Especially for isolated particles, a distinctive crown of bromine can be seen. Similar materials architecture have been characterized by Z-contrast STEM, [35]or by porosimetry and fluorescence labelling of reactive moieties [36]. This is the first direct imaging characterization ever reported for multifunctional porous silica particles.

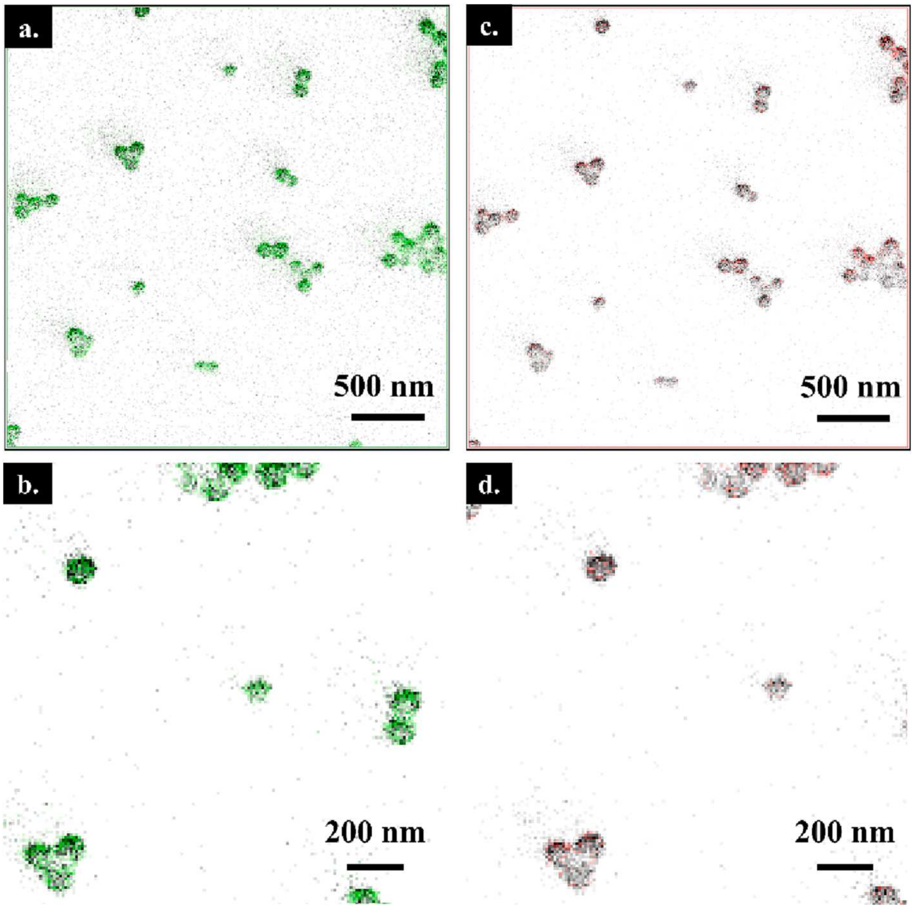

Fig. 3. HIM-SIMS elemental mapping of regio-selectively modified dendritic silica: oxygen (grey)/carbon (green) overlap (a, b), oxygen (grey)/bromine (red) overlap (c, d).

3.3. Characterization of silica-rubber composites and their mechanical properties

3.3.1. Effect of particle morphology and functionalization on rubber properties

The effect of silica fillers, and fillers in general, on a polymer matrix is a result of the four main ways the particles interact with the polymer chains, and how their dynamic is affected by these interactions [40–42]. The filler-filler interaction of silica is dependent on the hydrogen bonding of particles, which dictates how fillers interact, and is responsible for the aggregation of the particles. These interactions may be classified in two types. First, the low strain reversible interaction is responsible for reinforcement. It is assessed by the measurement of the drop of storage modulus at low strain, i.e. the Payne effect. This can be directly correlated to the rolling resistance and wet grip properties of a rubber compound [43]. Second, the high strain irreversible interaction is characterized by the Mullins effect, when a compound is deformed beyond a previous maximum. This effect can also include phenomenon such as filler-polymer debonding or crack initiation and propagation [44]. Moreover, fillers and polymer can interact in two ways, being first the steric hindrance of the particles over the polymer chain, resulting from the network of fillers trapping rubber, and from the covalent bonding of fillers with polymer when a coupling agent like mercapto organosilanes is used. Both are responsible for the reinforcement of the material. In a rubber compound, all these interactions work together and ultimately drive the mechanical properties of polymer-based nanocomposites. Consequently, the filler size and specific surface area, loading level, and surface modification are key parameters that will affect how and how much fillers interact with themselves and with the polymer chains. Fractal precipitated silicas like HDS 200MP are a gold standard and are commonly used in tire tread compounds. It consists in 10 nm primary particles in the form of large agglomerates (200 μm) **(see Figure S4 of Supporting Information)** that form a percolating network made of fractal shaped aggregates of medium size (50–100 nm) once mixed in the rubber (see **Figure S4 c and d**). This kind of silica is silanized in-situ by the addition of liquid organosilanes during the rubber mixing process. This filler reveals high interaction with the polymer thanks to the interaction with the trapped rubber within the fractal structure and its silanized surface. One limitation of such a filler architecture is the susceptibility to dislocations and breaks under mechanical stress, which increases hysteresis and impairs its reinforcing properties. It is important to note that the rubber recipe used in the present work is optimized for this kind of filler.

To identify the potential benefit of regio-selectively modified dendritic silica fillers, the effect of the filler morphology and its chemical modification were first investigated. Non-functionalized Stöber and stellate silica were used to show the impact of the porous structure and functionalization on the dispersion of fillers and on the mechanical properties of composites. Fig. 4 below presents the results of tensile test at break, the reinforcing index, and cyclic tensile test performed at 70 % of each sample maximum elongation. The reinforcing index is calculated as the ratio of the modulus at 150 % strain divided by the modulus at 50 % strain.

The non-porous and non-modified Stöber silica composites show the overall worst properties, with no strain hardening in tensile testing, low moduli and reinforcing index of 2.13, as well as the lowest stress at break of about 4 MPa. This composite is the only one unable to withstand>5 tensile cycles upon breaking. Non-modified stellate silica also displays no strain hardening and has an even lower reinforcing index of 1.77 despite its higher stress at break. This compound is capable of very high elongation, almost 800 % strain, and thus reach higher ultimate stress than Stöber particles. Interestingly, at low strain (below 25 %), the non-modified stellate particles provide the composite with a high strength (see Fig. 4**a.**), with a steeper increase of the strength compared to other samples. The porous structure seems to give an advantage over the non-porous Stöber particles in terms of ultimate properties and fatigue

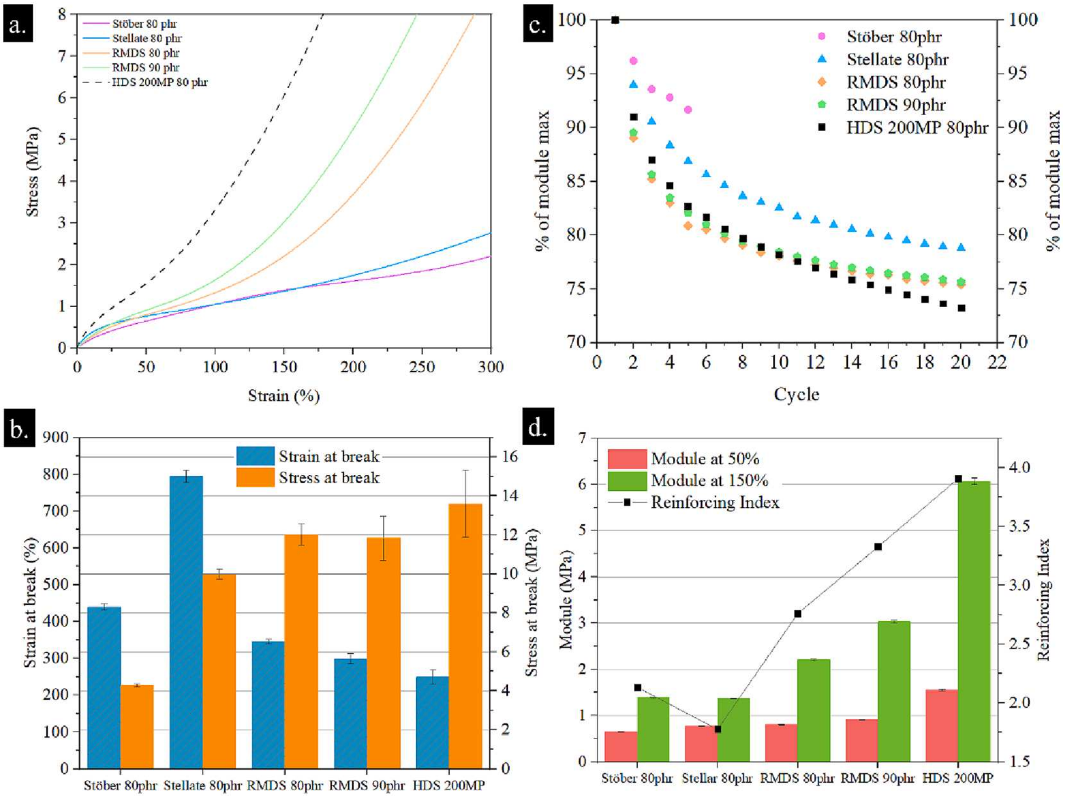

Fig. 4. Stress/Strain curves (a), evolution of maximum strength under cyclic tensile test (b), ultimate stress and strain at break (c) and reinforcing index (d) of composites materials.

resistance, as Stellate silica compounds show the lowest loss of strength over tensile cyclic testing. Without any coupling agent, silica-rubber phases are not efficiently crosslinked. In the case of Stöber or non-modified Stellate silica, only a linear deformation is observed after the initial deformation below 75 % strain. It can be suggested that the low-strain reinforcing effect of non-modified stellate silica arises from the hydrogen bonding of the bare silica surface. As RMDS contains about 9.5 % of silane (as reported in Fig. S1**c**.), the amount of silica for a given mass of filler is lower than for other pure silica fillers, especially HDS 200MP. To compensate this, 90 phr samples of pure RMDS on one side, and HDS 200MP on the other side, were tested. Results in Fig. S10**a** show that the tensile behavior of HDS 200MP silica-rubber samples is slightly worsen from 80 to 90 phr. The 90 phr HDS 200MP composite behaves similarly to the 70 phr sample. Graph b. of **Figure S10**, shows that the ultimate tensile properties are marginally improved by the addition of 10 phr from 80 to 90 phr. Based on these results, we concluded that the addition of 10 phr of HDS 200MP above 80 phr is marginally beneficial when the mechanical properties of the composite are considered. Indeed, the material reaches the percolation threshold at around 80 phr of HDS 200MP silica. STEM images in **Figure S11** support the conclusion that 80 phr is the optimal loading level for HDS 200MP, as the dispersion state is slightly worse at 90 phr. This leads to select HDS 200MP 80 phr as our reference sample. Unlike the two previous particles, RMDS silica shows strain hardening and has a higher reinforcing index of 2.76 and 3.32 at 80 phr and 90 phr respectively, as well as good ultimate properties, with ultimate strength of 12 and 11.8 MPa, respectively. The porous structure and regio-selective modification of the dendritic silica do provide obvious benefits over non-porous and non-modified porous silica. Though the additional 10 phr increases the reinforcement of the polymer, it does not compensate the mechanical properties discrepancy observed with the HDS 200MP fractal filler system. Dynamic Mechanical Analysis (DMA) was performed to further investigate the filler-filler interaction and understand the difference of behavior of RMDS particles versus the fractal HDS 200MP filler system. Results are presented in Fig. 5 below. The corresponding storage modulus E’ at 30 °C measured by DMA are displayed in **Figure S6 of Supporting Information.**

The amplitude of the tan δ peak is reflecting the chain mobility of a polymer reaching a maximum at the glass transition T_g. In the case of filled polymers where the chain dynamic is restricted close to the filler particles, the tan δ peak amplitude is lowered as the polymer chain mobility is reduced. In the case of Stöber silica composites, the limited dispersion and absence of functionalization prevent significant interaction between fillers and polymer chains, resulting in high tan δ peak, similar to unfilled SBR. [45] Tan δ also characterizes the tendency of rubber to lose energy at a given mechanical solicitation frequency. According to the Williams-Landel-Ferry [46] relationship of the time–temperature equivalence, high temperatures are equivalent to low frequency and low temperature to high frequency. In the present case tan δ at 0 °C serves as the indicators of traction performances, and at 60 °C, it represents the rolling resistance of the composites [47,48]. Ideally, high energy losses are desired for traction and breaking, and minimal losses are targeted to reduce rolling resistance. In the case of Stöber composite the filler-polymer interaction is so weak that aggregates are barely affected by the composite deformation which is corroborated by the height of the tan δ peak, translating the high mobility of the polymer chains. The low level of Payne effect is another element explaining the lack of reinforcement. Indeed, the amount and size of aggregates do not lead to a reinforcing percolating network. Fig. 5**d** shows the results obtained for the four different types of silica here described at 80 phr filling degree with corresponding fitting curves. The plot shows a more pronounced Payne effect for the sample HDS 200 MP followed respectively by Stellate 80 phr, RMDS 80 phr and Stöber 80 phr. The same trend is observed for the modulus at dynamic strain amplitudes smaller than 1 %. The decay for the different types of silica indicates that in the case of HDS 200 MP the fractal particles are more prone to form aggregates than the other silica fillers here studied. These aggregates are subject to strain-induced breakage that leads to a pronounced decay of E' in the dynamic strain range studied. An interesting

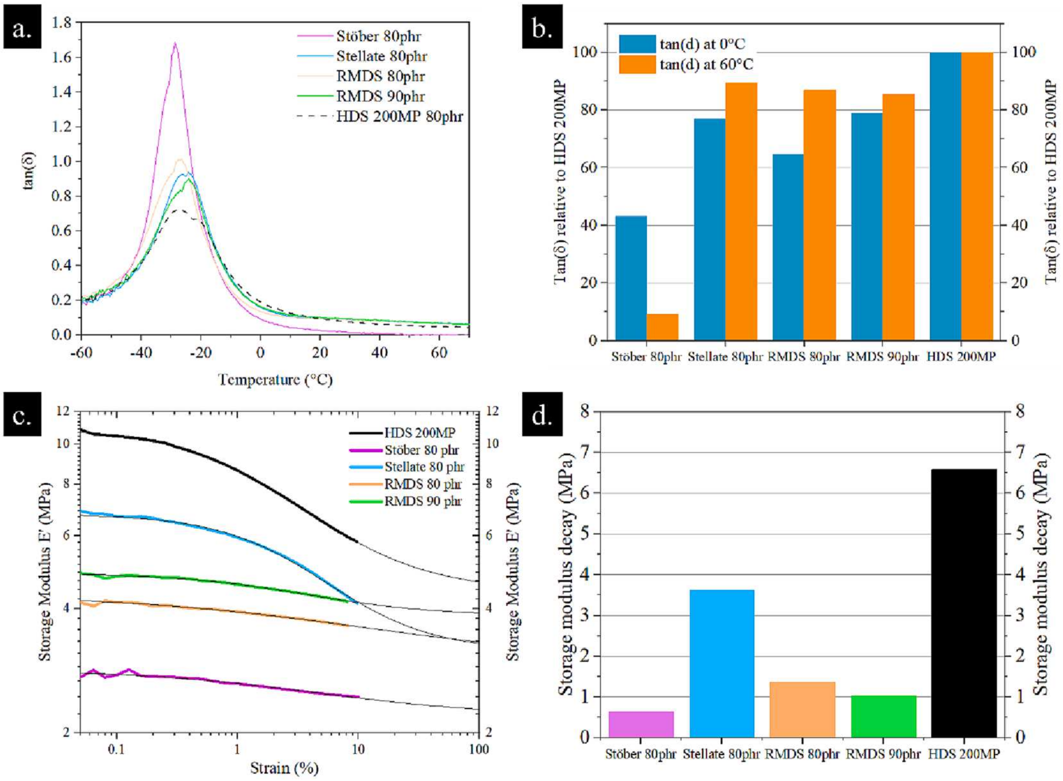

Fig. 5. Tan δ (at 1 Hz) curves of silica-rubber composites (a) and tan δ at 0 °C and 60 °C relative to HDS 200MP compound (b), Storage modulus E’ vs Strain with corresponding Kraus fits (black lines) (c) and Payne effect storage modulus decay (d) (at 10 Hz).

comparison between Stellate 80 phr and RMDS 80 phr highlights how the different silanization affects the formation of aggregates as well. Stellate silica particles exhibit strong inter-particle interactions at low strain, most likely through hydrogen bonding, corroborating the tensile behavior of these composite. The fitting parameter $\Delta E'$ reported in **Table S3 of Supporting Information** shows that the Payne effect is more significant in the case of Stellate than for RMDS, indicating that in the case of the latter, the composite is less affected by a filler network breakage or fillers occur predominantly as single particles. On the other hand, the spherical Stöber particles lead to a low reinforcement as well as a weak decay of E'. As reported in **Table S3 of Supporting Information**, the values of m fitted for the samples under investigation are lower than the literature values and seem to be dependent on the type of filler. The discrepancy could be attributed to the shape of the fillers used in this work. While the Stöber particles are spherical, Stellate silica and RDMS are characterized by lower density with respect to HDS 200 MP. The different shape as well as the different distribution of the silane coupling agent at the surface of the particles could be responsible for the deviation from the expected fractal dimension of the clusters. In addition, from Fig. 5**d** it is evident that in the case of Stöber 80 phr and RDMS 80 phr, the decay of the storage modulus occurs close to the limit of the measured dynamic strain. For this reason, the fitted parameter m, closely related to the slope of the decaying function E' is subject to a high uncertainty. RMDS composites exhibit very low Payne effect, with an elastic modulus decay 1.36 MPa and 1.03 MPa for 80 phr and 90 phr composite respectively, when compared to non-modified Stellate or HDS 200MP (6.58 MPa decay). This features low filler-filler interactions in the composite. Consequently, the wet traction indicator tan δ at 0 °C of RMDS 80 phr is lower than Stellate or HDS 200MP. The 90 phr composite manages to slightly increase this parameter while maintaining low tan δ at 60 °C, but still this does not reach the level of HDS 200MP. The comparison of Stöber, non-modified stellate silica and RMDS indicates that the dendritic structure and its regio-selective modification bring more reinforcement to the polymer by crosslinking and trapping rubber in the porous structure. However, the filler-filler interactions are too weak to provide sufficient reinforcement and traction properties. Also, RMDS behaves as a low energy dispersion filler compared to HDS 200MP, as seen with the low tan δ at 0 °C and 60 °C values seen in Fig. 5**b**. It is beneficial in term of rolling resistance but not for the grip and traction. STEM images and computed tomography micrograph are shown in Fig. 6 and Fig. 7 respectively. Additional tomography numerical data of agglomerates and strain induced volume increase are presented in **Figure S7 and S8 of Supporting Information.**

Stöber and non-modified Stellate silica both display particles agglomeration. The presence of agglomerates diminishes the density of silica in the homogeneous areas and prevents to reach a reinforcing percolation network at which the polymer chains would be significantly affected by the particle density. This is supported by tomography in Fig. 7, where the severe agglomeration and lack of silanization of Stöber silica is responsible for debonding and cracks propagation, explaining the low mechanical properties. On the other side, despite the absence of silane, non-modified stellate silica shows a better dispersion but still some agglomeration. This might be due to higher mixing forces (**see Figure S5 of Supporting information**) employed for this compound, arising from hydrogen bonding of Stellate particles. The absence of silanization on stellate silica promotes the hydrogen bonding of particles and thus the reinforcement at low strain (below 25 %). At higher strain, filler-rubber interactions are nonexistent, resulting in the absence of strain hardening and a lower reinforcement. The slight reinforcement over Stöber particles is due to the higher surface area and formation of a filler network leading to higher interaction of the polymer with the porous structure. Finally, RMDS shows a great dispersive behavior with very little aggregates. The low-density area of the RMDS 80 phr sample seen in tomography (Fig. 7 **g.**) can be interpreted as spots where the concentration of particles is lower. This feature is also present in non-solicited rubber sample, indicating that it is an intrinsic feature of the compound itself and it is not caused by the mechanical deformation of the sample. The low volume fraction of stress-induced cavities translates the very good filler-rubber interaction within the composite. But no percolation network is formed, even at 90 phr. This may be due to the size and spherical nature of the RMDS particles, preventing an optimal contact and interlock of the particles. These observations lead to the conclusion that on its own, this filler system is unable to form a percolating network, unlike a fractal system like HDS 200MP.

Mechanical properties of composites and microscopy corroborate the model that a good reinforcing filler should display good filler-filler and filler-rubber interaction. The latter is obtained via the use of coupling and dispersive silanes that prevent silica aggregation, allow for a good dispersion and coupling with the polymer chains. The absence of silane in Stöber and non-modified stellate particles is clearly responsible for the low reinforcing properties, but results hint that the porous structure already bring reinforcement on its own. RMDS show very good properties for reinforcement and low energy dispersion, but the impossibility to form a percolating network prevent it to reach the level of fractal system in term of reinforcement or wet grip. To overcome this, we hypothesize that the use of HDS 200MP as an additive in small amount should increase the filler-polymer interaction by densifying the filler network and fill the gaps between the spherical RMDS particles.

3.3.2. *Dual-filler systems characterization and properties*

STEM images of composites and computed micro-tomography results are displayed in Fig. 8. The addition 10 phr of HDS 200MP clearly

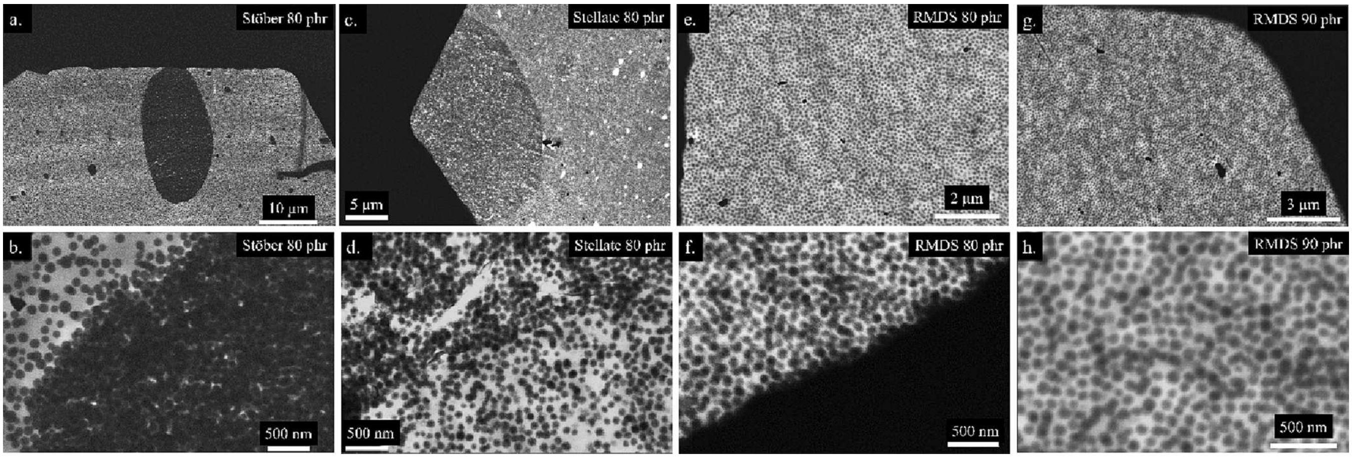

Fig. 6. STEM images of Stöber (a,b), non-modified Stellate (c,d), and RMDS silica-rubber at 80 phr (e,f) and 90 phr (g,h) composites in bright field mode.

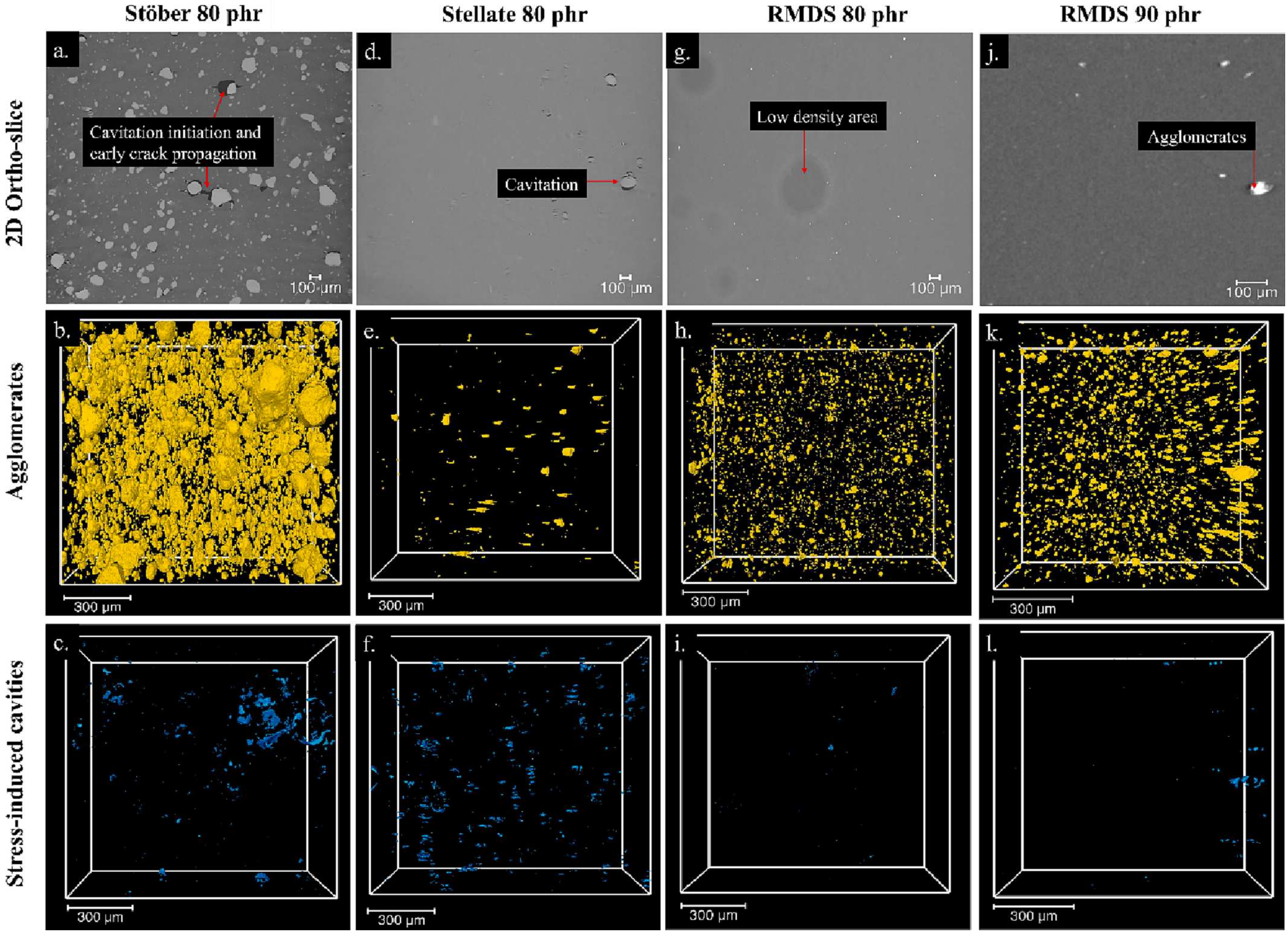

Fig. 7. 2D *ortho*-slice, agglomerates volume fraction (>5 μm) and strain-induced cavities (>5 μm) of Stöber (a,b,c), non-modified Stellate (d,e,f), RMDS 80 phr (g,h, i), and RMDS 90 phr (j,k,l) silica-rubber composites after cyclic tensile strength testing.

increases the particle density, and small HDS 200MP particles can be spotted in between the larger RMDS spheres. Additionally, low-density area previously seen in Fig. 7 are absent. Despite the increase in silica loading, RMDS shows no major agglomeration.

The composite shows minor agglomerates and almost no strain induced cavities. Interestingly, RMDS shows less agglomerates at 90 + 10 phr than 90 phr. This is likely because a higher filler loading induces higher mixing torque during compounding, as it can be seen in **Figure S5 of Supporting Information**. The resulting mechanical properties of dual filler composites are shown in Fig. 9 below. STEM images of composites at 80 + 5, 80 + 10 and 90 + 5 phr are available in of **Figure S9 of Supporting Information.**

The addition of HDS 200MP increases the reinforcement of the composites up to a point where RMDS 90 + 10 phr is higher than the pure fractal filler composite, with a reinforcing index of 4.15 versus 3.9 for HDS 200MP (Fig. 9**a**). RMDS 90 + 10 phr also display better fatigue properties as shown by the cyclic tensile results. The trade-off is a lower ultimate strain and consequently a lower stress at break for all composites over 90 phr of RMDS compared to 80 phr. But the main effect of this dual-filler system is the drastic increase of filler-polymer interaction, as shown by DMA data in Fig. 10.

The combination of the regio-selectively modified dendritic silica and the smaller fractal HDS 200MP allows to drastically increase the filler-filler interaction, as seen in the increase in storage modulus decay in Fig. 10**d**. The particle density also affects the filler-polymer network and limits the polymer chain mobility as seen in Fig. 10**a.** The increased level of interaction between filler and rubber is supported by the decrease of the tan δ peak intensity when increasing the filler loading. The addition of small amount of HDS 200MP increases the Payne effect linearly for 80 phr compounds, but the effect is more pronounced when 5 phr are added to 90 phr of RMDS. At the filler loading of about 90 + 5 phr, the percolation of the filler network is reached, and mechanical properties change drastically. This is seen especially for wet grip and rolling resistance indicator tan δ in Fig. 10**b**. The combination with HDS 200MP allows to improve the traction indicator tan δ at 0 °C for all samples, with the 90 + 10 phr combination surpassing the HDS 200MP while still having a lower rolling resistance. Interestingly, both tensile strength testing and DMA show that this filler combination seems to have a synergetic effect. The fact that the 90 phr HDS 200MP composite does not bring any additional reinforcement compared to 80 phr, as shown in **Figure S10 and S11**, enables us to confirm that it is not the additional 10 phr of fillers that brings more reinforcement, but the use of both fillers simultaneously at this specific loading. Overall, the 90 + 10 phr dual-filler sample benefits from the advantages of the two fillers: good fatigue resistance and lower rolling resistance due to RMDS silica, high wet grip indicator due to HDS 200MP (superior to the pure fractal filler sample), and good reinforcement due to both fillers.

The porous morphology of RMDS silica mimics a fractal structure and enable high interaction between silica particles and polymer chains while leading to a homogenous dispersion of particles with minimal agglomeration and strain induced cavities. RMDS can be qualified of an “unbreakable aggregate”. The addition of a small amount of HDS 200MP

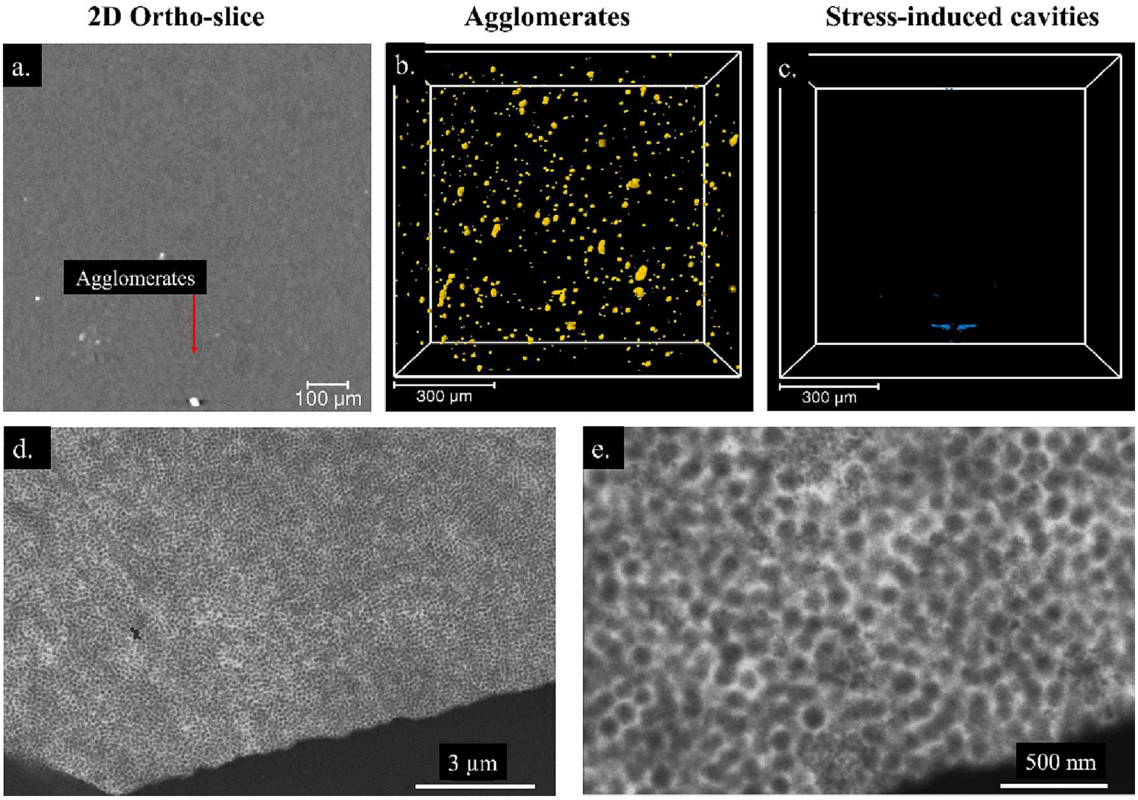

Fig. 8. 2D *ortho*-slice, agglomerates volume fraction (>5μm) and strain-induced cavities (>5μm) of RMDS 90 + 10 phr (a,b,c) and STEM images (d,e).

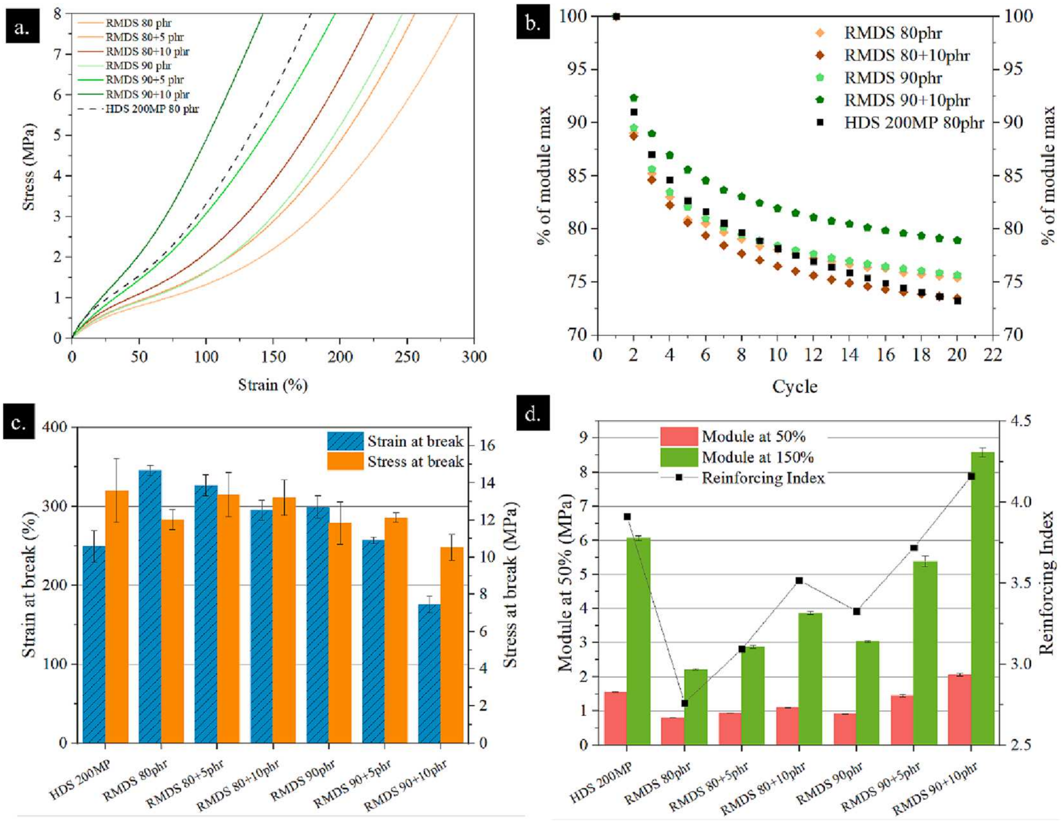

Fig. 9. Stress/Strain curves (a), evolution of maximum strength under cyclic tensile test (b), ultimate stress and strain at break (c) and reinforcing index (d) of dual-filler composites materials.

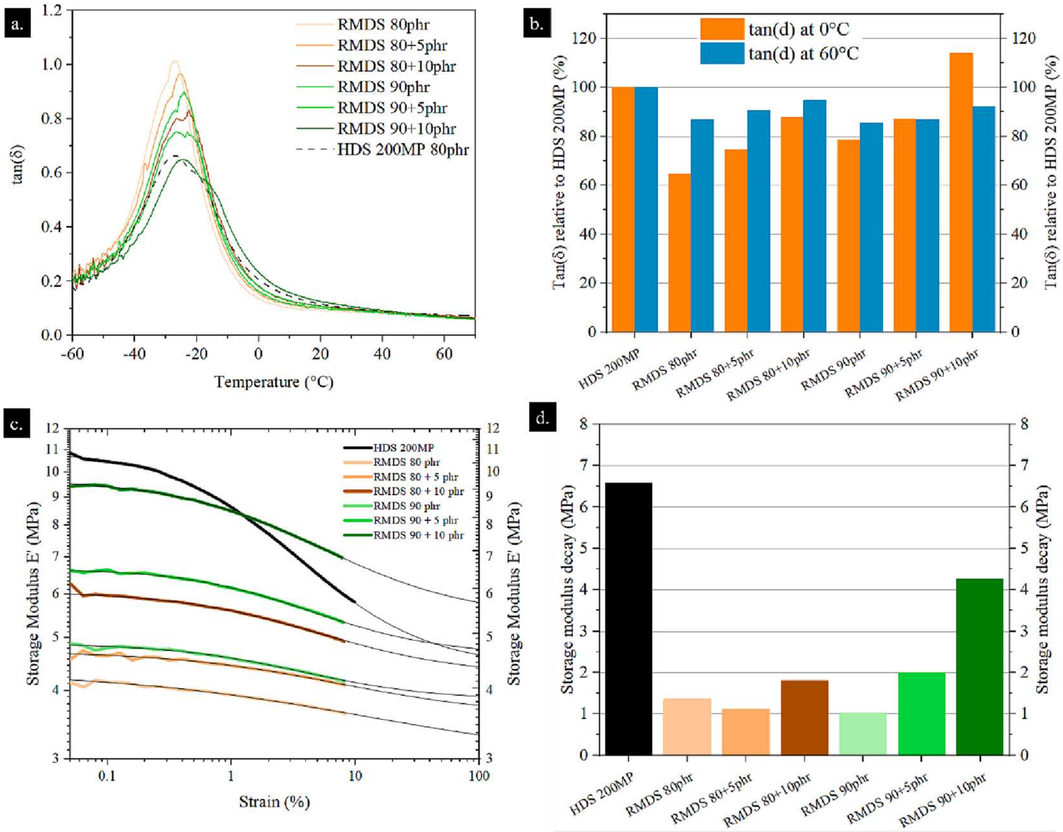

Fig. 10. Tan(δ) curves of silica-rubber composites (a) and tan δ at 0 °C and 60 °C relative to HDS 200MP compound (b), Storage modulus E' vs Strain with corresponding Kraus fits (black lines) (c) and Payne effect storage modulus decay (d).

fills the gaps between RMDS particles in the rubber matrix and enables to compensate for their lack of filler-filler interaction, as supported by the increase in Payne effect seen in Fig. 10**d**.

Under mechanical deformation and sufficient strain, silica particles are pulled apart one from another as the composite material is elongated. When large smooth particles without any silanization are used, silica particles do not interact with the polymer chains and barely restrain their dynamic, as in the case of the Stöber silica composite used in this study. For HDS 200MP, particle aggregates manage to trap rubber in so-called inter-particles porosity. In the case of RMDS, the intra-particle porosity plays the same role, but unlike HDS 200MP aggregates, RMDS particles cannot be pulled apart and do not suffer from permanent dislocation. Subsequently, RMDS composite behave much better under fatigue and show less hysteresis and Payne effect. Finally, the addition of a small amount of the HDS 200MP to RMDS composites enables to fill the gaps between the particles and further increases the filler-filler interaction without overly increasing the Payne effect, leading to a composite with superior reinforcement, wet grip and rolling resistance while keeping good fatigue resistance. This is a major breakthrough here as those three properties are usually antagonistic when their respective improvement is sought.

4. Conclusion

The use of porous silica particles as potent fillers for tire rubber has seen limited use for many years compared to nanometer-size fractal precipitated silica fillers. Indeed, the latter has shown to be more efficient in interacting with the polymer chains because of the fractal structure resulting from the mixing with the matrix. This percolating network enables high filler-polymer interactions by trapping rubber in interparticle porosity. High filler-filler interaction arises from the particle network, leading to good reinforcement. In this work are reported the synthesis and characterization of unique modified dendritic silica fillers with a regio-selective functionalization that are proven to be very efficient at reinforcing tire rubber with 110 nm spherical particles. The combination of the porous structure and the intricate silanization of particles allows the rubber to permeate into the pore and to crosslink with fillers while still allowing a great dispersion of particles. Microscopy, tomography, and mechanical properties characterization results presented here confirm the potential of such a filler technology. RMDS composites show minimal aggregation, cracks, and stress induced cavitation. The combination of RMDS with small amount of a smaller fractal silica filler increases the filler-filler interactions and enables better reinforcement than each filler on its own. Higher tensile strength and moduli, as well as better wet traction and rolling resistance properties are observed. Beyond the homogeneous distribution of particles in the rubber matrix, greater fatigue resistance properties of RMDS filler come from its capacity to behave as a high-interacting reinforcing aggregate regarding the polymer, but without suffering from the irreversible dislocation of those aggregates. It results in a better retention of the reinforcing properties over repeated deformation. The application of such a filler system for tire rubber reinforcement opens new perspectives in the engineering of tires with low rolling resistance and competitive traction with durable performances.

Funding Sources

The authors would like to thank the National Research Found of Luxembourg (FNR) for their financial support through the IPBG16/11514551/TireMat-Tech project.

Declaration of Competing Interest

The authors declare that they have no known competing financial interests or personal relationships that could have appeared to influence the work reported in this paper.

Data availability

Data will be made available on request.

Acknowledgements

We thank Régis Vaudémont and Benoît Marcolini for their precious help on thermal characterization on our fillers and composite, Reiner Dieden and Chuanyu Yan for their help on NMR data processing, Stephan Westermann for is precious advice on dynamic mechanical rubber properties, and Jaafar Ghanbaja for his expertise in electron microscopy and elemental analysis. Finally, we thank Frédéric Addiego for his precious help on X-ray Tomography.

Appendix A. Supplementary data

Supplementary data to this article can be found online at https://doi.org/10.1016/j.cej.2023.141964.

References

[1] M. Staropoli, V. Rogé, E. Moretto, J. Didierjean, M. Michel, B. Duez, P. Steiner, G. Thielen, D. Lenoble, J.-S. Thomann, Hybrid silica-based fillers in nanocomposites: Influence of isotropic/isotropic and isotropic/anisotropic fillers on mechanical properties of styrene-butadiene (SBR)-based rubber, Polymers 13 (2021) 2413.
[2] Y. Lin, S. Liu, J. Peng, L. Liu, The filler–rubber interface and reinforcement in styrene butadiene rubber composites with graphene/silica hybrids: A quantitative correlation with the constrained region, Compos. A Appl. Sci. Manuf. 86 (2016) 19–30.
[3] R. Scotti, L. Conzatti, M. D'Arienzo, B. Di Credico, L. Giannini, T. Hanel, P. Stagnaro, A. Susanna, L. Tadiello, F. Morazzoni, Shape controlled spherical (0D) and rod-like (1D) silica nanoparticles in silica/styrene butadiene rubber nanocomposites: Role of the particle morphology on the filler reinforcing effect, Polymer 55 (2014) 1497–1506.
[4] L. Tadiello, M. D'Arienzo, B. Di Credico, T. Hanel, L. Matejka, M. Mauri, F. Morazzoni, R. Simonutti, M. Spirkova, R. Scotti, The filler–rubber interface in styrene butadiene nanocomposites with anisotropic silica particles: morphology and dynamic properties, Soft Matter 11 (2015) 4022–4033.
[5] Chiola, V., Ritsko, E.J. and Vanderpool, D.C. (1971) Process for Producing Low-Bulk Density Silica. Application No. US 3556725D, Publication No. US 3556725.
[6] J.S. Beck, J.C. Vartuli, W.J. Roth, M.E. Leonowicz, C. Kresge, K. Schmitt, C. Chu, D. H. Olson, E. Sheppard, S. McCullen, A new family of mesoporous molecular sieves prepared with liquid crystal templates, J. Am. Chem. Soc. 114 (1992) 10834–10843.
[7] D. Zhao, J. Feng, Q. Huo, N. Melosh, G.H. Fredrickson, B.F. Chmelka, G.D. Stucky, Triblock copolymer syntheses of mesoporous silica with periodic 50 to 300 angstrom pores, Science 279 (1998) 548–552.
[8] L. Palanikumar, E.S. Choi, J.Y. Cheon, S.H. Joo, J.H. Ryu, Noncovalent polymer-gatekeeper in mesoporous silica nanoparticles as a targeted drug delivery platform, Adv. Funct. Mater. 25 (2015) 957–965.
[9] F. Hou, Z. Teng, J. Ru, H. Liu, J. Li, Y. Zhang, S. Sun, H. Guo, Flower-like mesoporous silica nanoparticles as an antigen delivery platform to promote systemic immune response, Nanomed. Nanotechnol. Biol. Med. 42 (2022), 102541.
[10] F. Perton, S. Harlepp, G. Follain, K. Parkhomenko, J.G. Goetz, S. Bégin-Colin, D. Mertz, Wrapped stellate silica nanocomposites as biocompatible luminescent nanoplatforms assessed in vivo, J. Colloid Interface Sci. 542 (2019) 469–482.
[11] L.C. Lin, M. Thirumavalavan, J.F. Lee, Facile Synthesis of Thiol-functionalized Mesoporous Silica-Their Role for Heavy Metal Removal Efficiency. *CLEAN–Soil, Air*, Water 43 (2015) 775–785.
[12] B. Ghalei, A. Pournaghshband Isfahani, M. Sadeghi, E. Vakili, A. Jalili, Polyurethane-mesoporous silica gas separation membranes, Polym. Adv. Technol. 29 (2018) 874–883.
[13] A. Galarneau, J. Iapichella, D. Brunel, F. Fajula, Z. Bayram-Hahn, K. Unger, G. Puy, C. Demesmay, J.L. Rocca, Spherical ordered mesoporous silicas and silica monoliths as stationary phases for liquid chromatography, J. Sep. Sci. 29 (2006) 844–855.
[14] X. Yang, D. Chen, S. Liao, H. Song, Y. Li, Z. Fu, Y. Su, High-performance Pd–Au bimetallic catalyst with mesoporous silica nanoparticles as support and its catalysis of cinnamaldehyde hydrogenation, J. Catal. 291 (2012) 36–43.
[15] Y. Luo, J. Lin, Synthesis and characterization of Co (II) salen functionalized MCM-41-type hybrid mesoporous silicas and their applications in catalysis for styrene oxidation with H2O2, Microporous Mesoporous Mater. 86 (2005) 23–30.
[16] N. Suzuki, Y. Kamachi, K. Takai, S. Kiba, Y. Sakka, N. Miyamoto, Y. Yamauchi, Effective use of mesoporous silica filler: comparative study on thermal stability and transparency of silicone rubbers loaded with various kinds of silica particles, Eur. J. Inorg. Chem. 2014 (2014) 2773–2778.
[17] Y. Luo, J.P. Wang, X. Cui, Y. Fu, G.L. Li, W. Wang, Surface-modified mesoporous silica nanorods for the highly aging resistance rubber through controlled release of antioxidant, Polym. Adv. Technol. 32 (2021) 3384–3391.
[18] D. Zhao, S. Ge, E. Senses, P. Akcora, J. Jestin, S.K. Kumar, Role of filler shape and connectivity on the viscoelastic behavior in polymer nanocomposites, Macromolecules 48 (2015) 5433–5438.
[19] R. Yang, Y. Song, Q. Zheng, Payne effect of silica-filled styrene-butadiene rubber, Polymer 116 (2017) 304–313.
[20] J. Ramier, C. Gauthier, L. Chazeau, L. Stelandre, L. Guy, Payne effect in silica-filled styrene–butadiene rubber: influence of surface treatment, J Polym Sci B 45 (2007) 286–298.
[21] M. Staropoli, D. Gerstner, M. Sztucki, G. Vehres, B. Duez, S. Westermann, D. Lenoble, W. Pyckhout-Hintzen, Hierarchical scattering function for silica-filled rubbers under deformation: Effect of the initial cluster distribution, Macromolecules 52 (2019) 9735–9745.
[22] S. Nuntang, S. Poompradub, S. Butnark, T. Yokoi, T. Tatsumi, C. Ngamcharussrivichai, Novel mesoporous composites based on natural rubber and hexagonal mesoporous silica: synthesis and characterization, Mater. Chem. Phys. 143 (2014) 1199–1208.
[23] L.D. Perez, L. Sierra, B.L. Lopez, Effect of the filler characteristics on the miscibility of styrene-butadiene rubber and nitrile-butadiene rubber blends, Polym. Eng. Sci. 48 (2008) 1986–1993.
[24] L.D. Perez, B.L. Lopez, Thermal characterization of SBR/NBR blends reinforced with a mesoporous silica, J. Appl. Polym. Sci. 125 (2012) E327–E333.
[25] H. Acharya, S.K. Srivastava, Mechanical, thermo-mechanical, thermal, and swelling properties of EPDM-organically modified mesoporous silica nanocomposites, Polym. Compos. 38 (2017) E371–E380.
[26] Y. Kojima, T. Matsuoka, H. Takahashi, Preparation of nylon 66/mesoporous molecular sieve composite under high pressure, J. Appl. Polym. Sci. 74 (1999) 3254–3258.
[27] N. Wang, M. Li, J. Zhang, Polymer-filled porous MCM-41: An effective means to design polymer-based nanocomposite, Mater. Lett. 59 (2005) 2685–2688.
[28] S. Kiba, N. Suzuki, Y. Okawauchi, Y. Yamauchi, Prototype of low thermal expansion materials: fabrication of mesoporous silica/polymer composites with densely filled polymer inside mesopore space, Chemistry–An Asian Journal 5 (2010) 2100–2105.
[29] X. Ji, J.E. Hampsey, Q. Hu, J. He, Z. Yang, Y. Lu, Mesoporous silica-reinforced polymer nanocomposites, Chem. Mater. 15 (2003) 3656–3662.
[30] Z. Zhou, S. Zhu, D. Zhang, Grafting of thermo-responsive polymer inside mesoporous silica with large pore size using ATRP and investigation of its use in drug release, J. Mater. Chem. 17 (2007) 2428–2433.
[31] I. Park, Z. Wang, T.J. Pinnavaia, Assembly of large-pore silica mesophases with wormhole framework structures from α, ω-diamine porogens, Chem. Mater. 17 (2005) 383–386.
[32] I. Park, T.J. Pinnavaia, Mesocellular silica foam as an epoxy polymer reinforcing agent, Adv. Funct. Mater. 17 (2007) 2835–2841.
[33] J. Jiao, X. Sun, T.J. Pinnavaia, Reinforcement of a rubbery epoxy polymer by mesostructured silica and organosilica with wormhole framework structures, Adv. Funct. Mater. 18 (2008) 1067–1074.
[34] E. Moretto, J.o.P. Fernandes, M. Staropoli, V. Rogé, P. Steiner, B. Duez, D. Lenoble, J.-S. Thomann, Dual-Silane Premodified Silica Nanoparticles─ Synthesis and Interplay between Chemical, Mechanical, and Curing Properties of Silica–Rubber Nanocomposites: Application to Tire Tread Compounds, ACS Omega 7 (21) (2022) 17692–17702.
[35] J. Kecht, A. Schlossbauer, T. Bein, Selective functionalization of the outer and inner surfaces in mesoporous silica nanoparticles, Chem. Mater. 20 (2008) 7207–7214.
[36] V. Cauda, A. Schlossbauer, J. Kecht, A. Zürner, T. Bein, Multiple core− shell functionalized colloidal mesoporous silica nanoparticles, J. Am. Chem. Soc. 131 (2009) 11361–11370.
[37] K. Zhang, L.-L. Xu, J.-G. Jiang, N. Calin, K.-F. Lam, S.-J. Zhang, H.-H. Wu, G.-D. Wu, B. Albela, l., Bonneviot, L., Facile large-scale synthesis of monodisperse mesoporous silica nanospheres with tunable pore structure, J. Am. Chem. Soc. 135 (2013) 2427–2430.
[38] K. Möller, J. Kobler, T. Bein, Colloidal suspensions of mercapto-functionalized nanosized mesoporous silica, J. Mater. Chem. 17 (2007) 624–631.
[39] N.T. Vo, A.K. Patra, D. Kim, Pore size and concentration effect of mesoporous silica nanoparticles on the coefficient of thermal expansion and optical transparency of poly (ether sulfone) films, PCCP 19 (2017) 1937–1944.
[40] P. Akcora, S.K. Kumar, J. Moll, S. Lewis, L.S. Schadler, Y. Li, B.C. Benicewicz, A. Sandy, S. Narayanan, J. Ilavsky, "Gel-like" mechanical reinforcement in polymer nanocomposite melts, Macromolecules 43 (2010) 1003–1010.
[41] C. Bartholome, E. Beyou, E. Bourgeat-Lami, P. Cassagnau, P. Chaumont, L. David, N. Zydowicz, Viscoelastic properties and morphological characterization of silica/polystyrene nanocomposites synthesized by nitroxide-mediated polymerization, Polymer 46 (2005) 9965–9973.
[42] J. Fröhlich, W. Niedermeier, H.-D. Luginsland, The effect of filler–filler and filler–elastomer interaction on rubber reinforcement, Compos. A Appl. Sci. Manuf. 36 (2005) 449–460.
[43] N. Vleugels, W. Pille-Wolf, W.K. Dierkes, J.W. Noordermeer, Understanding the influence of oligomeric resins on traction and rolling resistance of silica-reinforced tire treads, Rubber Chem. Technol. 88 (2015) 65–79.
[44] C. Federico, H. Padmanathan, O. Kotecký, R. Rommel, G. Rauchs, Y. Fleming, F. Addiego, Resolving cavitation in silica-filled styrene-butadiene rubber composites upon cyclic tensile testing, Polym. Test. 100 (2021), 107274.

[45] Z. Liu, H. Zhang, S. Song, Y. Zhang, Improving thermal conductivity of styrene-butadiene rubber composites by incorporating mesoporous silica@ solvothermal reduced graphene oxide hybrid nanosheets with low graphene content, Compos. Sci. Technol. 150 (2017) 174–180.

[46] M.L. Williams, R.F. Landel, J.D. Ferry, The temperature dependence of relaxation mechanisms in amorphous polymers and other glass-forming liquids, J. Am. Chem. Soc. 77 (1955) 3701–3707.

[47] H. Takino, R. Nakayama, Y. Yamada, S. Kohjiya, T. Matsuo, Viscoelastic properties of elastomers and tire wet skid resistance, Rubber Chem. Technol. 70 (1997) 584–594.

[48] Y. Li, B. Han, S. Wen, Y. Lu, H. Yang, L. Zhang, L. Liu, Effect of the temperature on surface modification of silica and properties of modified silica filled rubber composites, Compos. A Appl. Sci. Manuf. 62 (2014) 52–59.

Interplay of regio-selectively modified dendritic silica particles with styrene-butadiene rubber: the route towards better tires with lower rolling-resistance and higher grip.

Supporting Information

*Enzo Moretto, Charlotte Stoffels, Carlos Eloy Federico, Vincent Rogé, Mariapaola Staropoli, Likpoemugh Elo Imiete, Jean-Nicolas Audinot, Pascal Steiner, Benoît Duez, Damien Lenoble, Jean-Sébastien Thomann**

E.M., C.S., C.E.F., V.R., M.S., E.I.L, J-N.A., D.L., J-S.T.
MRT Department, Luxembourg Institute of Science and Technology, 41 Rue du Brill, L-4422 Belvaux, Luxembourg
E-mail: jean-sebastien.thomann@list.lu
P.S., B.D.
Goodyear S.A, Avenue Gordon Smith, L-7750 Colmar-Berg, Luxembourg

Keywords: mesoporous silica, silica-rubber composite, silanization, regio-selective silanization, SIMS, elemental mapping

Experimental section

Tetraethoxysilane (TEOS), Hexadecyltrimethylammonium p-toluene sulfonate (CTATos), Triethanolamine (TEA), were purchased from Merck. 3-mercaptopropyltriethoxysilane (MPTES), hexyltrimethoxysilane (C6) and 7-bromoheptyltrimethoxysilane (Br-C7) were purchased from Gelest. Aqueous ammonia solution 25wt%, absolute ethanol was purchased from Carl Roth. For the fabrication of silica-rubber nanocomposites, poly-styrene-butadiene (SBR, Solution SBR, 21% Styrene, 50% Vinyl) polybutadiene rubber (BR, Neodymium catalyzed polybutadiene), HDS 200Mp silica (precipitated silica, primary particle size 10nm, specific surface area 200 m²/g) ,treated distillate aromatic extracted (TDAE) lubricating oil, zinc oxide, stearic acid, N-(1,3-dimethylbutyl)-N'-phenyl-p-phenylenediamine (6-PPD), Sulfur, 2-mercaptobenzothaizole (MBT), di-phenylguanidine (DPG) and N-cyclohexyl-2-benzothiazolesulfenamide (CBS) have been used. All chemicals were used as such without any further purification.

Silica particles synthesis

Stöber silica particles synthesis

The production of Stöber silica particles was done according to the following protocol. 3537.4 g of absolute ethanol, 141.4 g of de-ionized water and 178.3 g of tetraethoxysilane (TEOS) are added to a 5 L reaction vessel and homogenized for 10 min. on a magnetic stirring plate. Then, 165,0 g of a 25wt% aqueous ammonia solution are added to the solution. The solution is let to react for 24 h at room temperature and constant mixing. After this delay, the silica suspension was transferred in a 20 L round-bottom flask and dried under reduced pressure using a Buchi R-220 Pro rotary evaporator to separate the particles from the liquid. Finally, Stöber silica powder was dried in the oven at 110°C for 48 h and stored in a sealed container.

Stellate silica particles synthesis

The production of stellate silica particles is inspired from this work.[1]. In 2 L reaction vessel, 3.47 g of triethanolamine and 19.2 g of hexadecyltrimethylammonium p-toluene sulfonate are dissolved in 1.0 L of de-ionized water. The solution is heated at 80°C and mixed for 2hrs. Then, 1458.0 g of tetraethoxysilane (TEOS) are added. The reaction is carried for 2 hrs. at 80°C under stirring. At the end of the reaction, stirring is stopped and the silica particles are let to settle at the bottom of the reaction vessel. Most of the supernatant above the settled silica is removed from the vessel and 1 L of de-ionized water is added. Silica and water are mixed for 12 hrs. at room temperature, then stirring is stopped and the silica particles are let to settle at the bottom of the reaction vessel. Supernatant above the settled silica is removed from the vessel and 1 L of ethanol is added. Silica and ethanol are mixed for 12 hrs. at reflux temperature under stirring. Finally, stirring is stopped and the silica particles are let to settle at the bottom of the reaction vessel. Ethanol supernatant above the settled silica is removed from the vessel. The highly concentrated silica particles in ethanol are then separated by centrifugation (4700 g for 1hr.). Regio selectively functionalized stellate silica are then dried in an oven at 110°C for 48 hrs. and stored in a sealed container.

Bromine-labelled regio-selectively modified dendritic silica particles (Br-RMDS)

Bromine-labelled regio-selectively modified dendritic silica particles are synthesized for elemental imaging purpose and have been synthesized as follow. In a 50 mL round-bottom flask, 25 mL of de-ionized water, 0.48 g of CTATos and 86.7 mg of triethanolamine were mixed at 80°C for 2 hrs. The reaction is kept at 80°C under stirring until the end of the reaction. 3.645 g of TEOS were added. 417 mg MPTES were added in the round-bottom flask 15 min. after the addition of TEOS. 522.5 mg of 7-bromoheptyltrimethoxysilane were added 2hrs after the TEOS addition. After this addition, the reaction is kept at 80°C under stirring for 2 hrs. At this stage the reaction was stopped, and the silica was separated by centrifugation at 10.000g for 10min. The supernatant was poured out and fresh de-ionized water was added to the centrifuge tube. The tube was vigorously shaken for to re-disperse the silica for 5 min. The silica was separated by centrifugation at 10.000g for 10 min and added to a 200 mL round-bottom flask. 100 mL of ethanol were added to this flask and the silica dispersion was heated to reflux temperature and stirred for 12 hrs. Finally, the silica was separated by centrifugation at 10.000g for 10 min, dried in an oven at 110°C for 48 hrs. and stored in a sealed container.

Silica-rubber composites fabrication

Component quantities and mixing steps are summarized in

Table S 1. Quantities are given in phr, meaning Per Hundred Rubber. For example, 80 phr of silica means that for 100 g of polymer, 80 g of silica are added. At each mixing step, ingredients have been mixed using a HAAKE™ PolyLab™ QC ThermoScientific internal mixer and then the green compound was further mixed in a roll-mill for 6 passes at 50°C. The material obtained at one step is then mixed with the ingredients of the following step. All final green compounds have been cured in a hydraulic press at 170°C for 10 min. under a pressure of 150 kPa.

Table S 1. Ingredients and mixing steps for the fabrication of silica-rubber composites

	Step 1 **80°C for 10'**	**Step 2** **80°C for 7'**	**Step 3** **60°C for 1'45''**
Poly styrene-butadiene	80	-	-
polybutadiene	20	-	-
TDAE Oil	25	-	-
Zinc Oxide	0.5	-	2
Stearic acid	3	-	-
Silica	65	15	-
6PPD	-	2.5	-
TESPD Silane	-	**varying**	-
Sulfur	-	-	1.1
MBT	-	-	0.3
DPG	-	-	3.2
CBS	-	-	2.3

Note: TESPD silane quantity is 10% of HDS 200MP. For 80 phr of HDS 200MP, 8phr are used. For 10 phr, 1phr of silane are used.

Table S 2. Silica filler composition of composites.

	Stöber	**Stellate**	**RMDS**	**HDS 200MP**
Stöber 80phr	80	-	-	-
Stöber 80+10phr	80	-	-	10
Stellate 80phr	-	80	-	-
Stellate 80+10phr	-	80	-	10
RMDS 80phr	-	-	80	-
RMDS 80+5phr	-	-	80	5
RMDS 80+10phr	-	-	80	10
RMDS 90phr	-	-	90	-
RMDS 90+5phr	-	-	90	5
RMDS 90+10phr	-	-	90	10
HDS 200MP 80phr	-	-	-	80

Characterization of silica particles and composites

Transmission Electron Microscopy and Energy Dispersive X-rays Spectroscopy of regio-selectively functionalized mesoporous silica

Transmission electron microscopy (TEM) investigations were carried out using a JEM - ARM 200F Cold FEG TEM/STEM operating at 200 kV and equipped with a spherical aberration (Cs) probe and image correctors (point resolution 0.12 nm in TEM mode and 0.078 nm in STEM mode). Energy Dispersive X-rays Spectroscopy (EDS) analyses were performed in STEM mode with a diameter of the probe of 1 nm, using Centurio Silicon Drift Detector (SDD) that collects X-rays from sample at large solid angle of up to 0.98 steradians from a detection area of 100 mm². The composition quantification of the collected X-ray spectra was performed using the Cliff-Lorimer method by dedicated software from Jeol.

Helium Ion Microscopy – Secondary Ion Mass Spectroscopy (HIM-SIMS) of regio-selectively functionalized mesoporous silica

The nanoparticles were deposited on silicon wafer (Siltronix, Archamps, France) beforehand. Measurements were performed with the Helium Ion Microscope (HIM) (Zeiss, Peabody, US)[2] coupled with a Secondary Ion Mass Spectrometer (SIMS) developed at LIST. A Ne^+ primary ion beam (accelerated at 25 keV and a current of 4 pA) was used for scanning over a 5x5 μm^2 area on the sample surface with a sub-20 nm spatial resolution. The images were recorded in a 512 by 512 pixels raster with an acquisition time of 1.5 $ms \cdot pixel^{-1}$. Negative mode was used for the simultaneous detection of oxygen ($^{16}O^-$), carbon ($^{24}C_2^-$) and bromine ($^{79}Br^-$) ions with a sub-20nm spatial resolution.[2] The data were treated with OpenMIMS Data Analysis Software (ImageJ plugin).

Scanning Transmission Electron Microscopy of silica-rubber composites

High-resolution Scanning Transmission Electron Microscopy (STEM) images were acquired with a Helios Nanolab 650 microscope (FEI, Eindhoven, Netherlands). SEM images were acquired at an acceleration voltage of 2 kV and a current of 50 pA. STEM images were acquired at an acceleration voltage of 20 kV and a current of 50 pA, in bright field mode. Nanocomposites lamellas around 80 nm of thickness were prepared using a Cryo-Ultramicrotome EM UC7 (Leica, Wetzlar, Germany), at a temperature of −120°C.

Dynamic Mechanical Analysis (DMA) of silica-rubber composites

Dynamic mechanical properties of nanocomposites were determined using a 242C dynamic mechanical analyzer (DMA) (Netzch, Selb, Germany). Thermograms were obtained in single cantilever mode, with a free length of 5 mm (15% strain amplitude) under a vibration frequency of 1 Hz. The studied temperature range was fixed between –100°C to 80°C with a heating rate of 0.5 $°C \cdot min^{-1}$ in air atmosphere.

DMA experiments were also performed for all rubber samples with the aim of identifying the strain-induced filler network breakdown, related to the Payne effect. For this purpose, the storage modulus E' is measured as function of the dynamic strain amplitude at constant frequency and temperature of, respectively, 10 Hz and 25 ℃. The decay of E' as function of the dynamic strain amplitude is here analyzed through the Kraus model (3) which correlates the decay of E' as function of the dynamic strain to the reversible breakage and re-aggregation of the fillers. The present model has been applied to the data collected for different types of silica fillers with the aim of identifying the effect of the particle shape and density on the network breakage. Within the used model, the drop of E' as function of the dynamic strain is empirically defined as:

$$\frac{E'(\gamma_0)-E'_\infty}{\Delta E'} = \frac{1}{1+\left(\frac{\gamma_0}{\gamma_c}\right)^{2m}} \qquad [\,1\,]$$

Where the amplitude $\Delta E' = E'_0 - E'_\infty$ represents the variation of the storage modulus with the increase of the strain amplitude. Here E'_0 is the value of the storage modulus at small strain corresponding to the filled network, while the value E'_∞ is obtained at infinite strain and is correlated to the pure hydrodynamic reinforcement effect of the de-aggregated fillers. γ_c indicates a critical strain at which $E'(\gamma_0) - E'_\infty$ has decreased to half of its initial value and the m exponent is correlated to the cluster fractal dimension. An experimental value of $m = 0.5 - 0.6$ has been reported in the literature (3,4).

Tensile strength test of silica-rubber composites

The tensile behavior of nanocomposites was determined at room temperature, under a strain rate of 200 $mm \cdot min^{-1}$, with a 5967 Series Universal Testing System (Instron, Norwood, MA, USA). Cyclic tensile testing was performed at 70% of the mean maximum elongation of each sample, for 20 cycles at 200 $mm \cdot min^{-1}$.

Thermogravimetric Analysis of regio-selectively functionalized mesoporous silica

Thermogravimetric Analysis (TGA) was performed with A Mettler TGA 2 (Mettler Toledo (Columbus, Ohio, USA). 10 to 20 mg of silica powder are placed in an alumina crucible and heated from 25°C to 1000°C at 10°C·min^{-1} in nitrogen atmosphere until a gas shift at 750°C with an atmosphere of 20% O_2 and 70% N_2 until the end of the analysis at 1000°C. An empty alumina crucible is placed in the furnace for reference.

Solid-state 29Si MAS (Magic Angle Spinning) NMR of regio-selectively functionalized mesoporous silica

Solid-state ^{29}Si MAS (Magic Angle Spinning) NMR spectra were acquired on a Bruker Avance 400MHz spectrometer (9.4 T wide bore magnet) equipped with a 4 mm BL4 X/Y/H probe. Magic angle spinning was performed at 6.5 kHz using ceramic zirconia rotors of 4 mm in diameter. The signal of talc was used to calibrate the silicon chemical shift scale (-98 ppm). Acquisition parameters used were the following: a spectral width of 300 ppm, a 90° pulse length of 4.5 µs, an acquisition time of 15ms, a recycle delay time of 60 s and about 3000 accumulations (48 hrs.). High power proton dipolar decoupling during the acquisition time was set to 70 kHz. Solid-state ^{29}Si MAS (Magic Angle Spinning) NMR spectra were also acquired on an Agilent VNMRS Direct Drive 400 MHz spectrometer (9.4 T wide bore magnet) equipped with a T3HX 3.2 mm probe. Magic angle spinning was performed at 6.5 kHz using ceramic zirconia rotors of 3.2 mm in diameter, the signal of talc was used to calibrate the silicon chemical shift scale (-98 ppm). Acquisition parameters used were the following: a spectral width of 300 ppm, a 90° pulse length of 5 µs, an acquisition time of 15 ms, a recycle delay time of 60 s and about 4400 accumulations (72 hrs.). High power proton dipolar decoupling during the acquisition time was set to 70 kHz.

Nitrogen adsorption porosimetry

The specific surface area and pore volume of mesoporous silica particles has been determined by the Barrett–Joyner–Halenda (BJH) method using an Autosorb-IQ-MP/XR analyser from the Quantachrome Instruments company (Boynton Beach, Florida, USA). Before to perform nitrogen sorption measurement, the sample was degassed at 100°C for 8h. Pores volumes were estimated using the Density Functional Theory (DFT) method.

Computed micro-tomography

Rubber composites were analyzed with a laboratory x-ray cone-beam CT system EasyTom 160 fabricated by RX solutions (Chavanod, France). The x-ray source voltage was set to 40 kV and the current to 80 µA. The exposure time was set to 600 ms and the number of average frames was 4. The sample was rotated 360° in angular steps of

0.25°. The experimental setup enabled to obtain a voxel size of 2.5 µm. The 3D volume reconstruction was achieved thanks to the software Xact64 after applying inherent geometrical corrections in the reconstruction. Image treatment and analysis was conducted with the commercial software Avizo (Thermo Fischer Scientific version 2020.1, Waltham, MA, USA). First, images were de-noised by means of a non-local means filter. Then, the different phases in the material (such as silica agglomerates and cavities) were binarized by thresholding the grayscale histogram. Binarized objects touching the borders of the scanned volume images were filtered out. From the remaining objects, those containing less than 2 voxels were considered inaccurate and thus, removed. Finally, binarized objects were labelled and quantified by their equivalent diameter, D_{eq}, which corresponds to the diameter of a sphere of same volume of the studied object; the sphericity, ψ, which measures how spherical an object is ($\psi = 1$ for a sphere); the volume fraction, V_f, and the number per unit volume, N/V_0, of the studied phase.

The definition of these expressions is summarized in equations (1)-(4).

$$D_{eq} = \sqrt[3]{\frac{6V}{\pi}}; \tag{1}$$

$$\psi = \frac{\pi^{1/3}(6V)^{2/3}}{A_S}; \tag{2}$$

$$V_f = \frac{\sum_{i=1}^{n} V_i}{V_{total}}; \tag{3}$$

$$N/V_0 = \frac{\sum_{i=1}^{n} N_i}{V_{total}}; \tag{4}$$

where V and A_S are the volume and the surface area of the object, V_{total} is the total analyzed volume and N_i is the number of heterogeneities (cracks or fillers) to be counted.

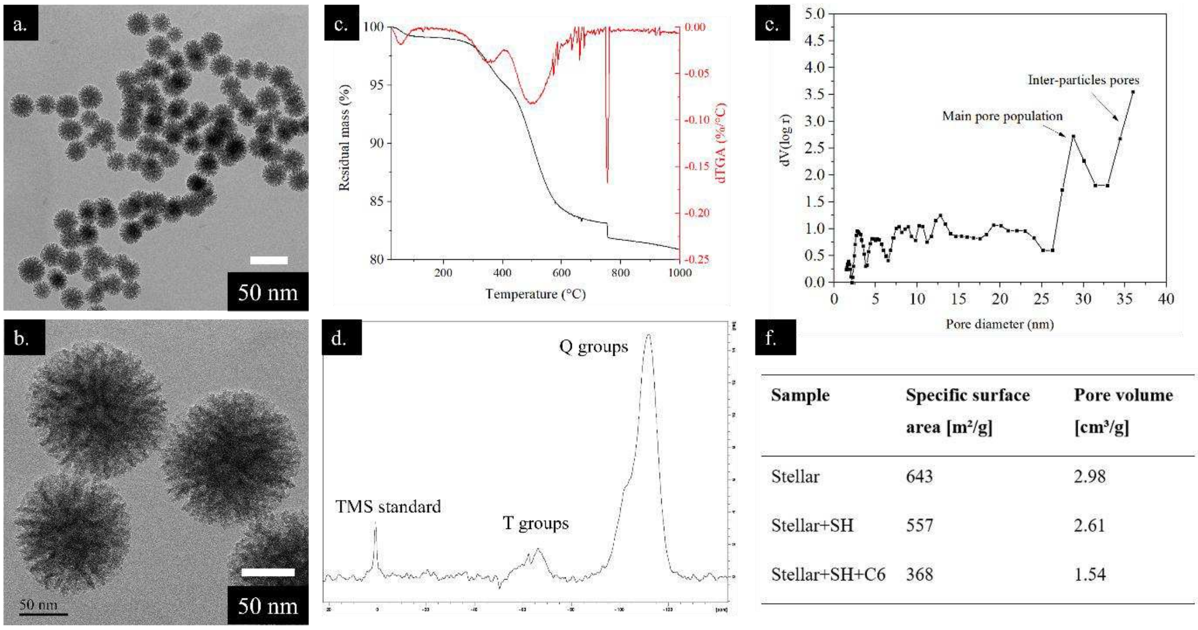

Sample	Specific surface area [m²/g]	Pore volume [cm³/g]
Stellar	643	2.98
Stellar+SH	557	2.61
Stellar+SH+C6	368	1.54

Figure S 1. TEM images (a,b), TGA and dTGA (c), 29Si solid state NMR (d), and (e) DFT pore size calculation from nitrogen adsorption porosimetry of regio-selectively modified dendritic silica. (f) Table of porosimetry results for the different synthesis steps.

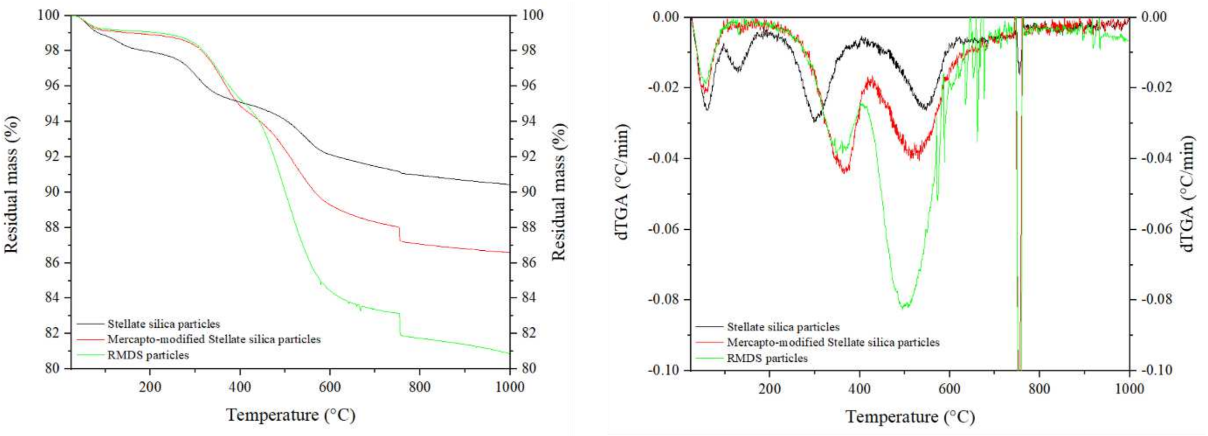

Figure S 2. Thermograms of the different stage of mesoporous silica modification

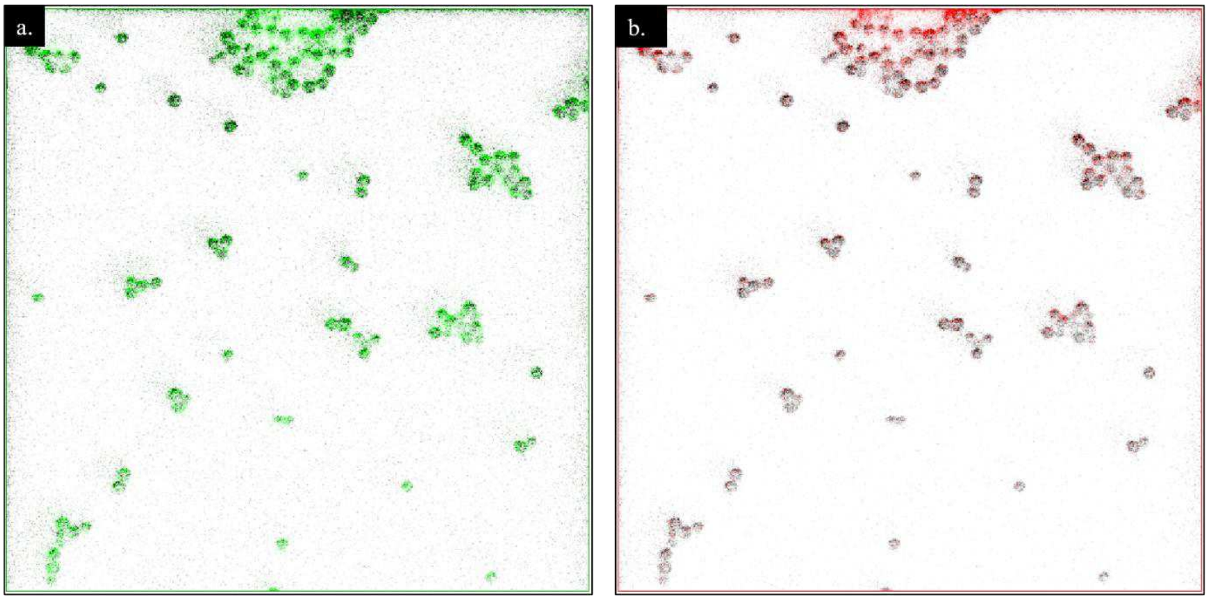

Figure S 3. HIM-SIMS elemental mapping of bromine labelled RMDS: oxygen (grey)/carbon (green) overlap (a), oxygen (grey)/bromine (red) overlap (b). Images are 512x512 pixels with a FOV of 5 µm.

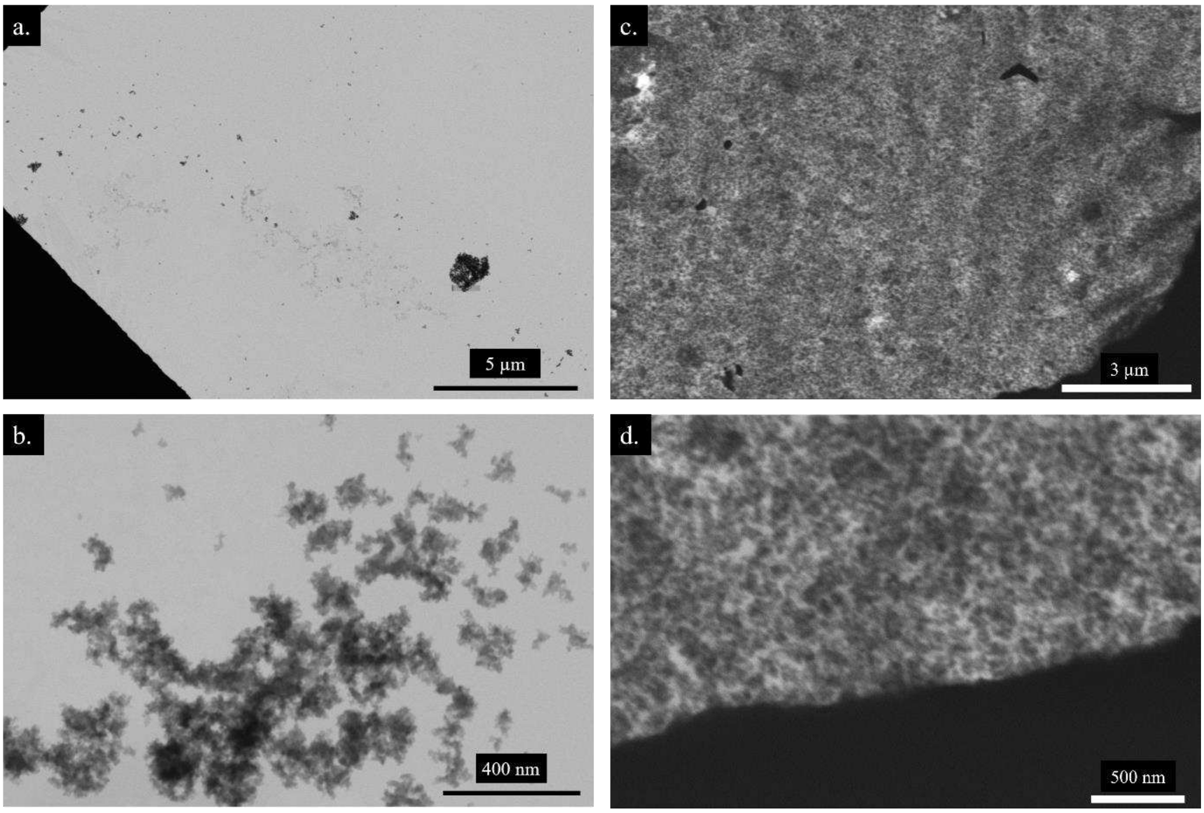

Figure S 4. HDS 200MP silica particles (a,b) and rubber composite (c,d) STEM images.

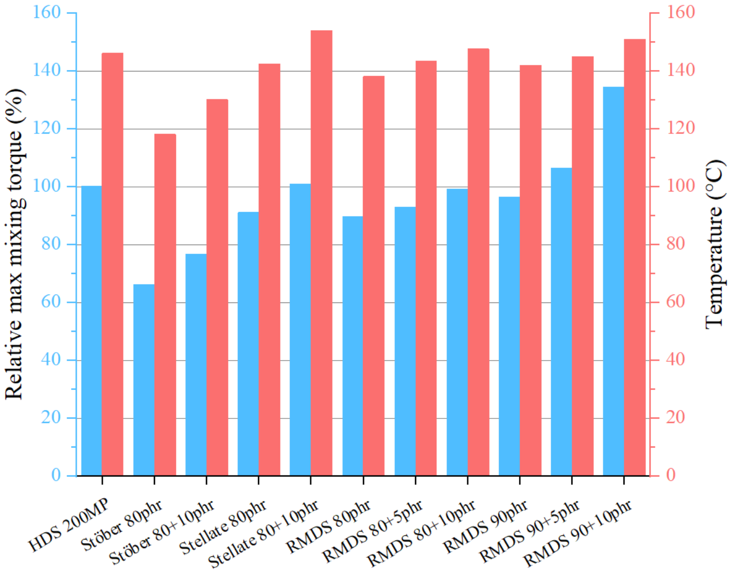

Figure S 5. Maximum torque and temperature of mixing step 2 (torque is normalize with respect to HDS 200MP compound).

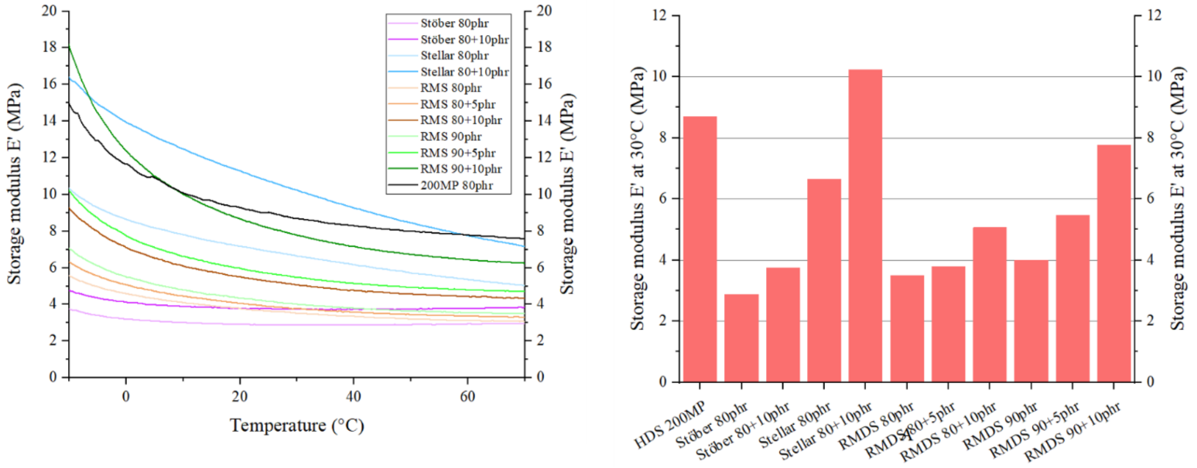

Figure S 6. Storage modulus curves (left) and Storage modulus at 30°C (right) measured in DMA at 1 Hz.

The storage modulus at 30°C illustrates the stiffness of the compounds at 15% strain. At this strain level, HDS 200MP and Stellate 80+10phr are very stiff due to the strong filler-filler interactions. In RMDS samples, E’ is lower but addition of HDS 200MP increases it substantially. With increasing temperature, the modulus of Stellate compounds decreases rapidly compared to HDS 200MP or RMDS compounds.

Table S 3. Fitting parameters for single and dual-filler compounds.

	HDS 200 MP	**Stöber 80phr**	**Stellate 80phr**	**RMDS 80phr**	**RDMS 80+5 phr**	**RDMS 80+10phr**	**RDMS 90 phr**	**RDMS 90+5phr**	**RDMS 90+10phr**
E'_∞	4.4 ± 0.02	2.2 ± 0.1	3.15 ± 0.1	2.96 ± 0.1	3.59 ± 0.2	4.26 ± 0.3	3.84 ± 0.1	4.64 ± 0.2	5.43 ± 0.2
$\Delta E'$	6.58 ± 0.08	0.64 ± 0.04	3.62 ± 0.07	1.36 ± 0.04	1.12 ± 0.04	1.8 ± 0.01	1.03 ± 0.01	2.0 ± 0.2	4.27 ± 0.3
γ_c	2.03 ± 0.03	3.6 ± 0.8	3.6 ± 0.2	8.0 ± 0.8	6.0 ± 0.5	4.02 ± 0.06	3.2 ± 0.1	3.5 ± 0.7	3.6 ± 0.5
m	0.42 ± 0.01	0.29 ± 0.05	0.48 ± 0.02	0.2 ± 0.01	0.31 ± 0.03	0.36 ± 0.06	0.4 ± 0.02	0.41 ± 0.03	0.36 ± 0.02

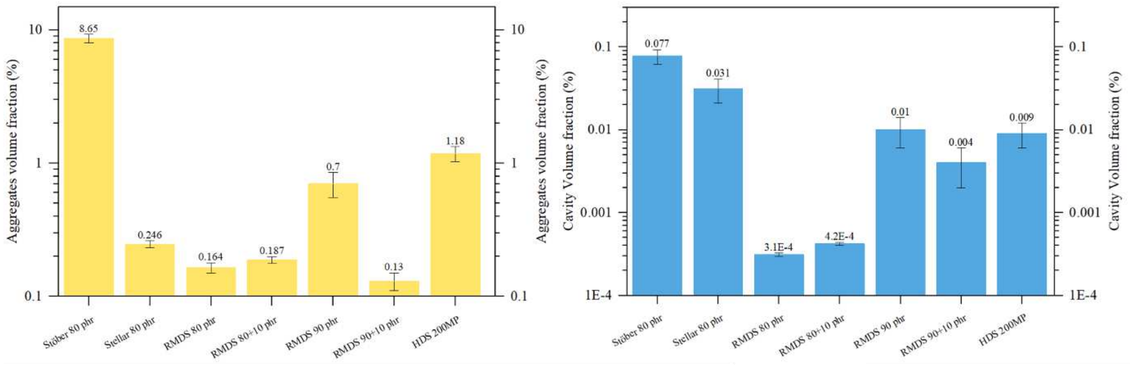

Figure S 7. Aggregates and stress-induced cavities volume fraction numerical data from computed tomography of composites materials.

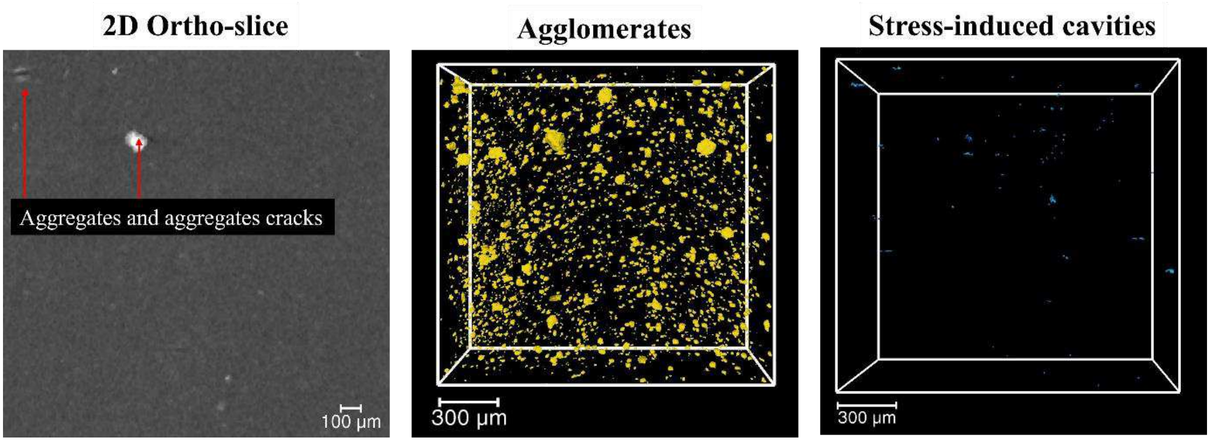

Figure S 8. 2D ortho-slice, agglomerates volume fraction (>5µm) and strain-induced cavities (>5µm) of HDS 200MP.

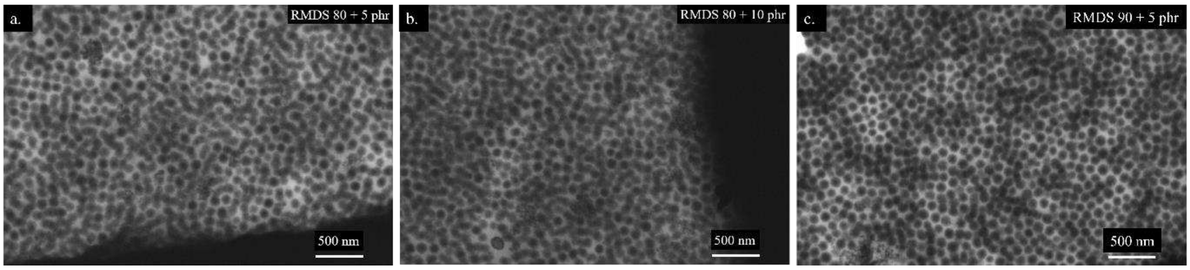

Figure S 9. STEM images of dual-filler composites RMDS 80+5 phr (a), RMDS 80+10 phr (b) and RMDS 90+5 phr (c).

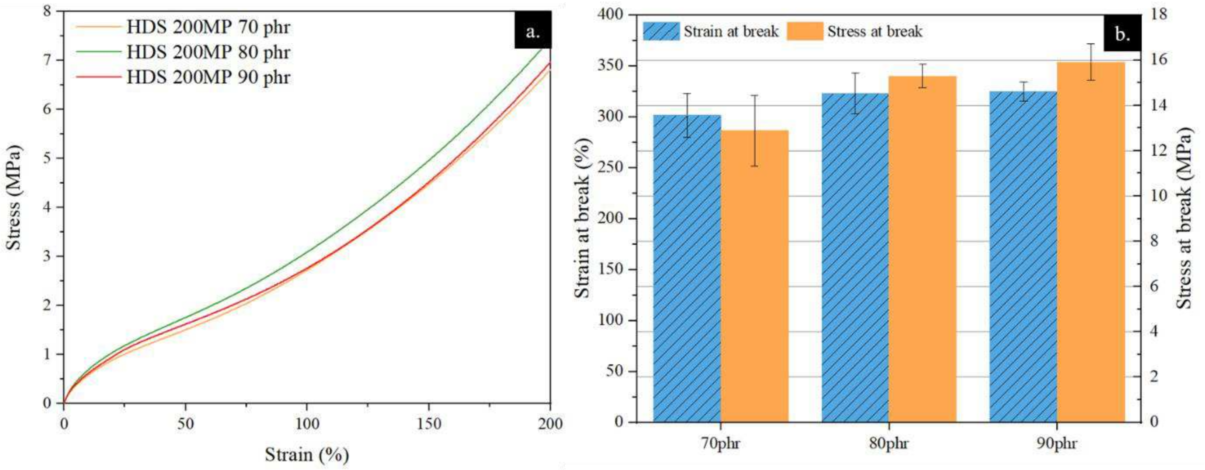

Figure S 10. Stress-strain curves (a) and ultimate stress and strain (b) of HDS 200MP 70, 80 and 90 phr silica-rubber composites.

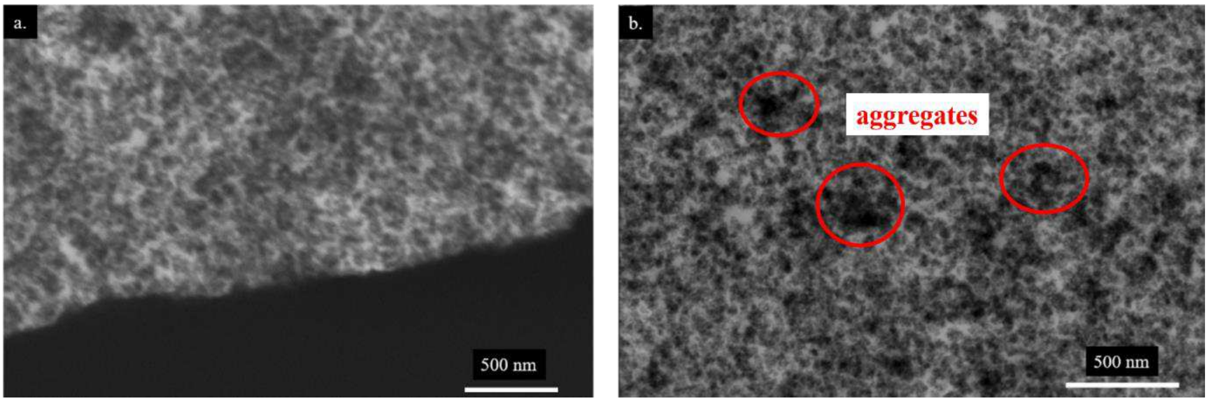

Figure S 11. STEM images of 80 phr (a) and 90 phr (b) HDS 200MP silica-rubber composites.

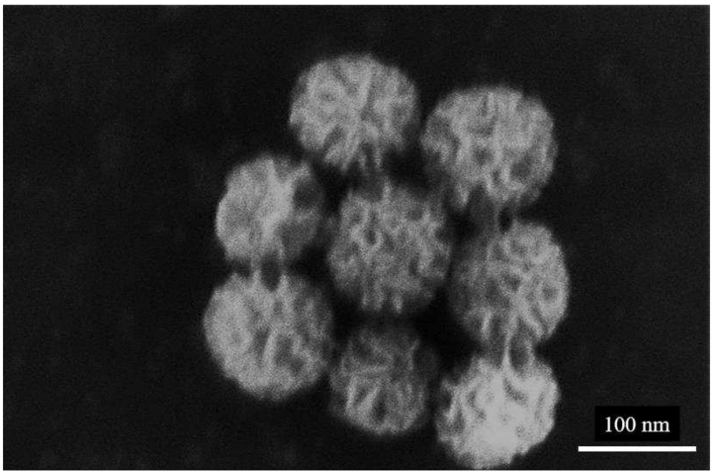

Figure S 12. SEM image of stellar particles. Mean pore entrance diameter is 19 nm +/- 6 nm (calculated over 30 measurements, software ImageJ).

1. Zhang, K.; Xu, L.-L.; Jiang, J.-G.; Calin, N.; Lam, K.-F.; Zhang, S.-J.; Wu, H.-H.; Wu, G.-D.; Albela, B.l.; Bonneviot, L. Facile large-scale synthesis of monodisperse mesoporous silica nanospheres with tunable pore structure. *J. Am. Chem. Soc.* **2013**, *135*, 2427-2430.
2. Audinot, J.-N.; Philipp, P.; De Castro, O.; Biesemeier, A.; Hoang, H.Q.; Wirtz, T. Highest resolution chemical imaging based on secondary ion mass spectrometry performed on the helium ion microscope. *Rep. Prog. Phys.* **2021**.
3. G. Heinrich, M. Klüppel, Recent Advances in the Theory of Filler Networking in Elastomers, Filled Elastomers Drug Delivery Systems, Springer Berlin Heidelberg, Berlin, Heidelberg, 2002, pp. 1-44.
4. G. Heinrich, T.A. Vilgis, Effect of filler networking on the dynamic mechanical properties of crosslinked polymer solids, Macromolecular Symposia 93(1) (1995) 253-260.

Conclusion and outlooks

In this doctoral thesis, entitled *Toward regio-selectively modified dendritic silica filler for tire tread rubber reinforcement – How silica particles silanization and morphology affect energy dissipation and performances,* we aimed to study and understand the influence of silica surface modification as well as silica particle morphology over the viscoelastic properties of tire tread rubber. Because the interaction of fillers and rubber have a central role in the behavior of the composite material, understanding the fundamental underlying phenomenon of rubber reinforcement is necessary when one seeks to target and achieve performances improvement.

Therefore, we studied the silanization reaction of silica filler particles and investigated the possibility to enhance the filler reactivity for better silica functionalization. We show that the activation of silica particles with the original base DBU allowed to reach higher silanization yield in dry organic solvent than other bases. Based on this, we further studied the role and impact of silane on mechanical properties of the composite by separating the coupling and dispersive functions. A two-step sequential silanization allowed us to synthesized dual-silane pre-treated silica particles. With this material, we studied the role of both silane and the effect of their respective length over the composite mechanical properties and viscoelastic performances. We showed that long alkylsilane are detrimental to the grip performances as they reduce the ability of particle to interact together while not increasing enough their ability to interact with rubber. On the other end, short silane combination showed to be efficient at improving the wet grip performance without increasing rolling resistance, showing that this combination allows for superior filler-filler interaction with contained energy dissipation. Finally, we combined a dual-silane functionalization with the versatility of soft-templated porous silica synthesis in order to achieve the first regio-selective silanization of a large pore dendritic silica particle. Upon complete characterization of the newly synthesized material, we studied the properties of the subsequent rubber composites materials. Results showed that this new filler yield very low energy dissipation and is resistant to aggregate dislocation, unlike traditional fillers. This results in superior fatigue properties. But the downside is that low energy dissipation means low traction performances. To remedy that, we implemented a dual-filler system in which smaller silica particles interfere in between the larger dendritic particles. This showed to drastically increased the filler-filler interaction and thus the traction performances, with still the benefit of lower rolling resistance. In a word, the traction/rolling resistance balance can be modulated by the relative composition of the two fillers. This results, beyond the possible technical application, ask new interrogations on the role the filler network dynamic in a composite, and how it responds to mechanical stress solicitation.

This doctoral thesis work is built over the pre-existing knowledges in the field of silica filler for tire tread rubber, and silica synthesis and silanization. It challenges the current model for silica reinforcement rubber by studying in more detail the two roles that silane coupling agents have, as well as demonstrating that a different filler morphology and filler network dynamic can lead to good performances and interesting new filler dynamic.

Regio-selectively modified dendritic silica filler already show good performances, but this system surely opens more questions and potential studies to be carried. Indeed, the versatility of this system give lots of opportunities for modification and investigation. We will develop some of them here.

In this work, the molar concentration of mercaptosilane co-condensed into the silica framework was not extensively studied. In term of cost efficiency and structure-related properties, it would be interesting to explore the properties variation of the material with a wide range of mercapto content. Similarly, the effect of the alkylsilane quantity was not studied. Because this silane is on the outside of the particle, it is likely to have an important role into the filler-filler and filler-rubber interaction. Also, the role of the remaining surface silanol is still unknown. Because these particles have a porous structure, it is hard to know if any exterior surface silanols remain after the silanization. Indeed, even with solid-state ^{29}Si NMR, interior and exterior silanols cannot be differentiated. To do so, one may try to chemically bond a probing molecule to accessible silanols and indirectly quantify the remaining content. This could be used to track the extent of conversion of silanols during silanization, but also understand if remaining silanols can have a significative effect, positive or negative, over the filler-filler interaction, through hydrogen bonding. Identically to the dual-silane pre-treated silica developed in Chapter 2, the study of the silane synergy could reveal interesting phenomenon and performances. Moreover, at the level of the particle architecture, many parameters can be varied, like the particle size, pore size or shape. It is possible to synthesize similar fillers with smaller size by stopping the growth early, or by reducing the amount of monomer used. Smaller particles will very likely interact more together as they would be more closely packed. The synergistic effect with the smaller fractal filler would be a valuable study to carry, but more generally, studying the effect of dual-filler systems while varying the size of the two fillers would very likely give the opportunity to observe unique filler network dynamic under stress and deformation. Because synthesis and modification parameters are so numerous, the potential for new research on this system alone is yet to be unravel.

Overall, the research for innovative fillers rubber is livelier than before, with the advent of the use of bio-source materials like cellulose or lignin. Lot of efforts are put into improving their properties to reach the performances level of silica and older, more experienced fillers. Surely, these new materials can benefit from the advances made for others, may it be with a better understanding of the filler-rubber dynamic and reinforcing mechanism, or from the advances in the field of fillers modification and architecture. Nevertheless, silica is not yet ready to be entirely replaced and many interesting investigations will be carried to develop even more its potential.

Publication List

Interplay of regio-selectively modified dendritic silica particles with styrene-butadiene rubber: The route towards better tires with lower rolling-resistance and higher grip

Moretto E., Stöffels C., Federico C. E., Rogé V., Staropoli M., Imiete I.E., Audinot J-N., Steiner P., Duez B., Lenoble D., Thomann J-S.

Chemical Engineering Journal, 2023

DOI: 10.1016/j.cej.2023.141964

Dual-silane pre-modified silica nanoparticles – Synthesis and interplay between chemistry, mechanical and curing properties of silica-rubber nanocomposites: Application to tire tread compounds.

Moretto E., Fernandes J.P.C., Staropoli M., Rogé V., Steiner P., Duez B., Lenoble D., Thomann J-S.

ACS Omega, 2022,

DOI: 10.1021/acsomega.2c00665

Original Basic Activation for Enhancing Silica Particle Reactivity: Characterization by Liquid Phase Silanization and Silica-Rubber Nanocomposite Properties.

Moretto E., Yan C., Dieden R., Steiner P., Duez B., Lenoble D., Thomann J-S.

Polymers 2022, 14, 1676.

DOI: 10.3390/polym14091676

Hybrid Silica-Based Fillers in Nanocomposites: Influence of Isotropic/Isotropic and Isotropic/Anisotropic Fillers on Mechanical Properties of Styrene-Butadiene (SBR)-Based Rubber.

Staropoli M., Rogé V., Moretto E., Didierjean J., Michel M., Duez B., Steiner P., Thielen G., Lenoble D., Thomann J-S.

Polymers 2021, 13, 2413.

DOI: 10.3390/polym13152413

Revealing the dehydration/deuteration processes at the liquid-solid interface by nuclear magnetic resonance spectroscopy.

Yan C., Moretto E., Kachouri O., Biagi J-L., Thomann J-S, Kayser F. and Dieden R.

Colloids and Surfaces A: Physicochemical and Engineering Aspects, 2022, 637, 128260.

DOI: 10.1016/j.colsurfa.2022.128260.

Semiquantitative Solid-State NMR Study of the Adsorption of Soybean Oils on Silica and Its Significance for Rubber Processing.

Yan C., Sarma A.D., Moretto E., Thomann J-S, Verge P., Schmidt D., Kayser F., and Dieden R.

Langmuir 2021 *37* (34), 10298-10307.

DOI: 10.1021/acs.langmuir.1c01280

Appendices

In this section, the collaborative works resulting in a published scientific peer-reviewed journal are presented. A brief description of the articles and of my scientific contribution can be found here below. The reprints of these second-author articles, listed in the publication list, are presented below.

The collaboration work entitled "*Hybrid Silica-Based Fillers in Nanocomposites: Influence of Isotropic/Isotropic and Isotropic/Anisotropic Fillers on Mechanical Properties of Styrene-Butadiene (SBR)-Based Rubber*" explores the effect of hybrid filler systems on tire tread compounds mechanical properties. It was observed that the anisotropic clay filler Sepiolite aligns when a critical concentration of HDS silica is used, stiffening the composite. On the other hand, the introduction of large Stöber spherical particles disturbs the HDS silica percolating network and leads to poor reinforcement. This work contributes to the understanding of how the filler-filler interaction can affect the final properties of a composite material.

My contributions to this work lays in the conceptualization of the experiments, the collaborative experimental work for the synthesis of the silica fillers and the composites, as well as the analysis of the results, the review, and corrections of the article.

The work "*Revealing the dehydration/deuteration processes at the liquid-solid interface by nuclear magnetic resonance spectroscopy*" develops a solid-state cross proton-silicon NMR polarization technique that shows efficient at studying surface silanols and adsorbed water on silica particles surface. Indeed, these two parameters are key when it comes to silica silanization. Surface hydroxyls groups, silanols, are the reactive anchor points for organosilanes. Adsorbed water is essential as a catalyst in hydrolysis-condensation reactions and enables the reaction between silane and silica. The development of this technique benefited from the synthesis of ^{29}Si-enriched precipitated silica as a gold standard for NMR technic testing and implementation. This NMR technique was used for the development of a more convenient liquid state methodology as an alternative to the classical TGA for the analysis of silanol and silica moisture.

I contributed to this work through the elaboration of synthesis process, synthesis, and full characterization of the ^{29}Si-enriched precipitated silica particle for the elaboration of the NMR technique, as well as through the conceptualization of the moisture and silanol quantification experiment.

"*Semiquantitative Solid-State NMR Study of the Adsorption of Soybean Oils on Silica and Its Significance for Rubber Processing*". This work uses a surface-selective NMR method developed with ^{29}Si-enriched precipitated silica to probe the affinity of newly synthesized soybean oil processing oil with silica filler in tire rubber compound. This method allowed to corroborate composites mixing energies with the degree of soybean oil epoxidation. This result helps to better establish structure-to-property relationship and bring more knowledge on the complex interaction of silica filler with various components of a tire rubber compound.

My contributions to this work are the elaboration of synthesis process, synthesis, and full characterization of the ^{29}Si-enriched precipitated silica particle for the elaboration of the NMR technique, as well as through the conceptualization and discussion around the interactions between the silica filler and the surrounding polymer and additives within the composites.

polymers

MDPI

Article

Hybrid Silica-Based Fillers in Nanocomposites: Influence of Isotropic/Isotropic and Isotropic/Anisotropic Fillers on Mechanical Properties of Styrene-Butadiene (SBR)-Based Rubber

Mariapaola Staropoli [1,*], Vincent Rogé [1], Enzo Moretto [1], Joffrey Didierjean [1], Marc Michel [1], Benoit Duez [2], Pascal Steiner [2], Georges Thielen [2], Damien Lenoble [1] and Jean-Sébastien Thomann [1]

[1] MRT Department, Luxembourg Institute of Science and Technology, 41 Rue du Brill, Belvaux, L-4422 Luxembourg, Luxembourg; vincent.roge@list.lu (V.R.); enzo.moretto@list.lu (E.M.); joffrey.didierjean@list.lu (J.D.); marc.michel@list.lu (M.M.); damien.lenoble@list.lu (D.L.); jean-sebastien.thomann@list.lu (J.-S.T.)
[2] Goodyear S.A, Avenue Gordon Smith, Colmar-Berg, L-7750 Luxembourg, Luxembourg; benoit_duez@goodyear.com (B.D.); pascal_steiner@goodyear.com (P.S.); georges_thielen@goodyear.com (G.T.)
* Correspondence: mariapaola.staropoli@list.lu; Tel.: +352-275-888-4449

check for updates

Citation: Staropoli, M.; Rogé, V.; Moretto, E.; Didierjean, J.; Michel, M.; Duez, B.; Steiner, P.; Thielen, G.; Lenoble, D.; Thomann, J.-S. Hybrid Silica-Based Fillers in Nanocomposites: Influence of Isotropic/Isotropic and Isotropic/Anisotropic Fillers on Mechanical Properties of Styrene-Butadiene (SBR)-Based Rubber. *Polymers* **2021**, *13*, 2413. https://doi.org/10.3390/polym13152413

Academic Editor: Francesco Paolo La Mantia

Received: 17 June 2021
Accepted: 19 July 2021
Published: 22 July 2021

Abstract: The improvement of mechanical properties of polymer-based nanocomposites is usually obtained through a strong polymer–silica interaction. Most often, precipitated silica nanoparticles are used as filler. In this work, we study the synergetic effect occurring between dual silica-based fillers in a styrene-butadiene rubber (SBR)/polybutadiene (PBD) rubber matrix. Precipitated Highly Dispersed Silica (HDS) nanoparticles (10 nm) have been associated with spherical Stöber silica nanoparticles (250 nm) and anisotropic nano-Sepiolite. By imaging filler at nano scale through Scanning Transmission Electron Microscopy, we have shown that anisotropic fillers align only in presence of a critical amount of HDS. The dynamic mechanical analysis of rubber compounds confirms that this alignment leads to a stiffer nanocomposite when compared to Sepiolite alone. On the contrary, spherical 250 nm nanoparticles inhibit percolation network and reduce the nanocomposite stiffness.

Keywords: nanocomposites; silica; Sepiolite; dual fillers

1. Introduction

The improvement of mechanical properties of rubber-based nanocomposites has been extensively investigated over the last decades. The development of composites for aeronautic, space, marine, military, or automotive applications is one of the main efforts of many industries at the present time [1]. Particularly, industrials are interested in improving the stiffness, the modulus, the fatigue resistance, the wear resistance, the corrosion resistance, or the rolling resistance with cheap, lightweight, and non-toxic materials. As an example, the reinforcement of soft synthetic rubbers like styrene-butadiene rubber (SBR) is crucial for tire technology industries [2]. Polymer-based composites are usually reinforced with fillers and coupling agents [3]. Consequently, many different types of fillers have been investigated for the improvement of mechanical properties of SBR-based polymers. They can be classified in three categories: reinforcing fillers, semi-reinforcing fillers, and non-reinforcing fillers, according to their size, shape, and composition [4]. Reinforcing fillers are usually nanometric objects with one dimension smaller than 100 nm. They have a strong interaction with the polymeric matrix and result in an increase of the tensile strength, tear resistance, and abrasion resistance [5]. Semi-reinforcing fillers (100–500 nm) induce a moderate improvement of the tensile strength and tear resistance, but have no effect on the abrasion resistance [6]. Non-reinforcing fillers (>500 nm) have no specific effect on mechanical properties; they are most often used as diluent.

Several types of reinforcing fillers have been already investigated. Inorganic fillers represent a large fraction of them. We can list natural mineral clays, like montmorillonite [7], mica [8], talc [9]; salts, like calcium carbonate $CaCO_3$ [10], Ca_2SO_4 [11], $BaSO_4$ [12], phosphates [13]; and metal oxides or hydroxides, like SiO_2 [14], ZnO [15], Al_2O_3 [16], MgO [17], $Al(OH)_3$ [18], or $Mg(OH)_2$ [19]. Organic fillers have also been studied as reinforcing fillers, like carbon-based materials: black carbon [20], graphite [21], and carbon nanotubes [22]; or bio-sourced cotton [23], wood flour [24], and cellulose fibres [25]. Among all cited reinforcing fillers, black carbon and silica nanoparticles are the most used for SBR rubber reinforcement in industrial applications [2,26,27]. Carbon black has been the first reinforcing filler largely used in the rubber industry owning to its ability to improve tear strength, hardness, and abrasion resistance of many rubbers [28]. Later, the development of "green tires" based on silica nanoparticles fillers has demonstrated enhanced reinforcing properties of silica on abrasion resistance, rolling resistance, and wet grip compared to black carbon [29]. The origin of the reinforcement in the composite arises from rigid SiO_2 particles that act as stress concentrators due to their different elastic properties compared to the polymer matrix [30].

Usually, fumed or precipitated silica nanoparticles are used as silica fillers. If they are relatively cheap to process, those silica nanoparticles tend to agglomerate in the rubber, due to silanol surface group interactions forming inter-particles bonding [31] and show poor filler–rubber interactions [32]. Unfortunately, those two parameters are crucial to reach efficient homogeneous reinforcing properties. Consequently, different strategies have been foreseen in order to improve the processability of silica, like the use of processing oils [33] or silane coupling agents, to enhance the dispersity and chemical interaction between the rubber and fillers. Most of the coupling agents used in silica tread compounds belong to the families of organo-silane. The hydrophilic part of the silane coupling agent reacts with silanol surface groups of the silica [34], while the hydrophobic alkyl-mercapto $(CH_2)_n$-SH) will enhance silica dispersion and covalently react with the accelerator, sulphur, and finally rubbers during the vulcanization step [35]. Sol-gel synthesised silica nanoparticles represent another strategy to reach efficient silica-based reinforced particles. The most known process is based on the poly-condensation of a silicon alkoxide precursor, usually the tetraethyl orthosilicate (TEOS), in basic conditions. It is referred to as the Stöber process [36]. Some studies have shown that Stöber silica nanoparticles are more homogeneously dispersed in rubbers [37–39]. The benefit of the Stöber process is that it allows the control of particles sizes, which is another parameter affecting composites' mechanical properties [14,30]. Other works have focused on the synthesis of silica nanoparticles in-situ during the composite processing. They highlight a homogeneous silica dispersion in the nanocomposite, even without silane coupling agent, with an improvement of the nanocomposite tensile strength [40–42].

In parallel to concentrated research efforts on spherical nanoparticle fillers, the interest in fillers' morphological aspect has recently been growing in the scientific community. Anisotropic structures have emerged as a new possibility to further strengthen mechanical properties of rubber-based nanocomposites. R. Scotti et al. have synthesized anisotropic silica nanorods (with an aspect ratio up to 10) using a Stöber-derived process with CTAB as surfactant [43]. They pointed out a stronger reinforcement of the nanocomposite with anisotropic silica. This phenomenon is partially explained by an alignment of anisotropic filler domains oriented in the main axis where a high rubber fraction is tightly trapped between fillers [44]. This alignment is favoured with higher nanorod aspect ratios. The same behaviour has been observed with anisotropic silica-based natural clays: Sepiolite. Different studies have shown that Sepiolite could be an effective substitute to spherical silica nanoparticles [45]. As observed in the case of silica nanorods, the formation of oriented Sepiolite aggregates in the rubber matrix reinforce mechanical properties of composites [46]. However, a surface state modification (HCl treatment) of Sepiolites nanofibers is often performed in order to create more silanol surface reactive groups and to favour the filler/rubber interaction [47]. Another alternative to conventional fillers could be the use of hybrid fillers with identical or different morphologies [48]. Dual fillers nanocomposites based on black carbon and precipitated silica have been widely studied and used over the last decades, particularly in the tire industry [49,50]. Other studies have shown an interest in the synergetic effect of fillers with different morphologies, like spherical nanoparticles associated with 1D materials such as carbon nanotube [22], montmorillonite [51] or Sepiolite [48].

According to those previous works, it appears that the study of the reinforcement of a type of rubber filled with precipitated silica partially substituted by spherical and anisotropic silica structures could strengthen the understanding of the reinforcement mechanism. The novelty of this study is to elucidate the origin of this reinforcement, by substituting the fractal spherical silica filler with anisotropic Sepiolite, or bigger spherical nanoparticles. For the first time, this study highlights the direct correlation between the specific orientation of the fillers at the microscopic level and the resulting macroscopic mechanical properties measured through DMA and tensile tests. Consequently, in this work, we aim at studying the synergetic effect occurring between two types of hybrid silica-based fillers, fractal/spherical and fractal/anisotropic, on the mechanical properties of the synthesized nanocomposite. HDS particles, characterized by a fractal surface, have been used as main filler type and mixed with Sepiolite and Stöber particles, rod-like and spherical, respectively, for obtaining dual filler compounds. Highly Dispersed Silica nanoparticles (HDS)/Stöber silica nanoparticles and precipitated silica HDS/Sepiolite have been processed in a SBR-based rubber matrix.

2. Materials and Methods

All chemical used for the synthesis of sol-gel silica nanoparticles have been purchased from Sigma Aldrich. The growth of silica nanoparticles was performed as follows: in 1 l of ethanol (99%), 80 mL of ultra-pure water (>18 Ω·cm), and 45 mL of ammonium hydroxide solution (NH_4OH 25%) were added at room temperature under stirring at 500 rpm. After homogenisation, 46 mL of Tetraethyl orthosilicate (TEOS 99%) were quickly added to the solution and left under stirring for 2 h. The grown silica nanoparticles were extracted from the solution by centrifugation at 2500 rpm for 10 min and cleaned in water and ethanol twice. This process allowed the synthesis of homogeneous and dispersed silica nanoparticles with a diameter of 250 nm.

High-resolution Scanning Transmission Electron Microscopy (STEM) images of nanocomposites were recorded with a Helios Nanolab 650 microscope (FEI, Eindhoven, Netherlands), at an acceleration voltage of 30 kV and a current of 50. STEM analyses were performed in bright field mode. Nanocomposites lamellas around 50–70 nm of thickness were prepared using a Cyro-Ultramicrotom EM UC7 (Leica, Wetzlar, Germany), at a temperature of −120 °C. Dynamic modulus of nanocomposites were determined using a 242C dynamic mechanical analyser (DMA) (Netzch, Selb, Germany). Thermograms were obtained in single cantilever mode, with a free length of 5 mm (15% strain amplitude) under a vibration frequency of 10 Hz. The studied temperature range was fixed between –100 °C to 8 °C with a heating rate of 0.5 $°C·min^{-1}$ in air atmosphere. The tensile behaviour of nanocomposites was determined at room temperature, under a strain rate of 3 $mm·s^{-1}$, with a 5967 Series Universal Testing System (Instron, Norwood, MA, USA).

Nanocomposite Synthesis Procedure

Nanocomposites based on SBR and PBD (polybutadiene) were compounded in a Brabender Plasti-Corder Lab station internal mixer, working with 85 cm^3 mixing chamber and a 0.75 fill factor. The Goodyear Tire & Rubber Company (Colmar-Berg, Luxembourg) provided all raw materials: HDS nanoparticles (10 nm, 200 $m^2·g^{-1}$ silica grade), SBR rubber, polybutadiene rubber, zinc oxide, Treated Distillate Aromatic Extracted oil (TDAE oil), stearic acid, N-(1,3-Dimethylbutyl)-N′-phenyl-p-phenylenediamine (6PPD), Bis(triethoxysilylpropyl) disulphide (TESPD), sulfur, 2-Mercaptobenzothiazole (MBT), Diphenylguanidine (DPG), and N-Cyclohexyl-2-benzothiazolesulfenamide (CBS). The composition of composites (expressed in phr) is presented in Table 1. Typically, 80 phr of SBR and 20 phr of PBD were blended in the mixing chamber at 80 °C, 40 rpm. Then, 25 phr of TDAE oil, 2.5 phr of zinc oxide, 3 phr of stearic acid, 2.5 phr of 6PPD, 8 phr of TESPD, and 80 phr of silica fillers were introduced under mixing for 10 min. After this first step, the nanocomposites were passed six times in a roll mill system at 50 °C, 5 mm gap, 32–24 rpm, and left for cooling for one hour. In a second step, the cooled composite was introduced in the mixer with 1.1 phr sulphur, 0.3 phr MBT, 3.2 phr DPG, and 2.3 phr CBS at 60 °C, 40 rpm for 2 min. Another six passes in the roll mill system were performed and the nanocomposite was finally cured under a hot press at 170 °C, 150 Bars for 10 min.

Table 1. Nano-composite composition in phr.

Element	Element Concentration (phr)
SBR	80
PBD	20
TDAE Oil	25
Zinc Oxide	2.5
Stearic Acid	3
6PPD	2.5
TESPD	8
Sulfur	1.1
MBT	0.3
DPG	3.2
CBS	2.3
Silica-based filler	**80**

As the composition of all samples was identical, independently of the type of filler used, we assumed that the degree of crosslinking by sulphur in all nanocomposites was constant. For this reason, it is not discussed in the paper.

3. Results and Discussion

The influence of spherical/spherical and spherical/anisotropic dual fillers in nanocomposites has been studied through nine samples prepared with precipitated silica HDS nanoparticles (used as the major filler in dual filler nanocomposites, forming fractal silica aggregates), silica Stöber nanoparticles of 250 nm diameter, and Sepiolite silica nanorods as fillers. The classification and filling degree of the samples studied within this work is indicated in Table 2. Three composites have been prepared with 80 phr only one type of silica filler (i.e., HDS, or Stöber nanoparticles of 250 nm diameter, or Sepiolite silica nanorods) as references (Figure 1).

Table 2. Sample classification-filler amount in SBR rubber matrix.

Sample	HDS (phr)	Sepiolite (phr)	Stöber (phr)
HDS-80 phr	80		
Sepiolite-80 phr		80	
Stöber-80 phr			80
HDS/Sepiolite-70/10	70	10	
HDS/Sepiolite-60/20	60	20	
HDS/Sepiolite-50/30	50	30	
HDS/Stöber-70/10	70		10
HDS/Stöber-60/20	60		20
HDS/Stöber-50/30	50		30

Three nanocomposites have been prepared with different ratios of fractal/anisotropic fillers HDS/Sepiolite: respectively, 70/10 phr, 60/20 phr, and 50/30 phr (Figure 2).

Three other samples have been prepared with different ratios of spherical/spherical fillers HDS/Stöber nanoparticles 250 nm: respectively, 70/10 phr, 60/20 phr, and 50/30 phr (Figure 3).

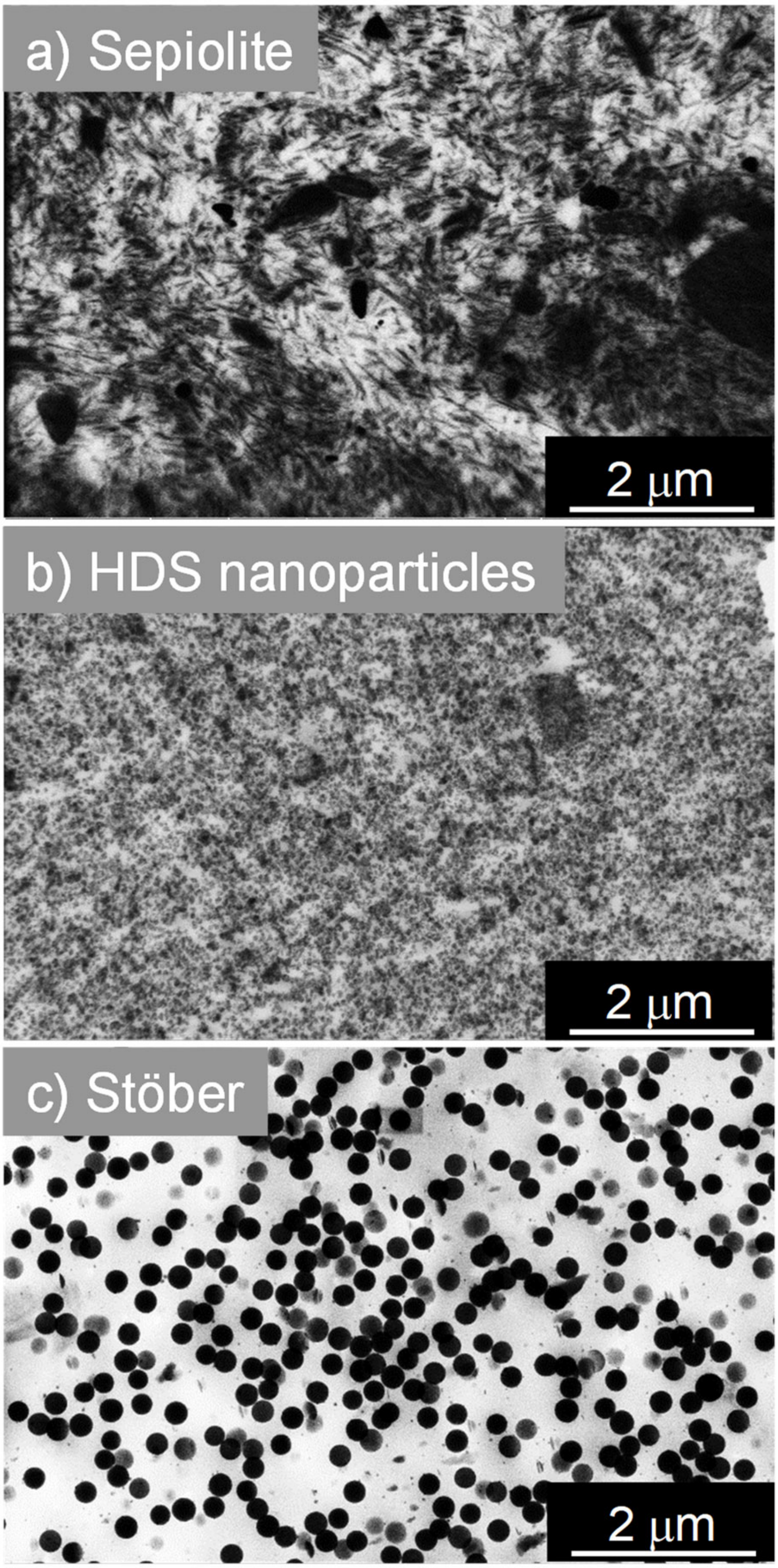

Figure 1. STEM images of reference nanocomposites synthesized with 80 phr of one type of filler only: (**a**) Sepiolite, (**b**) HDS, and (**c**) Stöber nanoparticles (250 nm).

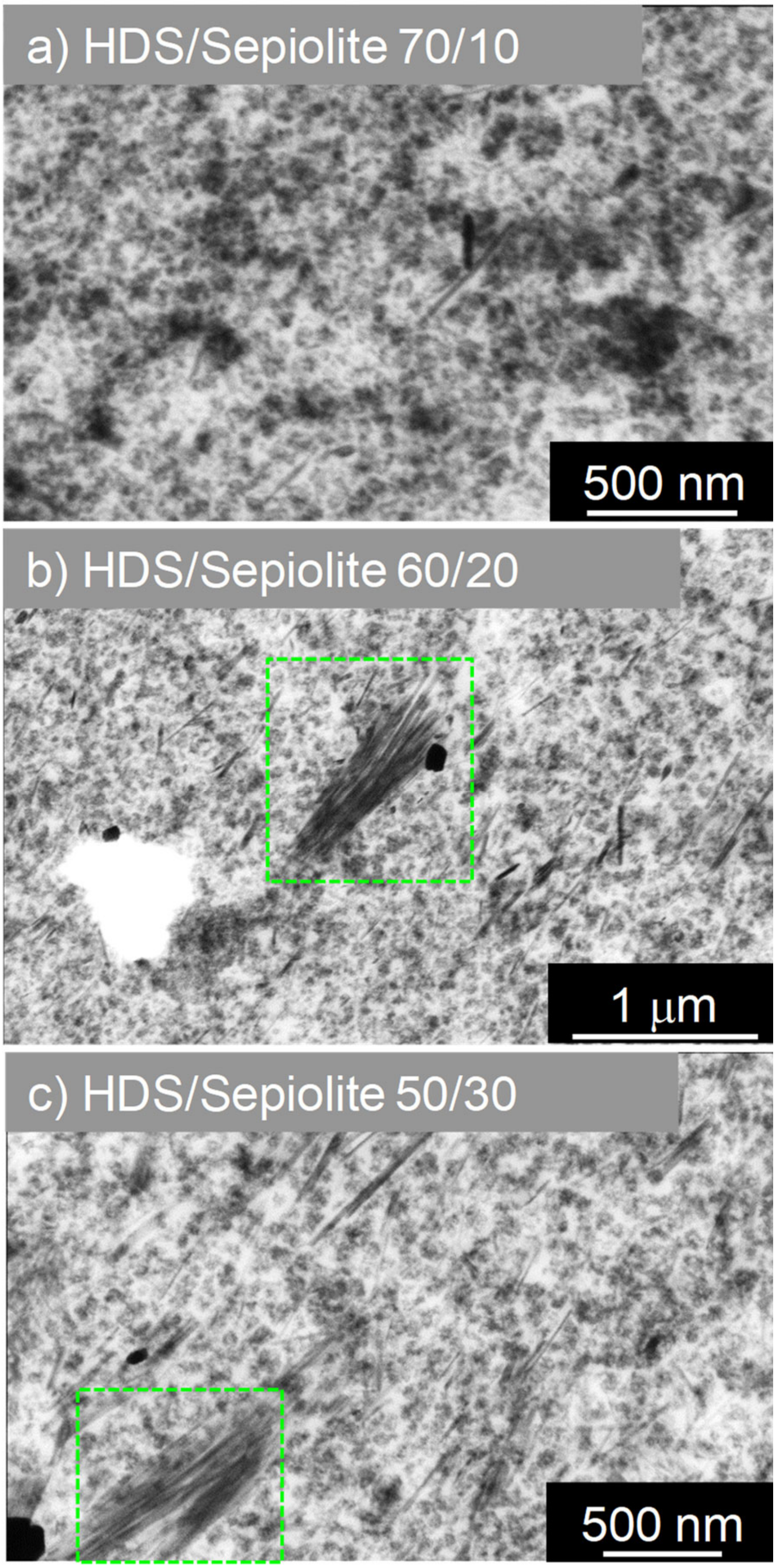

Figure 2. STEM images of nanocomposites synthesized with dual filler: (**a**) HDS/Sepiolite-70/10, (**b**) HDS/Sepiolite-60/20 (60/20), (**c**) HDS/Sepiolite-50/30.

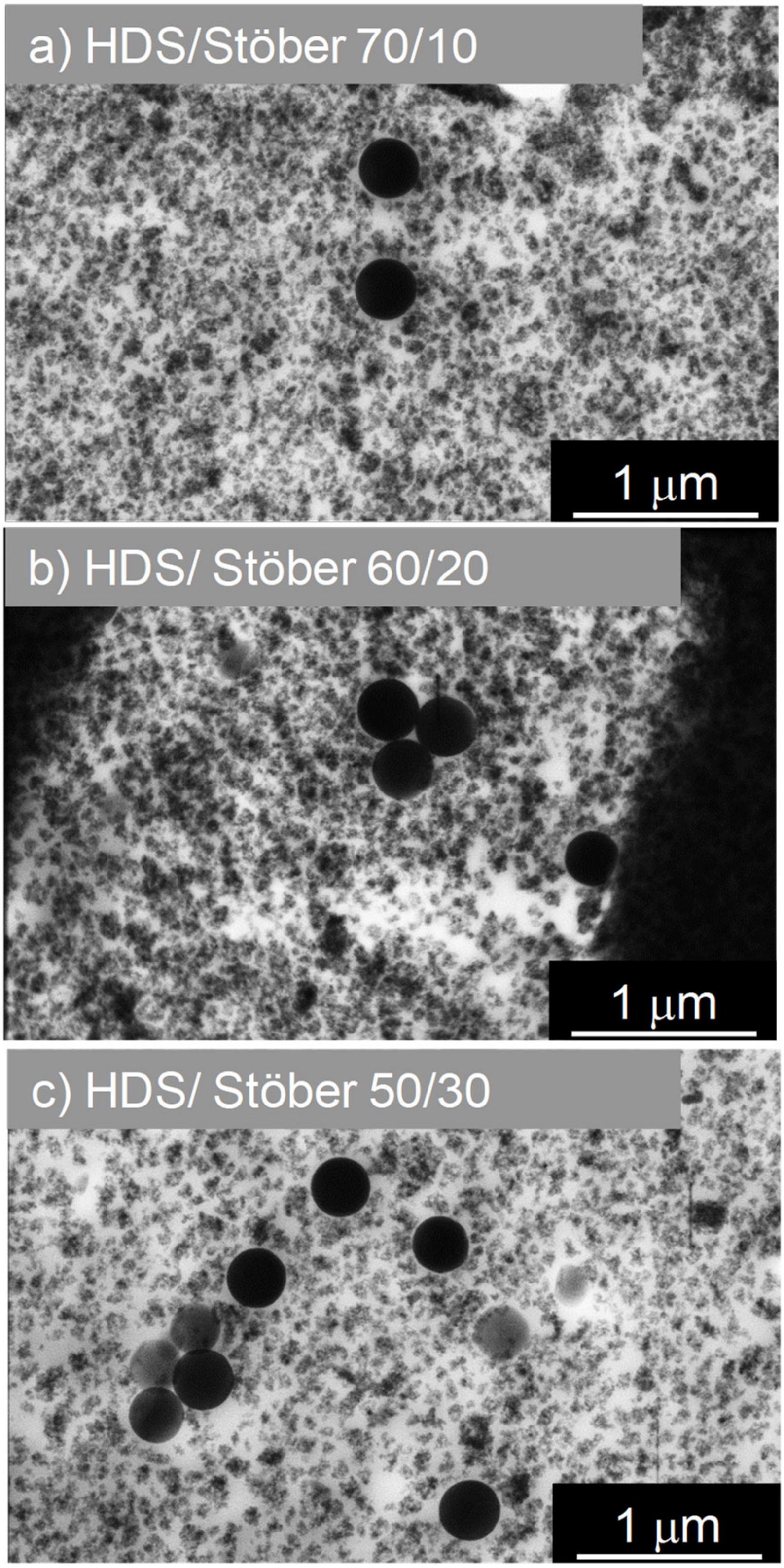

Figure 3. STEM images of nanocomposites synthesized with dual filler: (**a**) HDS/Stöber-70/10, (**b**) HDS/Stöber-60/20, (**c**) HDS/Stöber-50/30.

The total silica filler charge in all nanocomposites was kept constant at 80 phr. We can clearly distinguish on STEM pictures reported in Figure 1 the spatial distribution of silica fillers in composites. In the case of nanocomposites prepared with Sepiolite nanorods (Figure 1a), HDS nanoparticles (Figure 1b), or Stöber nanoparticles (Figure 1c) as single filler, there is no observable preferential orientation for any kind on filler. Fillers are randomly dispersed in the polymeric matrix. Concerning the percolation threshold of fillers in those nanocomposites, the two samples containing 80 phr of HDS nanoparticles and Sepiolite seem to outreach this percolation point within the rubber matrix. Together with well-distributed material, Sepiolite already shows bundles of silicate nanorods which may be due to an insufficient de-lamination or exfoliation-like process in the mixer. HDS clusters, beyond the percolation threshold, are in contact and seem to form an agglomerate exhibiting a uniform filler background. On the contrary, in the case of Stöber 80 phr, the particles are well dispersed and do not form a percolating network. Stöber nanoparticles are 250 nm diameter. They are approximately twenty times bigger than HDS nanoparticles or than the Sepiolite width. Consequently, an equal "mass" of 80 phr of Stöber nanoparticles in the rubber corresponds with a smaller number of nanoparticles per unit volume compared to HDS or Sepiolite. The same conclusion applies to the overall silica surface area that is much lower for Stöber NPs than in the case of HDS. Those two behaviours explain the non-percolating state of Stöber nanoparticles in the compound (Figure 1c). When HDS nanoparticles and anisotropic Sepiolite (Figure 2) are mixed as dual fillers in a ratio of 70/10 (Figure 2a), the structure looks very similar to the HDS single-filler nanocomposite, but few dispersed Sepiolite needles are visible within the structure. Increasing the amount of Sepiolite in the compound, i.e., HDS/Sepiolite-60/20 (Figure 2b) and HDS/Sepiolite-50/30 (Figure 2c), leads to the formation of bundles of Sepiolite in the matrix (highlighted with green boxes). Interestingly, they are showing a preferential orientation toward one direction. It is worth mentioning that the orientation of the Sepiolite rods was not observed in absence of Silica HDS (Figure 1a). The presence of HDS is apparently responsible for this Sepiolite alignment. Having oriented structures within the composite at the nanometric/micrometric scale could lead to improved macroscopic properties of the nanocomposite. Dual spherical/spherical fillers are presented in the Figure 3, with ratios of HDS/Stöber nanoparticles of 70/10 (Figure 3a), 60/20 (Figure 3b), and 50/30 (Figure 3c). Those STEM images show dispersed Stöber and HDS nanoparticles in the rubber matrix. On the picture Figure 3c, it appears that the replacement of 30 phr of HDS with larger Stöber nanoparticles prevents the percolation of HDS fillers in the rubber matrix.

3.1. Dynamic Mechanical Analysis

DMA analysis has been performed in order to determine mechanical properties of nanocomposites. Figure 4 shows the evolution of the storage modulus E' with the temperature in a range from −120 °C and 80 °C at the frequency of 1 Hz for the reference SBR samples containing, respectively, HDS-80 phr, Sepiolite-80 phr, and Stöber-80 phr with same filling degree.

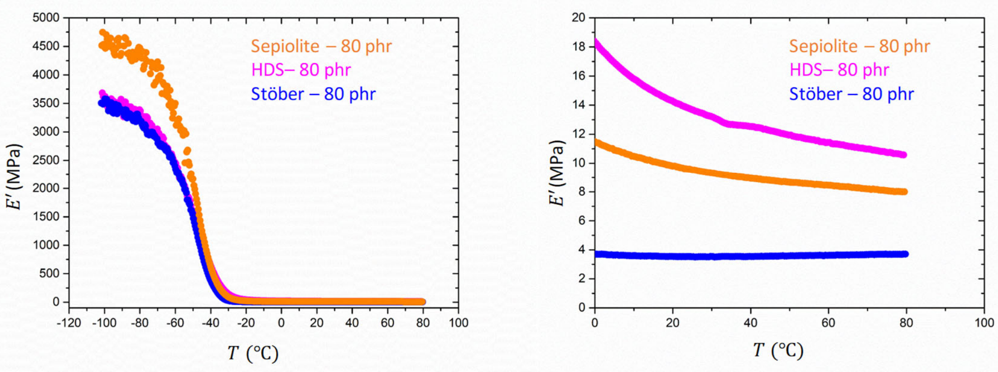

Figure 4. Evolution of E' with temperature for the reference SBR samples, HDS-80 phr (magenta), Sepiolite-80 phr (orange), and Stöber-80 phr (blue).

In the rubbery state, the sample HDS-80 phr shows a higher elastic modulus compared to the other references. This result could be explained considering that fractal silica particles as HDS tend to form aggregates and agglomerates. This hierarchical structure, depending on the extension of the filler network, can occlude a large amount of rubber, leading to an immobilization of the occluded portion of the matrix and therefore to an increase of the stiffness in respect to the case of a dispersed system. The occluded and immobilized rubber is responsible for the increase of the effective volume fraction of the rubber. Despite the different geometry of the Sepiolite fillers, characterized by a more rod-like shape, sample Sepiolite-80 phr exhibits a lower value of the elastic modulus in the high temperature range. Rod-like silica fillers are expected to enhance the reinforcement with respect to the unaggregated spherical ones. The foreseen reinforcement of non-interacting spherical particles follows the Einstein prediction, which depends linearly on the volume fraction ϕ but does not depend on the size, as obtained from $f = 1 + 2.5\,\phi$ where f is the reinforcement factor, i.e., the ratio of the reinforced modulus over the unfilled modulus. For rods, a similar expression is known, with $f = 1 + (2/3)\ p\phi$ [52]. Here, p represents the aspect ratio as explained above. The thinner the rod is or the longer it is, the more reinforcement is expected. Only for values of $p \sim 4$, rods cannot be distinguished from spheres. The formation of a network due to an alignment of the fibers, as reported in the literature, could lead to an increase of the trapped rubber between layers of fibers [40]. However, in our case, the formation of clusters in the case of Silica HDS-80 phr seems to have a dominant effect on the reinforcement in comparison to the anisotropic fillers. The higher reinforcement of HDS, although rods should be more efficient given the aspect ratio, is caused by the aggregate morphology which expresses itself in a corresponding Payne effect. Higher moduli are due to the additional intra- and inter-aggregate bonds. The STEM analysis, indeed, did not reveal a preferential orientation of the Sepiolite anisotropic fillers in the SBR rubber in absence of HDS. The lowest modulus was instead observed for the third reference sample analyzed: Stöber-80 phr. In this case, the isotropic spherical fillers (Stöber particles) are known to give rise to a highly dispersed system, reducing, therefore, the immobilization of the polymer at the filler–matrix interphase [53]. This last sample exhibits the lowest value of the storage modulus in the rubbery regime.

The values of the elastic modulus for the different types of fillers are corroborated by the trend of $tan\delta$ as a function of the temperature. All samples, as shown in Figure 5, show a prominent peak at ~ -25 °C, attributed to the glass transition. The sample Silica HDS-80 phr shows the lowest intensity peak at T_g. An intermediate peak intensity is observed for sample Sepiolite-80 phr followed by sample Stöber-80 phr, which exhibit the stronger dissipation in proximity of the transition temperature. This behaviour is explained considering the increase of the polymer chain amount involved in the transition. In the case of aggregating fillers like HDS, the degree of freedom of the polymer chains seems to be significantly decreased respective to the case of spherical particles as well as rod-like fillers.

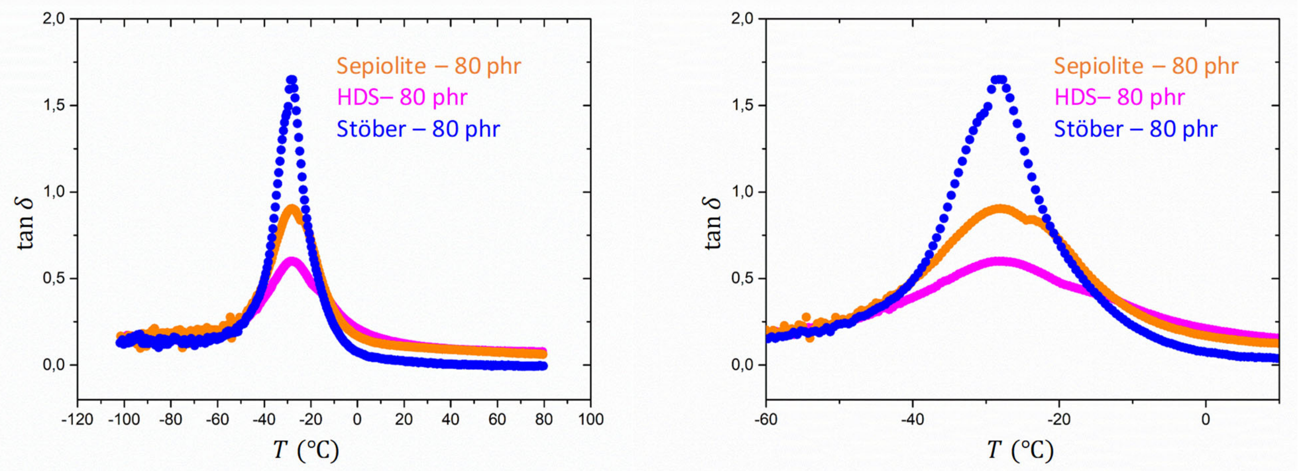

Figure 5. Evolution of $tan\delta$ for reference 80 phr SBR samples filled with Silica HDS-80 phr (magenta), Sepiolite-80 phr (orange) and Stöber-80 phr (blue).

A second peak with lower magnitude is observed for sample Silica HDS-80 phr and Sepiolite-80 phr at higher temperatures than T_g. This peak could be related to the slower relaxation process of the polymer segments bounded at the rubber-fillers interphase, characterized by a higher activation energy. The position of these peaks confirms the trend observed for the T_g. Sample Stöber-80 phr shows instead one dominant peak corresponding to T_g, possibly due to the very low amount of bounded rubber at the matrix–filler interphase [54].

The dual filler samples are now analysed in comparison to the references. Silica HDS has been gradually substituted, respectively, by Sepiolite and Stöber particles in order to obtain dual filler systems with total loading of 80 phr.

Three different dual filler SBR samples were analysed with the same filling degree. Figure 6 shows the storage modulus and the loss factor $tan\delta$ as a function of the temperature for Sepiolite/HDS dual filler compounds. Despite the lower modulus at high temperature observed for the Sepiolite-filled rubber compared to the HDS one, the increase of the Sepiolite content in the dual-filler system yields an increase of the storage modulus in the temperature range between 0 and 80 °C This evidence could be attributed to the cooperative effect of the two types of fillers. If 10 phr of HDS is replaced by Sepiolite, a strong drop of the modulus is observed in the rubbery regime. However, this drop seems to be compensated by the increase of the Sepiolite amount in the other dual filler compounds. The addition of a higher amount of Sepiolite in the dual filler compounds leads, as observed, to an increase of E' even though the sample containing HDS only exhibits the highest modulus value in the rubbery regime. This increase could be explained by considering the preferential arrangement of the anisotropic filler in the presence of the fractal one. The arrangement seems to be dependent on the amount of rod-like fillers in the dual filler mixture and is observed to be more effective for the compounds containing, respectively, 20 and 30 phr of Sepiolite (see Figure 2). The substitution of HDS with 10 phr of Sepiolite could, at first, give rise to a decrease of the stiffness of the compound, as the rod-like filler might induce a breakage of the HDS clusters. The increment of Sepiolite amount at the expenses of silica content in the case of HDS/Sepiolite-60/20 and HDS/Sepiolite 50/30 could, however, restore a more uniform mixture where now percolation of both silica and Sepiolite fillers occur and, because of an induced preferential orientation of the rods, yield a higher elastic modulus. In addition, during the mixing steps (internal mixer and roll mill), the formation of such a percolating network can play a key role in the Sepiolite orientation.

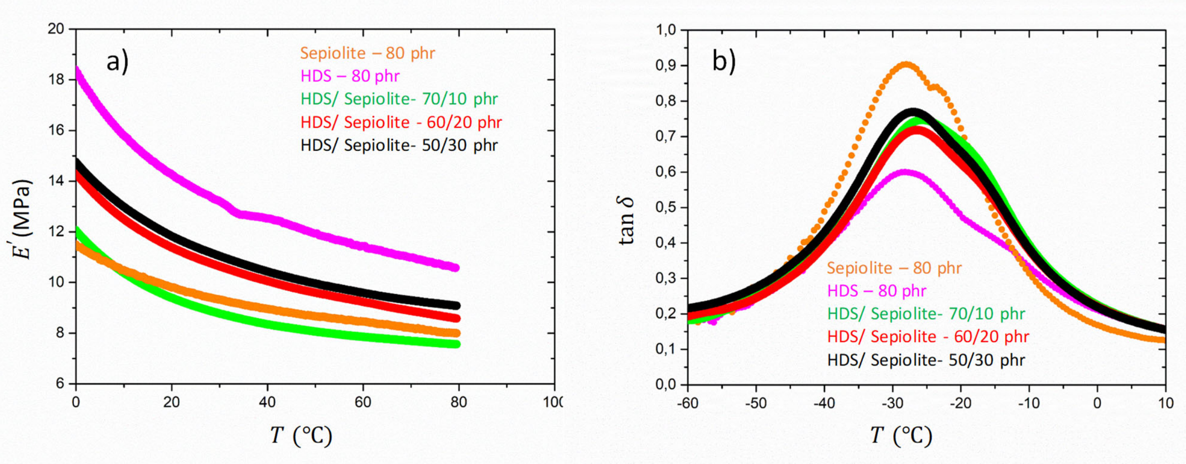

Figure 6. Plot of E' (**a**) and $tan\delta$ (**b**) versus temperature for reference SBR samples and dual fillers Sepiolite/HDS-10/70 phr, Sepiolite/HDS-20/60 phr, Sepiolite/HDS-30/50 phr.

The mixing energy required at the mixing/milling steps is higher when percolation is reached (see Table S1 in supporting information). As a consequence, the shearing forces applied to the compound will increase and those forces can be highly oriented, especially during the mixing or roll mill steps.

The evolution of *tanδ* (Figure 6) with the temperature is also analysed. In this case, the two peaks corresponding, respectively, to T_g and to the dynamic of the bounded rubber at the interphase are not well separated. The increased Sepiolite amount is not reflected by a shift of the secondary peak intensity as expected from the increase of the storage modulus. This result can be explained by the different structural arrangement occurring in the mixture of two different types of fillers with different geometry. The orientation of Sepiolite in the presence of percolating fillers such as HDS, as evidenced in Figure 2b,c, could, on the other hand, affect the specific arrangement of the Silica HDS clusters as a consequence of a cooperative effect. The preferential orientation of silica filler clusters, which is known to significantly affect the hysteresis behaviour as well as the elastic modulus of the rubbery compounds, is, however, not highlighted by the STEM images in our case. [55].

A different trend is instead reported for the mixtures of HDS and Stöber particles. Figure 7 shows the storage modulus and the loss factor *tanδ* as a function of the temperature for Stöber/HDS dual filler compounds.

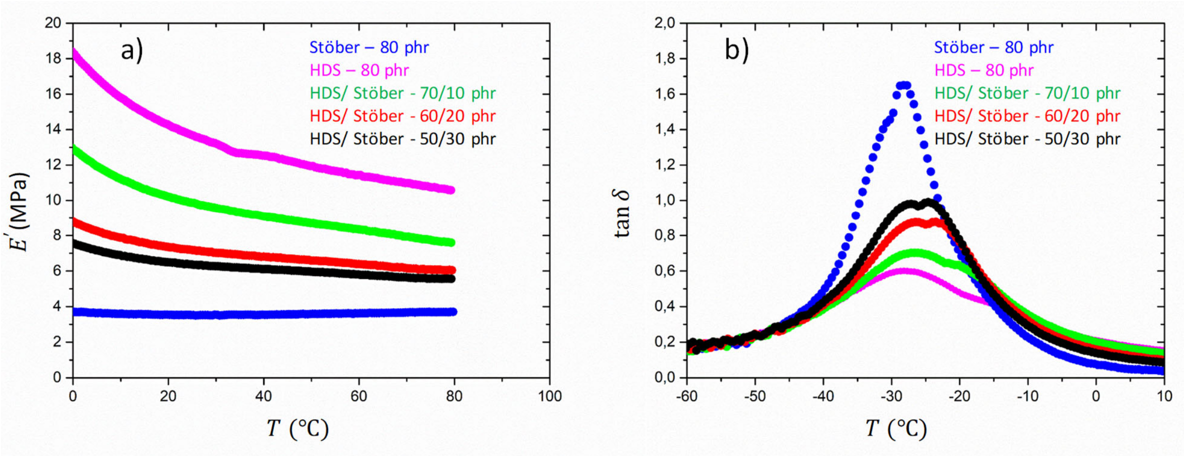

Figure 7. Plot of E' (**a**) and *tanδ* (**b**) versus temperature for reference SBR samples and dual fillers Scheme 10. phr (R-31), Stöber/HDS-20/60 phr (R-32), Stöber/HDS-30/50 phr (R-33).

The evolution of E' for the reference samples and the mixtures shows that the increase of the Stöber content in the dual-filler systems yields a decrease of the elastic modulus.

This behaviour could be attributed to the lower tendency of Stöber particles to form aggregates, as shown in the STEM pictures in Figure 3. A cooperative effect of the two fillers is, however, envisaged in this system, too. The higher content of Stöber particles in the mixture leads to a higher dispersion of the fillers in the rubber and, therefore, to a lower constraint exerted by the fillers on the rubber. The lower fraction of aggregates formed by HDS fillers is reflected in a smaller amount of bounded rubber. The reduction of aggregates formation with the substitution of HDS with Stöber particles has been confirmed by the STEM analysis. Figure 3 reveals that the decrease of HDS in the dual fillers system causes a different dispersion of the clusters and that the Stöber particles do not mix themselves into the aggregates due to their size, but position themselves in between agglomerates, therefore reducing the network. This leads to a lower modulus and can be compared to the effects of adding a non-interacting solvent to rubbers. This effect is not compensated by the increased amount of the spherical Stöber particles that are not forming aggregates and do not contribute to the reinforcement.

This observation is confirmed by the analysis of *tanδ* as a function of the temperature (Figure 7). The dual-filler compounds show a clear distinction between the main peak corresponding to the glass transition and the secondary peak at higher temperature related to the relaxation of the bounded rubber. A shift of the secondary peak to lower temperatures as well as an increase of its magnitude is observed with the increase of Stöber content in the mixture, indicating a lower constraint at the filler-rubber interphase.

For the dual filler systems, a cooperative interaction between the two types of fillers is observed. This synergic interaction, leading to a change in the elastic modulus in the rubbery regime, is found to be dependent on the geometry of the fillers as well as on their ability of forming hierarchical structures.

3.2. Tensile Tests

Figure 8 shows the stress-strain curves obtained for the mixtures of HDS and Sepiolite and the two reference samples containing only one type of filler. First, the analysis of the stress at low deformation is indicating that the sample SBR HDS 80 phr has a higher modulus than SBR Sepiolite-80 phr. A value of $E' \sim 14$ MPa was estimated for the sample HDS Silica-80 phr, while for the other reference, Sepiolite-80 phr, a value of $E' \sim 10$ MPa was found. These values seem to be approximately in agreement with the DMA values observed in Figure 6 at room temperature. For the mixtures, however, a value of $E' \sim 13$ MPa was observed, although the DMA experiments revealed clear differences among the moduli in the rubbery regime and, specifically, a significant drop when 10 phr of HDS silica were replaced by Sepiolite. To explain this discrepancy, the different sensitivity of the two techniques has to be taken into account. The tensile test does not allow a clear distinction of the moduli for the mixtures at very low strain as in the case of DMA test, which is instead carried out with a small deformation.

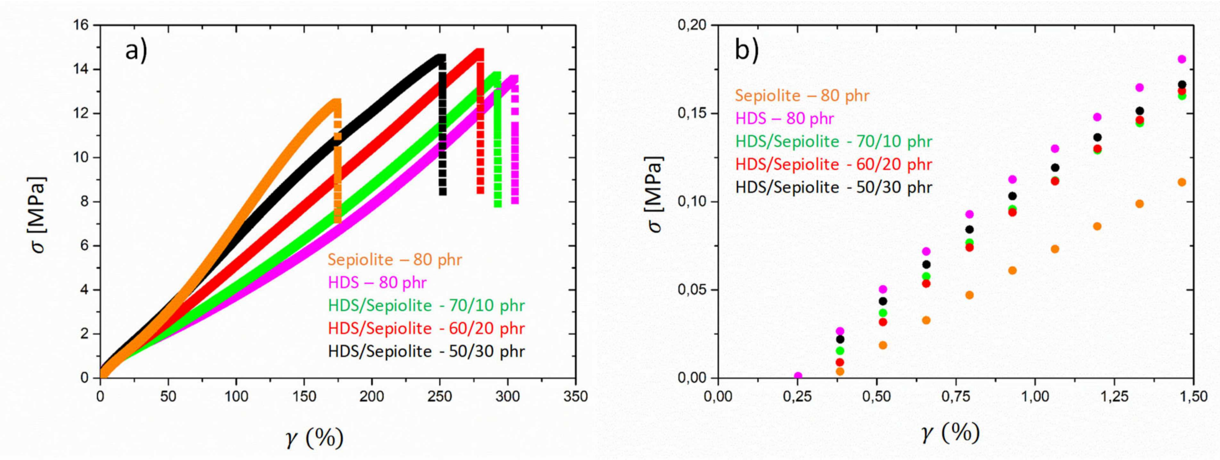

Figure 8. Stress-strain curves for mixtures of Sepiolite and HDS Silica dual filler compounds in the full deformation range (**a**) and at low deformation (**b**).

The high strain behaviour reveals the highest stress value for the SBR Sepiolite-80 phr, while a decrease is observed for the dual filler blends when the amount of Sepiolite decreases. The sample SBR HDS-80 phr shows the lower stress value at higher deformation. On the other hand, the value of elongation at break follows the opposite trend. These different behaviours could be explained by considering that, despite the higher reinforcement at low strain conferred by the silica HDS filler, the gradual strain induced by the orientation of the rods gives rise to a strain hardening of the rubbers containing the Sepiolite filler. This observation would also explain the decrease of the elongation at break with the increase of the Sepiolite amount. The rigid rods orienting along the deformation direction at high strain might cause a reduction of the rubber elongation ability.

Different behaviour was observed for the dual filler compounds containing Stöber particles and Silica HDS. The spherical Stöber filler was found to "dilute" the aggregates formed by HDS particles, leading to a decrease of the elastic modulus in the rubbery regime, as highlighted by SEM pictures in Figure 3. Stress-strain curves for dual fillers samples containing Stöber and Silica HDS particles are reported in Figure 9. The low strain regime shows the highest reinforcement for the sample SBR HDS-80 phr, while the other reference sample SBR Stöber-80 phr exhibits the lowest stress in the whole deformation range and the lowest elongation at break, with an estimated modulus of $E' \sim 3$ MPa. The dual filler compounds show that the increase of the Stöber amount in the mixtures leads to a decrease of the stress value. For the three mixtures containing increasing amounts of Stöber from 10 to 30 phr, the elastic modulus was estimated as $E' \sim 10$ MPa, $E' \sim 8$ MPa, and $E' \sim 7$ MPa, respectively. A decrease of the elongation at break was also reported with the increase of the Stöber content in the case of Stöber/HDS-20/60 and Stöber/HDS-30/50. Although the Stöber particles were found to be responsible for a decrease of the modulus at the rubbery regime in DMA and for the reduction of the fraction of immobilized rubber, the increase of these particle amounts induces an increase of the rubber brittleness. The reason could be related to the fact size of the Stöber particles, which, as shown by the STEM figures (see Figure 1), are significantly bigger than the average size of HDS clusters. At high deformation, while the clusters are subjected to the strain due to a certain amount of bounded rubber, the Stöber particles are acting as undeformed cross-links. This observation could explain the lower elongation at break with the increase of Stöber amount, despite their higher dispersibility.

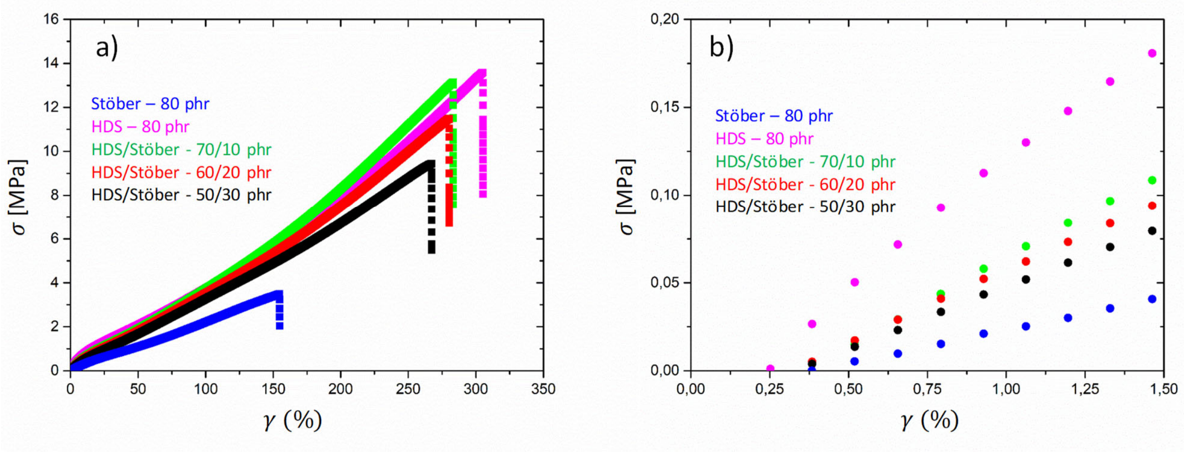

Figure 9. Stress-strain curves for mixtures of Stöber and HDS Silica dual filler compounds in the full deformation range (**a**) and at low deformation (**b**).

4. Conclusions

This work has been dedicated to the study of mechanical properties of SBR-based nanocomposites containing spherical or anisotropic dual fillers. Fractal/spherical and fractal/anisotropic dual filler nanocomposites were prepared with HDS nanoparticles/Stöber nanoparticles and HDS nanoparticles/Sepiolite nanoneedles, respectively. We highlight, using STEM and DMA analysis, that, in the system Sepiolite/HDS, both fillers work cooperatively, and the HDS induces a preferential alignment of Sepiolite clusters in the rubber matrix. We hypothesize that the orientation of the Sepiolite is activated by the presence of a HDS percolating network, and the resulting oriented forces which will occur at the mixing steps. The induced preferential orientation gives rise to an increase of nanocomposites' storage modulus in the rubbery regime, as by the DMA. The tensile tests carried out at a higher deformation range on the same samples evidenced a reduction of rubber elongation ability with the increased amount of nanorods in the mixture, indicating an orientation of the rods along the deformation direction induced this time by the high strain applied. On the other hand, in the Stöber/HDS dual filler system, the spherical component seemed to show more of a diluting effect than a reinforcing one. This observation is associated with the trend of tan δ as a function of temperature in DMA, which clearly shows a decrease of the immobilized rubber with the increase of Stöber amount in the mixture. At the same time, a decrease of the elastic modulus at high temperature with the increase of Stöber concentration has been reported. An apparent contradiction with the lower elongation at break observed for the mixtures containing a higher amount of Stöber particles could instead be explained by considering the non-deformability of these spherical fillers that might act as permanent cross-links under the condition of high strain, leading to an earlier rupture of the rubbery material.

Based on those observations, the dual filler system fractal/anisotropic silica-based structure appears as a promising solution to reach reinforced nanocomposites. As raw Sepiolite fibres or nanoneedles can differ in quality, composition, structure, and surface state depending on their origin, it may be worth studying the behaviour of dual filler nanocomposites prepared with anisotropic silica nanorods instead of Sepiolite.

Supplementary Materials: The following are available online at https://www.mdpi.com/article/10.3390/polym13152413/s1, Table S1: Mixing energies required to process nanocomposites with different fillers.

Author Contributions: Conceptualization, M.S., V.R., M.M., B.D. and J.-S.T.; methodology, M.S., V.R., E.M., J.D. and P.S.; validation, B.D., G.T., D.L. and J.-S.T.; formal analysis, M.S., V.R., J.D. and J.-S.T.; resources, G.T., B.D., D.L., and J.-S.T.; writing—original draft preparation, M.S. and V.R.; writing—review and editing, E.M., J.D., M.M., B.D., P.S., G.T., D.L. and J.-S.T.; supervision, M.M., D.L., J.-S.T.; project administration, G.T., D.L., J.-S.T.; funding acquisition, G.T., B.D. and D.L. All authors have read and agreed to the published version of the manuscript.

Funding: The authors would like to thank the National Research Found of Luxembourg (FNR) for their financial support through the IPBG16/11514551/TireMat-Tech project.

Acknowledgments: The authors would like to thank Goodyear S.A. for the permission to publish the paper. In addition, the authors would like to thank Régis Vaudemont, Benoit Marcolini, Sébastien Gergen, and Vincent Berthe for their support on mechanical characterisation.

Conflicts of Interest: The authors declare no conflict of interest.

References

1. Koniuszewska, A.G.; Kaczmar, J.W. Application of Polymer Based Composite Materials in Transportation. *Prog. Rubber Plast. Recycl. Technol.* **2016**, *32*, 1–24. [CrossRef]
2. Zhong, B.; Jia, Z.; Hu, D.; Luo, Y.; Jia, D. Reinforcement and reinforcing mechanism of styrene–butadiene rubber by antioxidant-modified silica. *Compos. Part A. Appl. Sci. Manuf.* **2015**, *78*, 303–310. [CrossRef]
3. Štěpek, J.; Daoust, H. Reinforcing fillers, reinforcing agents, and coupling agents. In *Additives for Plastics*; Štěpek, J., Daoust, H., Eds.; Springer: New York, NY, USA, 1983; pp. 70–98. [CrossRef]
4. Leblanc, J.L. Rubber–filler interactions and rheological properties in filled compounds. *Prog. Polym. Sci.* **2002**, *27*, 627–687. [CrossRef]
5. Kamal, M.M.; Clarke, J.; Ahmad, M. Comparison of Properties of Natural Rubber Compounds with Various Fillers. *J. Rubber Res.* **2009**, *12*, 27–44.
6. Rothon, R. *Particulate-Filled Polymer Composites*; Smithers Rapra Technology: Shawbury, UK, 2003.
7. Usha Devi, K.S.; Ponnamma, D.; Causin, V.; Maria, H.J.; Thomas, S. Enhanced morphology and mechanical characteristics of clay/styrene butadiene rubber nanocomposites. *Appl. Clay Sci.* **2015**, *114*, 568–576. [CrossRef]
8. Castro, D.; Suarez, J.; Nunes, R.C.; Visconte, L. Effect of Mica Addition on the Properties of Natural Rubber and Polybutadiene Rubber Vulcanizates. *J. Appl. Polym. Sci.* **2003**, *90*, 2156–2162. [CrossRef]
9. Dannenberg, E.M. Filler Choices in the Rubber Industry. *Rubber Chem. Technol.* **1982**, *55*, 860–880. [CrossRef]
10. Fang, Q.; Song, B.; Tee, T.-T.; Sin, L.T.; Hui, D.; Bee, S.-T. Investigation of dynamic characteristics of nano-size calcium carbonate added in natural rubber vulcanizate. *Compos. Part B. Eng.* **2014**, *60*, 561–567. [CrossRef]
11. Jincheng, W.; Lijuan, T.; Ding, W.; Xi, G.; Wenli, H. Application of Modified Calcium Sulfate Whisker in Methyl Vinyl Silicone Rubber Composites. *Polym. Polym. Compos.* **2012**, *20*, 453–462. [CrossRef]
12. Wang, J.; Liu, H.; Wen, S.; Shen, Y. The Performance of Barium Sulfate/Nature Rubber Composites Using in Sport Shoes. *Adv. Mater. Res.* **2010**, *152–153*, 1184–1187. [CrossRef]
13. El-Nashar, D.E.; Youssef, E.A.M.; El-Ghaffar, M.A.A. Modified phosphate pigments as high performance reinforcing materials for rubber vulcanizates. *Mater. Des.* **2010**, *31*, 1350–1359. [CrossRef]
14. Fu, S.-Y.; Feng, X.-Q.; Lauke, B.; Mai, Y.-W. Effects of particle size, particle/matrix interface adhesion and particle loading on mechanical properties of particulate–polymer composites. *Compos. Part B. Eng.* **2008**, *39*, 933–961. [CrossRef]
15. Panampilly, B.; Thomas, S. Nano ZnO as cure activator and reinforcing filler in natural rubber. *Polym. Eng. Sci.* **2013**, *53*, 1337–1346. [CrossRef]

16. Zhou, W.; Qi, S.; Tu, C.; Zhao, H.; Wang, C.; Kou, J. Effect of the particle size of Al2O3 on the properties of filled heat-conductive silicone rubber. *J. Appl. Polym. Sci.* **2007**, *104*, 1312–1318. [CrossRef]
17. Chokanandsombat, Y.; Sirisinha, C. MgO and ZnO as reinforcing fillers in cured polychloroprene rubber. *J. Appl. Polym. Sci.* **2013**, *128*, 2533–2540. [CrossRef]
18. Vijayan, D.; Mathiazhagan, A.; Joseph, R. Aluminium trihydroxide: Novel reinforcing filler in Polychloroprene rubber. *Polymer* **2017**, *132*, 143–156. [CrossRef]
19. Pegoretti, A.; Dorigato, A. Polymer composites: Reinforcing fillers. In *Encyclopedia of Polymer Science and Technology*, Inc ed.; John Wiley & Sons: Hoboken, NJ, USA, 2020; pp. 1–72. [CrossRef]
20. Spahr, M.E.; Rothon, R. Carbon black as a polymer filler. In *Polymers and Polymeric Composites: A Reference Series*; Palsule, S., Ed.; Springer: Berlin/Heidelberg, Germany, 2016; pp. 1–3. [CrossRef]
21. Imiela, M.; Anyszka, R.; Bieliński, D.M.; Masłowski, M.; Pędzich, Z.; Ziąbka, M.; Rybiński, P.; Syrek, B. Effect of graphite and common rubber plasticizers on properties and performance of ceramizable styrene–butadiene rubber-based composites. *J. Therm. Anal. Calorim.* **2019**, *138*, 2409–2417. [CrossRef]
22. Gao, J.; He, Y.; Gong, X.; Xu, J. The role of carbon nanotubes in promoting the properties of carbon black-filled natural rubber/butadiene rubber composites. *Results Phys.* **2017**, *7*, 4352–4358. [CrossRef]
23. Sanprasert, P.; Sombatsompop, N.; Sae-oui, P.; Sirisinha, C. Cotton fibers reinforcement of HNBR: Control of fiber alignment and its influence on properties of HNBR vulcanizates. *J. Appl. Polym. Sci.* **2014**, *131*. [CrossRef]
24. Vladkova, T.; Dineff, P.; Gospodinova, D.; Avramova, I. Wood flour: New filler for the rubber processing industry. IV. Cure characteristics and mechanical properties of natural rubber compounds filled by non-modified or corona treated wood flour. *J. Appl. Polym. Sci.* **2006**, *101*, 651–658. [CrossRef]
25. Lopattananon, N.; Jitkalong, D.; Seadan, M. Hybridized reinforcement of natural rubber with silane-modified short cellulose fibers and silica. *J. Appl. Polym. Sci.* **2011**, *120*, 3242–3254. [CrossRef]
26. Hall, D.E.; Moreland, J.C. Fundamentals of Rolling Resistance. *Rubber Chem. Technol.* **2001**, *74*, 525–539. [CrossRef]
27. Farida, E.; Bukit, N.; Ginting, E.M.; Bukit, B.F. The effect of carbon black composition in natural rubber compound. *Case Stud. Therm. Eng.* **2019**, *16*, 100566. [CrossRef]
28. Kim, N.C.; Song, S.H. Effects of Zinc-Free Processing Aids on Silica-Reinforced Tread Compounds for Green Tires. *Int. J. Polym. Sci.* **2019**, *2019*, 1–9. [CrossRef]
29. Sattayanurak, S.; Noordermeer, J.W.M.; Sahakaro, K.; Kaewsakul, W.; Dierkes, W.K.; Blume, A. Silica-Reinforced Natural Rubber: Synergistic Effects by Addition of Small Amounts of Secondary Fillers to Silica-Reinforced Natural Rubber Tire Tread Compounds. *Adv. Mater. Sci. Eng.* **2019**, *2019*, 1–8. [CrossRef]
30. Davris, T.; Mermet-Guyennet, M.R.B.; Bonn, D.; Lyulin, A.V. Filler Size Effects on Reinforcement in Elastomer-Based Nanocomposites: Experimental and Simulational Insights into Physical Mechanisms. *Macromolecules* **2016**, *49*, 7077–7087. [CrossRef]
31. Bassett, D.R.; Boucher, E.A.; Zettlemoyer, A.C. Adsorption studies on hydrated and dehydrated silicas. *J. Colloid Interface Sci.* **1968**, *27*, 649–658. [CrossRef]
32. Noriman, N.Z.; Ismail, H. Properties of styrene butadiene rubber (SBR)/recycled acrylonitrile butadiene rubber (NBRr) blends: The effects of carbon black/silica (CB/Sil) hybrid filler and silane coupling agent, Si69. *J. Appl. Polym. Sci.* **2012**, *124*, 19–27. [CrossRef]
33. Zhang, C.; Liu, L.; Zhang, Z.; Pal, K.; Kim, J. Effect of Silica and Silicone Oil on the Mechanical and Thermal Properties of Silicone Rubber. *J. Macromol. Sci. Part B Phys.* **2011**, *50*, 1144–1153. [CrossRef]
34. Seo, J.G.; Lee, C.K.; Lee, D.; Song, S.H. High-performance tires based on graphene coated with Zn-free coupling agents. *J. Ind. Eng. Chem.* **2018**, *66*, 78–85. [CrossRef]
35. Brinker, C.J. Hydrolysis and condensation of silicates: Effects on structure. *J. Non-Cryst. Solids* **1988**, *100*, 31–50. [CrossRef]
36. Greasley, S.L.; Page, S.J.; Sirovica, S.; Chen, S.; Martin, R.A.; Riveiro, A.; Hanna, J.V.; Porter, A.E.; Jones, J.R. Controlling particle size in the Stober process and incorporation of calcium. *J. Colloid Interface Sci.* **2016**, *469*, 213–223. [CrossRef]
37. Kapgate, B.P.; Das, C.; Basu, D.; Das, A.; Heinrich, G. Rubber composites based on silane-treated stöber silica and nitrile rubber: Interaction of treated silica with rubber matrix. *J. Elastomers Plast.* **2013**, *47*, 248–261. [CrossRef]
38. Ten Brinke, J.W.; Litvinov, V.M.; Wijnhoven, J.E.G.J.; Noordermeer, J.W.M. Interactions of Stöber Silica with Natural Rubber under the Influence of Coupling Agents, Studied by 1H NMR T2 Relaxation Analysis. *Macromolecules* **2002**, *35*, 10026–10037. [CrossRef]
39. Peng, C.-C.; Göpfert, A.; Drechsler, M.; Abetz, V. "Smart" silica-rubber nanocomposites in virtue of hydrogen bonding interaction. *Polym. Adv. Technol.* **2005**, *16*, 770–782. [CrossRef]
40. Bokobza, L.; Chauvin, J.-P. Reinforcement of natural rubber: Use of in situ generated silicas and nanofibres of sepiolite. *Polymer* **2005**, *46*, 4144–4151. [CrossRef]
41. Yin, C.; Zhang, Q. Effects of octamethylcyclotetrasiloxane grafting and in situ silica particle generation on the curing and mechanical properties of a styrene butadiene rubber composite. *RSC Adv.* **2019**, *9*, 34330–34341. [CrossRef]
42. Li, Q.; Li, X.; Cho, U.R. Mechanical Properties of Styrene-Butadiene Rubber Reinforced with Silica by in situ Tetraethoxysilane Hydrolysis over Acid Catalyst. *Elastomers Compos.* **2018**, *53*, 57–66. [CrossRef]
43. Scotti, R.; Conzatti, L.; D'Arienzo, M.; Di Credico, B.; Giannini, L.; Hanel, T.; Stagnaro, P.; Susanna, A.; Tadiello, L.; Morazzoni, F. Shape controlled spherical (0D) and rod-like (1D) silica nanoparticles in silica/styrene butadiene rubber nanocomposites: Role of the particle morphology on the filler reinforcing effect. *Polymer* **2014**, *55*, 1497–1506. [CrossRef]

44. Tadiello, L.; D'Arienzo, M.; Di Credico, B.; Hanel, T.; Matejka, L.; Mauri, M.; Morazzoni, F.; Simonutti, R.; Spirkova, M.; Scotti, R. The filler-rubber interface in styrene butadiene nanocomposites with anisotropic silica particles: Morphology and dynamic properties. *Soft Matter* **2015**, *11*, 4022–4033. [CrossRef]
45. Alsultani, K.F.; Winya, N.; Hansupalak, N.; Eguchi, K.; Heeres, H.J.; Al-Baidhani, J.H.; Su, Y.; Al-Zuhair, S.; Yang, S.T.; Chen, Y.S. A comparison between the effects of sepiolite and silica on mechanical properties and thermal stability of NR/EPDM blend. *MATEC Web Conf.* **2016**, *69*. [CrossRef]
46. Di Credico, B.; Cobani, E.; Callone, E.; Conzatti, L.; Cristofori, D.; D'Arienzo, M.; Dirè, S.; Giannini, L.; Hanel, T.; Scotti, R.; et al. Size-controlled self-assembly of anisotropic sepiolite fibers in rubber nanocomposites. *Appl. Clay Sci.* **2018**, *152*, 51–64. [CrossRef]
47. Cobani, E.; Tagliaro, I.; Geppi, M.; Giannini, L.; Leclere, P.; Martini, F.; Nguyen, T.C.; Lazzaroni, R.; Scotti, R.; Tadiello, L.; et al. Hybrid Interface in Sepiolite Rubber Nanocomposites: Role of Self-Assembled Nanostructure in Controlling Dissipative Phenomena. *Nanomaterials* **2019**, *9*, 486. [CrossRef]
48. Bokobza, L.; Leroy, E.; Lalanne, V. Effect of filling mixtures of sepiolite and a surface modified fumed silica on the mechanical and swelling behavior of a styrene-butadiene rubber. *Eur. Polym. J.* **2009**, *45*, 996–1001. [CrossRef]
49. Gabriel, C.F.S.; Gabino, A.D.A.P.; de Sousa, A.M.F.; Furtado, C.R.G.; Nunes, R.C.R. Tire tread rubber compounds with ternary system filler based on carbon black, silica, and metakaolin: Contribution of silica/metakaolin content on the final properties. *J. Elastomers Plast.* **2019**, *51*, 712–726. [CrossRef]
50. Al-Hartomy, O.A.; Al-Ghamdi, A.A.; Al Said, S.A.F.; Dishovsky, N.; Ward, M.B.; Mihaylov, M.; Ivanov, M. Characterization of carbon silica hybrid fillers obtained by pyrolysis of waste green tires by the STEM–EDX method. *Mater. Charact.* **2015**, *101*, 90–96. [CrossRef]
51. Galimberti, M.; Coombs, M.; Cipolletti, V.; Riccio, P.; Riccò, T.; Pandini, S.; Conzatti, L. Enhancement of mechanical reinforcement due to hybrid filler networking promoted by an organoclay in hydrocarbon-based nanocomposites. *Appl. Clay Sci.* **2012**, *65–66*, 57–66. [CrossRef]
52. Ahmed, S.; Jones, F.R. A review of particulate reinforcement theories for polymer composites. *J. Mater. Sci.* **1990**, *25*, 4933–4942. [CrossRef]
53. Ver Meer, M.A.; Narasimhan, B.; Shanks, B.H.; Mallapragada, S.K. Effect of Mesoporosity on Thermal and Mechanical Properties of Polystyrene/Silica Composites. *ACS Appl. Mater. Interfaces* **2009**, *2*, 41–47. [CrossRef]
54. Chevigny, C.; Jouault, N.; Dalmas, F.; Boué, F.; Jestin, J. Tuning the mechanical properties in model nanocomposites: Influence of the polymer-filler interfacial interactions. *J. Polym. Sci. Part B. Polym. Phys.* **2011**, *49*, 781–791. [CrossRef]
55. Staropoli, M.; Gerstner, D.; Sztucki, M.; Vehres, G.; Duez, B.; Westermann, S.; Lenoble, D.; Pyckhout-Hintzen, W. Hierarchical Scattering Function for Silica-Filled Rubbers under Deformation: Effect of the Initial Cluster Distribution. *Macromolecules* **2019**, *52*, 9735–9745. [CrossRef]

Colloids and Surfaces A: Physicochemical and Engineering Aspects 637 (2022) 128260

Contents lists available at ScienceDirect

Colloids and Surfaces A: Physicochemical and Engineering Aspects

journal homepage: www.elsevier.com/locate/colsurfa

Revealing the dehydration/deuteration processes at the liquid-solid interface by nuclear magnetic resonance spectroscopy

Chuanyu Yan [a,b], Enzo Moretto [a,b], Oussema Kachouri [a,b], Jean-Luc Biagi [a], Jean-Sébastien Thomann [a], François Kayser [c], Reiner Dieden [a,*]

[a] *Department of "Materials Research and Technology", Luxembourg Institute of Science and Technology, Avenue des Hauts-Fourneaux, L-4362 Esch-sur-Alzette, Luxembourg*

[b] *Faculty of Science, Technology and Medicine, University of Luxembourg, Avenue des Hauts-Fourneaux, L-4365 Esch-sur-Alzette, Luxembourg*

[c] *Goodyear Innovation Center Luxembourg, Avenue Gordon Smith, L-7750 Colmar Berg, Luxembourg*

GRAPHICAL ABSTRACT

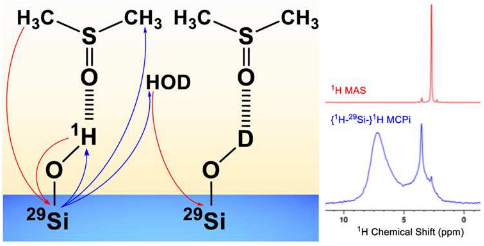

ARTICLE INFO

Keywords:
Silica
Solid state NMR
Surface/interface
Adsorption
Alumina
Micro-cellulose

ABSTRACT

The liquid-solid interface is of great importance in fundamental and applied research. However, the *in-situ* characterization of liquid-solid interfaces is very challenging. In this work, we demonstrated that $\{^1H–^{29}Si‐\}^1H$ multiple-contact cross polarization with indirect detection (MCPi) solid-state nuclear magnetic resonance (ssNMR) spectroscopy is an excellent tool for studying dehydration and deuterium exchange at the solvent-silica interface. The results provided direct evidence that the physically adsorbed water molecules present on the silica surface were completely removed in the presence of DMSO, while the silanol groups were satisfactorily deuterated in the presence of a DMSO-D_2O mixture. The knowledge obtained from the $\{^1H–^{29}Si‐\}^1H$ MCPi experiment was also extended to the development of an ^1H liquid-state NMR-based technique for the quantification of moisture and hydroxyls on inorganic and organic solids, as an alternative to the conventional thermogravimetric analysis (TGA) but with broader applicability. Moreover, this study offers a promising tool for studying the challenging questions involving liquid-solid interface.

1. Introduction

Molecular structures of the liquid-solid interface play a critical role in numerous biological [1], chemical [2], and physical [3] systems. A molecular understanding of the liquid-solid interface is therefore needed for the rational design and application of these systems [4]. For example,

---

* Corresponding author.
E-mail address: reiner.dieden@list.lu (R. Dieden).

https://doi.org/10.1016/j.colsurfa.2022.128260
Received 16 November 2021; Received in revised form 31 December 2021; Accepted 3 January 2022
Available online 5 January 2022

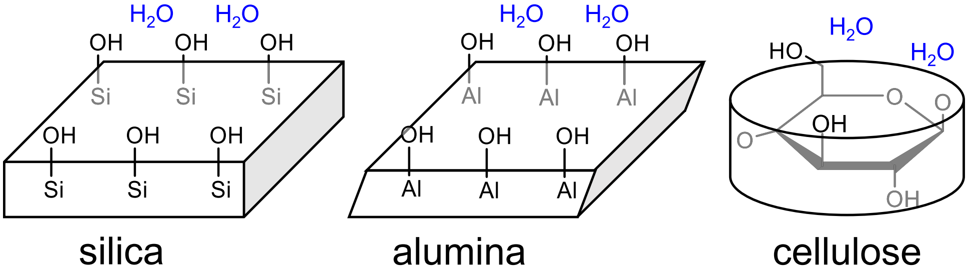

Fig. 1. Schematic representation of the surfaces of silica, alumina, and cellulose, which are characterized by the physically adsorbed water and hydroxyls.

the underwater adhesion of marine mussels to a variety of solid surfaces has attracted considerable attention [5], and has led to the invention of many bio-inspired adhesives [6]. However, *in-situ* characterization of the liquid-solid interface at the molecular level is very challenging [7,8]. So far, there have been many prominent techniques such as sum frequency generation (SFG) [9], attenuated total reflectance Fourier transform infrared spectroscopy (ATR-FTIR) [10], surface-enhanced Raman spectroscopy (SERS) [11], quartz crystal microbalance (QCM) [12], and scanning tunneling microscopy (STM) [13], available for *in-situ* interface-specific characterizations. However, as pointed out by Zaera et al. [7,8] these techniques have certain limitations in terms of sample requirement, spatial selectivity, or chemical information. As for the sample requirement, SFG requires a flat reflective surface, which is oftentimes inapplicable to nanoparticles and amorphous solids, and SERS requires the sample to either consist of metallic particles or have a metallic coating. Similarly, QCM also requires the grafting of receptor molecules prior to the measurement. In terms of spatial selectivity, the evanescent wave in the ATR-FTIR experiment has a penetration depth roughly equal to the incident infrared wavelength (μm), which is much larger than the first few atomic layers at the liquid-solid interface. In terms of chemical information, QCM registers the interaction events only as a shift of resonance frequency, which contain no information about molecular structures. STM also lacks detailed information about molecular interaction, though its spatial selectivity could be as good as single-atom level [14].

Solid-state NMR spectroscopy (ssNMR) can be an ideal tool for the *in-situ* characterization of liquid-solid interfaces due to its non-invasive nature and little need for sample preparation. The nuclear chemical shift is very sensitive to the nature of chemical bonds and chemical environments. However, direct excitation ssNMR (or NMR in general) is not intrinsically surface/interface-selective because all the nuclei within the bulk sample are excited indiscriminately. Although ^{1}H direct excitation ssNMR under magic angle spinning (^{1}H MAS) is frequently employed to study solid surfaces such as silica [15,16], the sample is either pure and clean (or at least assumed to be so), or *a priori* knowledge of molecular species present is available, such that the observed ^{1}H peaks can be used to assign the surface species. Fortunately, it has been demonstrated in numerous cases that surface-selective information can be obtained from one- and two-dimensional (1D/2D) MAS NMR experiments based on double cross polarization with inverse/indirect detection (DCPi) [17,18]. The working principle of DCPi is as follows: 1) the first ^{1}H→X cross polarization contact gives rise to polarization of the X-nuclei (*e.g.*, ^{29}Si in silica) that are located on the surface and in close proximity to protons; 2) the inverse X→^{1}H cross polarization contact transfers the spin magnetization back to ^{1}H for detection such that the surface species can be identified by their ^{1}H chemical shifts. The driving force of ^{1}H—X cross polarization is nuclear dipolar coupling, which occurs within an effective range of typically a few angstroms *i.e.*, a few atoms thick [17,19]. This short-range nature of DCPi makes it particularly suitable for characterizing surfaces and interfaces. Recently, we have demonstrated that a combination of multiple contact cross polarization with inverse detection (MCPi) [20] can provide additional robustness to DCPi and can even be employed to semi-quantitatively measure the adsorption affinity of organic molecules on the silica surface [21].

In this study, we took a step further to demonstrate that MCPi can also be a suitable technique for the *in-situ* characterization of liquid-solid interfaces with the simultaneous advantages of simple sample preparation, excellent spatial selectivity, and rich chemical information. Specifically, the dehydration and deuteration at the mixed solvent-silica interface were under investigation. To alleviate the low sensitivity due to ^{29}Si natural abundance and limited sample size, a fully ^{29}Si-labeled sample was used in the mechanistic study. After showing that the dehydration and deuteration of silica can occur efficiently in organic/mixed solvents as evidenced by the MCPi results, we proposed a simple experimental approach to quantify the water and hydroxyl groups on the surfaces of silica, alumina and cellulose (Fig. 1), which only requires a set of liquid state ^{1}H NMR experiments using the same solvent composition as in the MCPi experiments. This dehydration-deuteration approach using mixed solvents was then compared to the conventional thermogravimetric analysis (TGA), which is a time-proven technique for the quantification of moisture and hydroxyls on silica [22], but is not fully applicable to other solids. In this study, silica, alumina and cellulose were chosen because they represent a large class of important inorganic and organic solids that are widely used as catalyst supports [23–25], polymer composite fillers [26–28], drug delivery carriers [29–31], *etc.*, and the amount of their surface groups is a central part of their surface characteristics.

2. Experimental section

2.1. Materials

The following chemicals were purchased with the given specifications and used as received if not noted otherwise: calcinated ^{29}Si-enriched silica (*c*-^{29}SiO$_2$, ^{29}Si isotopic purity $>$ 98%, obtained from Cortecnet), concentrated sulfuric acid (H_2SO_4, 96%, Carl Roth); dimethyl sulfoxide (DMSO, $>$ 99.7%) and acetone (Ace, 99.8%) were obtained from Acros Organics; sodium hydroxide pellets (NaOH, $\geq$ 98%), deuterated dimethyl sulfoxide (DMSO-d$_6$, 99.8%D), deuterated water (D_2O, 99.8%D), potassium sulfate (K_2SO_4, $\geq$ 99.0%), potassium carbonate (K_2CO_3, $\geq$ 99.0%) and silica gel (type II, 3.5 mm beads) were from Sigma-Aldrich; commercial silica (trade name Zeosil® Premium 200MP) was obtained from Solvay, and will be referred to as simply "SiO$_2$" in the next sections (as opposed to the labeled ^{29}SiO$_2$); γ-alumina (99.99%, product no. AL606022) was obtained from Goodfellow, and will be referred to as "γ-Al_2O_3"; microcrystalline cellulose was obtained from Sigma-Aldrich (product no. 435236), and will be referred to as "mc-cellulose". In addition, NaOH pellets and concentrated H_2SO_4 were dissolved/diluted in distilled water to be used as 10 wt% and 30 wt% stock aqueous solutions, respectively.

2.2. Preparation of *p*-^{29}SiO$_2$

Fully ^{29}Si-labeled precipitated silica (*p*-^{29}SiO$_2$) was prepared *via* a "gel-sol-gel" reaction using the as-received *c*-^{29}SiO$_2$ (Scheme S1), the

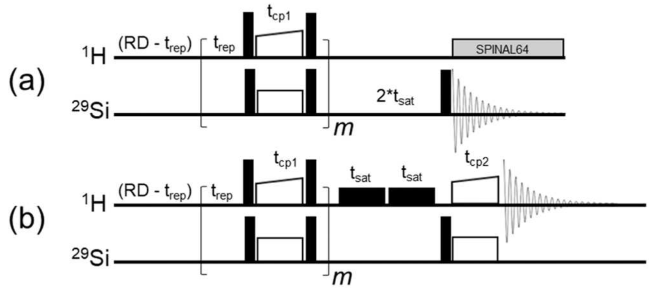

Scheme 1. Diagrams of (a) $\{^1H\}^{29}Si$ MCP and (b) $\{^1H–^{29}Si-\}^1H$ MCPi pulse sequences. Critical parameters are: the recycle delay (RD), ^1H repolarization delay (t_{rep}), ^{29}Si magnetization build-up contact pulse (t_{cp1}), number of build-up contact pulses (m), duration of ^1H low-power saturating pulse (t_{sat}), and inverse cross polarization contact pulse (t_{cp2}). The vertical filled rectangles represent the 90° pulses of $^1H/^{29}Si$.

similar synthesis procedure of which can be found in literature [32,33]. There are four major steps in the synthesis. The first step is to dissolve the c-$^{29}SiO_2$ that contains mostly siloxane (Q^4) structures and little silanols (Q^2 and Q^3). One gram of this raw silica was dissolved in 30 mL of 10 wt% NaOH aqueous solution in a Teflon beaker (note that Teflon was used in order to prevent the dilution of ^{29}Si due to the possible dissolved ^{28}Si from the glassware). Under vigorous stirring at room temperature, all the raw silica is transformed into a transparent solution overnight ($^{29}SiO_2 + 2NaOH \rightarrow Na_2{}^{29}SiO_3 + H_2O$). To precipitate the silica, 16 mL of 30 wt% H_2SO_4 aqueous solution is added dropwise into the solution at 90 °C. The reaction mixture was kept at 90 °C overnight to allow the complete precipitation ($Na_2{}^{29}SiO_3 + H_2SO_4 \rightarrow {}^{29}SiO_2(OH)_x + Na_2SO_4$, where x is the number of silanol groups). Subsequently, the freshly precipitated silica was rinsed by distilled water and centrifuged to remove the residual acid and salt. This rinse-centrifuge cycle was repeated until the pH of the supernatant was neutral. Finally, the product, *i.e.,* precipitated silica (p-$^{29}SiO_2$) was oven-dried at 105 °C overnight.

2.3. *SEM/STEM characterization*

Around 1 mg of (c-)p-$^{29}SiO_2$ powder was dispersed in 0.5 mL of ethanol and sonicated to break down the silica aggregates. One to three drops of this dispersion were then deposited on a copper sample holder and left to dry in the air. Scanning Electron Microscopy (SEM) images of the silica particles were recorded with a Helios Nanolab 650 microscope (FEI, Eindhoven, Netherlands). The scanning transmission electron microscopy (STEM) analysis was performed on the same instrument, where the suspension of $^{29}SiO_2$ powder in ethanol was deposited on a copper TEM grid with a carbon film and left to dry in the air. For the commercial $SiO_2/\gamma\text{-}Al_2O_3$/mc-cellulose, both SEM and STEM analyses were done on a Quanta 200F microscope (FEI, Eindhoven, Netherlands), where these samples were also deposited on a copper TEM grid with a carbon film. The analysis of particle sizes was done in ImageJ (version 64-bit Java 1.8.0_172).

2.4. *Control of humidity levels*

Three relative humidity levels (96, 48 and 0 RH%) were considered in this study, which cover the whole range encountered in practical applications. These RH% levels were achieved by placing about 300 mL of saturated K_2SO_4 and K_2CO_3 aqueous solutions [34] and 600 g of dried silica beads, respectively, at the bottom of closed desiccators (type-DN250, total volume 8 L, Duran glassware, Germany) located in an air-conditioned lab, where the temperature fluctuation is less than 0.5 °C (Fig. S1). The temperature and humidity inside the desiccators were monitored by a wireless dual thermometer-hygrometer (SwitchBot Meter, China).

For the quantification of surface moisture and hydroxyls, 40 mg of the as-received solid powder (*i.e.,* silicas/alumina/cellulose) were placed in 4 mL vials (with screw caps) and stored in the humidity-controlled desiccators for 24 h while keeping the vials open during the whole time. Then, the vials were immediately capped tightly and weighed on a balance (Denver Instrument, ± 0.0001 g) to record the initial net mass (m_0). Note that empty vials plus the caps were previously stored in the desiccators and were found to effectively have no mass change ($\leq$ 0.0001 g) at all the given RH% levels, suggesting the vials and caps did not pick up moisture during the storage.

2.5. *Solid-state NMR experiments*

All the ssNMR experiments were performed at 303 K on a 600 MHz spectrometer (^1H Larmor frequency, Bruker Avance III HD) equipped with a double channel (^1H-X) magic angle spinning (MAS) probe. Unless noted otherwise, a MAS speed of 8 kHz was used throughout this study. The samples were loaded into 4 mm rotors made of zirconium oxide. For the comparison of ^{29}Si spectra of the as-received c-$^{29}SiO_2$ and as-prepared p-$^{29}SiO_2$, 2.5 mg of the samples were loaded into the high-resolution MAS (HRMAS) inserts made of Kel-F®, which were then inserted into the 4 mm rotors (Fig. S2). For the study of the liquid-solid interface, 2.5 mg of p-$^{29}SiO_2$ were loaded into the HRMAS inserts and stored/exposed to the 48RH% atmosphere for 24 h. Then, the capped HRMAS inserts, with and without aliquots of solvents added by Eppendorf pipette, were inserted into 4 mm rotors. Two solvent blends were used: 1) 99.0 wt% DMSO + 1.0 wt% acetone (labeled as "DMSO-Ace") and 2) 85.0 wt% DMSO + 14.0 wt% D_2O + 1.0 wt% acetone (labeled as "DMSO-D_2O-Ace"). The labels of HRMAS inserts containing p-$^{29}SiO_2$ and the solvents indicated the sample contents (Fig. S3). For example, the "DMSO-Ace@p-29SiO2–48RH%" was the sample containing p-29SiO2 stored at 48 RH% for 24 h plus 25 μL of the mixed solvent "DMSO-Ace"). In addition, to ensure a complete deuteration, the "DMSO-D_2O-Ace@$^{29}SiO_2$" has been rinsed three times by 25 μL of "DMSO-D_2O-Ace" solvent before adding the last 25 μL. Furthermore, 2.5 mg of the as-received c-$^{29}SiO_2$ and 2.5 mg of the as-prepared p-$^{29}SiO_2$ were loaded into the HRMAS inserts without special treatment. These two samples were used to compare the spectral differences in ^{29}Si direct polarization (DP) experiments.

For the ^{29}Si DP spectrum of p-$^{29}SiO_2$, the following parameters were used: recycle delay (RD) is 600 s, 90° pulse length of ^{29}Si is 5.0 μs (nutation rate = 50 kHz), "SPINAL64" decoupling scheme [35] at a ^1H decoupling strength of 86 kHz, and an accumulation of 256 scans. Prior to the ^{29}Si DP experiments, a saturation recovery experiment was performed on the p-$^{29}SiO_2$ to measure the ^{29}Si spin-lattice (T_1) relaxation constants (Fig. S4), which showed that the longest ^{29}Si T_1 relaxation is 89 ± 20 s and hence RD = 600 s was used ($> 5 * T_{1,Si}$). Similarly, RD = 850 s was used to acquire the ^{29}Si DP spectrum of c-$^{29}SiO_2$ with an accumulation of 64 scans. For ^1H MAS and the experiments shown in Scheme 1, unless noted differently, the parameters used were: 90° pulse lengths of ^1H and ^{29}Si were 2.9 and 5.0 μs, respectively; 4, 128, and 128 scans for the ^1H MAS, $\{^1H\}^{29}Si$ MCP, and $\{^1H–^{29}Si-\}^1H$ MCPi experiments, respectively; ^{29}Si and ^1H spin locking fields ($B_{1,Si}/B_{1,H}$) during the CP contact were 50 kHz and a ramp from 34 to 66 kHz (or 0 kHz for calculating the contribution of the DP signal in the MCP block), respectively; ^{29}Si build-up CP pulse duration (t_{cp1}) was 10 ms, number of CP contact pulses (m) was 6, and the duration of the saturating pulse (t_{sat}) was 1 s. Other relevant experimental parameters (RD, t_{rep} and t_{cp2}) are given in the respective figures and captions. The optimization of the parameters (RD and t_{rep}) was done in a way similar to our recent study (Fig. S5) [21]. All chemical shifts of ssNMR spectra were externally referenced to diluted tetramethyl silane [36,37]. All the NMR spectra (including the liquid-state ones) were processed using TopSpin (Bruker, version 4.0.9).

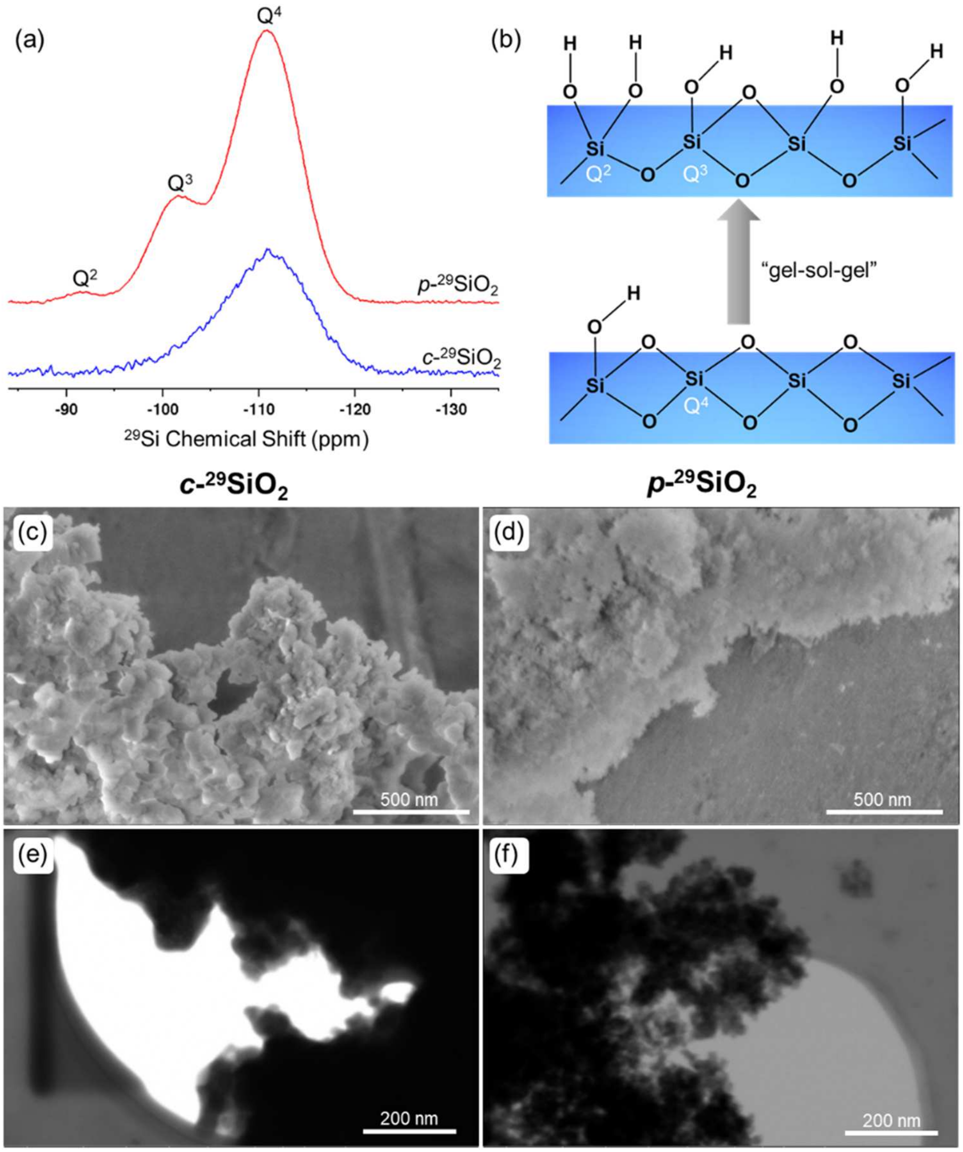

Fig. 2. (a) ^{29}Si DP/MAS ssNMR spectra of c-$^{29}SiO_2$ and p-$^{29}SiO_2$; (b) an illustration of the "gel-sol-gel" transformation from c-$^{29}SiO_2$ to p-$^{29}SiO_2$. (c) and (d) the scanning electron microscopy (SEM) and (e) and (f) scanning transmission electron microscopy (STEM) images of the as-received c-$^{29}SiO_2$ and as-prepared p-$^{29}SiO_2$, respectively. Size analysis of (f) is provided in Fig. S7.

2.6. Liquid-state NMR experiments

The quantitative ^{1}H liquid-state NMR experiments were performed on the same spectrometer as used for ssNMR, but using a 5 mm BBO liquid-state probe at 298 K. Prior to the experiments, blends of deuterated solvents were added to the solid powders that were previously exposed to different humidity levels for 24 h (see Section 2.4). Two solvent blends were prepared beforehand: 1) 99.0 wt% DMSO-d_6 + 1.0 wt% acetone (labeled as "DMSO-d_6-Ace") and 2) 85.0 wt% DMSO-d_6 + 14.0 wt% D_2O + 1.0 wt% acetone (labeled as "DMSO-d_6-D_2O-Ace"). About 0.9 g of one of these solvents (the exact mass was recorded as m_s) was added into the vials and hand-shaken for 30 s to disperse the powders evenly. After around 1 min, the suspended solid particles had settled down to the bottom of the vials, and the supernatant was transferred to 5 mm NMR tubes.

For the acquisition of ^{1}H liquid-state spectra, the following parameters were used: a RD of 60 s, a flip angle of 30°, and an accumulation of 8 scans. All chemical shifts of liquid-state NMR spectra were internally referenced to the residual DMSO peak.

2.7. Thermogravimetric analysis (TGA)

The TGA experiments were performed on a NETZSCH STA 409PC thermal analyser. 40 mg of the samples were loaded in alumina crucibles. The samples were heated at a rate of 10 K/min from room temperature to 1400 °C under a constant nitrogen flush at a rate of 50 mL/min. The data was exported and processed in Origin (OriginLab, version 2019b-32Bit).

3. Results and discussion

3.1. Preparation of p-$^{29}SiO_2$

Since only a limited amount (~ mg) of silica can be loaded into the HRMAS inserts and the natural abundance of ^{29}Si is only 4.7%, it is important to use ^{29}Si-labeled silica in order to reduce the time of – ssNMR experiments involving ^{29}Si to a reasonable scale. The signal-to-noise ratio (SNR) of an NMR spectrum increases linearly with the isotope concentration but only does so with the square root of the number of accumulated transients. A ^{29}Si enrichment degree of 98%

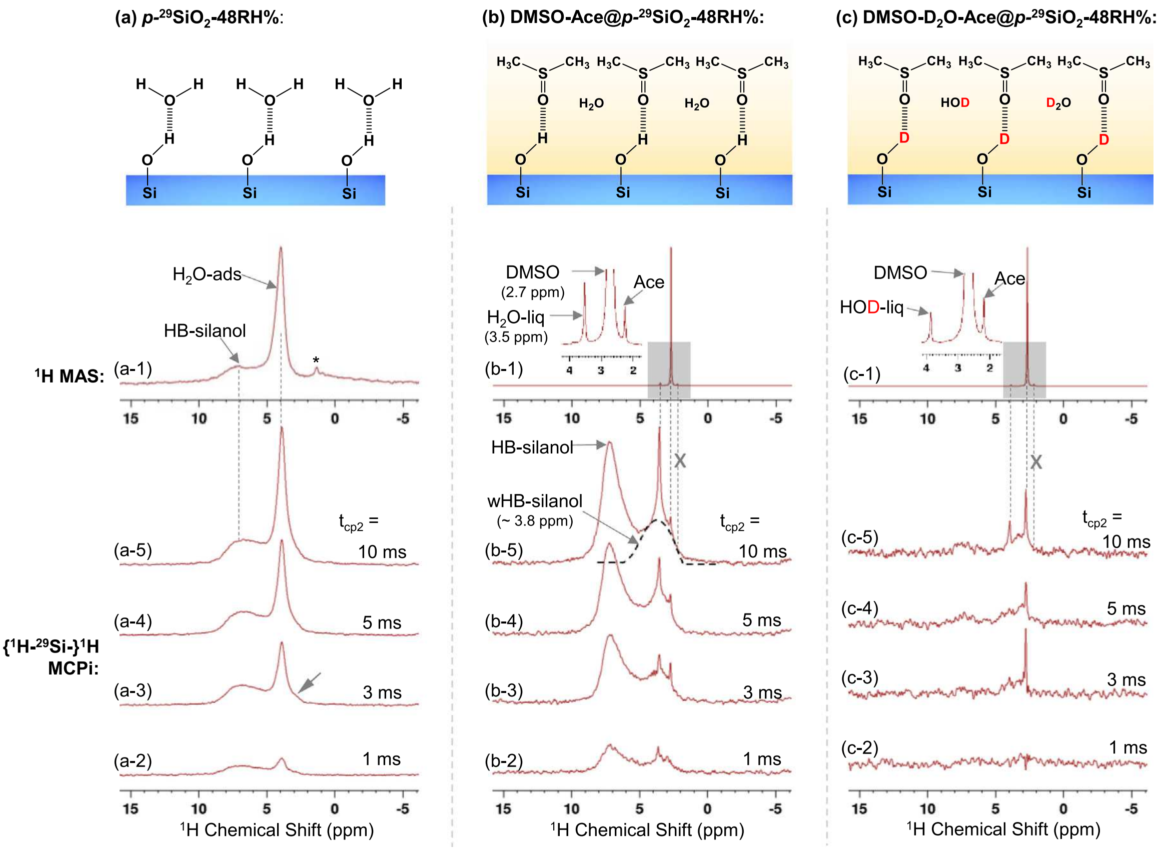

Fig. 3. ^{1}H MAS and {^{1}H–^{29}Si-}^{1}H MCPi spectra of the *p*-$^{29}SiO_2$ without (a) and with (b and c) contact with the liquid phase (the physical appearances of these samples were shown in Fig. S3). For spectra in columns (a)–(c), experimental parameters are: (a) RD = 3 s & t_{rep} = 1 s; (b) RD = 16 s & t_{rep} = 6.4 s; and (c) RD = 12 s & t_{rep} = 4.8 s. A rapid optimization of RD (and therefore t_{rep}) was shown in Fig. S5. *Note: impurity ^{1}H signal from the HRMAS insert (Fig. S8).

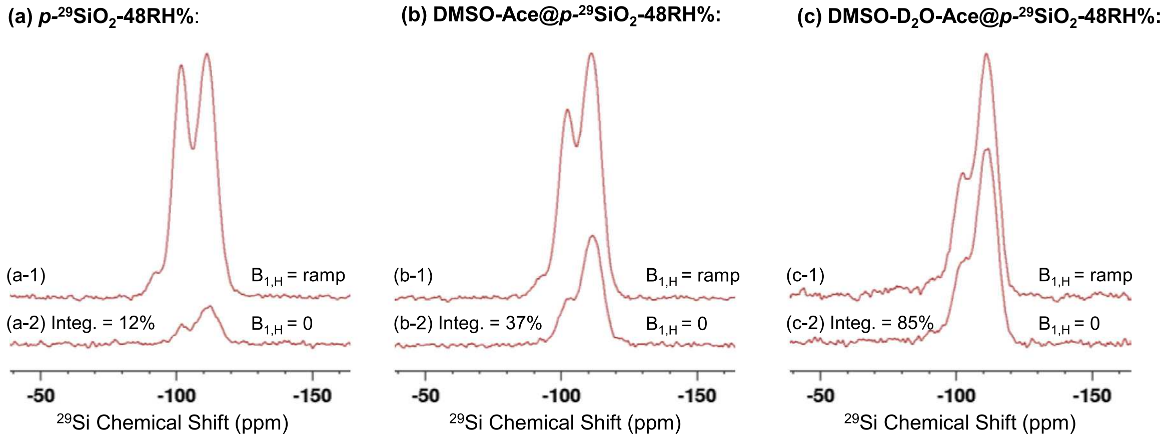

Fig. 4. {^{1}H}^{29}Si MCPi spectra of the *p*-$^{29}SiO_2$ without (a) and with (b and c) contact with the liquid phase (same samples as Fig. 2). The parameters (RD/t_{rep}/t_{cp1}/m) used to acquire these spectra were the same as those in the corresponding spectra of Fig. 2. However, the ^{1}H spin locking field ($B_{1,H}$) during the CP contacts of the MCP block was set at either a ramp from 34 to 66 kHz to build up the ^{29}Si magnetization, or at 0 kHz to examine the contribution of ^{29}DP signal due to $T_{1,Si}$ relaxation. The spectral integral (Integ.) from − 80 to − 130 ppm of the bottom-row spectrum was normalized to the respective top-row one.

leads to an approximate 21-fold increase in concentration *versus* natural abundance, at which the experimental time under the same conditions would need to be increased by a factor of 441 in order to achieve the same SNR level as for the isotopically enriched sample. Nevertheless, we have also demonstrated in our previous studies that the {^{1}H}^{29}Si MCP and {^{1}H–^{29}Si-}^{1}H MCPi experiments are applicable to non-labeled silica systems [20,21]. In addition, one could also reduce the experimental time for non-labeled systems by, for example, using a larger ssNMR rotor (*e.g.* 7 mm), and/or increasing the amount of silica sample packed in the rotor.

As shown in Fig. 2**a**, the molecular structure of the as-received *c*-$^{29}SiO_2$ is dominated by the siloxane group (Q^4, δ_{Si} = − 111 ppm), whereas the *p*-$^{29}SiO_2$ contains abundant silanols ($Q^{2/3}$, δ_{Si} = − 92/ − 102 ppm, respectively) suggesting the “gel-sol-gel” process indeed creates more silanols in this case (Fig. 2**b**). The deconvolution of the ^{29}Si DP spectra showed that the amount of Q^3 groups in *p*-$^{29}SiO_2$ was doubled with an additional 3% of Q^2 groups (Fig. S6). The morphology analysis by SEM (Fig. 2**c and d**) and STEM (Fig. 2**e and f**) showed that

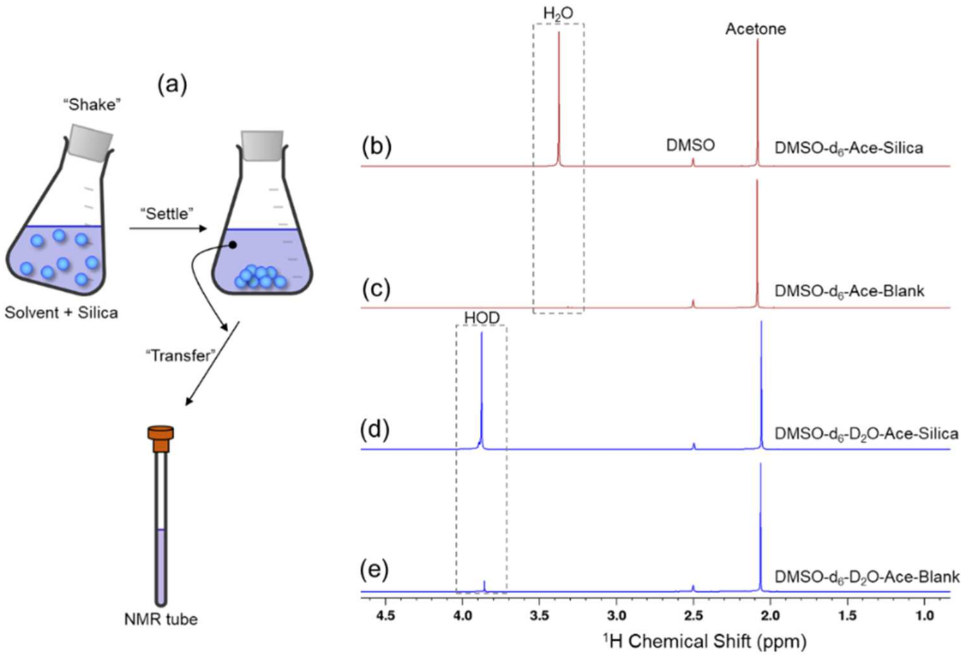

Fig. 5. (a) Illustration of the moisture extraction process by DMSO-d_6-Ace and deuterium exchange by DMSO-d_6-D_2O-Ace of the commercial SiO_2 (as well as γ-Al_2O_3 and mc-cellulose). (b–e) Representative ^1H one-pulse liquid-state NMR spectra showing the quantification of H_2O and HOD. In this case, the commercial SiO_2 was stored at 96 RH% for 24 h prior to the moisture extraction and deuterium exchange processes.

the c-$^{29}SiO_2$ consisted of large and dense fused scales, whereas the *p*-$^{29}SiO_2$ was an aggregation of primary nanoparticles whose average size was around 19 nm (Fig. S7). It is worth noting that silica nanoparticles at this size range are commonly used to prepare polymer nanocomposites [26], and hence the characterization of this *p*-$^{29}SiO_2$ could offer fundamental insights into the silica nanoparticle surface/interface for relevant applications.

3.2. *Solvent-Silica Interface*

The study of silica surface groups by $^1H/^{29}Si$ ssNMR has attracted considerable attention during the last decades [15,16], which was partially fueled by the widespread use of silica nanoparticles as catalyst support, filler material for polymer composite and drug delivery carrier, *etc.* [23,26,29]. Most of the assignments for physically adsorbed water (moisture) and silanol (Si-OH) in these studies were done by direct polarization ^1H ssNMR using ^1H–^1H homonuclear decoupling schemes and/or high MAS speeds (simply referred to as "^1H MAS") in order to obtain narrow line shapes. So far, it has been clear that the broad ^1H peak covering the chemical shift range from ~ 5 to 8 ppm can be attributed to the hydrogen-bonded silanol (HB-silanol), while the relatively sharp ^1H peak at ~ 4 ppm is due to the physically adsorbed water (H_2O-ads) [16,38–40]. As shown in the ^1H MAS spectrum of *p*-$^{29}SiO_2$ (Fig. 3**(a-1)**), these two ^1H peaks were also observed in the present study.

However, ^1H MAS is a bulk technique rather than a surface-selective one. Hence, whatever signals are observed in the ^1H MAS spectrum, they might not necessarily originate from the chemical structures present on the silica surface. In fact, the small ^1H peak at 1.26 ppm (denoted with *) in the ^1H MAS spectrum of *p*-$^{29}SiO_2$ shown in Fig. 3**(a-1)** is found to be due to the materials of the HRMAS insert (Fig. S8). This result illustrates the importance of surface-selective characterization. In this regard, the {^1H–^{29}Si-}^1H DCPi technique [17,18] and its robust version {^1H–^{29}Si-}^1H MCPi [20,21] have been employed in many surface-selective studies of silica, in which the duration of the inverse CP contact (t_{cp2}) can be modulated to achieve a certain degree of "distance-profiling" off the silica surface [17]. As shown in the {^1H–^{29}Si-}^1H MCPi spectra of the present work (Fig. 3**(a-2)**), the intensity of the ^1H peak (height) of H_2O-ads is almost the same as that of HB-silanol at t_{cp2} = 1 ms, whereas it is much stronger than the latter at t_{cp2} = 10 ms (Fig. 3**(a-5)**). This is most likely due to the fact that there are multiple layers of water molecules adsorbed on the silica surface while there is only one silanol layer. Thus, more and more ^{29}Si magnetization is transferred to the water layers further away as t_{cp2} is increased.

As mentioned in the Introduction, the *in-situ* characterization of molecular structures at the liquid-solid interface is challenging due to certain limitations of the existing techniques [7,8]. Here, upon a small modification of the experimental setup using HRMAS inserts, which hold liquid-solid mixtures tightly inside the ssNMR rotors (Figs. S2 and S3), we demonstrated that the {^1H–^{29}Si-}^1H MCPi technique is suitable not only for characterizing silica surface but also for solvent-silica interface (Fig. 3**b and c**). Two simple chemical processes, *i.e.*, dehydration and deuterium exchange, were investigated more closely to better understand the distribution of moisture and hydroxyls at the solvent-silica interface as well as competitive adsorption. Conventionally, the distribution of moisture and hydroxyls on the silica surface has been examined by treating silica samples at elevated temperature in combination with ^1H ssNMR [15,16] or mass spectrometry [22], and competitive adsorption has been mostly studied through the adsorption isotherm [41,42]. In this study, as the {^1H–^{29}Si-}^1H MCPi technique is based on the ^1H–^{29}Si dipolar coupling, the effective range of which is a few angstroms, it is particularly suitable for studying the solvent-silica interfacial structure at the molecular level. In general, the closer the ^1H–^{29}Si interatomic distance, the stronger the ^1H–^{29}Si dipolar coupling and, hence, the detected ^1H signal. For the dehydration process, as the H_2O-ads will be removed from the solvent-silica interface (hence out of the effective range of ^1H–^{29}Si dipolar coupling), while the ^1H–^{29}Si distance of the silanol groups remains unchanged, it is expected that the detected ^1H signal of H_2O-ads will be greatly diminished, while the ^1H signal of silanol groups will become dominant. For the deuterium exchange process, it is expected that the dominant ^1H signal of the silanol groups will also disappear since there will be only trace amounts of ^1H–^{29}Si spin pairs remaining at the interface.

Here, DMSO was used to replace and extract the H_2O-ads from the

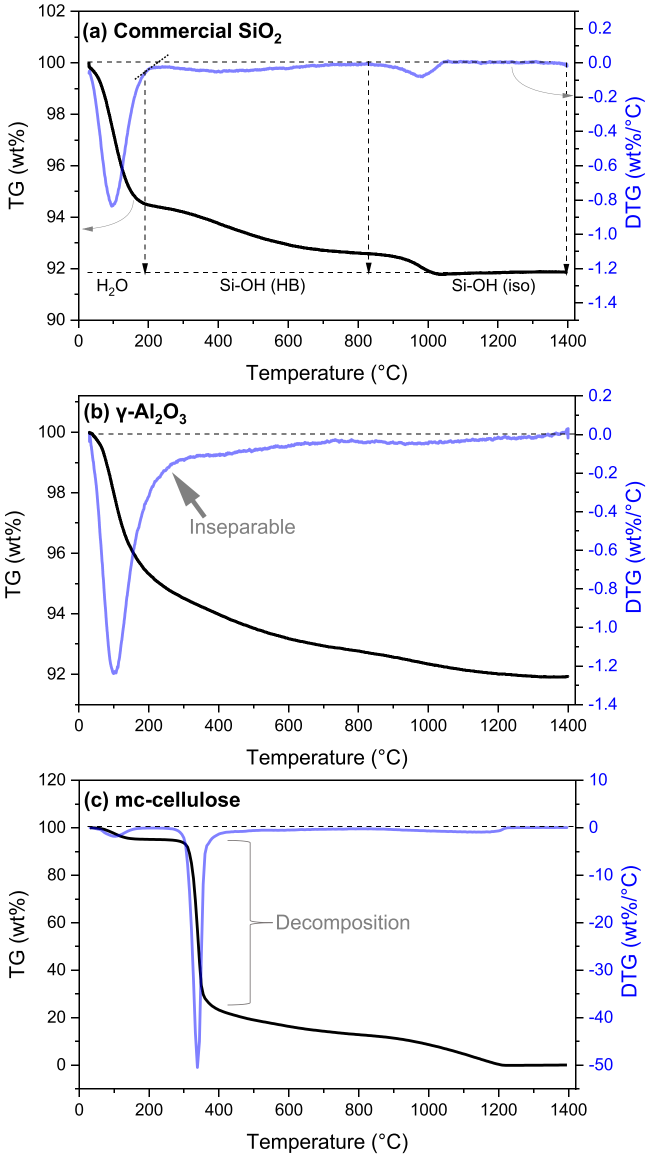

Fig. 6. Representative TGA thermographs of (a) the commercial SiO_2, (b) γ-Al_2O_3, and (c) mc-cellulose. In this case, the commercial SiO_2 was stored at 48 RH% for 24 h prior to the TGA experiments.

silica surface, and hence resulted in a sort of “soft” dehydration at ambient conditions as opposed to the “hard” dehydration at elevated temperatures, which can cause unwanted dehydroxylation. As shown on $\{^1H–^{29}Si-\}^1H$ MCPi spectra of DMSO-$^{29}SiO_2$ interface (Fig. 3**(b2–b5)**), the ^1H peak at 7.1 ppm of HB-silanol now became the dominating one after the H_2O-ads was removed by DMSO, in opposition to the case in native silica surface (Fig. 3**(a2–a5)**). Interestingly, a small broad ^1H peak that was initially hidden underneath the strong H_2O-ads peak of *p*-$^{29}SiO_2$-48RH% (see the grey arrow in Fig. 3**(a-2)**) became visible in the DMSO-Ace@ *p*-$^{29}SiO_2$-48RH% at ~ 3.8 ppm (see the dashed Gaussian contour in Fig. 3**(b-5)**). This ^1H peak at ~ 3.8 ppm could possibly originate from two species (Fig. S9): a) water molecules that are located inside the nanopores of silica or adsorbed on the surface, which have a broad ^1H chemical shift range depending on the water content [16,43], or b) weakly hydrogen-bonded silanols (wHB-silanol) [40]. If it is the former case (Fig. S9a), it means either these confined water molecules cannot escape from the confinement or cannot partition into the hygroscopic DMSO phase due to extremely small pore size (~ angstrom), which is quite extraordinary and has not been reported, to the best of our knowledge. In addition, if it is the physically adsorbed water on the silica surface, it would mean that there are, in total, two types of H_2O-ads simultaneously present on the silica surface (Fig. 3(a-3)), which is also quite extraordinary. From the line shape analysis of the spectra shown in Fig. 3(a-3) and (b-3), it was found that the peak width of the ^1H peak at ~ 3.8 ppm is more similar to the HB-silanol than to the H_2O-ads, which is probably linked to the amorphous nature of the *p*-$^{29}SiO_2$ (Fig. S10 and Table S1). Therefore, ^1H peak at ~ 3.8 ppm is most likely attributed to the silanols in vicinal position (Fig. S9b), which, due to the restrained bond angle, can’t form hydrogen bonds with DMSO molecules.

Furthermore, it is worth pointing out that the null result shown in Fig. 3**(c-2)** is not due to poor ^{29}Si magnetization. In fact, in the $\{^1H\}^{29}Si$ MCP block (Scheme 1), the ^{29}Si magnetization can build up to a sufficient level due to the contribution of ^{29}Si DP signal gained from ^{29}Si T_1 relaxation during the multiple t_{rep} periods, regardless of the protonated states (Fig. 4). For the well-protonated silica surface, the majority of ^{29}Si magnetization is gained from CP (Fig. 4**a**), whereas for the less-protonated surface the majority is from the DP contribution (Fig. 4**c**).

It was also found that the ^1H NMR peaks of DMSO and the dissolved water (H_2O-liq) in it were narrower and less intense compared to those of silanols (Fig. 3**(b2–b5)**), which is probably due to the mobility of these molecules in the liquid phase. Interestingly, the acetone molecule (Ace) seemed to act as a “spectator” with no detectable ^1H signal in the $\{^1H–^{29}Si-\}^1H$ MCPi experiments although it has a concentration similar to that of water (Fig. 3**b and c**). This result suggested that Ace molecules can’t compete with DMSO and H_2O-liq for the adsorption on the silica surface, which is probably due to its weak electron-donicity [44]. In addition, Fig. 3**(c-5)** showed that the deuterium exchange taking place at the solvent-silica interface was near completion, where the trace amount of remaining silanols was probably due to the H/D equilibrium governed by the D% of the D_2O (see Section 2.1).

The results shown above clearly demonstrate that the $\{^1H–^{29}Si-\}^1H$ MCPi experiment can provide direct evidence of the molecular structure at the silica-solvent interface. In the literature, the most common ways to deduce the molecular picture of the interface are molecular dynamics (MD) simulation [45] and SFG experiments [46,47]. Compared to MD simulations, the advantage of the $\{^1H–^{29}Si-\}^1H$ MCPi experiment is of course that it is a direct measurement. For SFG experiments, in which the identity of adsorbed species is revealed by the absorption of infrared light, it is required to have a macroscopic fused silica or quartz crystal (millimeters in diameter). However, these macroscopic silica surfaces might not be exactly the same as the surface of silica nano-/micro-particles, which are commonly used in practical applications such as catalyst supports and drug delivery agents. Therefore, the advantage of the $\{^1H–^{29}Si-\}^1H$ MCPi experiment over SFG is that it allows us to directly study the silica of interest.

3.3. *Quantification of moisture/hydroxyl on the silica surface*

The results shown in Fig. 3 practically suggest that one could run quantitative ^1H liquid-state NMR experiments to compare the integrals of the H_2O-liq and HOD-liq present in the supernatant to the known amount of the “spectator” acetone (as an internal standard) (Fig. 5), and hence to quantify the moisture and hydroxyl of silica or similar solids (Fig. S11). Note that deuterium exchange in combination with ATR-IR has been reported as a method for the quantification of silanol in silica samples [48]. However, this method requires the sample to be dried prior to deuterium exchange to avoid overestimation due to the presence of moisture. In comparison, our method presented in this study does not require the drying of the sample, as the moisture and silanol are determined in two consecutive steps, which eliminates this ambiguity.

The exact quantitative relation for moisture is as follows:

$$Moisture \quad (wt\%) = \frac{\left(S_1^{H2O} - S_0^{H2O}\right) * \left(\frac{C_{Ace}}{58.08}\right) * M_{Sol} * 6 * \left(\frac{18.01}{2}\right)}{M_{Solid}} * 100\% \quad (1)$$

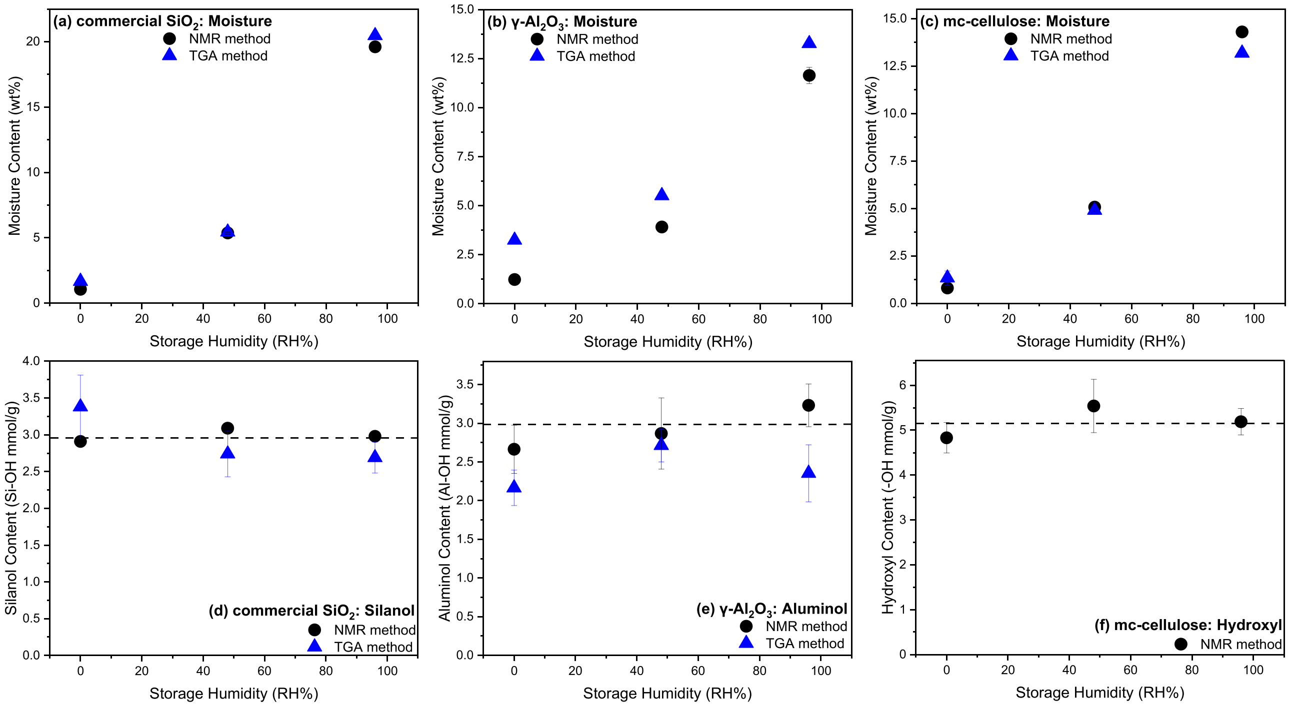

Fig. 7. The (a–c) moisture and (d–f) hydroxyls under different storage humidity of the commercial SiO_2, γ-Al_2O_3, and mc-cellulose, measured by quantitative ^{1}H liquid-state NMR method and TGA method.

where S_1^{H2O} and S_0^{H2O} are the integrals of the ^{1}H NMR peak of H_2O (normalized to the acetone peak) in the presence and absence of silica, respectively (Fig. 5**b and c**). C_{Ace} (g/g) is the mass fraction of acetone in the DMSO-d_6. M_{Sol} and M_{Solid} (g) are the masses of DMSO-d_6 solvent and silica, respectively. “58.08 and 18.01 (g/mol)” are the molecular weights of acetone and water molecules, respectively. “6 and 2” are the number of protons per molecule for acetone and water, respectively. Similarly, the quantitative relations for the hydroxyls are as follows:

$$C_{Si-OH}\quad (mol/g) = \frac{OH_{total} - OH_{moisture}}{M_{DrySolid}} \tag{2}$$

$$OH_{total}\quad (moles) = \left(S_1^{HOD} - S_0^{HOD}\right) * \left(\frac{C_{Ace}}{58.08}\right) * M_{Sol} * 6 \tag{3}$$

$$OH_{moisture}\quad (moles) = \frac{M_{Solid} * Moisture\% * 2}{18.01} \tag{4}$$

$$M_{DrySolid} = M_{Solid} * (1 - Moisture\%) \tag{5}$$

where C_{Si-OH} is moles of silanol per unit weight of dry silica ($M_{DrySolid}$), *i.e.*, the fraction of M_{Solid} excluding moisture, OH_{total} is the total molar amount of -OH groups exchanged from the silica while $OH_{moisture}$ corresponds to the molar amount of the -OH groups contributed by moisture, S_1^{HOD} and S_0^{HOD} are the integrals of the ^{1}H NMR peak of HOD (normalized to the acetone peak) in the presence and absence of silica (Fig. 5**d and e**), respectively. Note that the C_{Si-OH} should be a constant value for a given silica even at various humidity levels as long as the storage temperature has not exceeded the thermal stability of the silanol [22].

3.4. Quantification of moisture/hydroxyl: ^{1}H NMR versus TGA

TGA is a classical method for quantifying the moisture and silanol of silica, in which there are typically multiple temperature ranges for distinct stages for dehydration and dehydroxylation, *i.e.*, condensation of HB- and isolated (iso-) silanols [22], as well as mc-cellulose [49]. As shown in Fig. 6**a**, one could tell from the differential thermogravimetric (DTG) curve that there are three stages: 1) room temperature to 190 °C; 2) 190–820 °C; and 3) 820–1400 °C. These observed temperatures were consistent with the dehydration, dehydroxylation of HB-silanol and dehydroxylation of isolated silanols in the Zhuravlev’s model [22]. Hence, the quantitative relations for moisture and silanols of silica (or in general, for the hydroxyls of other solids) can be easily derived from the TGA thermo graph as follows:

$$Moisture\quad (wt\%) = TG\quad (190\quad ^\circ C) \tag{6}$$

$$C_{Si-OH}\quad (mol/g) = \frac{\{TG\quad (1400\quad ^\circ C) - TG\quad (190\quad ^\circ C)\} * \frac{2}{18.01}}{\{1 - TG\quad (190\quad ^\circ C)\}} \tag{7}$$

Therefore, Eqs. (1) and (6) and Eqs. (2) and (7) are the quantitative relations for quantifying the surface water and silanols of silica (for γ-Al_2O_3 and mc-cellulose as well) in the ^{1}H NMR and TGA methods, respectively.

As shown in Fig. 7**a and d**, the ^{1}H NMR and TGA methods yielded consistent results for a commercial silica that was stored at a broad range of humidity levels within the experimental uncertainty. This result suggests that one could use the proposed method of moisture extraction by DMSO and deuterium exchange by DMSO-D_2O as an alternative method of the TGA. Examples where the TGA method cannot be applied are solids where the stages of dehydration and dehydroxylation are overlapping, or organic solids that could undergo thermal decomposition within the same thermal stages. As shown in Fig. 6**b**, the dehydration and dehydroxylation stages of γ-Al_2O_3 were inseparable, which is commonly observed in alumina samples [50]. This inseparability leads to the overestimation of moisture and underestimation of aluminol (Fig. 7**b and e**). For mc-cellulose, the dehydration stage was very distinct as evidenced by the plateau at ~ 190 °C on the DTG curve, which explained the consistence of moisture% between ^{1}H NMR and TGA methods (Fig. 7**c**). As estimated by the chemical formula of cellulose, *i.e.*, $(C_6H_{10}O_5)_n$, the mass loss due to complete dehydroxylation ($-$ $3H_2O$) should be no more than 33.3 wt%. However, as can be seen in Fig. 6**c**, the mass loss during the temperature range of 190–400 °C was around 70 wt%, which was far more than the theoretical value, suggesting the occurrence of thermal decomposition (that could release molecular fragments $C_xH_yO_z$ rather than only H_2O). Hence, the TGA method is considered unsuitable for analyzing the hydroxyl contents of cellulose. The theoretical hydroxyl concentration in cellulose is 3 moles/162 g, *i.e.* 18.5 mmol/g, which is much higher than the value measured by ^{1}H NMR (Fig. 7**f**). This result is reasonable, as mc-cellulose has a dense crystalline phase (unlike silica and γ-Al_2O_3) and thus not all hydroxyls are accessible for deuterium exchange (Fig. S9). Therefore, the hydroxyl content measured by ^{1}H NMR in the deuterium exchange using DMSO-D_2O could, in the future, provide a realistic estimation of the quantity of chemical modifying agents needed for the chemical modifications of cellulose such as silanization [51].

4. Conclusion

In this study, we proposed and applied a recently developed ssNMR technique called $\{^1H–^{29}Si-\}^1H$ MCPi to study the solvent-silica interface. The model study of dehydration and deuterium exchange at the DMSO-silica interface showed that the $\{^1H–^{29}Si-\}^1H$ MCPi technique has the advantages of *in-situ* characterization, excellent surface selectivity and rich chemical information. In the dehydration experiment, the $\{^1H–^{29}Si-\}^1H$ MCPi results showed that the physically adsorbed water molecules were fully removed from silica surface in the presence of DMSO. The deuterium exchange experiment, it was shown that the silanol groups present on silica surface can be satisfactorily deuterated in the presence of a DMSO-D_2O mixture. On the basis of these findings we propose a simple liquid-state NMR method to quantify the ubiquitous moisture and hydroxyls on the surfaces of inorganic and organic solids, especially when the conventional thermogravimetric analysis is inapplicable due to overlap of dehydration and dehydroxylation stages. In the future, $\{^1H-X-\}^1H$ MCPi ($X = {}^{29}Si, {}^{13}C, {}^{15}N, {}^{15}P, \ldots$) experiment could be a powerful method for studying various fundamental questions involving liquid-solid interface, *e.g.* capturing the intermediates on heterogeneous catalyst surface and the binding configuration of drug-acceptor interactions.

CRediT authorship contribution statement

Chuanyu Yan: Investigation, Methodology, Conceptualization, Writing – original draft. **Enzo Moretto:** Investigation, Methodology. **Oussema Kachouri:** Investigation, Methodology. **Jean-Luc Biagi:** Resources. **Jean-Sébastien Thomann:** Supervision. **François Kayser:** Conceptualization, Writing – review & editing. **Reiner Dieden:** Conceptualization, Writing – review & editing, Project administration, Supervision.

Declaration of Competing Interest

The authors declare that they have no known competing financial interests or personal relationships that could have appeared to influence the work reported in this paper.

Acknowledgement

This work was supported by the Luxembourg National Research Fund (FNR) (IPBG16/11514551/TireMat-Tech).

Appendix A. Supporting information

Supplementary data associated with this article can be found in the online version at doi:10.1016/j.colsurfa.2022.128260.

References

[1] X.-H.N. Xu, E.S. Yeung, Long-range electrostatic trapping of single-protein molecules at a liquid-solid interface, Science 281 (5383) (1998) 1650.

[2] B. Hulsken, R. Van Hameren, J.W. Gerritsen, T. Khoury, P. Thordarson, M. J. Crossley, A.E. Rowan, R.J.M. Nolte, J.A.A.W. Elemans, S. Speller, Real-time single-molecule imaging of oxidation catalysis at a liquid–solid interface, Nat. Nanotechnol. 2 (5) (2007) 285–289.

[3] J.T. Ye, S. Inoue, K. Kobayashi, Y. Kasahara, H.T. Yuan, H. Shimotani, Y. Iwasa, Liquid-gated interface superconductivity on an atomically flat film, Nat. Mater. 9 (2) (2010) 125–128.

[4] G.A. Somorjai, Y. Li, Impact of surface chemistry, Proc. Natl. Acad. Sci. USA 108 (3) (2011) 917.

[5] H.G. Silverman, F.F. Roberto, Understanding marine Mussel adhesion, Mar. Biol. 9 (6) (2007) 661–681.

[6] H. Lee, S.M. Dellatore, W.M. Miller, P.B. Messersmith, Mussel-inspired surface chemistry for multifunctional coatings, Science 318 (5849) (2007) 426.

[7] F. Zaera, Surface chemistry at the liquid/solid interface, Surf. Sci. 605 (13) (2011) 1141–1145.

[8] F. Zaera, Probing liquid/solid interfaces at the molecular level, Chem. Rev. 112 (5) (2012) 2920–2986.

[9] C.D. Bain, Sum-frequency vibrational spectroscopy of the solid/liquid interface, J. Chem. Soc., Faraday Trans. 91 (9) (1995) 1281–1296.

[10] A.R. Hind, S.K. Bhargava, A. McKinnon, At the solid/liquid interface: FTIR/ATR—the tool of choice, Adv. Colloid Interface Sci. 93 (1) (2001) 91–114.

[11] K. Kneipp, H. Kneipp, I. Itzkan, R.R. Dasari, M.S. Feld, Surface-enhanced Raman scattering and biophysics, J. Phys.: Condens. Matter 14 (18) (2002) R597–R624.

[12] K.A. Marx, Quartz crystal microbalance: a useful tool for studying thin polymer films and complex biomolecular systems at the solution–surface interface, Biomacromolecules 4 (5) (2003) 1099–1120.

[13] S. De Feyter, A. Gesquière, M.M. Abdel-Mottaleb, P.C.M. Grim, F.C. De Schryver, C. Meiners, M. Sieffert, S. Valiyaveettil, K. Müllen, Scanning tunneling microscopy: a unique tool in the study of chirality, dynamics, and reactivity in physisorbed organic monolayers, Acc. Chem. Res. 33 (8) (2000) 520–531.

[14] D.M. Eigler, E.K. Schweizer, Positioning single atoms with a scanning tunnelling microscope, Nature 344 (6266) (1990) 524–526.

[15] C.E. Bronnimann, R.C. Zeigler, G.E. Maciel, Proton NMR study of dehydration of the silica gel surface, J. Am. Chem. Soc. 110 (7) (1988) 2023–2026.

[16] J. Trébosc, J.W. Wiench, S. Huh, V.S.Y. Lin, M. Pruski, Solid-state NMR study of MCM-41-type mesoporous silica nanoparticles, J. Am. Chem. Soc. 127 (9) (2005) 3057–3068.

[17] N. Baccile, G. Laurent, C. Bonhomme, P. Innocenzi, F. Babonneau, Solid-state NMR characterization of the surfactant–silica interface in templated silicas: acidic versus basic conditions, Chem. Mater. 19 (6) (2007) 1343–1354.

[18] N. Folliet, C. Roiland, S. Bégu, A. Aubert, T. Mineva, A. Goursot, K. Selvaraj, L. Duma, F. Tielens, F. Mauri, G. Laurent, C. Bonhomme, C. Gervais, F. Babonneau, T. Azaïs, Investigation of the interface in silica-encapsulated liposomes by combining solid state NMR and first principles calculations, J. Am. Chem. Soc. 133 (42) (2011) 16815–16827.

[19] I. Ben Shir, S. Kababya, T. Amitay-Rosen, Y.S. Balazs, A. Schmidt, Molecular level characterization of the inorganic–bioorganic interface by solid state NMR: alanine on a silica surface, a case study, J. Phys. Chem. B 114 (18) (2010) 5989–5996.

[20] C. Yan, F. Kayser, R. Dieden, Sensitivity enhancement via multiple contacts in the $\{^1H–^{29}Si\}–^1H$ cross polarization experiment: a case study of modified silica nanoparticle surfaces, RSC Adv. 10 (39) (2020) 23016–23023.

[21] C. Yan, A. Datta Sarma, E. Moretto, J.-S. Thomann, P. Verge, D. Schmidt, F. o Kayser, R. Dieden, Semiquantitative solid-state NMR study of the adsorption of soybean oils on silica and its significance for rubber processing, Langmuir 37 (34) (2021) 10298–10307.

[22] L.T. Zhuravlev, The surface chemistry of amorphous silica. Zhuravlev model, Colloids Surf. A Physicochem. Eng. Asp. 173 (1–3) (2000) 1–38.

[23] P.S. Shinde, P.S. Suryawanshi, K.K. Patil, V.M. Belekar, S.A. Sankpal, S.D. Delekar, S.A. Jadhav, A brief overview of recent progress in porous silica as catalyst supports, J. Compos. Sci. 5 (3) (2021).

[24] M. Trueba, S.P. Trasatti, γ-Alumina as a support for catalysts: a review of fundamental aspects, Eur. J. Inorg. Chem. 2005 (17) (2005) 3393–3403.

[25] S. Kamel, T.A. Khattab, Recent advances in cellulose supported metal nanoparticles as green and sustainable catalysis for organic synthesis, Cellulose 28 (8) (2021) 4545–4574.

[26] D.W. Lee, B.R. Yoo, Advanced silica/polymer composites: materials and applications, J. Ind. Eng. Chem. 38 (2016) 1–12.

[27] S. Mallakpour, E. Khadem, Recent development in the synthesis of polymer nanocomposites based on nano-alumina, Prog. Polym. Sci. 51 (2015) 74–93.

[28] A. Dufresne, Cellulose nanomaterial reinforced polymer nanocomposites, Curr. Opin. Colloid Interface Sci. 29 (2017) 1–8.

[29] I.I. Slowing, J.L. Vivero-Escoto, C.-W. Wu, V.S.Y. Lin, Mesoporous silica nanoparticles as controlled release drug delivery and gene transfection carriers, Adv. Drug Deliv. Rev. 60 (11) (2008) 1278–1288.

[30] P. Kapruwan, J. Ferré-Borrull, L.F. Marsal, Nanoporous anodic alumina platforms for drug delivery applications: recent advances and perspective, Adv. Mater. Interfaces 7 (22) (2020), 2001133.

[31] Z. Liu, S. Zhang, B. He, S. Wang, F. Kong, Synthesis of cellulose aerogels as promising carriers for drug delivery: a review, Cellulose 28 (5) (2021) 2697–2714.

[32] R. Sharafudeen, J.M. Al-Hashim, M.O. Al-Harbi, A.I. Al-Ajwad, A.A. Al-Waheed, Preparation and characterization of precipitated silica using sodium silicate prepared from Saudi Arabian desert sand, Silicon 9 (6) (2017) 917–922.

[33] I.M. Joni, Rukiah, C. Panatarani, Synthesis of silica particles by precipitation method of sodium silicate: effect of temperature, pH and mixing technique, AIP Conf. Proc. 2219 (1) (2020), 080018.

[34] F.E.M. O`Brien, The control of humidity by saturated salt solutions, J. Sci. Instrum. 25 (1948) 73–76.
[35] B.M. Fung, A.K. Khitrin, K. Ermolaev, An improved broadband decoupling sequence for liquid crystals and solids, J. Magn. Reson. 142 (1) (2000) 97–101.
[36] C.R. Morcombe, K.W. Zilm, Chemical shift referencing in MAS solid state NMR, J. Magn. Reson. 162 (2) (2003) 479–486.
[37] R.K. Harris, E.D. Becker, S.M. Cabral De Menezes, P. Granger, R.E. Hoffman, K. W. Zilm, Further conventions for NMR shielding and chemical shifts IUPAC recommendations 2008, Solid State Nucl. Magn. Reson. 33 (3) (2008) 41–56.
[38] C.C. Liu, G.E. Maciel, Quantitative analysis of solids by high-resolution ^{1}H NMR, Anal. Chem. 68 (8) (1996) 1401–1407.
[39] C.C. Liu, G.E. Maciel, The fumed silica surface: a study by NMR, J. Am. Chem. Soc. 118 (21) (1996) 5103–5119.
[40] J. Brus, J. Dybal, Hydrogen-bond interactions in organically-modified polysiloxane networks studied by 1D and 2D CRAMPS and double-quantum ^{1}H MAS NMR, Macromolecules 35 (27) (2002) 10038–10047.
[41] S.K. Parida, S. Dash, S. Patel, B.K. Mishra, Adsorption of organic molecules on silica surface, Adv. Colloid Interface Sci. 121 (1) (2006) 77–110.
[42] J. Ghodbane, R. Denoyel, Competitive adsorption between non-ionic polymers and surfactants on silica, Colloids Surf. A Physicochem. Eng. Asp. 127 (1) (1997) 97–104.
[43] B. Grünberg, T. Emmler, E. Gedat, I. Shenderovich, G.H. Findenegg, H.-H. Limbach, G. Buntkowsky, Hydrogen bonding of water confined in mesoporous Silica MCM-41 and SBA-15 studied by ^{1}H solid-state NMR, Chem. Eur. J. 10 (22) (2004) 5689–5696.
[44] Y.H. Ou, C.M. Chang, Y.S. Chen, A QSPR study on the solvent-induced frequency shifts of acetone and dimethyl sulfoxide in organic solvents, Spectrochim. Acta A Mol. Biomol. Spectrosc. 162 (2016) 109–114.
[45] M. Soloviev, G. Siligardi, D. Roccatano, E. Ferrari, Modelling the adsorption of proteins to nanoparticles at the solid-liquid interface, J. Colloid Interface Sci. 605 (2022) 286–295.
[46] Z. Yang, Q. Li, M.R. Gray, K.C. Chou, Structures of water molecules at solvent/silica interfaces, Langmuir 26 (21) (2010) 16397–16400.
[47] T.T. Bui, L.A. Colón, L. Velarde, Intermolecular interactions at the silica–liquid interface modulate the fermi resonance coupling in surface methanol, J. Phys. Chem. Lett. 12 (24) (2021) 5695–5702.
[48] A.A. Christy, P.K. Egeberg, Quantitative determination of surface silanol groups in silicagel by deuterium exchange combined with infrared spectroscopy and chemometrics, Analyst 130 (5) (2005) 738–744.
[49] F.C. Mayville, R.J. Wigent, J.B. Schwartz, Thermogravimetric analysis for the determination of water release rate from microcrystalline cellulose dry powder and wet bead systems, Pharm. Dev. Technol. 11 (3) (2006) 359–370.
[50] M.K. Mardkhe, B. Huang, C.H. Bartholomew, T.M. Alam, B.F. Woodfield, Synthesis and characterization of silica doped qlumina catalyst support with superior thermal stability and unique pore properties, J. Porous Mater. 23 (2) (2016) 475–487.
[51] B.P. Frank, D.P. Durkin, E.R. Caudill, L. Zhu, D.H. White, M.L. Curry, J.A. Pedersen, D.H. Fairbrother, Impact of silanization on the structure, dispersion properties, and biodegradability of nanocellulose as a nanocomposite filler, ACS Appl. Nano Mater. 1 (12) (2018) 7025–7038.

LANGMUIR

pubs.acs.org/Langmuir Article

Semiquantitative Solid-State NMR Study of the Adsorption of Soybean Oils on Silica and Its Significance for Rubber Processing

Chuanyu Yan, Arpan Datta Sarma, Enzo Moretto, Jean-Sébastien Thomann, Pierre Verge, Daniel Schmidt, François Kayser, and Reiner Dieden*

Cite This: *Langmuir* 2021, 37, 10298−10307 Read Online

ACCESS | Metrics & More | Article Recommendations | Supporting Information

ABSTRACT: Soybean oil (SBO) is a renewable material used as an alternative to conventional petroleum-derived oils in the processing of rubber composites. Upon chemical modifications, such as epoxidation, its performance in the processing of rubber can be significantly improved, as indicated by a considerable reduction of the mixing energy. Although it has been hypothesized that hydrogen bonding between functional groups (e.g., epoxy) of SBOs and silanols present on the silica surface plays a key role, there is still a lack of direct evidence supporting this hypothesis. In this work, it is demonstrated that there is an overall correlation between the epoxy concentration of SBOs and the mixing energy, consistent with the long-held hypothesis. In particular, a correlation between the SBO−silica adsorption affinity and the degree of epoxidation is revealed by a set of surface-selective solid-state nuclear magnetic resonance (ssNMR) experiments. In addition, the surface-selective ssNMR technique demonstrated in this work could also be used to evaluate the adsorption affinity of other oils and/or additives more broadly.

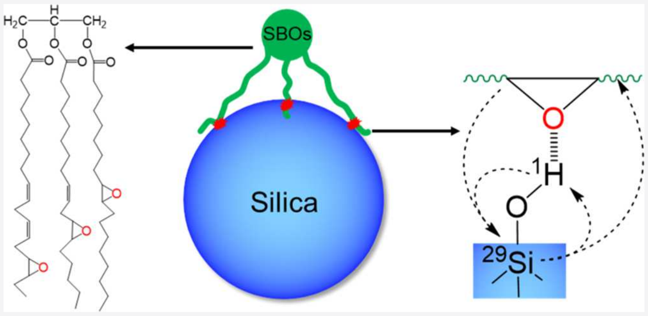

1. INTRODUCTION

With climate change increasingly tangible, the sustainability of industrial production is emphasized more than ever.[1,2] For example, silica, a reinforcing filler frequently used in the manufacturing of tires, is now partially produced from rice husks.[3,4] Similarly, it has recently been shown that vegetable oils such as soybean oil (SBO) are promising alternatives to conventional rubber processing aids such as treated distillate aromatic extracts (TDAEs).[5−17] Chemically modified SBOs can be synthesized through the controlled epoxidation of SBO.[18−22] The use of vegetable oils provides many benefits. For example, vegetable oils are generally recognized for their attractive safety profile related to humans, animals, and the environment[14,23−25] and for reducing our dependence on petroleum. Most importantly, these benefits can be realized with no performance penalty. In fact, numerous reports have shown that modified vegetable oils can significantly improve the processability of silica-filled elastomer composites.[9−12,26,27]

Given the increased use of (modified) vegetable oils in the rubber industry, there is an urgent need to understand how these oils interact with silica (as well as with other components in rubber compounds) and how chemical modification affects their performance. Although improved processability is generally attributed to the formation of hydrogen bonding (HB) between polar groups (e.g., epoxy) in modified vegetable oils and silanol groups present on the silica surface, direct evidence of such interactions is lacking. This is mostly due to the challenging task of surface- and/or interface-specific characterization. On the one hand, imaging techniques such as transmission electron microscopy can provide excellent spatial resolution of the interfacial layer but require sophisticated data processing to reveal chemical information.[28] On the other hand, standard spectroscopic techniques are not surface (interface)-selective, and therefore, signals from the surface are usually obscured by those from the bulk of the sample. This applies to the single-pulse ^{1}H solid-state nuclear magnetic resonance (ssNMR) study of silica, in which moisture often produces a much stronger signal than those of silanols, necessitating exhaustive drying prior to the measurement.[29−32] For silica-filled elastomer composites, the dominating signals of the elastomer matrix make it even more difficult to observe the silica surface. Due to a lack of suitable characterization techniques, an increasing number of research groups have often turned to theoretical approaches (e.g., Hansen solubility parameters) for understanding and predicting adsorption on the silica surface.[14]

Received: May 13, 2021
Revised: July 11, 2021
Published: August 18, 2021

Table 1. Composition of Oil-Adsorbed *d*-Silicas Used for the ssNMR Study

sample	composition (grams)							
	d-silica	TDAE	SBO	SBO-E20	SBO-E40	SBO-E50	SBO-E75	SBO-E100
TDAE@*d*-silica	0.2	0.02						
SBO@*d*-silica	0.2		0.02					
SBO-E20@*d*-silica	0.2			0.02				
SBO-E40@*d*-silica	0.2				0.02			
SBO-E50@*d*-silica	0.2					0.02		
SBO-E75@*d*-silica	0.2						0.02	
SBO-E100@*d*-silica	0.2							0.02

The aim of this work is to study the molecular interactions between SBOs and the silica surface using ssNMR. The ssNMR technique of choice is $\{^1H-^{29}Si-\}^1H$ double cross-polarization (CP) inverse detection, which consists of two CP steps: $^1H \rightarrow {}^{29}Si$ (for the buildup of ^{29}Si magnetization) and $^{29}Si \rightarrow {}^1H$ (for the identification of surface groups).[33−35] CP occurs between dipolar-coupled nuclear spins (typically, ^1H-X or $X-Y$; X, Y = ^{13}C, ^{15}N, ^{29}Si, etc.) within a typical internuclear distance of only a few angstroms, making it ideal for surface-/interface-specific characterization.[33,36−38] Furthermore, since the interaction of species that are adsorbed at the surface will reduce their mobility, the efficiency of the CP transfer will be enhanced by both spatial proximity and the reduced mobility of the adsorbed species. Since the $^1H \rightarrow X$ CP process transfers the magnetization from protons to heteronuclei, it inevitably results in a magnetization difference between the proton-rich heteronuclei and proton-poor ones. In order to alleviate this difference, a multiple-contact CP (MCP) block can be used in the $^1H \rightarrow X$ magnetization transfer step. In fact, MCP has found numerous applications, often in quantitative studies.[39−43] As demonstrated in our recent work,[44] $\{^1H-^{29}Si-\}^1H$ MCP inverse detection (MCPi) is a robust technique that requires only a minimal optimization of acquisition parameters. Here, we refer to MCPi as a semiquantitative method because only the relative ratio of ^1H peak intensities of adsorbed (modified) SBOs and the native surface groups (i.e., the silanol hydroxyls and the physically adsorbed water) is taken to serve as a semiquantitative index of the adsorption affinity.

This work is divided into three parts: first, a raw SBO is chemically modified through a series of controlled epoxidation reactions in order to obtain SBOs with a wide range of epoxy concentrations, which are quantified by ^1H liquid-state NMR. These SBOs, along with conventional TDAE oil, are later used as process oils for preparing model rubber compounds; second, $\{^1H-^{29}Si-\}^1H$ MCPi ssNMR experiments are performed on a set of deuterated silica/process oil mixtures to evaluate the oil adsorption affinities to the silica surface; and finally, a structure−composition−property relationship is established between the adsorption affinities of these oils and the mixing energies of model rubber compounds.

2. EXPERIMENTAL SECTION

2.1. Materials. The following chemicals were obtained from the respective suppliers and used as received unless otherwise mentioned: styrene-butadiene rubber (SBR, trade name "SPRINTAN SLR 4602" from Trinseo), silica (trade name "ZEOSIL Premium 200MP" from Solvay), TDAE oil (from PSP Specialties, which is a complex mixture of aromatic, naphthenic, and paraffinic hydrocarbons),[45] and SBO (technical grade, from Cargill). Hydrogen peroxide (H_2O_2, 35 wt % in water), acetic acid (CH_3COOH, 99.6%), magnesium sulfate hydrate ($MgSO_4 \cdot 7H_2O$, 99%, later dried to the anhydrous form), dichloromethane (CH_2Cl_2, 99%), and toluene (C_7H_8, 98%) were purchased from Acros Organics. *p*-Toluenesulfonic acid monohydrate (*p*TSA, $C_7H_8O_3S \cdot H_2O$, 98%), deuterium oxide (D_2O, 99.9 D %), deuterated chloroform ($CDCl_3$, ≥99.8 D %, used for preparing silica suspension), and deuterated chloroform [$CDCl_3$, 99.96 D %, containing 0.03 vol % of tetramethyl silane (TMS), used for liquid-state NMR] were purchased from Sigma-Aldrich. Commercially available epoxidized SBO (SBO-E100, tradename "Makplast-SN") was purchased from Makwell Plasticizers. The anhydrous form of magnesium sulfate was prepared by heating a saturated aqueous solution of magnesium sulfate using a hot plate and a stainless-steel pan. The hot plate was set to the maximum heating. All the liquid water was first evaporated, and the heating was continued for an additional ~6−8 h ($T > 200$ °C) to obtain a cake of anhydrous magnesium sulfate. The cake was cooled and broken into small pieces for further use.

2.2. Chemical Modifications of SBO. A series of epoxidized SBOs (SBO-E) were prepared following well-established synthetic procedures.[5,18,19] The digits at the end of their short names indicate the percentage of epoxidation (as quantified by ^1H liquid-state NMR). For example, "SBO-E20" means 20% of the SBO double bonds are epoxidized. Unless indicated otherwise, the SBO-E100 used for preparing rubber compounds is the commercially available product (i.e., from "Makplast-SN"). Nevertheless, we confirm that the difference between the lab-synthesized and the commercial SBO-E100s is negligible.

The general procedures for a small-scale epoxidation of SBO were as follows: SBO (2.10 g, ~2.3 mmol), *p*TSA (0.04 g, ~0.2 mmol), acetic acid (0.35 g, ~5.8 mmol), and toluene (1.25 g) were charged into a 100 mL round-bottom two-neck flask equipped with a magnetic stirrer (Hei-Tec, Heidolph) and a reflux condenser. The mixture was heated up to 50 °C under stirring, and 1.73 g of H_2O_2 solution (17 mmol) was simultaneously added into it dropwise. Then, the temperature was increased to 75 °C and kept constant. After a certain time, the reaction was stopped by removing the reaction mixture from the heating source, which resulted in different degrees of epoxidation (45 min, 2, 4, 6, and 17 h for SBO-E20, -E40, -E50, -E75, and -E100, respectively). In order to remove the residual acetic acid, the mixture was transferred to a separatory funnel and washed with 5 mL of 5 wt % $NaHCO_3$ aqueous solution, which was repeated three times. Then, the residual salts were further removed by three cycles of washing with 5 mL of distilled water. The residual water in the SBOs was absorbed by anhydrous magnesium sulfate. Finally, toluene was removed by rotary evaporation (Rotavapor R-300, Buchi) at room temperature at a pressure of <4 mbar for half an hour, followed by the application of a dynamic vacuum (generated by an oil pump, Edwards RV3, and a liquid-nitrogen-cooled cold trap) of 0.5−4 mbar for 8−12 h. For obtaining a larger batch of the product, the quantities of starting materials used were scaled up accordingly.

All the process oils (TDAE, SBO, and SBO-E) were characterized by liquid-state NMR prior to use in the preparation of model rubber compounds.

2.3. Preparation of Oil-Adsorbed Deuterated Silicas. Preparation of deuterated silica (*d*-silica): In order to attenuate signals from water and silanol protons so that the adsorbed organic species could be easily detected by ssNMR,[46] the as-received silica (unless noted otherwise, this raw silica is referred to as "h-silica" or simply "silica") was subjected to two cycles of deuteration—2 g of h-silica was mixed with 10 mL of D_2O, vortexed for 30 s, and centrifuged at 15,000 rpm for 10 min. The supernatant was decanted, and the first step was repeated with 20 mL of D_2O. The deuterated silica (*d*-silica) was then dried at 100 °C for 4 h and stored in a sealed tube prior to the preparation of the oil-adsorbed silicas. The degree of deuteration was estimated to be ∼63% by comparing the ^{1}H one-pulse ssNMR spectra of h- and *d*-silicas with close moisture (H_2O/D_2O) contents (Figure S1).

The process oil-adsorbed silicas were prepared using the following procedures: *d*-silica (0.2 g) was suspended in 0.5 mL of $CDCl_3$ together with the process oils (0.02 g) (Table 1) in a glass vial (with a screw cap having a polytetrafluoroethylene inner liner). The suspension was vortexed (Phoenix Instrument, RS-VA 10, at maximum speed) for 30 s and left to settle for 1 h. The mixture was then dried at 60 °C in an oven (Memmert, Germany) for 6 h to remove the solvent.

2.4. Preparation of Model Rubber Compounds and Mixing Energy. A series of model rubber compounds (Table 2) were prepared in a HAAKE PolyLab QC internal mixer (Thermo Scientific, see Figure S2). The mixer was equipped with two cam-type rotating blades, and 75% of the free-volume of 85 mL was used for mixing. The rubber, silica (h-silica and *d*-silica in one occasion), and process oils were mixed following the same protocol: 1st step, the mixer was preheated to 80 °C; 2nd step, the rubber was charged into the mixer at a rotor speed of 40 rpm and masticated for 1 min; 3rd step, the rotor speed was slowed down to 3 rpm to allow the addition of silica and processing oils (for the first 2.5 min); and 4th step, the rotor speed was then increased to 80 rpm and continued for overall 10 min. During the 4th stage, the pressing ram was lifted and lowered into the mixing chamber twice (at 6.25 and 8.25 min) to press the rubber against the rotating blades in order to achieve a more homogeneous mixing. Inside the internal mixer, there is a torque sensor (a metallic pin, see Figure S2) which can provide an indication of changes in the sample rheology during the mixing. The dump temperature was found to be 145 ± 5 °C for all samples. The energy consumed by the instrument to perform a preprogrammed mixing procedure (applied to all compounds) is referred to as mixing energy (Figure S3) and is recorded by the control software (HAAKE PolySoft OS).

Table 2. Composition of Silica-Filled Model Rubber Compounds Used for Performing the Mixing Tasks[a]

model rubber compounds	basic composition (phr): "SBR + silica[b] + TDAE"	additional oils (phr)
TDAE−silica−SBR	(100 + 65 + 20)	
SBO−silica−SBR	(100 + 65 + 13.5)	SBO (6.5)
SBO-E20−silica−SBR	(100 + 65 + 13.5)	SBO-E20 (6.5)
SBO-E20(13 phr)−silica−SBR	(100 + 65 + 7.0)	SBO-E20 (13)
SBO-E40−silica−SBR	(100 + 65 + 13.5)	SBO-E40 (6.5)
SBO-E50−silica−SBR	(100 + 65 + 13.5)	SBO-E50 (6.5)
SBO-E75−silica−SBR	(100 + 65 + 13.5)	SBO-E75 (6.5)
SBO-E100−silica−SBR	(100 + 65 + 13.5)	SBO-E100 (6.5)
SBO(20 phr)−silica−SBR	(100 + 65 + 0)	SBO (20)
SBO-E50(20 phr)−silica−SBR	(100 + 65 + 0)	SBO-E50 (20)
SBO-E100(20 phr)−silica−SBR	(100 + 65 + 0)	SBO-E100 (20)
SBO-E100(20 phr)−*d*-silica−SBR	[100 + 65(*d*) + 0]	SBO-E100 (20)

[a] "phr" is a relative weight unit referring to part(s) per hundred parts of rubber, where the 100 phr SBR is equal to 39.7 g. [b] h-Silica was used in all cases except where (*d*) is indicated, implying the use of *d*-silica instead.

2.5. Liquid-State NMR. NMR samples were prepared by dissolving 30 μL of each oil in 600 μL of $CDCl_3$ (containing 0.03% TMS), and the spectra were recorded by using an AVANCE III HD Bruker spectrometer (600 MHz) at 298 K. Quantitative one-dimensional (1D) ^{1}H NMR spectra were recorded by using 30° excitation pulses at a repetition delay of 40 s and a total accumulation of 16 scans. The covalent connectivity of the molecular structures was further confirmed by two-dimensional (2D) ^{1}H−^{1}H correlation spectroscopy with a double quantum filter (COSY-DQF).

2.6. Solid-State NMR. For the ssNMR samples, the oil-adsorbed silicas were loaded into 4 mm zirconium oxide rotors with Kel-F caps (∼70 mg of silica/rotor), and the rotors were spun at a magic angle spinning (MAS) rate of 8 kHz at 303 K in the same NMR spectrometer (as for the liquid-state experiments) equipped with a double resonance probe. The MAS rate of 8 kHz was chosen in order to avoid overlap between isotropic peaks and spinning side bands for both ^{1}H and ^{29}Si. The chemical shifts were externally referenced to TMS, that is, setting the $\delta(^{13}CH_2)$ of adamantane to 37.77 ppm.[47,48]

In order to assess the relative adsorption affinities of the various process oils for the silica surface, two ssNMR techniques were employed: {^{1}H−}^{29}Si MCP and {^{1}H−^{29}Si−}^{1}H MCPi (see Scheme 1). Details concerning the MCPi pulse sequence can be found in our recent report on the topic,[44] and it is applied in this study to investigate the SBO−silica interaction (Scheme 1D). The MCP pulse sequence is slightly different from the "multiCP" sequence reported by Schmidt-Rohr and co-workers,[39,40] except that the last CP period in "multiCP" was replaced by a simple ^{29}Si 90° readout pulse in MCP (Scheme 1A) in order to reflect the true ^{29}Si polarization right before the ^{29}Si → ^{1}H CP step in the MCPi experiment (Scheme 1B,C). Nevertheless, the optimization of the MCP sequence followed the same principles of "multiCP", and a rapid optimization of parameters was found to be sufficient for a semiquantitative analysis as in this study: first, the recycle delays (RDs) needed for ^{1}H thermal equilibrium polarization and 99.3% of equilibrium (RD = 5 × $T_{1,H}$) were estimated in a series of ^{1}H MAS experiments (Figure S4A,B), repolarization delay (t_{rep}) was set as 2 × $T_{1,H}$, the contact time of single CP step (t_{cp}) was optimized in a series of ^{29}Si MCP experiments when the number of CP period (m) was fixed at 1 (Figure S4C), and then, m was optimized using the optimal t_{cp} from the previous step (Figure S4D). The optimal parameters were chosen to maximize the ^{29}Si intensity of the Q^3 group, as it is the main contributor for HB, and to enhance the Q^4 group to a moderate level. If not stated otherwise in the figure caption, the following acquisition parameters were used for the pulse sequences shown in Scheme 1A−C: RD = 3 s, t_{rep} = 1 s, ^{1}H−^{29}Si 90° pulse lengths of 2.9/5.0 μs, spin lock field strength (B_1) on the ^{29}Si channel during CP was 50 kHz and a ramp pulse (34 to 60 kHz) on the ^{1}H, all CP durations t_{cp} were set to 10 ms for MCP and MCPi (including the last inverse ^{29}Si → ^{1}H CP period), six CP contacts (m = 6), two long low-power saturation pulses (90° out of phase) for proton (t_{sat} = 0.5 s), and a total accumulation of 4096 scans for each spectrum. In addition, the number of t_1 increments for ^{1}H−^{29}Si 2D HETCOR was 128 with an accumulation of 64 scans for each increment. Note that a delay of 1 s was inserted before the last ^{29}Si 90° pulse in Scheme 1A (corresponding to t_{sat} × 2 in Scheme 1B,C). The ^{1}H MAS spectra shown in the next section were acquired with RD = 2 s and four scans. All solid and liquid NMR spectra were processed in TopSpin 4.0 software.

3. RESULTS AND DISCUSSION

3.1. Synthesis and Characterization of (Modified) SBOs. SBO is a triglyceride whose three fatty acid chains are a mixture of saturated, linolenic, linoleic, and oleic acyl groups (Figure 1).[49−51] The percentages of these acyl groups are slightly different depending on the variety of the soybean crop as well as the region and conditions of production.[51] The

Scheme 1. (A,B) Diagrams of the Pulse Sequences of $^1H-^{29}Si$ MCP ssNMR Experiments: (A) ^{29}Si Detected (MCP), (B) ^1H (i.e., Inverse) Detection (MCPi), (C) 2D MCPi-HETCOR, and (D) Directions of Polarization Transfer: ① $^1H \rightarrow {}^{29}Si$ in (A) and ② $^1H \rightarrow {}^{29}Si \rightarrow {}^1H$ in (B)

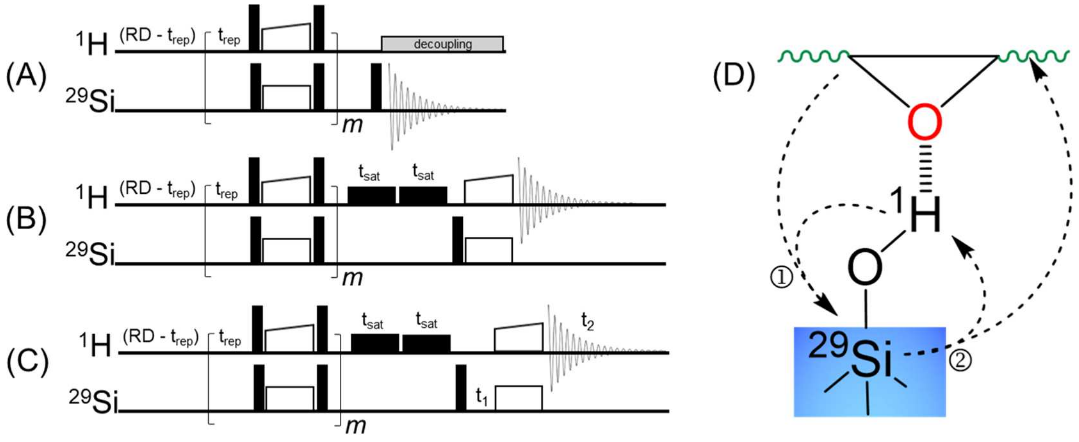

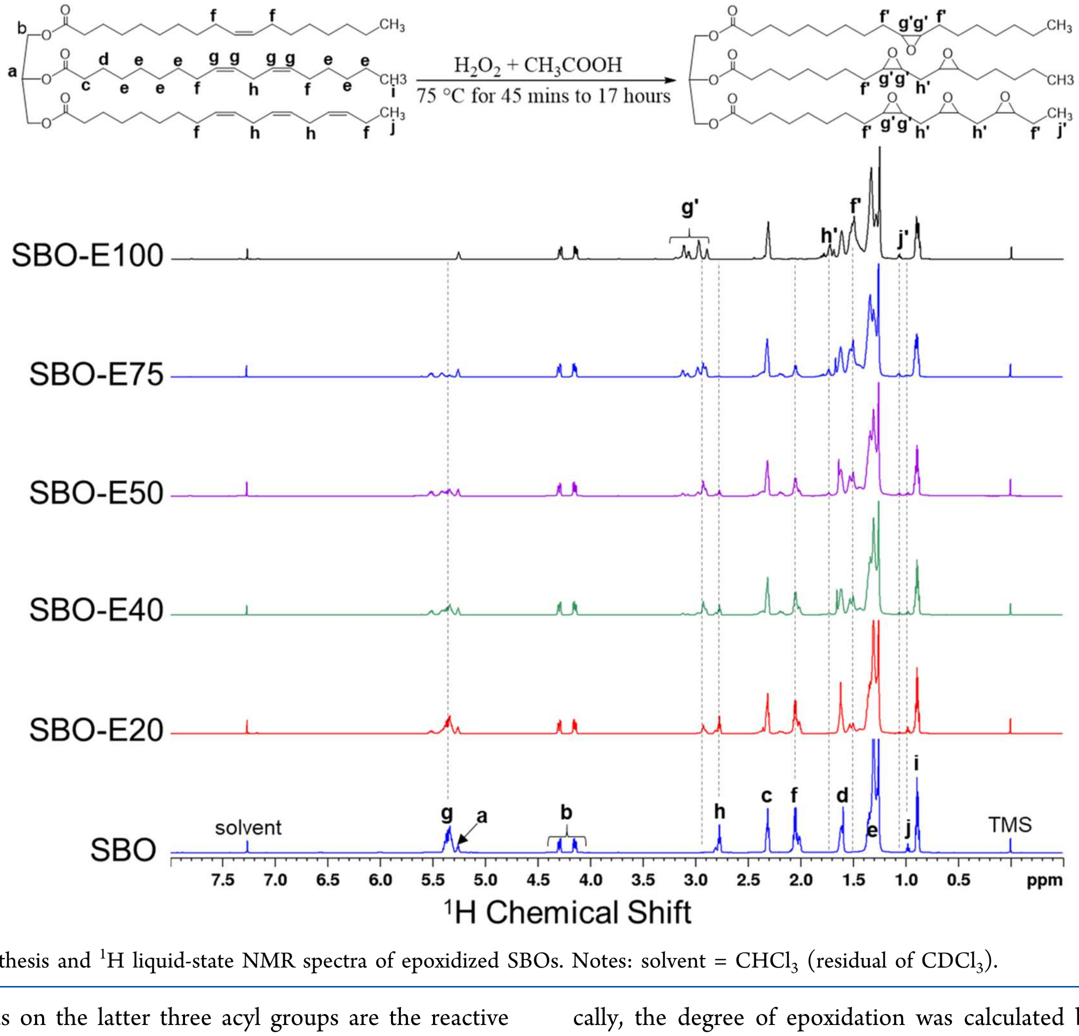

Figure 1. Synthesis and ^1H liquid-state NMR spectra of epoxidized SBOs. Notes: solvent = $CHCl_3$ (residual of $CDCl_3$).

double bonds on the latter three acyl groups are the reactive groups in an epoxidation reaction (Figure 1). The experimental protocol for epoxidation of vegetable oils (including SBO, palm oil, sunflower seed oil, etc.) is well established in the literature.[5,18−21,52] In this work, the degrees of epoxidation of epoxidized SBOs (SBO-E) were quantified by ^1H liquid-state NMR (Figures S5 and S6) and are reflected in the materials' names. For example, SBO-E50 provides an epoxidation level of approximately 50% (Table S1). Specifically, the degree of epoxidation was calculated based on the decrease in the integration of the double-bond protons, that is, peak H_g (5.3−5.7 ppm) (Figure 1). The spectral difference between SBO-E100 synthesized in-house and the commercial one (Figure S5, top) was observed to be negligible (100 vs 97%, Table S1). Throughout this work, SBO-E100 is referred to the commercial one if not otherwise noted.

The structural characterization of these oils by 1D and 2D NMR spectroscopy is also well known.[12,15,17,20−22,49−51,53]

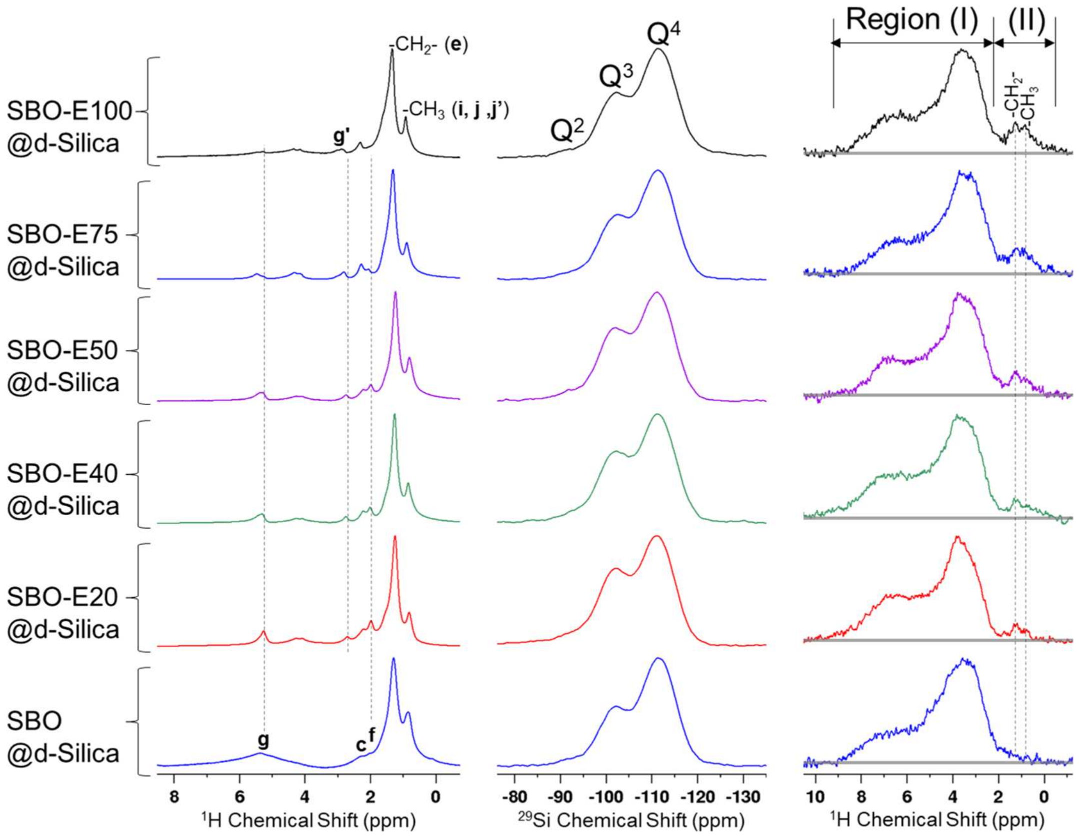

Figure 2. Left to right columns: ^{1}H MAS, {^{1}H−}^{29}Si MCP, and {^{1}H−^{29}Si−}^{1}H MCPi spectra of SBO-adsorbed *d*-silicas. Note: $Q^2/Q^3/Q^4$ = geminal/silanol/siloxane groups, respectively. The {^{1}H−^{29}Si−}^{1}H MCPi spectrum consists of two regions: (I) the native groups, i.e., silanol and physisorbed water; (II) the adsorbed organic groups, i.e., methylene and methyl.

Overall, the assignments of ^{1}H chemical shifts (Figure 1) for the molecular structures of unmodified SBO and SBO-E100 were in excellent agreement with previous reports,[20,49−51] and ^{1}H−^{1}H COSY-DQF provided further confirmation of the connectivity between different functional groups within the molecular structures (Figure S7).

3.2. Adsorption of SBOs on the Silica Surface. The adsorption of polymers, additives, and even medicinal molecules onto silica surfaces has attracted considerable attention in recent years because a molecular understanding of the surface chemistry of silica is critical for designing high-performance composite materials, efficient drug delivery systems, and better catalysts for organic reactions.[54−56] Therefore, the aim of this section is to better understand what happens at the silica surface when process oils of different chemical structures are mixed with silica via ^{1}H−^{29}Si CP (the next section will be dedicated to interactions at the silica surface within a rubber matrix). The oil-to-silica ratio was kept constant at 1:10 by weight, which is a typical concentration in the "green tire" technology.[12,16,57] Here, the as-received silica was partially deuterated ("*d*-silica") in order to suppress the dominating ^{1}H NMR signals of the native surface species, that is, physically adsorbed water and silanols. The first experiment performed with these samples was standard ^{1}H MAS ssNMR (Figures 2 and S8, left columns). As can be seen in Figure S8 (bottom left), there were mainly three weak ^{1}H peaks observed for the bare *d*-silica (6−9, ∼4.7, and ∼3.8 ppm). The broad peak in the 6−9 ppm range was attributed to residual hydrogen-bonded silanols (HB-silanols), the peak at ∼4.7 ppm to physically adsorbed water, and the peak at ∼3.8 ppm possibly to weakly hydrogen-bonded silanols and possible confined water.[29−32,58] As for the SBO-adsorbed silicas (Figure 2), the dominating ^{1}H peaks were those identified in the liquid-state ^{1}H spectra of the SBOs (Figures 1 and S5). For example, the peaks H_g and H_f related to the double bonds were still obvious for less-epoxidized SBOs, whereas the peak H_c from acyl $-CH_2-$ groups was present for all SBOs. Moreover, the peaks H_e, H_i, H_j, and $H_{j'}$ (i.e., $-CH_2-$ and $-CH_3$ groups) were merged into two broad peaks centered around 1.3 and 0.9 ppm, which were also present in the sample of TDAE@*d*-silica (Figure S8, top-left).

The second experiment performed on the SBO-adsorbed *d*-silicas was {^{1}H−}^{29}Si MCP NMR (Figures 2 and S7, middle columns). As mentioned in the Introduction, one of the advantages of using the MCP-block is its ability to achieve similar ^{29}Si polarizations even though there are different abundances of the ^{1}H-species present on the silica surface. As can be seen in the {^{1}H−}^{29}Si MCP spectra (Figures 2 and S7, middle columns), the signal-to-noise ratios for the silanediol (Q^2, −90.8 ppm), silanol (Q^3, −101.7 ppm), and siloxane (Q^4, −111.2 ppm) peaks are very similar from sample to sample. The relative ratio between Q^3 and Q^4 was also very similar for all samples except the bare "*d*-silica" (slightly higher).

Moreover, a series of 1D {^{1}H−^{29}Si−}^{1}H MCPi experiments were carried out (Figures 2 and S8, right columns). These experiments were aimed at locating the organic groups in close proximity to the silica surface. The ^{1}H one-pulse spectrum of the bare "*d*-silica" (Figure S8, bottom left) is different from its {^{1}H−^{29}Si−}^{1}H MCPi spectrum in terms of the relative peak intensity. For example, the intensity of the HB-silanols (6−9

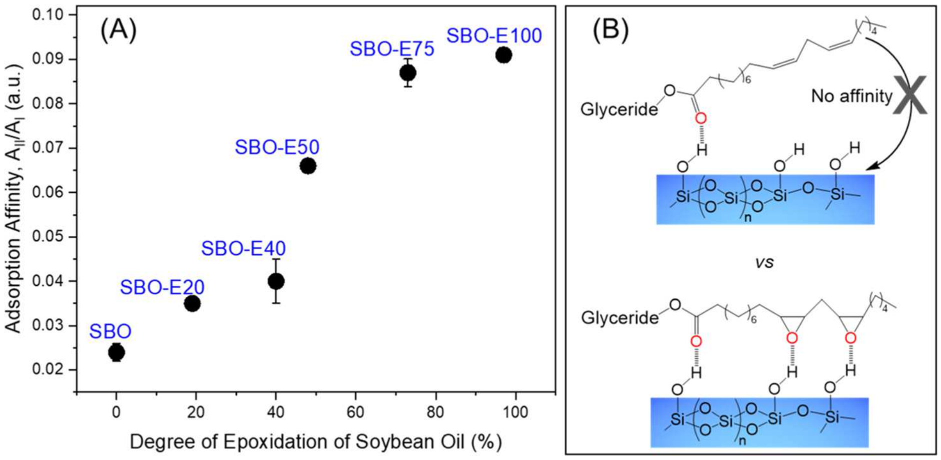

Figure 3. (A) Correlation between the silica−SBO adsorption affinity and the degree of epoxidation of SBOs. (B) Proposed mechanism for the increased silica−SBO adsorption affinity with increasing degrees of epoxidation. The hydrogen bonding interaction between C═O and silanol groups was proposed in the recent literature[10] and supported in this work by the observed adsorption affinity of SBO as compared to the baseline value measured on the bare *d*-silica (i.e., 0.024 vs 0.009, see Table S2).

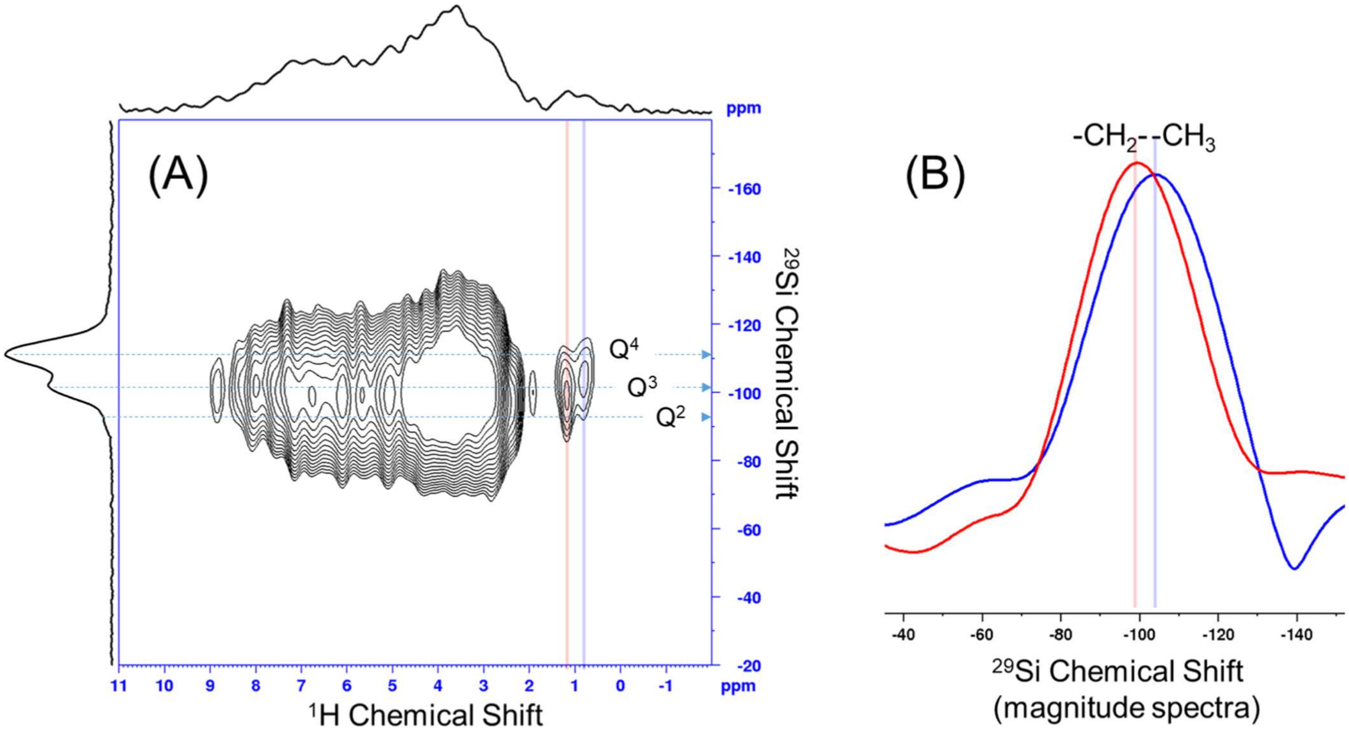

Figure 4. (A) $^{1}H-^{29}Si$ MCPi-HETCOR spectrum of SBO-E100@*d*-silica: for clarity, the projection on the ^{29}Si dimension is an external one using the corresponding $\{^{1}H-\}^{29}Si$ MCP spectrum from Figure 2. (B) Cross sections along the indicated vertical lines of (A).

ppm) is higher in the MCPi spectrum than in the one-pulse spectrum, as expected, due to the fact that the HB-silanols' protons are closer to the surface ^{29}Si than the physisorbed water (~4.7 ppm). For the raw "*d*-silica", the 2−0 ppm region of the $\{^{1}H-^{29}Si-\}^{1}H$ MCPi spectrum is essentially as flat as the spectral baseline (Figure S8, bottom right). In contrast, in the $\{^{1}H-^{29}Si-\}^{1}H$ MCPi spectra of the SBO-adsorbed *d*-silicas (Figure 2, right columns), the intensities of the "$-CH_2-$" and "$-CH_3$" peaks increase with a higher degree of SBO epoxidation. These $\{^{1}H-^{29}Si-\}^{1}H$ MCPi spectra consist of two regions (I/II). "Region I" covers the ^{1}H peaks of native species on the silica surface, whereas "region II" covers the ^{1}H peaks of "$-CH_2-$" and "$-CH_3$" groups that are associated with the adsorbed oils. Although other peaks (such as those for H_g, H_c, H_f, or $H_{g'}$) from the process oils might also be hidden under the broad "region I", their contributions to the deconvoluted peaks (Figure S9 and Table S2) can be largely neglected because the intensities of these peaks are significantly smaller than those of the $-CH_2-/-CH_3$ groups (Figures 2 and S8, left columns) and, therefore, much smaller than those of the silanols and physisorbed water.

Since the mass ratio of SBO to *d*-silica in these oil-adsorbed silica samples (Figure 2) was fixed and the only difference between these samples was the degree of epoxidation, the ratio of ^{1}H integral region-II to region-I (A_{II}/A_{I}) could, therefore, serve as a semiquantitative measurement of the SBOs−silica adsorption affinity. As expected, the more epoxidized the SBO is, the higher affinity it has (Table S2 and Figure 3A), that is,

SBO < SBO-E20 < E40 < E50 < E75 < E100. The TDAE oil has an adsorption affinity similar to SBO (Table S2). This correlation of adsorption affinity with the epoxidation degree can be explained by the HB interactions between the epoxy and the silanol groups. The more epoxidized the SBO is, the more epoxy groups it has, the more HB bonds can form between the SBO and silica, and the closer the glyceride chain is drawn to the silica surface (Figure 3B).

The close proximity of epoxidized SBOs to the silica surface was revealed by the proton-detected 2D ^{1}H−^{29}Si HETCOR experiment (Figure 4). As can be seen, the "−CH$_2$−" and "−CH$_3$" cross peaks are centered around the Q^3 peak (though one is slightly shifted toward the Q^2 peak, while the other slightly shifted toward Q^4). These results confirm that the Q^3 group on the silica surface is the main contributor for the SBOs−silica interaction.

3.3. Effects of Epoxidation on Mixing Energy.

In this section, we assess the significance of the semiquantitative index of adsorption affinity in industrial scenarios, that is, elastomer processing. To this end, we recorded the mixing energies for two sets of model rubber compounds, prepared by partial (6.5/13 phr) or full (20 phr) substitution of TDAE by SBOs (Table 2 and Figure S10).

Higher torque response during mixing indicates higher rubber compound viscosities, while a torque value that remains constant with time is interpreted as indicative of the realization of a homogeneous rubber compound. Three representative torque−time evolution curves are shown in Figure 5. In step ①, there is only rubber present, so the torque responses are effectively identical for all the samples. After the silica and oils are added (Figure 5, step ②), the torque responses began to differ. After two cycles of ram-down pressing [Figure S2, part (a)], the torque response for the SBO-E100-containing compound levels out (Figure 5, step ⑤), indicating that homogeneity is reached. These effects of SBOs on the torque response of rubber compounds were consistent with a recent report by Datta Sarma et al.[59] By visual inspection, the texture of the prepared rubber compounds (Figure S10) where TDAE oil has been partially substituted by SBO-E100 appears more homogeneous as compared to those containing only TDAE ("TDAE−silica−SBR") or nonmodified SBO ("SBO−silica−SBR", "SBO(20phr)−silica−SBR", and "SBO(20phr)−*d*-silica−SBR").

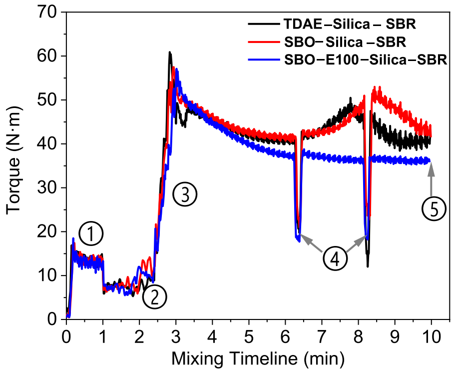

Figure 5. Torque evolution during the mixing of model rubber compounds. ① Rubber is charged and masticated at a low speed; ② silica and process oils are added; ③ all ingredients are mixed at a higher speed; ④ the pressing ram is raised and lowered (twice); and ⑤ end of the preprogrammed mixing tasks.

As shown in Table 3, the mixing energies of model rubber compounds vary with different concentrations (phr) of various process oils. With the partial substitution of TDAE (i.e., by 6.5 or 13 phr SBO), there is a 4−8% reduction in mixing energy, where the use of SBO-E100 leads to the largest reduction and the use of unmodified SBO causes an increase instead (i.e., negative reduction). A plot of mixing energy versus the epoxy concentration (and adsorption affinity index) shows a decreasing trend (Figure 6). This trend is consistent with the observations that epoxidized vegetable oils improved the processability of silica-filled rubber compounds.[10,12,59]

Table 3. Mixing Energies of Different Model Compounds[a]

model compounds	mixing energies (kJ)
TDAE−silica−SBR	174.3 ± 1.7
SBO−silica−SBR	181.4 ± 1.2
SBO-E20−silica−SBR	174.5 ± 4.3
SBO-E20(13 phr)−silica−SBR	166.9 ± 1.8
SBO-E40−silica−SBR	165.0 ± 2.0
SBO-E50−silica−SBR	163.9 ± 0.3
SBO-E75−silica−SBR	164.7 ± 3.0
SBO-E100−silica−SBR	161.0 ± 2.3
SBO(20phr)−silica−SBR	188.9 ± 2.1
SBO-E50(20phr)−silica−SBR	171.0 ± 2.1
SBO-E100(20phr)−silica−SBR	186.6 ± 9.0

[a] Unless noted otherwise, all samples contain 13.5 phr TDAE + 6.5 phr TDAE or SBOs.

One interesting addendum to this discussion is the fact that when TDAE oil is fully substituted with (raw or epoxidized) SBOs, the mixing energies are not significantly reduced (Table 3). Instead, the mixing energies increased by ∼8% when 20 phr SBO or SBO-E100 was used in the place of 20 phr TDAE oil,

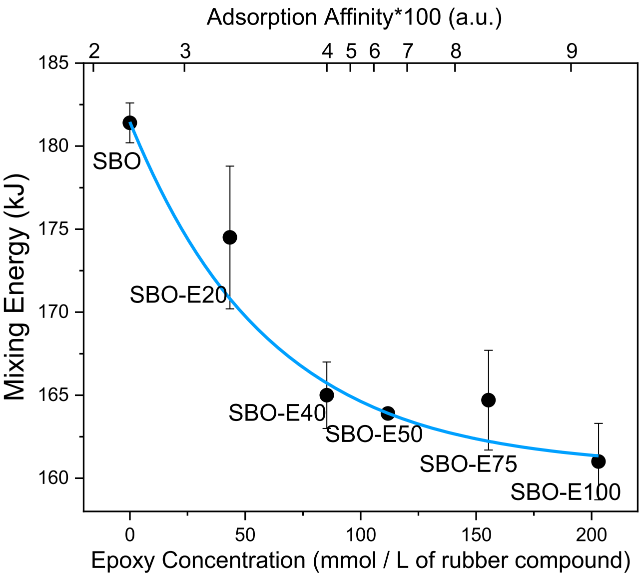

Figure 6. Effects of epoxy concentration (bottom *X*-axis) and adsorption affinity (top *X*-axis) on the mixing energies (*Y*-axis) of model rubber compounds (formula = SBR +13.5 phr TADE + 6.5 phr SBOs). Note that the spacing on the top *X*-axis is not linearly scalable with the epoxy concentration (bottom *X*-axis) due to the nonlinear relationship between the adsorption affinity and the degree of epoxidation seen in Figure 3A. The solid line serves as a guide to the eye.

while the reduction brought about by the use of 20 phr SBO-E50 is marginal. This phenomenon is probably due to the dual role of process oils, that is, hydrophobization and plasticization.[5,8,10,12,16] On the one hand, the adsorption of process oils on the silica surface renders it more hydrophobic (compared to the native surface covered by silanols and physisorbed water) and thus increases the compatibility between silica and SBR. As a result, the incorporation of silica is facilitated. On the other hand, the oil molecules also act as plasticizers, aiding in the mastication of SBR by reducing its viscosity. This dual role of process oils could explain why the complete replacement of TDAE oil by SBO-E50 leads to a lower mixing energy than the complete replacement by unmodified SBO or SBO-E100: (1) unmodified SBO is more soluble in the rubber phase but experiences limited adsorption on the silica surface, meaning that silica−rubber friction is not significantly reduced; (2) SBO-E100 has a greater affinity to the silica surface but is more polar than the unmodified SBO, making it less compatible with the rubber matrix and less efficient as a plasticizer; (3) SBO-E50 provides intermediate levels of both hydrophobization and plasticization, resulting in a reasonable efficiency in both roles and reducing mixing energy. In contrast, when considering only partial replacement of the TDAE oil, the TDAE oil is posited to take on the role of the primary plasticizer, making the adsorption-induced silica hydrophobization by the (modified) SBO the primary determinant of the mixing energy.

Finally, an attempt (Figure S11) was made to perform the same set of ssNMR experiments (as shown in Figure 2) on rubber compounds, in which molecular interactions are assumed to be much more complex. It was found that the A_{II}/A_{I} ratio of SBO-E100 was much smaller in the rubber compound (Figure S11, top row) than in the simple mixture with *d*-silica (Figure 2) even after the mass ratio of SBO-E100 to *d*-silica has been increased from 1:10 to ∼1:3 (20 phr:65 phr), indicating that the amount of SBO-E100 located at the silica surface is lower in the compound than in the mixture. This likely results from the partitioning of the SBO-E100 oil between the rubber phase and the silica surface. In addition, the results shown in Figure S11 also suggest that deuteration of the silica is greatly helpful for observing the weak ^{1}H aliphatic group signals (i.e., region II of the MCPi spectra as shown in Figure 2). The production of actual rubber compounds using *d*-silica, while not practical in this work, could represent a long-term strategy for gaining a better understanding of what happens in such compounds.

4. CONCLUSIONS

In order to establish structure-to-property relationships describing the behavior of process oils in the context of silica-filled rubber processing, we proposed to semiquantitatively measure the adsorption affinities of a series of SBOs using a ssNMR technique called $\{^{1}H-^{29}Si-\}^{1}H$ MCPi. The results showed that the mixing energies of model silica-filled rubber compounds correlate very well with the adsorption affinities of the SBOs, which confirmed a long-held hypothesis: the vegetable oil−silica interaction is responsible for aiding the rubber processing. One of the major limitations encountered within this study was related to the deuteration of the silica surface, the imperfection of which caused certain difficulties in the spectral fitting and in observing the remaining sites of SBOs on the silica surface. In future studies, one could consider a more sophisticated deuteration procedure such as applying sonication and using other more efficient deuterating agents. Overall, the findings shown in this study open up a wide range of opportunities for the semiquantitative study of surface interactions, such as the interactions of medicinal molecules, polymers, additives, and catalysts with silica/silicate in the applications of drug delivery, nanocomposite materials, and high-performance catalysts.

■ ASSOCIATED CONTENT

Supporting Information

The Supporting Information is available free of charge at https://pubs.acs.org/doi/10.1021/acs.langmuir.1c01280.

> Extended liquid-state and solid-state NMR data, information of the optimization of the ssNMR experiments, and detailed information about the internal mixer (PDF)

■ AUTHOR INFORMATION

Corresponding Author

Reiner Dieden − *Department of "Materials Research and Technology", Luxembourg Institute of Science and Technology, L-4362 Esch-sur-Alzette, Luxembourg;* orcid.org/0000-0001-5116-1742; Phone: (+352) 275 888 4576; Email: reiner.dieden@list.lu

Authors

Chuanyu Yan − *Department of "Materials Research and Technology", Luxembourg Institute of Science and Technology, L-4362 Esch-sur-Alzette, Luxembourg; Faculty of Science, Technology and Medicine, University of Luxembourg, L-4365 Esch-sur-Alzette, Luxembourg*

Arpan Datta Sarma − *Department of "Materials Research and Technology", Luxembourg Institute of Science and Technology, L-4362 Esch-sur-Alzette, Luxembourg; Faculty of Science, Technology and Medicine, University of Luxembourg, L-4365 Esch-sur-Alzette, Luxembourg*

Enzo Moretto − *Department of "Materials Research and Technology", Luxembourg Institute of Science and Technology, L-4362 Esch-sur-Alzette, Luxembourg; Faculty of Science, Technology and Medicine, University of Luxembourg, L-4365 Esch-sur-Alzette, Luxembourg*

Jean-Sébastien Thomann − *Department of "Materials Research and Technology", Luxembourg Institute of Science and Technology, L-4362 Esch-sur-Alzette, Luxembourg*

Pierre Verge − *Department of "Materials Research and Technology", Luxembourg Institute of Science and Technology, L-4362 Esch-sur-Alzette, Luxembourg;* orcid.org/0000-0001-9844-0394

Daniel Schmidt − *Department of "Materials Research and Technology", Luxembourg Institute of Science and Technology, L-4362 Esch-sur-Alzette, Luxembourg;* orcid.org/0000-0003-2511-1906

François Kayser − *Goodyear Innovation Center Luxembourg, L-7750 Colmar Berg, Luxembourg*

Complete contact information is available at:
https://pubs.acs.org/10.1021/acs.langmuir.1c01280

Notes

The authors declare no competing financial interest.

■ ACKNOWLEDGMENTS

This work was supported by the Luxembourg National Research Fund (FNR) (IPBG16/11514551/TireMat-Tech).

■ REFERENCES

(1) Poliakoff, M.; Fitzpatrick, J. M.; Farren, T. R.; Anastas, P. T. Green Chemistry: Science and Politics of Change. *Science* **2002**, *297*, 807.

(2) Poliakoff, M.; Licence, P. Sustainable Technology—Green Chemistry. *Nature* **2007**, *450*, 810−812.

(3) Chen, H.; Wang, W.; Martin, J. C.; Oliphant, A. J.; Doerr, P. A.; Xu, J. F.; DeBorn, K. M.; Chen, C.; Sun, L. Extraction of Lignocellulose and Synthesis of Porous Silica Nanoparticles from Rice Husks: A Comprehensive Utilization of Rice Husk Biomass. *ACS Sustainable Chem. Eng.* **2013**, *1*, 254−259.

(4) Bahrami, A.; Simon, U.; Soltani, N.; Zavareh, S.; Schmidt, J.; Pech-Canul, M. I.; Gurlo, A. Eco-Fabrication of Hierarchical Porous Silica Monoliths by Ice-Templating of Rice Husk Ash. *Green Chem.* **2017**, *19*, 188−195.

(5) Sahakaro, K.; Beraheng, A. Epoxidized Natural Oils as the Alternative Safe Process Oils in Rubber Compounds. *Rubber Chem. Technol.* **2011**, *84*, 200−214.

(6) Kim, W.; Argento, A.; Flanigan, C.; Mielewski, D. F. Effects of Soy-Based Oils on the Tensile Behavior of EPDM Rubber. *Polym. Test.* **2015**, *46*, 33−40.

(7) Mauck, S. C.; Wang, S.; Ding, W.; Rohde, B. J.; Fortune, C. K.; Yang, G.; Ahn, S.-K.; Robertson, M. L. Biorenewable Tough Blends of Polylactide and Acrylated Epoxidized Soybean Oil Compatibilized by a Polylactide Star Polymer. *Macromolecules* **2016**, *49*, 1605−1615.

(8) Shafranska, O.; Webster, D. C.; Chisholm, B. J.; McFarlane, S.; Tardiff, J. Modified Soybean Oil as a Processing Oil for Styrene-Butadiene Rubber Tire Tread Compounds. *Tire Sci. Technol.* **2019**, *47*, 280−291.

(9) Hassan, A. A.; Formela, K.; Wang, S. Reclaimed Rubber in Situ Grafted with Soybean Oil as a Novel Green Reactive Plasticizer in SBR/Silica Compounds. *ACS Sustainable Chem. Eng.* **2019**, *7*, 14991−15001.

(10) Hayichelaeh, C.; Reuvekamp, L. A. E. M.; Dierkes, W. K.; Blume, A.; Noordermeer, J. W. M.; Sahakaro, K. Silica-Reinforced Natural Rubber Tire Tread Compounds Containing Bio-Based Process Oils. I: Aspects of Mixing Sequence and Epoxide Content. *Rubber Chem. Technol.* **2019**, *93*, 360−377.

(11) Espósito, L. H.; Marzocca, A. J. Silica-Filled S-SBR with Epoxidized Soybean Oil: Influence of the Mixing Process on Rheological and Mechanical Properties of the Compound. *J. Appl. Polym. Sci.* **2020**, *137*, 48504.

(12) Hayichelaeh, C.; Reuvekamp, L. A. E. M.; Dierkes, W. K.; Blume, A.; Noordermeer, J. W. M.; Sahakaro, K. Silica-Reinforced Natural Rubber Tire Tread Compounds Containing Bio-Based Process Oils. II: Influence of Epoxide and Amino Functional Groups. *Rubber Chem. Technol.* **2020**, *93*, 195−207.

(13) Siriwong, C.; Khansawai, P.; Boonchiangma, S.; Sirisinha, C.; Sae-Oui, P. The Influence of Modified Soybean Oil as Processing Aids in Tire Application. *Polym. Bull.* **2021**, *78*, 3589−3606.

(14) Sovtić, N.; Predrag, K. S.; Bera, O. J.; Pavličević, J. M.; Govedarica, O. M.; Jovičić, M. C.; Govedarica, D. D. A Review of Environmentally Friendly Rubber Production using Different Vegetable Oils. *Polym. Eng. Sci.* **2020**, *60*, 1097−1117.

(15) Wang, Z.; Zhang, X.; Wang, R.; Kang, H.; Qiao, B.; Ma, J.; Zhang, L.; Wang, H. Synthesis and Characterization of Novel Soybean-Oil-Based Elastomers with Favorable Processability and Tunable Properties. *Macromolecules* **2012**, *45*, 9010−9019.

(16) Petrović, Z. S.; Ionescu, M.; Milić, J.; Halladay, J. R. Soybean Oil Plasticizers as Replacement of Petroleum Oil in Rubber. *Rubber Chem. Technol.* **2013**, *86*, 233−249.

(17) Wang, Z.; Han, Y.; Huang, Z.; Zhang, X.; Zhang, L.; Lu, Y.; Tan, T. Plasticization Effect of Hydrogenated Transgenic Soybean Oil on Nitrile-Butadiene Rubber. *J. Appl. Polym. Sci.* **2014**, *131*, 40643.

(18) Rangarajan, B.; Havey, A.; Grulke, E. A.; Culnan, P. D. Kinetic Parameters of A Two-Phase Model for in situ Epoxidation of Soybean Oil. *J. Am. Oil Chem. Soc.* **1995**, *72*, 1161−1169.

(19) Petrović, Z. S.; Zlatanić, A.; Lava, C. C.; Sinadinović-Fišer, S. Epoxidation of soybean oil in toluene with peroxoacetic and peroxoformic acids—kinetics and side reactions. *Eur. J. Lipid Sci. Technol.* **2002**, *104*, 293−299.

(20) Biswas, A.; Adhvaryu, A.; Gordon, S. H.; Erhan, S. Z.; Willett, J. L. Synthesis of Diethylamine-Functionalized Soybean Oil. *J. Agric. Food Chem.* **2005**, *53*, 9485−9490.

(21) Farias, M.; Martinelli, M.; Bottega, D. P. Epoxidation of Soybean Oil Using a Homogeneous Catalytic System based on a Molybdenum (VI) Complex. *Appl. Catal., A* **2010**, *384*, 213−219.

(22) Nalawade, P. P.; Mehta, B.; Pugh, C.; Soucek, M. D. Modified Soybean Oil as a Reactive Diluent: Synthesis and Characterization. *J. Polym. Sci., Part A: Polym. Chem.* **2014**, *52*, 3045−3059.

(23) Dasgupta, S.; Agrawal, S. L.; Bandyopadhyay, S.; Chakraborty, S.; Mukhopadhyay, R.; Malkani, R. K.; Ameta, S. C. Characterization of Eco-Friendly Processing Aids for Rubber Compound. *Polym. Test.* **2007**, *26*, 489−500.

(24) Dasgupta, S.; Agrawal, S. L.; Bandyopadhyay, S.; Chakraborty, S.; Mukhopadhyay, R.; Malkani, R. K.; Ameta, S. C. Characterisation of Eco-Friendly Processing Aids for Rubber Compound: Part II. *Polym. Test.* **2008**, *27*, 277−283.

(25) Dasgupta, S.; Agrawal, S. L.; Bandyopadhyay, S.; Mukhopadhyay, R.; Malkani, R. K.; Ameta, S. C. Eco-Friendly Processing Oils: A New Tool to Achieve the Improved Mileage in Tyre Tread. *Polym. Test.* **2009**, *28*, 251−263.

(26) Xu, H.; Fan, T.; Ye, N.; Wu, W.; Huang, D.; Wang, D.; Wang, Z.; Zhang, L. Plasticization Effect of Bio-Based Plasticizers from Soybean Oil for Tire Tread Rubber. *Polymers* **2020**, *12*, 623.

(27) Wang, Z.; Peng, Y.; Zhang, L.; Zhao, Y.; Vyzhimov, R.; Tan, T.; Fong, H. Investigation of Palm Oil as Green Plasticizer on the Processing and Mechanical Properties of Ethylene Propylene Diene Monomer Rubber. *Ind. Eng. Chem. Res.* **2016**, *55*, 2784−2789.

(28) Dohi, H.; Horiuchi, S. Locating a Silane Coupling Agent in Silica-Filled Rubber Composites by EFTEM. *Langmuir* **2007**, *23*, 12344−12349.

(29) Bronnimann, C. E.; Zeigler, R. C.; Maciel, G. E. Proton NMR Study of Dehydration of the Silica Gel Surface. *J. Am. Chem. Soc.* **1988**, *110*, 2023−2026.

(30) Liu, C. C.; Maciel, G. E. The Fumed Silica Surface: A Study by NMR. *J. Am. Chem. Soc.* **1996**, *118*, 5103−5119.

(31) d'espinose de la Caillerie, J.-B.; Aimeur, M. R.; Kortobi, Y. E.; Legrand, A. P. Water Adsorption on Pyrogenic Silica Followed by ^{1}H MAS NMR. *J. Colloid Interface Sci.* **1997**, *194*, 434−439.

(32) Trébosc, J.; Wiench, J. W.; Huh, S.; Lin, V. S.-Y.; Pruski, M. Solid-State NMR Study of MCM-41-type Mesoporous Silica Nanoparticles. *J. Am. Chem. Soc.* **2005**, *127*, 3057−3068.

(33) Baccile, N.; Laurent, G.; Bonhomme, C.; Innocenzi, P.; Babonneau, F. Solid-State NMR Characterization of the Surfactant−Silica Interface in Templated Silicas: Acidic versus Basic Conditions. *Chem. Mater.* **2007**, *19*, 1343−1354.

(34) Folliet, N.; Roiland, C.; Bégu, S.; Aubert, A.; Mineva, T.; Goursot, A.; Selvaraj, K.; Duma, L.; Tielens, F.; Mauri, F.; Laurent, G.; Bonhomme, C.; Gervais, C.; Babonneau, F.; Azaïs, T. Investigation of the Interface in Silica-Encapsulated Liposomes by Combining Solid State NMR and First Principles Calculations. *J. Am. Chem. Soc.* **2011**, *133*, 16815−16827.

(35) Cadars, S.; Guégan, R.; Garaga, M. N.; Bourrat, X.; Le Forestier, L.; Fayon, F.; Huynh, T. V.; Allier, T.; Nour, Z.; Massiot, D. New Insights into the Molecular Structures, Compositions, and Cation Distributions in Synthetic and Natural Montmorillonite Clays. *Chem. Mater.* **2012**, *24*, 4376−4389.

(36) Ben Shir, I.; Kababya, S.; Amitay-Rosen, T.; Balazs, Y. S.; Schmidt, A. Molecular Level Characterization of the Inorganic−Bioorganic Interface by Solid State NMR: Alanine on a Silica Surface, a Case Study. *J. Phys. Chem. B* **2010**, *114*, 5989−5996.

(37) Azaïs, T.; Laurent, G.; Panesar, K.; Nossov, A.; Guenneau, F.; Sanfeliu Cano, C.; Tourné-Péteilh, C.; Devoisselle, J.-M.; Babonneau, F. Implication of Water Molecules at the Silica−Ibuprofen Interface in Silica-Based Drug Delivery Systems Obtained through Incipient Wetness Impregnation. *J. Phys. Chem. C* **2017**, *121*, 26833−26839.

(38) Ben Shir, I.; Kababya, S.; Schmidt, A. Molecular Details of Amorphous Silica Surfaces Determine Binding Specificity to Small Amino Acids. *J. Phys. Chem. C* **2014**, *118*, 7901−7909.

(39) Johnson, R. L.; Schmidt-Rohr, K. Quantitative Solid-State ^{13}C NMR with Signal Enhancement by Multiple Cross Polarization. *J. Magn. Reson.* **2014**, *239*, 44−49.

(40) Duan, P.; Schmidt-Rohr, K. Composite-Pulse and Partially Dipolar Dephased multiCP for Improved Quantitative Solid-State ^{13}C NMR. *J. Magn. Reson.* **2017**, *285*, 68−78.

(41) King, C.; Stein, R. S.; Shamshina, J. L.; Rogers, R. D. Measuring the Purity of Chitin with a Clean, Quantitative Solid-State NMR Method. *ACS Sustainable Chem. Eng.* **2017**, *5*, 8011−8016.

(42) Zhou, N.; Cao, X.; Du, X.; Wang, H.; Wang, M.; Liu, S.; Nguyen, K.; Schmidt-Rohr, K.; Xu, Q.; Liang, G.; Xu, B. Hyper-Crosslinkers Lead to Temperature- and pH-Responsive Polymeric Nanogels with Unusual Volume Change. *Angew. Chem., Int. Ed.* **2017**, *56*, 2623−2627.

(43) Saïdi, F.; Taulelle, F.; Martineau, C. Quantitative ^{13}C Solid-State NMR Spectra by Multiple-Contact Cross-polarization for Drug Delivery: From Active Principles to Excipients and Drug Carriers. *J. Pharm. Sci.* **2016**, *105*, 2397−2401.

(44) Yan, C.; Kayser, F.; Dieden, R. Sensitivity Enhancement via Multiple Contacts in the {^{1}H−^{29}Si}−^{1}H Cross Polarization Experiment: A Case Study of Modified Silica Nanoparticle Surfaces. *RSC Adv.* **2020**, *10*, 23016−23023.

(45) Petchkaew, A.; Sahakaro, K.; Noordermeer, J. M. J. Petroleum-based Safe Process Oils in NR, SBR and their Blends: Study on Unfilled Compounds. Part I. Oil Characteristics and Solubility Aspects. *Kautsch. Gummi Kunstst.* **2013**, *4*, 43−47.

(46) Trebosc, J.; Wiench, J. W.; Huh, S.; Lin, V. S.-Y.; Pruski, M. Studies of organically functionalized mesoporous silicas using heteronuclear solid-state correlation NMR spectroscopy under fast magic angle spinning. *J. Am. Chem. Soc.* **2005**, *127*, 7587−7593.

(47) Morcombe, C. R.; Zilm, K. W. Chemical Shift Referencing in MAS Solid State NMR. *J. Magn. Reson.* **2003**, *162*, 479−486.

(48) Harris, R. K.; Becker, E. D.; Cabral De Menezes, S. M.; Granger, P.; Hoffman, R. E.; Zilm, K. W. Further Conventions for NMR Shielding and Chemical Shifts IUPAC Recommendations 2008. *Solid State Nucl. Magn. Reson.* **2008**, *33*, 41−56.

(49) Jafari, M.; Kadivar, M.; Keramat, J. Detection of Adulteration in Iranian Olive Oils Using Instrumental (GC, NMR, DSC) Methods. *J. Am. Oil Chem. Soc.* **2009**, *86*, 103−110.

(50) Chira, N.; Todasca, C.; Nicolescu, A.; Paunescu, G.; Rosca, S. Determination of the Technical Quality Indices of Vegetable Oils by Modern Physical Techniques. *UPB Sci. Bull. B: Chem. Mater. Sci.* **2009**, *71*, 3−12.

(51) Kim, W.; Rho, H.; Hong, Y.; Yeom, M.; Shin, S.; Yi, J.; Lee, M.-S.; Park, H.; Cho, D. Determination and Comparison of Seed Oil Triacylglycerol Composition of Various Soybeans (Glycine max (L.)) Using H-1-NMR Spectroscopy. *Molecules* **2013**, *18*, 14448−14454.

(52) Vianello, C.; Piccolo, D.; Lorenzetti, A.; Salzano, E.; Maschio, G. Study of Soybean Oil Epoxidation: Effects of Sulfuric Acid and the Mixing Program. *Ind. Eng. Chem. Res.* **2018**, *57*, 11517−11525.

(53) Luo, Q.; Liu, M.; Xu, Y.; Ionescu, M.; Petrović, Z. S. Thermosetting Allyl Resins Derived from Soybean Oil. *Macromolecules* **2011**, *44*, 7149−7157.

(54) Zou, H.; Wu, S.; Shen, J. Polymer/Silica Nanocomposites: Preparation, Characterization, Properties, and Applications. *Chem. Rev.* **2008**, *108*, 3893−3957.

(55) Rimola, A.; Costa, D.; Sodupe, M.; Lambert, J.-F.; Ugliengo, P. Silica Surface Features and Their Role in the Adsorption of Biomolecules: Computational Modeling and Experiments. *Chem. Rev.* **2013**, *113*, 4216−4313.

(56) Brus, J.; Albrecht, W.; Lehmann, F.; Geier, J.; Czernek, J.; Urbanova, M.; Kobera, L.; Jegorov, A. Exploring the Molecular-Level Architecture of the Active Compounds in Liquisolid Drug Delivery Systems Based on Mesoporous Silica Particles: Old Tricks for New Challenges. *Mol. Pharm.* **2017**, *14*, 2070−2078.

(57) Sato, M.; Mihara, S.; Amino, N.; Dierkes, W. K.; Blume, A. Reactivity Study of Mercapto-Silane and Sulfide-Silane with Polymer. *Rubber Chem. Technol.* **2020**, *93*, 319−345.

(58) Brus, J.; Dybal, J. Hydrogen-Bond Interactions in Organically-Modified Polysiloxane Networks Studied by 1D and 2D CRAMPS and Double-Quantum ^{1}H MAS NMR. *Macromolecules* **2002**, *35*, 10038−10047.

(59) Datta Sarma, A.; Federico, C. E.; Staropoli, M.; Nzulu, F.; Weydert, M.; Verge, P.; Schmidt, D. F. Properties of Silica-Filled Rubber Compounds vs. Epoxidized Oil Content and Degree of Epoxidation. *Ind. Crops Prod.* **2021**, *168*, 113600.